



Ricerca di Sistema elettrico

## Development of best estimate numerical tools for LFR design and safety analysis

T. Barani, A. Cammi, C. Castagna, L. Cognini, M. Giola, S. Lorenzi  
L. Luzzi, E. Macerata, A. Magni, M. Mariani, E. Mossini  
M. Negrin, D. Pizzocri  
N. Abrate, R. Bonifetto, S. Dulla, E. Guadagni, G. F. Nallo, P. Ravetto  
L. Savoldi, D. Valerio, R. Zanino  
A. Chierici, L. Chirco, R. Da Vià, F. Franceschini, V. Giovacchini,  
S. Manservisi  
G. Barone, N. Forgione, F. Galleni, S. Khani, R. Marinari, D. Martelli  
G. Caruso, F. Giannetti, V. Narcisi, A. Subioli  
A. Cervone, A. Del Nevo, I. Di Piazza, M. Tarantino

#### Development of best estimate numerical tools for LFR design and safety analysis

T. Barani, A. Cammi, C. Castagna, L. Cognini, M. Giola, S. Lorenzi, L. Luzzi, E. Macerata, A. Magni, M. Mariani, E. Mossini, M. Negrin, D. Pizzocri (POLIMI)  
N. Abrate, R. Bonifetto, S. Dulla, E. Guadagni, G. F. Nallo, P. Ravetto L. Savoldi, D. Valerio, R. Zanino (POLITO)  
A. Chierici, L. Chirco, R. Da Vià, F. Franceschini, V. Giovacchini, S. Manservigi (UNIBO)  
G. Barone, N. Forgione, F. Galleni, S. Khani, R. Marinari, D. Martelli (UNIPI)  
G. Caruso, F. Giannetti, V. Narcisi, A. Subioli (UNIROMA1)  
A. Cervone, A. Del Nevo, I. Di Piazza, M. Tarantino (ENEA)

Gennaio 2019

#### Report Ricerca di Sistema Elettrico

Accordo di Programma Ministero dello Sviluppo Economico - ENEA

Piano Annuale di Realizzazione 2018

Area: Generazione di Energia Elettrica con Basse Emissioni di Carbonio

Progetto: Sviluppo competenze scientifiche nel campo della sicurezza nucleare e collaborazione ai programmi internazionali per il nucleare di IV Generazione.

Linea: Collaborazione ai programmi internazionali per il nucleare di IV Generazione

Obiettivo: Progettazione di sistema e analisi di sicurezza

Responsabile del Progetto: Mariano Tarantino, ENEA

**Titolo**

## Development of best estimate numerical tools for LFR design and safety analysis (2018)

**Descrittori**

**Tipologia del documento:** Rapporto Tecnico  
**Collocazione contrattuale:** Accordo di programma ENEA-MSE su sicurezza nucleare e Reattori di IV generazione  
**Argomenti trattati:** Reattori Nucleari Veloci, Termoidraulica dei reattori nucleari  
 Sicurezza nucleare, Analisi incidentale

**Sommario**

*Nell'ambito della linea LP2, sono state condotte attività di ricerca al fine di sviluppare, aggiornare e convalidare codici di calcolo e modelli numerici per sostenere la progettazione ed effettuare analisi di sicurezza di un reattore veloce refrigerato a metallo liquido. Nell'ambito del PAR 2016, sono state messe in atto delle azioni al fine di integrare e coordinare tali attività. Si sono, pertanto, definite le aree di simulazione e le interconnessioni rilevanti per la progettazione e sicurezza di reattori Gen-IV. Il presente report rappresenta il proseguimento di tale azione. Ognuna di queste aree di simulazione è coperta da uno o più codici e simula un set di fenomeni multi-fisica e multi-scala rilevanti, e.g. termoidraulica di sistema, di contenimento, di sotto-canale, fluidodinamica tridimensionale, termo-meccanica della barretta di combustibile, del fuel assembly e di componenti, generazione di sezioni d'urto e sviluppo di metodi di aggiustamento delle stesse mediante utilizzo di dati sperimentali, dinamica neutronica tridimensionale, rilascio e trasporto di prodotti di fissione, etc. Tale attività fa parte di un'azione di sviluppo e convalida di una piattaforma di calcolo per sistemi nucleari innovativi.*




*Relativamente a sviluppo e convalida, riportate nella parte 2 del presente report, sono state effettuate attività relative a:*

1. *termo-meccanica della barretta di combustibile – supporto allo sviluppo del codice TRANSURANUS.*
2. *termoidraulica di sistema – supporto alla validazione del codice RELAP5-3D per applicazione ai sistemi a piscina*
3. *accoppiamento codici CFD/SYS-TH e loro validazione a fronte delle campagne sperimentali TALL*
4. *dinamica accoppiata neutronica-termoidraulica tridimensionale - sviluppo e applicazione codice FRENETIC*
5. *modellazione multifisica neutronica – termoidraulica - accoppiamento OpenFoam-Serpent*
6. *termoidraulica multifluid/multiphase e analisi di incidenti severi – supporto allo sviluppo e alla validazione del codice SIMMER-III e -IV*
7. *applicazioni CFD alle analisi di fuel blockage*


**Note: --**

**Autori:** T. Barani, A. Cammi, C. Castagna, L. Cognini, M. Giola, S. Lorenzi, L. Luzzi, E. Macerata, A. Magni, M. Mariani, E. Mossini, M. Negrin, D. Pizzocri (**POLIMI**)  
 N. Abrate, R. Bonifetto, S. Dulla, E. Guadagni, G. F. Nallo, P. Ravetto, L. Savoldi, D. Valerio, R. Zanino (**POLITO**)  
 A. Chierici, L. Chirco, R. Da Vià, F. Franceschini, V. Giovacchini, S. Manservigi (**UNIBO**)  
 G. Barone, N. Forgiione, F. Galleni, S. Khani, R. Marinari, D. Martelli (**UNIPI**)  
 G. Caruso, F. Giannetti, V. Narcisi, A. Subioli (**UNIROMA1**)  
 A. Cervone, A. Del Nevo, I. Di Piazza, M. Tarantino (**ENEA**)


**Copia n.**
**In carico a:**

REV.	DESCRIZIONE	DATA	REDAZIONE	CONVALIDA	APPROVAZIONE	
1			NOME			
			FIRMA			
0	EMISSIONE	29/01/2019	NOME	A. Del Nevo	M. Utili	M. Tarantino
			FIRMA			


*(Page intentionally left blank)*

 <b>RICERCA SISTEMA ELETTRICO</b>	<u>Title:</u> Development of BE numerical tools for LFR design and safety analysis (2018)	<u>Distribution</u> <b>PUBLIC</b>	<u>Issue Date</u> 29.01.2019	<u>Pag.</u>
	<u>Project:</u> ADP ENEA-MSE PAR 2017	Ref. ADPFISS-LP2-167	Rev. 0	3 di 163

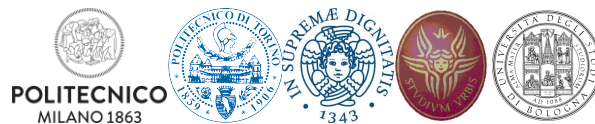
## LIST OF REVISIONS


Revision	Date	Scope of revision	Page
0	29/01/2019	First issue	163



 <b>RICERCA SISTEMA ELETTRICO</b>	<u>Title:</u> Development of BE numerical tools for LFR design and safety analysis (2018)	<u>Distribution</u> <b>PUBLIC</b>	<u>Issue Date</u> 29.01.2019	<u>Pag.</u>
	<u>Project:</u> ADP ENEA-MSE PAR 2017	Ref. ADPFISS-LP2-167	Rev. 0	4 di 163

*(Page intentionally left blank)*




 <b>RICERCA SISTEMA ELETTRICO</b>	<u>Title:</u> Development of BE numerical tools for LFR design and safety analysis (2018)	<u>Distribution</u> <b>PUBLIC</b>	<u>Issue Date</u> 29.01.2019	<u>Pag.</u>
	<u>Project:</u> ADP ENEA-MSE PAR 2017	Ref. ADPFISS-LP2-167	Rev. 0	5 di 163

## LIST OF CONTENTS

<b>LIST OF REVISIONS .....</b>	<b>3</b>
<b>LIST OF FIGURES .....</b>	<b>9</b>
<b>LIST OF TABLES .....</b>	<b>13</b>
<b>LIST OF ABBREVIATIONS .....</b>	<b>15</b>
<b>FOREWORD.....</b>	<b>17</b>
<b>1 THERMO-MECHANICS OF THE FUEL PIN – DEVELOPMENT AND ASSESSMENT OF MODELS AND ALGORITHMS DESCRIBING INERT GAS BEHAVIOR FOR USE IN TRANSURANUS .....</b>	<b>19</b>
1.1 Progress from the results presented in the previous PARs .....	21
1.2 List of References .....	23
<b>2 VALIDATION OF RELAP53D BY CIRCE-ICE EXPERIMENTAL TESTS.....</b>	<b>25</b>
2.1 Background and references .....	27
2.2 Body of the report concerning the ongoing activities .....	28
2.2.1 CIRCE-ICE facility .....	28
2.2.2 Experimental test .....	29
2.2.3 Thermal-hydraulic model .....	29
2.2.4 Simulation results .....	31
2.3 Conclusive remarks .....	32
2.4 List of References .....	45
<b>3 APPLICATION OF RELAP5-3D ON PHENIX EXPERIMENTAL TESTS .....</b>	<b>47</b>
3.1 Background and references .....	49
3.2 Body of the report concerning the ongoing activities .....	49
3.2.1 Phénix reactor .....	49
3.2.2 Dissymmetric test .....	50
3.2.3 Phénix model .....	51
3.2.4 Results .....	53
3.3 Conclusive remarks .....	54
3.4 List of References .....	67
<b>4 DEVELOPMENT AND VALIDATION OF CODES FOR THE COUPLING OF THE OPENFOAM-SALOME-FEMLCORE-CATHARE SOFTWARE FOR THE STUDY</b>	



 <b>RICERCA SISTEMA ELETTRICO</b>	<u>Title:</u> Development of BE numerical tools for LFR design and safety analysis (2018)	<u>Distribution</u> <b>PUBLIC</b>	<u>Issue Date</u> 29.01.2019	<u>Pag.</u>
	<u>Project:</u> ADP ENEA-MSE PAR 2017	Ref. ADPFISS-LP2-167	Rev. 0	6 di 163

## OF 4<sup>TH</sup> GENERATION LEAD-COOLED FAST REACTORS. VALIDATION OF THE COUPLING WITH DATA EXPERIMENTS FROM THE TALL-3D FACILITY..... 69

4.1	Background and reference .....	71
4.2	Developed boundary conditions in OpenFOAM .....	72
4.2.1	Heat exchange with surrounding environment.....	72
4.2.2	Heat exchange with immersed steel disk.....	72
4.2.3	Results obtained with new boundary conditions .....	73
4.3	Model of the TALL-3D test section with simple heat dispersion effects .....	74
4.3.1	Geometry and physical properties of the basic new model .....	74
4.3.2	Boundary conditions.....	75
4.3.3	Initial conditions of the coupled simulation .....	76
4.3.4	CATHARE stand alone and previous model simulations .....	76
4.3.5	Cathare-OpenFOAM coupling with heat dispersion in the TALL-3D test section.....	77
4.4	Role of the activity, general goals and future development.....	77
4.5	List of References .....	96

## 5 THREE-DIMENSIONAL NEUTRONIC-THERMAL-HYDRAULIC DYNAMICS MODELLING: SERPENT-OPENFOAM-FRENETIC COMPARISON AND APPLICATION TO ALFRED DESIGN..... 99

5.1	Introduction.....	101
5.2	ALFRED steady-state critical configuration in FRENETIC .....	101
5.3	ALFRED time-dependent neutronic simulation: safety rod insertion .....	102
5.4	ALFRED time-dependent coupled NE-TH simulations: LOFA.....	102
5.5	ALFRED time-dependent coupled NE-TH simulations: reactivity insertion.....	102
5.6	Conclusive remarks.....	103
	List of References.....	109

## 6 MONTE CARLO – CFD COUPLING FOR LFR MULTIPHYSICS MODELLING .. 111


6.1	Background and references .....	113
6.1.1	Monte Carlo - CFD coupling.....	113
6.2	Body of the report concerning the ongoing activities .....	114
6.2.1	Monte Carlo – CFD coupling techniques.....	114
6.2.2	Full core SERPENT model of the ALFRED reactor.....	117
6.2.3	CFD model for the FA of ALFRED.....	117
6.2.4	SERPENT – OpenFOAM coupling for one-sixth of FA.....	119
6.3	Role of the activity, general goals and future development.....	119
6.4	Activity PAR 2018 – Porous media approach for the LFR design and safety analysis...	120
6.5	List of References .....	129

## 7 SIMMER III-RELAP5 COUPLING CODES DEVELOPMENT ..... 131

7.1	Background.....	133
7.2	Qualitative results .....	133






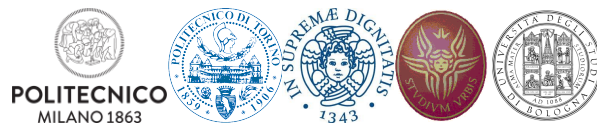
 <b>RICERCA SISTEMA ELETTRICO</b>	<u>Title:</u> Development of BE numerical tools for LFR design and safety analysis (2018)	<u>Distribution</u> <b>PUBLIC</b>	<u>Issue Date</u> 29.01.2019	<u>Pag.</u>
	<u>Project:</u> ADP ENEA-MSE PAR 2017	Ref. ADPFISS-LP2-167	Rev. 0	7 di 163


7.3	Qualitative results .....	133
7.4	List of References .....	138
<b>8</b>	<b>FUEL-COOLANT CHEMICAL INTERACTION.....</b>	<b>139</b>
8.1	Progress of the computational and experimental activities.....	141
<b>9</b>	<b>CFD ANALYSIS OF FLOW BLOCKAGE IN THE ALFRED FA .....</b>	<b>143</b>
9.1	Abstract .....	145
9.2	Introduction.....	145
9.3	Models and Methods.....	147
9.4	Numerical methods .....	147
9.5	Alfred Fa CFD Model And Test Matrix .....	148
9.6	Results and Discussion.....	149
9.7	Conclusions.....	150
9.8	List of References .....	161
	<b>DISTRIBUTION LIST .....</b>	<b>163</b>



 <b>RICERCA SISTEMA ELETTRICO</b>	<u>Title:</u> Development of BE numerical tools for LFR design and safety analysis (2018)	<u>Distribution</u> <b>PUBLIC</b>	<u>Issue Date</u> 29.01.2019	<u>Pag.</u>
	<u>Project:</u> ADP ENEA-MSE PAR 2017	Ref. ADPFISS-LP2-167	Rev. 0	8 di 163

*(Page intentionally left blank)*



 <b>RICERCA SISTEMA ELETTRICO</b>	<b>Title:</b> Development of BE numerical tools for LFR design and safety analysis (2018)	<u>Distribution</u> <b>PUBLIC</b>	<u>Issue Date</u> 29.01.2019	<u>Pag.</u>
	<b>Project:</b> ADP ENEA-MSE PAR 2017	Ref. ADPFISS-LP2-167	Rev. 0	9 di 163

## LIST OF FIGURES

<i>Fig. 2.1 – CIRCE isometric view</i> .....	34
<i>Fig. 2.2 – ICE test section</i> .....	34
<i>Fig. 2.3 – ICE test section: primary flow path</i> .....	35
<i>Fig. 2.4 – FPS cross section</i> .....	36
<i>Fig. 2.5 – HX bayonet tube</i> .....	36
<i>Fig. 2.6 – CIRCE instrumentation: FPS (1)</i> .....	37
<i>Fig. 2.7 – CIRCE instrumentation: FPS (2)</i> .....	38
<i>Fig. 2.8 – CIRCE instrumentation: pool</i> .....	39
<i>Fig. 2.9 – Nodalization scheme: mono-dimensional model</i> .....	40
<i>Fig. 2.10 – Nodalization scheme: multi-dimensional model</i> .....	41
<i>Fig. 2.11 – Nodalization scheme: FPS</i> .....	41
<i>Fig. 2.12 – LBE mass flow rate</i> .....	42
<i>Fig. 2.13 – FPS inlet/outlet temperature</i> .....	42
<i>Fig. 2.14 – HX inlet/outlet temperature</i> .....	42
<i>Fig. 2.15 – DHR inlet/outlet temperature</i> .....	42
<i>Fig. 2.16 – TS and MC: 25000 s</i> .....	43
<i>Fig. 2.17 – TS and MC: 80000 s</i> .....	43
<i>Fig. 2.18 – TS and MC: 200000 s</i> .....	44
<i>Fig. 3.1 – Reactor block</i> .....	55
<i>Fig. 3.2 – Intermediate heat exchanger</i> .....	56
<i>Fig. 3.3 – Reactor top view</i> .....	56
<i>Fig. 3.4 – Primary pump</i> .....	57
<i>Fig. 3.5 – Vessel cooling system flow path</i> .....	57
<i>Fig. 3.6 – Reactor core top view</i> .....	58
<i>Fig. 3.7 – Fuel and fertile SA axial composition</i> .....	58
<i>Fig. 3.8 – Overview of radial and azimuthal meshes of MULTID component</i> .....	59
<i>Fig. 3.9 – Scheme of MULTID component for porosity factor</i> .....	59
<i>Fig. 3.10 – SAs inlet area (m<sup>2</sup>)</i> .....	60
<i>Fig. 3.11 – SAs inlet K loss</i> .....	60
<i>Fig. 3.12 – Pumps, IHXs and VCS nodalization scheme</i> .....	61
<i>Fig. 3.13 – Comparison of the model and design relevant height</i> .....	61
<i>Fig. 3.14 – Steady state conditions</i> .....	62




 <b>RICERCA SISTEMA ELETTRICO</b>	<u>Title:</u> Development of BE numerical tools for LFR design and safety analysis (2018)	<u>Distribution</u> <b>PUBLIC</b>	<u>Issue Date</u> 29.01.2019	<u>Pag.</u>
	<u>Project:</u> ADP ENEA-MSE PAR 2017	Ref. ADPFISS-LP2-167	Rev. 0	10 di 163

Fig. 3.15 – Power removed by IHXs .....	62
Fig. 3.16 – Power % removed by IHXs .....	63
Fig. 3.17 – IHXs outlet coolant temperature.....	63
Fig. 3.18 – Transient conditions.....	64
Fig. 3.19 – Primary pumps inlet temperatures.....	64
Fig. 3.20 – Primary pumps mass flow rate.....	65
Fig. 3.21 – Core temperature .....	65
Fig. 3.22 – IHXS inlet temperatures.....	66
Fig. 4.1 - TALL-3D facility (left) with geometric dimensions (right).....	83
Fig. 4.2 - Experimental data for test series TG03S301(03) [4.9]. .....	83
Fig. 4.3 - STH modeling for TALL-3D. Left, central and right vertical leg (from left to right) in 1D system model with 3D test section [4.9].....	84
Fig. 4.4 - STH modeling for TALL-3D. One-dimensional CATHARE model (left) and point of interests S1-S2 of the left leg (right), S3-S4 of the central leg and S5-S6 of the right vertical leg. For details see [4.9].....	84
Fig. 4.5 - Modelling for TALL-3D. Geometry and dimensions. ....	85
Fig. 4.6 - Simulated geometry for the study with heat exchange between the TALL-3D main section and the surrounding environment between fluid and steel disk (a) together with a close up view of the test section (b). ....	85
Fig. 4.7 - Comparison between case A and experimental values of temperature difference between outlet and inlet section (a) and outlet temperature values (b). ....	86
Fig. 4.8 - Comparison between case A, case B and experimental values of temperature difference between outlet and inlet section (a) and outlet temperature values (b). ....	86
Fig. 4.9 - Comparison between case A, B, C and experimental values of temperature difference between outlet and inlet section (a) and outlet temperature values (b). ....	87
Fig. 4.10 - Different profile between outlet and steel disk temperature values for case C. ....	87
Fig. 4.11 - Comparison between case A, B, C, D and experimental values of temperature profiles between outlet and inlet section (a) and outlet temperature values (b). ....	88
Fig. 4.12 - Comparison of outlet temperature values between cases A, C, E and experimental data.....	88
Fig. 4.13 - Geometry: HA=axis (AX), NMLI=disk (DSK), EO=uprightwall (URW), DO=downrightwall (DRW), FE=top (TOP), CD=bottom (BOT), AB=inlet (IN), HG=outlet (OUT), CB=downleftwall (CB), GF=upleftwall (GF).....	89
Fig. 4.14 - Initial steady state and turbulent variables for CFD OpenFOAM code with the turbulent flow model $\kappa$ - $\omega$ .....	91
Fig. 4.15 - Cathare standalone simulation. Computed mass flow rate $m$ (left) and temperature (right) at the points S3-S4 of the central leg as a function of time $t$ , from [4.9]. ....	91
Fig. 4.16 - Mass flow rate (right) and temperature (left) at reference point S4 (top) and S3 (below) of the central leg for Cathare standalone (C) and coupling Cathare-OpenFoam with $k$ - $\omega$ turbulence model.....	91




 <b>RICERCA SISTEMA ELETTRICO</b>	<b>Title:</b> Development of BE numerical tools for LFR design and safety analysis (2018)	<u>Distribution</u> <b>PUBLIC</b>	<u>Issue Date</u> 29.01.2019	<u>Pag.</u>
	<b>Project:</b> ADP ENEA-MSE PAR 2017	Ref. ADPFISS-LP2-167	Rev. 0	11 di 163

Fig. 4.17 - Mass flow rate (right) and temperature (left) at reference point S4 (top) and S3 (below) of the central leg for experimental data (E) and coupling Cathare-OpenFOAM with heat dispersion on the TALL-3D test section. .... 92

Fig. 4.18 - Velocity module  $U$  and streamline profiles over the 3D test component at time  $t = 0, 4, 20, 80, 180, 580, 1780$  and  $2780s$  by using two-equation  $\kappa\text{-}\omega$  turbulence model in OpenFOAM. .... 93

Fig. 4.19 - Temperature  $T$  and streamline profiles over the 3D test component at time  $t = 0, 4, 20, 80, 180, 580, 1780$  and  $2780s$  by using two-equation  $\kappa\text{-}\omega$  turbulence model in OpenFOAM. .... 94

Fig. 4.20 - Turbulent viscosity  $\nu_t$  and streamline profiles over the 3D test component at time  $t = 0, 4, 20, 80, 180, 580, 1780$  and  $2780s$  by using two-equation  $\kappa\text{-}\omega$  turbulence model in OpenFOAM. .... 95

Fig. 5.1 – Neutron flux spectra computed by Serpent for selected regions of the core. Black dashed lines identify the 5-group energy subdivision originally adopted, while the blue dashed line identifies the additional group added to better account for the reflector spectrum. .... 103

Fig. 5.2 – Radial scheme of the FRENETIC model of the ALFRED core. .... 104

Fig. 5.3 Radial (left) and axial (right) view of the ALFRED configuration simulated in Serpent. .... 104

Fig. 5.4: core configuration with rod position adjusted to reach a condition closer to criticality. .... 105

Fig. 5.5: ALFRED core configuration as in the benchmark calculations against Serpent/OpenFoam [5.1]. .... 105

Fig. 5.6: Core power distribution with rods insertion adjusted to reach a condition closer to criticality (left) and relative difference with respect to the previous case. .... 106

Fig. 5.7: Identification of the position of the safety rod inserted in the pure NE transient. .... 106

Fig. 5.8: Thermal power and reactivity evolution in the safety rod insertion NE transient. .... 106

Fig. 5.9: Safety rod insertion transient: radial power map (in MW per FA) at  $t=0s$  (left) and  $t=7s$  (right). Different scales are adopted to highlight the differences and the spatial distortion around the safety rod location. .... 107

Fig. 5.10: Mass flow rate reduction adopted in the LOFA simulation. .... 107

Fig. 5.11: Reactivity and thermal power evolution during the LOFA. .... 107

Fig. 5.12: Evolution of the maximum temperature for both the coolant and the fuel in the central fuel assembly during the LOFA. .... 108

Fig. 5.13: Radial power map (in MW per FA) at  $t=0s$  (left) and  $t=1s$  (right) during the control rod extraction transient. .... 108

Fig. 6.1 – Unstable behavior of Monte Carlo – CFD coupling (EPR case). Evolution of a) volumetric power, b) fuel temperature in the first 4 iterations. .... 123

Fig. 6.2 – The fixed-point coupling algorithm. .... 124

Fig. 6.3 – The stochastic approximation coupling algorithm .... 125

Fig. 6.4 – Radial view (a) and longitudinal view (b) of the SERPENT model of the ALFRED reactor. .... 125


Fig. 6.5 – Power peaking factor of one-fourth of ALFRED reactor core for BOC. .... 126

Fig. 6.6 – a) Geometry and b) mesh of ALFRED one-sixth of FA. .... 126

Fig. 6.7 – Relative power variation at each iteration for the fixed-point scheme. .... 127


Fig. 6.8 – Temperature profile calculated with the Monte Carlo – CFD coupling scheme. .... 127



 <b>RICERCA SISTEMA ELETTRICO</b>	<u>Title:</u> Development of BE numerical tools for LFR design and safety analysis (2018)	<u>Distribution</u> <b>PUBLIC</b>	<u>Issue Date</u> 29.01.2019	<u>Pag.</u>
	<u>Project:</u> ADP ENEA-MSE PAR 2017	Ref. ADPFISS-LP2-167	Rev. 0	12 di 163

<i>Fig. 6.9 – Velocity profile calculated with the Monte Carlo – CFD coupling scheme. ....</i>	<i>128</i>
<i>Fig. 7.1 – Injection transient, qualitative results. Time = 0 to 1 secs (TOP), time = 1.03 (MIDDLE), time = 1.05 (BOTTOM) .....</i>	<i>135</i>
<i>Fig. 7.2 – Time evolution of liquid fraction at first cell .....</i>	<i>136</i>
<i>Fig. 7.3 – Time evolution of global pressure in the vessel .....</i>	<i>136</i>
<i>Fig. 7.4 – Time evolution of global temperature (mass averaged) inside the vessel.....</i>	<i>137</i>
<i>Fig. 7.5 – Time evolution of hydrogen mass inside the vessel.....</i>	<i>137</i>
<i>Fig. 9.1 Sketch of the ALFRED Fuel Assembly: top view. ....</i>	<i>153</i>
<i>Fig. 9.2 Sketch of the ALFRED Fuel Assembly: lateral view.....</i>	<i>154</i>
<i>Fig. 9.3 Sketch of the 3D CFD model adopted.....</i>	<i>154</i>
<i>Fig. 9.4 Computational mesh in the fuel pin bundle active region.....</i>	<i>155</i>
<i>Fig. 9.5 Velocity and temperature distribution in a cross-section placed 200 mm downstream the beginning of the active region for the unperturbed case 0. ....</i>	<i>155</i>
<i>Fig. 9.6 Clad temperature distribution for the unperturbed case 0. ....</i>	<i>155</i>
<i>Fig. 9.7 Cross-section averaged pressure distribution along the streamwise direction for case 0. ....</i>	<i>156</i>
<i>Fig. 9.8 Vortex behind the sector blockage for case 1. ....</i>	<i>156</i>
<i>Fig. 9.9 Streamwise velocity contours in a cross section at the beginning of the active region for case1. ...</i>	<i>156</i>
<i>Fig. 9.10 Temperature distribution in the clad for case 1.....</i>	<i>157</i>
<i>Fig. 9.11 Streamwise velocity contours at the beginning of the active region (z=0) for case2. ....</i>	<i>157</i>
<i>Fig. 9.12 Pin temperature distribution for case2, double sector blockage at the lower spacer grid.....</i>	<i>158</i>
<i>Fig. 9.13 Pin temperature distribution for case 3, corner blockage at the lower spacer grid.....</i>	<i>158</i>
<i>Fig. 9.14 Maximum pin temperature in the active region for the 3 test cases with blockage in the lower grid.....</i>	<i>158</i>
<i>Fig. 9.15 Pin temperature distribution for case 5, single sector blockage at the middle spacer grid. ....</i>	<i>159</i>
<i>Fig. 9.16 Streamwise velocity contours in the blockage region for case9 (double sector upper blockage). .</i>	<i>159</i>
<i>Fig. 9.17 Pin temperature distribution for case 9, double sector blockage at the upper spacer grid.....</i>	<i>159</i>
<i>Fig. 9.18 Maximum pin temperature in the active region for case 8(upper double sector) and case0(unblocked). ....</i>	<i>160</i>




 <b>RICERCA SISTEMA ELETTRICO</b>	<u>Title:</u> Development of BE numerical tools for LFR design and safety analysis (2018)	<u>Distribution</u> <b>PUBLIC</b>	<u>Issue Date</u> 29.01.2019	<u>Pag.</u>
	<u>Project:</u> ADP ENEA-MSE PAR 2017	Ref. ADPFISS-LP2-167	Rev. 0	13 di 163

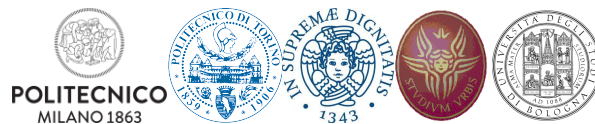
## LIST OF TABLES

<i>Tab. 2.1 – CIRCE S100 main parameters</i> .....	33
<i>Tab. 2.2 – TEST IV boundary conditions</i> .....	33
<i>Tab. 2.3 – CIRCE-ICE nodalization scheme: main parameters</i> .....	33
<i>Tab. 3.1 – Dissymmetrical test: sequence of events</i> .....	55
<i>Tab. 3.2 – Steady state conditions</i> .....	55
<i>Tab. 4.1 – Physical properties used in the modeling of the TALL-3D facility.</i> .....	79
<i>Tab. 4.2 - OpenFOAM boundary field <math>U</math>, <math>\phi</math> and <math>p</math> for the Navier-Stokes equation.</i> .....	79
<i>Tab. 4.3 - OpenFOAM boundary properties values for the Navier-Stokes equation.</i> .....	80
<i>Tab. 4.4 - OpenFOAM boundary field for temperature <math>T</math> of the heat equation.</i> .....	80
<i>Tab. 4.5 - OpenFOAM boundary field for properties of the heat equation.</i> .....	81
<i>Tab. 4.6 - OpenFOAM boundary field for temperature turbulent variables (<math>k, \omega</math>) and turbulent property <math>\nu_t</math> of the <math>k-\omega</math> two equation model (I).</i> .....	81
<i>Tab. 4.7 - OpenFOAM boundary field for temperature turbulent variables (<math>k, \omega</math>) and turbulent property <math>\nu_t</math> of the <math>k-\omega</math> two equation model (II).</i> .....	81
<i>Tab. 4.8 - Initial condition for OpenFOAM volume field before coupling.</i> .....	82
<i>Tab. 4.9 - Initial state condition for the one-dimensional Problem C (Cathare). The STH code initial condition satisfies the steady state equation.</i> .....	82
<i>Tab. 6.1 – Comparison of some core parameters.</i> .....	121
<i>Tab. 6.2 – Comparison of the reactivity coefficients, BoC.</i> .....	121
<i>Tab. 6.3 – Default parameters applied in the OpenFOAM solver for <math>k-\epsilon</math> turbulence model.</i> .....	121
<i>Tab. 6.4 – Correlations for density and thermal conductivity of coolant and fuel.</i> .....	121
<i>Tab. 7.1 – Initial and boundary conditions for the SIMMER/RELAP5 simulation of LIFUS5.</i> .....	134
<i>Tab. 9.1 Physical properties of Lead at 450 °C.</i> .....	152
<i>Tab. 9.2 Physical properties of SS 15-15 Ti (Clad material) at 450 °C.</i> .....	152
<i>Tab. 9.3 Basic Geometrical and Thermal-hydraulic parameters of the DEMO ALFRED Core.</i> .....	152
<i>Tab. 9.4 Test matrix adopted for the flow blockage computations in the ALFRED FA.</i> .....	153




 <b>RICERCA SISTEMA ELETTRICO</b>	<u>Title:</u> Development of BE numerical tools for LFR design and safety analysis (2018)	<u>Distribution</u> <b>PUBLIC</b>	<u>Issue Date</u> 29.01.2019	<u>Pag.</u>
	<u>Project:</u> ADP ENEA-MSE PAR 2017	Ref. ADPFISS-LP2-167	Rev. 0	14 di 163

*(Page intentionally left blank)*






 <b>RICERCA SISTEMA ELETTRICO</b>	<b>Title:</b> Development of BE numerical tools for LFR design and safety analysis (2018)	<u>Distribution</u> <b>PUBLIC</b>	<u>Issue Date</u> 29.01.2019	<u>Pag.</u>
	<b>Project:</b> ADP ENEA-MSE PAR 2017	Ref. ADPFISS-LP2-167	Rev. 0	15 di 163

## LIST OF ABBREVIATIONS


AdP	Accordo di Programma
ALFRED	Advanced Lead Fast Reactor European Demonstrator
ATHENA	Advanced Thermal Hydraulic Experiment for Nuclear Application
BE	Best Estimate
BEPU	Best Estimate Plus Uncertainty
BoP	Balance of Plant
BoT	Beginning of Transient
CEA	Commissariat a l'Energie Atomique et aux Energies Alternatives
CFD	Computational Fluid Dynamics
CIRCE	Circolazione Eutettico
CIRTEN	Interuniversity Consortium for Technological Nuclear Research
CHEOPEIII	Chemistry Operation III Facility
$c_p$	Specific heat
CR	Control Rod
d	Pin diameter
DBA	Design Base Accident
$D_{eq}$	Subchannel equivalent diameter
DHR	Decay Heat Removal
DHRS	Decay Heat Removal System
DOC	Design-Oriented Code
DSA	Deterministic Safety Analysis
ENEA	Italian National Agency for New Technologies, Energy and Sustainable Economic Development
ESFRI	European Strategy Forum on Research Infrastructures
EOt	End of Transient
FA	Fuel Assembly
FALCON	Fostering ALFRED Construction
FPC	Fuel Performance Code
FPS	Fuel Pin Simulator
FR	Fast Reactor
GEN-IV	Generation IV
GIF	Generation IV forum
GIORDI	Grid to Rod fretting facility
HBS	High Burnup Structure
HELENA	Heavy Liquid Metal Experimental Loop for Advanced Nuclear Applications
HLM	Heavy Liquid Metal
HX or HEX	Heat Exchanger
I&C	Instrumentation and Control
k	Thermal conductivity
L	Active Length
LBE	Lead Bismuth Eutectic
LECOR	Lead Corrosion Loop
LEADER	Lead-cooled Advanced Demonstration Reactor
LIFUS5	Lead-Lithium for Fusion Facility (5)
LFR	Lead Fast Reactor
LM	Liquid Metal
LMR	Liquid Metal Reactor
LWR	Light Water Reactor
$\dot{m}$	Mass flow rate
$\dot{m}_0$	Nominal mass flow rate



 <b>RICERCA SISTEMA ELETTRICO</b>	<b>Title:</b> Development of BE numerical tools for LFR design and safety analysis (2018)	<u>Distribution</u> <b>PUBLIC</b>	<u>Issue Date</u> 29.01.2019	<u>Pag.</u>
	<b>Project:</b> ADP ENEA-MSE PAR 2017	Ref. ADPFISS-LP2-167	Rev. 0	16 di 163

MA	Minor Actinide
MABB	Minor Actinides Bearing Blankets
MOX	(U-Pu) Mixed Oxide
NACIE	Natural Circulation Experiment Loop
NPPs	Nuclear Power Plants
O&M	Operation and Maintenance
PAR	Piani Annuali di Realizzazione
PID	Proportional-Integral-Derivative controllers
PLD	Pulsed Laser Deposition
POLIMI	Politecnico di Milano
POLITO	Politecnico di Torino
PP	Primary Pump
Pr	Prandtl number
PSA	Probabilistic Safety Analysis
RACHELE	Reactions and Advanced chemistry for Lead
Q	Thermal power
$q_{wall}$	Wall heat flux
RANS	Reynolds Averaged Navier-Stokes
RMS	Root Mean Square
RSE	Ricerca Sistema Elettrico
RV	Reactor Vessel
RVACS	Reactor Vessel Air-Cooling System
SA	Safety Analysis
SET-PLAN	Strategic Energy Technology Plan
SG	Steam Generator
SGTR	Steam Generator Tube Rupture
SISO	Single Input Single Output
SYS	System
SYS-TH	System- ThermalHydraulics
SS	Stainless Steel
TH	Thermal-Hydraulics
$T_{inlet}$	Inlet temperature
TKE	Turbulent Kinetic Energy
$T_{max}$	Maximum temperature
$T_{outlet}$	Outlet temperature
TRL	Technological Readiness Level
TSO	Technical Safety Organization
ULOF	Unprotected Loss of Flow
UNIBO	Università di Bologna
UNIPI	Università di Pisa
UNIROMA1	Università di Roma - Sapienza
VOC	Verification-Oriented Code
V&V	Verification & Validation
$y^+$	Dimensionless distance from the wall
$\alpha$	Thermal expansion coefficient
$\beta$	Blockage area factor
$\rho$	Density
$\nu$	Fluid kinematic viscosity




 <b>RICERCA SISTEMA ELETTRICO</b>	<u>Title:</u> Development of BE numerical tools for LFR design and safety analysis (2018)	<u>Distribution</u> <b>PUBLIC</b>	<u>Issue Date</u> 29.01.2019	<u>Pag.</u>
	<u>Project:</u> ADP ENEA-MSE PAR 2017	Ref. ADPFISS-LP2-167	Rev. 0	17 di 163

## FOREWORD

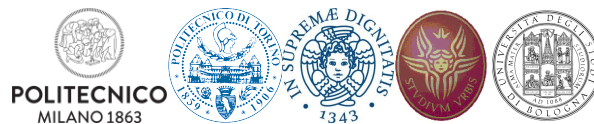
The Lead-cooled Fast Reactor (LFR) technology brings about the possibility of fully complying with all the Generation IV requirements. This capability being more and more acknowledged in international fora, the LFR is gathering a continuously increasing interest, with new industrial actors committing on LFR-related initiatives. In this context, the Italian nuclear community evaluates strategic to continue elevating the competences and capabilities, with the perspective of extending the support to the design and safety analysis of future LFR systems. The most appropriate framework for this advancement is the Accordo di Programma (AdP), within which ENEA and CIRTEN (the consortium gathering all Italian universities engaged in nuclear education, training and research) are already cooperating on the LFR technology since 2006, along with national industry as main stakeholder. Within the AdP, the LFR system chosen as reference for all studies and investigations is ALFRED, the Advanced Lead-cooled Fast Reactor European Demonstrator. As a demonstration reactor, indeed, it was reckoned as the system best fitting with the research and development (R&D) nature of the activities performed in the AdP, being demonstration the step that logically follows R&D in the advancement of the LFR technology by readiness levels. Moreover, ALFRED is envisaged as the key facility of a distributed research infrastructure of pan-European interest, open to scientists and technologists for relevant experiments to be performed on a fully LFR-representative and integral environment, with the long-term perspective of supporting to the safe and sustainable operation of future LFRs, thereby fulfilling the general objectives of the AdP itself.


In the wide spectrum of possible activities to support the further development of the LFR technology, and exploiting the specific expertise acquired by the universities in the past years, within the scope of the 2016 Piano Annuale di Realizzazione (PAR) it was decided to focus the cooperative efforts shared between ENEA and CIRTEN towards the development of an **best estimate computational tools supporting the various stages of design and safety analyses of LFR systems**, so to increase – or help in viewing how to fill the gaps – the modeling capabilities.



 <b>RICERCA SISTEMA ELETTRICO</b>	<u>Title:</u> Development of BE numerical tools for LFR design and safety analysis (2018)	<u>Distribution</u> <b>PUBLIC</b>	<u>Issue Date</u> 29.01.2019	<u>Pag.</u>
	<u>Project:</u> ADP ENEA-MSE PAR 2017	Ref. ADPFISS-LP2-167	Rev. 0	18 di 163

*(Page intentionally left blank)*



 <b>RICERCA SISTEMA ELETTRICO</b>	<u>Title:</u> Development of BE numerical tools for LFR design and safety analysis (2018)	<u>Distribution</u> <b>PUBLIC</b>	<u>Issue Date</u> 29.01.2019	<u>Pag.</u>
	<u>Project:</u> ADP ENEA-MSE PAR 2017	Ref. ADPFISS-LP2-167	Rev. 0	19 di 163


# 1 THERMO-MECHANICS OF THE FUEL PIN – DEVELOPMENT AND ASSESSMENT OF MODELS AND ALGORITHMS DESCRIBING INERT GAS BEHAVIOR FOR USE IN TRANSURANUS

*L. Luzzi, D. Pizzocri, T. Barani, L. Cognini, A. Magni*

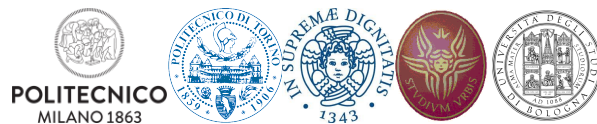



**POLITECNICO**  
MILANO 1863



 <b>RICERCA SISTEMA ELETTRICO</b>	<u>Title:</u> Development of BE numerical tools for LFR design and safety analysis (2018)	<u>Distribution</u> <b>PUBLIC</b>	<u>Issue Date</u> 29.01.2019	<u>Pag.</u>
	<u>Project:</u> ADP ENEA-MSE PAR 2017	Ref. ADPFISS-LP2-167	Rev. 0	20 di 163

*(Page intentionally left blank)*



 <b>RICERCA SISTEMA ELETTRICO</b>	<b>Title:</b> Development of BE numerical tools for LFR design and safety analysis (2018)	<u>Distribution</u> <b>PUBLIC</b>	<u>Issue Date</u> 29.01.2019	<u>Pag.</u>
	<b>Project:</b> ADP ENEA-MSE PAR 2017	Ref. ADPFISS-LP2-167	Rev. 0	21 di 163

## 1.1 Progress from the results presented in the previous PARs

This document summarizes the activities performed by POLIMI in continuation of those included in the PAR2017 (and previous PARs). The objective of POLIMI's activities for PAR2016 [1.1] and PAR2017 [1.2] was twofold: (1) we derived new correlations for key properties of the helium/oxide fuel system, i.e., helium diffusivity [1.3] and helium solubility [1.4], and (2) we developed new algorithms for the treatment of mathematical models describing inert gas behaviour, tailored for use in fuel performance codes such as TRANSURANUS [1.5],[1.6].

As briefly reported hereafter, these parameters are of critical importance for the ongoing development of a physics-based model describing helium behaviour in MOX fuel. Helium behaviour is fundamental in MOX fuel, both in-reactor as well as during storage. Due to the enrichment in plutonium, higher concentrations of minor actinides are produced during irradiation compared to UO<sub>2</sub>. Most of these isotopes undergo  $\alpha$ -decay, which are effectively helium nuclei created in the fuel matrix<sup>1</sup>.

To describe the intra-granular behaviour of helium in MOX fuel, we propose a physics-based model that extends the one proposed by Talip et al. [1.7]. Namely:

$$\frac{\partial}{\partial t} c_{\text{He}} = D_{\text{He}} \frac{1}{r^2} \frac{\partial}{\partial r} r^2 \frac{\partial}{\partial r} c_{\text{He}} - \beta(c_{\text{He}} - c_{S,\text{He}}) + \alpha m_{\text{He}} + S_{\text{He}} \quad (1.1)$$

$$\frac{\partial}{\partial t} m_{\text{He}} = \beta(c_{\text{He}} - c_{S,\text{He}}) - \alpha m_{\text{He}} \quad (1.2)$$

where  $c_{\text{He}}$  (at m<sup>-3</sup>) and  $m_{\text{He}}$  (at m<sup>-3</sup>) are the concentration of helium dissolved in the fuel matrix and trapped in intra-granular bubbles, respectively.  $D_{\text{He}}$  (m<sup>2</sup> s<sup>-1</sup>) is the diffusion coefficient,  $\beta$  (s<sup>-1</sup>) is the trapping rate [1.8],  $\alpha$  (s<sup>-1</sup>) is the re-resolution rate [1.9],[1.10], and  $S_{\text{He}}$  (at m<sup>-3</sup> s<sup>-1</sup>) is the production rate of helium.  $c_{S,\text{He}}$  (at m<sup>-3</sup>) is the solubility limit of helium in the fuel matrix.  $t$  (s) and  $r$  (m) are respectively time and the radial coordinate within the fuel grain, assumed as spherical [1.11]. Eq. 1,2 are to be solved imposing a Dirichlet boundary condition at the grain radius.


Eqs. 1,2 physically describe the behaviour of intra-granular helium. The helium atoms are produced in the fuel matrix. The excess of atoms with respect to the solubility is progressively trapped into intra-granular bubbles. The trapping process is counteracted by the re-resolution of atoms from the intra-granular bubbles caused by the interaction of the fission fragments. The proposed model is thus physics-based and describes helium behaviour at the scale of fuel grains, therefore being in line with the development guidelines detailed in Section 1.

The effective application of Eqs. 1,2 requires the definition of the model parameters specific to helium, i.e., the production rate  $S_{\text{He}}$ , the diffusion coefficient  $D_{\text{He}}$ , and the solubility limit  $c_{S,\text{He}}$ . A new suitable correlation for the diffusion coefficient has been derived as part of the activities of PAR2016 [1.1],[1.3], while a new correlation for the solubility limit is the one of the outcomes of PAR2017 [1.2],[1.4].

The effective use of the above described model (Eqs. 1,2) in fuel performance codes requires special numerical treatment. This requirement arises from the difference in scales between this helium behaviour

<sup>1</sup> Secondary mechanisms of helium formation are from ternary fissions (yield around 0.2%) and (n, $\alpha$ )-reactions on <sup>16</sup>O for high-energy neutrons.




 <b>RICERCA SISTEMA ELETTRICO</b>	<u>Title:</u> Development of BE numerical tools for LFR design and safety analysis (2018)	<u>Distribution</u> <b>PUBLIC</b>	<u>Issue Date</u> 29.01.2019	<u>Pag.</u>
	<u>Project:</u> ADP ENEA-MSE PAR 2017	Ref. ADPFISS-LP2-167	Rev. 0	22 di 163

model (fuel grain scale, i.e., few micrometres) and the typical domain of a fuel performance code such as TRANSURANUS (fuel pin scale, i.e., from centimetres to metres). For this reason, as part of the previous PARs, we developed dedicated numerical algorithms [1.5],[1.6].

The next step in the development of this model is going to be its implementation in SCIANTIX [12] and its validation against separate effect data of annealed fuel samples [1.8],[1.13].






 <b>RICERCA SISTEMA ELETTRICO</b>	<u>Title:</u> Development of BE numerical tools for LFR design and safety analysis (2018)	<u>Distribution</u> <b>PUBLIC</b>	<u>Issue Date</u> 29.01.2019	<u>Pag.</u>
	<u>Project:</u> ADP ENEA-MSE PAR 2017	Ref. ADPFISS-LP2-167	Rev. 0	23 di 163

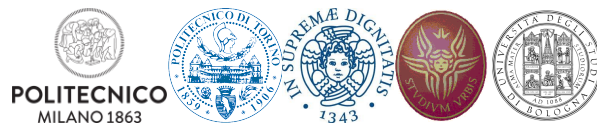
## 1.2 List of References


- [1.1] L. Luzzi, D. Pizzocri, T. Barani, L. Cognini, Development/assessment of models describing the inert gas behavior in the fuel for application to the TRANSURANUS fuel pin thermo-mechanical code, PAR2016: LP2.A.3\_a. (2017).
- [1.2] L. Luzzi, D. Pizzocri, T. Barani, L. Cognini, A. Magni, Thermo-mechanics of the fuel pin – Development and assessment of models and algorithms describing inert gas behavior for use in TRANSURANUS, PAR2017: LP2.a.3.1. (2018).
- [1.3] L. Luzzi, L. Cognini, D. Pizzocri, T. Barani, G. Pastore, A. Schubert, T. Wiss, P. Van Uffelen, Helium diffusivity in oxide nuclear fuel: Critical data analysis and new correlations, Nucl. Eng. Des. 330 (2018) 265–271.
- [1.4] L. Cognini, D. Pizzocri, T. Barani, P. Van Uffelen, A. Schubert, T. Wiss, L. Luzzi, Helium solubility in oxide nuclear fuel: Derivation of new correlations for Henry’s constant, Nucl. Eng. Des. 340 (2018) 240–244. doi:10.1016/j.nucengdes.2018.09.024.
- [1.5] D. Pizzocri, C. Rabiti, L. Luzzi, T. Barani, P. Van Uffelen, G. Pastore, PolyPole-1: An accurate numerical algorithm for intra-granular fission gas release, J. Nucl. Mater. 478 (2016) 333–342.
- [1.6] G. Pastore, D. Pizzocri, C. Rabiti, T. Barani, P. Van Uffelen, L. Luzzi, An effective numerical algorithm for intra-granular fission gas release during non-equilibrium trapping and resolution, J. Nucl. Mater. 509 (2018) 687–699.
- [1.7] Z. Talip, T. Wiss, V. Di Marcello, A. Janssen, J.Y. Colle, P. Van Uffelen, P. Raison, R.J.M. Konings, Thermal diffusion of helium in 238Pu-doped UO<sub>2</sub>, J. Nucl. Mater. 445 (2014) 117–127. doi:10.1016/j.jnucmat.2013.10.066.
- [1.8] F.S. Ham, Theory of diffusion-limited precipitation, J. Phys. Chem. Solids. 6 (1958) 335–351.
- [1.9] P. Lösönen, On the behaviour of intragranular fission gas in UO<sub>2</sub> fuel, J. Nucl. Mater. 280 (2000) 56–72. doi:10.1016/S0022-3115(00)00028-3.
- [1.10] D.R. Olander, D. Wongsawaeng, Re-resolution of fission gas - A review: Part I. Intragranular bubbles, J. Nucl. Mater. 354 (2006) 94–109. doi:10.1016/j.jnucmat.2006.03.010.
- [1.11] A.H. Booth, A method of calculating fission gas diffusion from UO<sub>2</sub> fuel and its application to the X-2-f loop test, At. Energy Canada Ltd. Chalk River Proj. Res. Dev. Rep. AECL-496. (1957) 1–23.
- [1.12] D. Pizzocri, T. Barani, L. Luzzi, SCIANITIX, <https://gitlab.com/poliminrg/sciantix>. (2018).
- [1.13] Z. Talip, T. Wiss, E.A. Maugeri, J.Y. Colle, P.E. Raison, E. Gilabert, M. Ernstberger, D. Staicu, R.J.M. Konings, Helium behaviour in stoichiometric and hyper-stoichiometric UO<sub>2</sub>, J. Eur. Ceram. Soc. 34 (2014) 1265–1277. doi:10.1016/j.jeurceramsoc.2013.11.032.



 <b>RICERCA SISTEMA ELETTRICO</b>	<u>Title:</u> Development of BE numerical tools for LFR design and safety analysis (2018)	<u>Distribution</u> <b>PUBLIC</b>	<u>Issue Date</u> 29.01.2019	<u>Pag.</u>
	<u>Project:</u> ADP ENEA-MSE PAR 2017	Ref. ADPFISS-LP2-167	Rev. 0	24 di 163

*(Page intentionally left blank)*




 <b>RICERCA SISTEMA ELETTRICO</b>	<u>Title:</u> Development of BE numerical tools for LFR design and safety analysis (2018)	<u>Distribution</u> <b>PUBLIC</b>	<u>Issue Date</u> 29.01.2019	<u>Pag.</u>
	<u>Project:</u> ADP ENEA-MSE PAR 2017	Ref. ADPFISS-LP2-167	Rev. 0	25 di 163

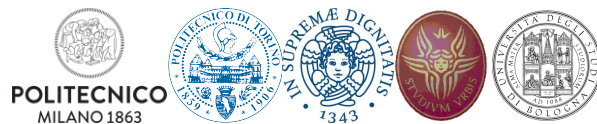
## 2 VALIDATION OF RELAP53D BY CIRCE-ICE EXPERIMENTAL TESTS


*V. Narcisi, F. Giannetti, G. Caruso*



 <b>RICERCA SISTEMA ELETTRICO</b>	<u>Title:</u> Development of BE numerical tools for LFR design and safety analysis (2018)	<u>Distribution</u> <b>PUBLIC</b>	<u>Issue Date</u> 29.01.2019	<u>Pag.</u>
	<u>Project:</u> ADP ENEA-MSE PAR 2017	Ref. ADPFISS-LP2-167	Rev. 0	26 di 163

*(Page intentionally left blank)*



 <b>RICERCA SISTEMA ELETTRICO</b>	<u>Title:</u> Development of BE numerical tools for LFR design and safety analysis (2018)	<u>Distribution</u> <b>PUBLIC</b>	<u>Issue Date</u> 29.01.2019	<u>Pag.</u>
	<u>Project:</u> ADP ENEA-MSE PAR 2017	Ref. ADPFISS-LP2-167	Rev. 0	27 di 163

## 2.1 Background and references

The Lead-cooled Fast Reactor (LFR) belongs to the six concepts selected by the Generation IV International Forum (GIF) as Generation IV systems (GEN-IV). GEN-IV reactors are developing in order to help meet the world's future energy needs and to minimize the long-term stewardship burden. The goals of the innovative Nuclear Power Plants (NPP) are summarized in four main topics: sustainability, economics, safety & reliability and proliferation resistance & physical protection.

The LFR concept includes the lead and lead-bismuth eutectic alloy (LBE) technologies. Both coolants are chemically inert and they offer other attractive characteristics in terms of interaction with structural materials and thermodynamic features. LFR systems also well respond to lesson of Fukushima accident allowing natural circulation both in nominal and accident conditions. This feature offers considerable grace time in order to cope with unprotected loss of flow transient and permits to introduce fully passive decay heat removal system (DHR), assuring very high safety features over long periods without need for operator actions, combined with active systems.


Several R&D programs has been promoted in the UE, focused on the development of the LFR systems. In this framework, the validation of the best estimate computer codes is a crucial aspect. The most computational codes are improved to include the capability to simulates the main phenomena occurring in the GEN-IV system reactors. In order to use these analytical tools for the NPP safety assessment, each improvement must be validated against several experimental data which cover every operational scenario of the nuclear system, including accidental sequences. The validation approach is not possible against experimental tests performed on NPP; however, the accidental scenario can be replaced with dedicated facility and the experimental data can be compared with the analytical results.

In this framework, from 2010, "Sapienza" University of Rome (UNIROMA1), in collaboration with ENEA Brasimone Research Center, was involved in the development of innovative LFR technologies (Ref. [2.1], [2.2], [2.3], [2.4] and [2.5]), dealing with several operative aspects. In 2013, UNIROMA1 started to investigate the capability of RELAP5-3D<sup>®</sup> code (R5-3D) to reproduce the main thermal-hydraulic phenomena in a lead-cooled fast reactor. In Ref. [2.6], a comparison between RELAP5 mod.3.3 and RELAP5-3D highlighted that the correlation implemented in R5-3D for the evaluation of the heat transfer coefficient (HTC) in bundle geometry (the Westinghouse correlation, in Ref. [2.7]), underestimates the HTC in comparison with the actual state of art. In Ref. [2.8], a tool for the generation of new lead and LBE thermophysical properties (according to the NEA recommendation, in Ref. [2.9]) binary files was presented, showing a comparison between the state-of-art data and the RELAP5-3D default properties.

In 2010, in the framework of LEADER project, a new configuration of the steam generator (SG) was proposed for ALFRED (Advanced Lead Fast Reactor European Demonstrator): the super-heated steam double wall bayonet tube type with leakage monitoring. ENEA Brasimone Research Center designed and constructed the HERO (Heavy liquid mEtal pRessurized water cOoled tubes) test section to investigate the capability of a bundle of double wall bayonet tubes 1:1 in length with the ALFRED SG (Ref. [2.10]). In the framework of the H2020 SESAME project (<http://sesame-h2020.eu/>), a validation benchmark has been proposed, based on the experimental campaign conducted on CIRCE-HERO test facility (Ref. [2.11]). UNIROMA1 has been involved in this experimental campaign, performing the pre-test calculations (Ref. [2.12], [2.13], [2.14] and [2.15]) and carrying out the experiment in collaboration with ENEA.

The CIRCE-HERO pre-test calculation has been performed using RELAP5-3D; the nodalization scheme has been developed starting from the thermal-hydraulic model of previous configuration of the facility, called CIRCE-ICE facility. ICE test section was installed into CIRCE facility in order to reproduce a typical primary system of a HLM cooled pool-type reactor; the experimental campaign aimed to investigate mixing convection and thermal stratification phenomena in a HLM pool and to provide experimental data for the



 <b>RICERCA SISTEMA ELETTRICO</b>	<u>Title:</u> Development of BE numerical tools for LFR design and safety analysis (2018)	<u>Distribution</u> <b>PUBLIC</b>	<u>Issue Date</u> 29.01.2019	<u>Pag.</u>
	<u>Project:</u> ADP ENEA-MSE PAR 2017	Ref. ADPFISS-LP2-167	Rev. 0	28 di 163

validation of analytical codes. The simulation activities carried out by UNIROMA1 in the previous years, has been highlighted that the nodalization scheme has well reproduced the thermal-hydraulics of the primary flow path in full power conditions and the implementation in RELAP5-3D of the most recent LBE thermophysical properties correlations has allowed a better estimation of the HLM conditions. Concerning the thermal-hydraulic phenomena into the pool, the calculations has highlighted the prospect to reproduce the thermal stratification with RELAP5-3D, but some discrepancy has been noticed comparing the calculated results with the experimental data (Ref. [2.16], [2.17] and [2.18]).

This report follows the activity of the past year. The thermal-hydraulic model of CIRCE-ICE has been used for the simulation of an integral test aimed to reproduce a protected loss of heat sink (PLOHS) with loss of flow (LOF).

## 2.2 Body of the report concerning the ongoing activities


### 2.2.1 CIRCE-ICE facility

CIRCE is a multipurpose pool facility designed to host different test sections welded to and hung from bolted vessel heads for the investigation of thermal-hydraulic aspects related to the HLM pool system. The facility consists of a main vessel, earmarked for containing test section and filled with about 70 tons of molten LBE, two auxiliary tanks, dedicated to store LBE during maintenance phases and to transfer liquid metal during loading and drainage phases, and data acquisition system. The main vessel (S100) is characterized by the outer diameter of 1200 mm and the height of 8500 mm. The Fig. 2.1 depicts the isometric view of the facility and the main parameters are summarized in Tab. 2.1.

The experimental campaign is conducted on ICE test section, installed into the main vessel. ICE aims to simulate the primary system of a HLM pool type reactor and the main objectives of the experimental campaign were to investigate thermal stratification and mixing convection phenomena into the pool and to provide experimental data for the validation of analytical codes. These are two of the main topics for the development of LFR system: the thermal stratification could induce thermo-mechanical stress on the structure and the validation of TH (Thermal Hydraulics) codes against the experimental data is a fundamental step in order to justify their use in the design phase for improving safety aspects.

The principal components and the primary main flow path of the test section are depicted in Fig. 2.2 and Fig. 2.3; the inlet section consists of the feeding conduit, which allows the hydraulic connection between the lower plenum of the pool and the fuel pin simulator (FPS). The value of the LBE mass flow rate entering the FPS is measured by a Venturi-nozzle flow meter, installed into the feeding conduit. The fuel pin simulator represents the heat source of the unit. It consists of an electrical pin bundle with a nominal thermal power of 800 kW and an active length of 1000 mm. The bundle is composed of 37 electrically heated pins arranged in a wrapped hexagonal lattice and characterized by a pitch to diameter ratio equal to 1.8 (Fig. 2.4); the relative position between the pin bundle and the external wrapper is fixed by three spacer grids, located along the heat source, and the unit rests to the lower grid, placed at the inlet section of the FPS. Each pin has an outer diameter of 8.2 mm, a thermal power of 25 kW and a heat flux at the pin wall of 1 MW/m<sup>2</sup>. The hot fluid exits the core and it is introduced into the fitting volume, which allows the connection between the fuel pin simulator and the riser, double wall insulated pipe connecting the fitting volume and the separator. At the inlet section of the riser, a nozzle is installed allowing the injection of argon in order to promote the circulation of the primary coolant. The mixture flows upward and collects inside the separator, where the separation of LBE and Ar occurs (LBE enters the heat exchanger while Ar flows upward into the gas plenum through the free surface). The HX (heat exchanger) is made of 91 bayonet tubes, characterized by an active length of 3462 mm, contained into a cylindrical shell. The relative position between the tubes and the external shell is fixed by only one grid at the outlet section of the HX. Fig. 2.5 shows a sketch of the bayonet element which consists of three concentric tubes. The feed-water flows downward into the inner tube and



 <b>RICERCA SISTEMA ELETTRICO</b>	<u>Title:</u> Development of BE numerical tools for LFR design and safety analysis (2018)	<u>Distribution</u> <b>PUBLIC</b>	<u>Issue Date</u> 29.01.2019	<u>Pag.</u>
	<u>Project:</u> ADP ENEA-MSE PAR 2017	Ref. ADPFISS-LP2-167	Rev. 0	29 di 163

then upward into the annular riser between inner and middle tube, where the change of phase take place; the double physical separation is obtained with the second and the third tube and the LBE flows downwards outside the tubes.

The volume between middle and outer tube is filled by pressurized helium to detect any leakage. Exiting the HX, primary coolant flows through the downcomer reaching the lower plenum. The DHR system is located in the upper zone of the pool, as shown in Fig. 2.2. It consists of only one bayonet tube and the decay power is removed by forced circulation of air. The tube is located inside a double wall shell with a thin air insulation gap to thermally decouple the DHR from the external LBE pool. Hot LBE enters the DHR by the upper inlet section, it flows downward decreasing the temperature and it exits the component in the downcomer (Ref. [2.19]).

The test section is equipped with several thermocouples to investigate the thermal behavior of the LBE. The primary coolant temperature inside the FPS is measured by 36 TCs (thermocouples), arranged at 7 different axial levels. Two series of penetration are obtained at the inlet and outlet section of the active zone, as shown in Fig. 2.6. In addition, along the HS active length, four different sections are monitored as depicted in Fig. 2.7, investigating the temperature of the LBE along three characteristic sub-channels and the pin clads. Several TCs are also installed inside the pool in order to investigate mixing convection and thermal stratification phenomena. 119 thermocouples are installed in 17 axial levels and 9 different azimuthal positions, as shown in Fig. 2.8.

### 2.2.2 Experimental test

The objective of the experimental campaign is to investigate the thermal stratification and the mixing convection phenomena inside the pool of the facility, in both enhanced and natural circulation conditions. The experimental test analyzed is called TEST 9; it aims to reproduce a protected loss of heat sink (PLOHS) plus a loss of flow (LOF) simulating the total loss of primary flow, the loss of the secondary circuit, the consequent scram of the reactor and the activation of the DHR system. To reproduce the accident in CIRCE-ICE facility, the thermal power supplied to the FPS is reduced to the 7% of the nominal power, following a typical decay heat curve for a HLM fast reactor, the argon injection is stopped, simulating the blackout of the primary pumping system, the secondary system is disabled and the DHR system is activated, injected air on the DHR secondary side. The boundary conditions of the TEST 9 are summarized in Tab. 2.2.


### 2.2.3 Thermal-hydraulic model

The nodalization scheme of CIRCE-ICE test facility has been developed using RELAP5-3D© ver. 4.3.4. RELAP5 is a light water reactor transient analysis code developed by the U.S. Nuclear Regulatory Commission (NRC) for use in rulemaking, licensing audit calculations, evaluation of operator guidelines and as a basis for a nuclear plant analyzer. It is a generic code that, in addition to calculating the behavior of a reactor coolant system during a transient, can be used for simulation of a wide variety of hydraulic and thermal transients in both nuclear and non-nuclear systems involving mixtures of steam, water, non-condensable and solute. R5-3D is the last version of the series of RELAP5 code and contains several improvements; two enhancements from the previous versions are the multi-dimensional thermal-hydraulic capability and the addition of new working fluids, including heavy liquid metals (Ref.[2.20]).

The geometrical model consists of two macro-regions, coupled to reproduce the whole test facility: a mono-dimensional model, that simulate the primary main flow path, the HX secondary system and the DHR system (see Fig. 2.9), and a multi-dimensional component, shown in Fig. 2.10, where the internal components are depicted only to display the positioning, to investigate phenomena such as mixing convection and thermal stratification inside the pool.

The 1D scheme reproduces the components described in previous section. The HS is simulated sub-channel by sub-channel using 72 parallel pipes (Fig. 2.11), each composed of 15 control volumes, hydraulically



 <b>RICERCA SISTEMA ELETTRICO</b>	<u>Title:</u> Development of BE numerical tools for LFR design and safety analysis (2018)	<u>Distribution</u> <b>PUBLIC</b>	<u>Issue Date</u> 29.01.2019	<u>Pag.</u>
	<u>Project:</u> ADP ENEA-MSE PAR 2017	Ref. ADPFISS-LP2-167	Rev. 0	30 di 163

linked with 1536 cross junction to reproduce the mass transfer between the sub-channels. The thermal power supplied by the electrical heated pins is simulated with 5760 heat structure active nodes and other 1728 thermal nodes reproduce the heat dissipation through the hexagonal shroud. In order to simulate the heat transfer between the sub-channels, 3456 heat transfer nodes are introduced, assuming a “fake” material with negligible heat capacity and with LBE thermal conductivity. The FPS nodalization scheme is obtained to compare the LBE temperature in the exact position of the thermo-couples. For the evaluation of the heat transfer coefficient (HTC) on heavy liquid metals, Todreas & Kazimi correlation (Ref. [2.7]) is implemented in R5-3D.

$$Nu = 4.0 + 0.33 \left(\frac{p}{d}\right)^{3.8} \left(\frac{Pe}{100}\right)^{0.86} + 0.16 \left(\frac{p}{d}\right)^5$$

Previous calculations on HLM system showed that this correlation underestimates the Nusselt number for pitch-to-diameter ratio greater than 1.2 (Ref. [2.6]). Additionally, R5- 3D does not permit a pitch-to-diameter ratio of 1.8 and the p/d of the pin bundle was set to the maximum allowed value of 1.4. In order to improve the HTC according to Ushakov correlation (more accurate in this case)

$$Nu = 7.55 \frac{p}{d} - 20 \left(\frac{p}{d}\right)^{-13} + \frac{3.67}{\left(90 \frac{p}{d}\right)^2} Pe^{(0.56+0.19\frac{p}{d})}$$

and to correct the heat exchange to experimental p/d value, an artificial multiplicative factor of 1.31, evaluated as the ratio between the two correlations in nominal flow conditions, was applied to the HTC. For the non-bundle geometry, the Seban-Shimazaki correlation is used:

$$Nu = 5.0 + 0.025Pe^{0.8}$$

Upstream the FPS, the pressure drop of the Venturi nozzle was simulated by a concentrated pressure loss coefficient K, dependent on the flow conditions, according to the equation:

$$K_{Venturi} = 10.5Re^{-0.014}$$

The argon injection at the riser inlet section is simulated with boundary conditions: the time-dependent volume sets the gas inlet conditions and the time-dependent junction, connected with the bottom edge of the riser second control volume, adjusts the mass flow rate injection. The pressure of the gas plenum of the facility is regulated by an additional time-dependent volume, that simulates the gas extraction through the gas circuit. The HX primary side is simulated by a single equivalent pipe and one heat structure, which thermally couples the primary and the secondary side. A calibrated fouling factor of 1.02 is evaluated as the ratio between Ushakov and Todreas & Kazimi correlation and it is applied on the LBE side to increase the HTC. The bayonet tubes are modelled using two pipes in order to simulate the descending and ascending side of water/steam tubes and one heat structure to model heat dispersion between the two pipes.


The pressure losses due to grids installed into FPS and heat exchanger are calculated by the Rheme correlation (Ref. [2.21]):

$$\Delta p_{grid} = C_v \cdot \varepsilon^2 \cdot 0.5 \cdot \rho \cdot v^2$$

where  $\rho$  and  $v$  are respectively the density and the velocity of the fluid while  $\varepsilon$  represents the blockage factor of the grids, calculated as:





 <b>RICERCA SISTEMA ELETTRICO</b>	<u>Title:</u> Development of BE numerical tools for LFR design and safety analysis (2018)	<u>Distribution</u> <b>PUBLIC</b>	<u>Issue Date</u> 29.01.2019	<u>Pag.</u>
	<u>Project:</u> ADP ENEA-MSE PAR 2017	Ref. ADPFISS-LP2-167	Rev. 0	31 di 163

$$\varepsilon = \frac{A_{grid}}{A_{flow}}$$

The  $C_v$  parameter is a modified drag coefficient and it is calculated as:

$$C_v = MIN \left[ 3.5 + \frac{73.14}{Re^{0.264}} + \frac{2.79 \cdot 10^{10}}{Re^{2.79}}, \frac{2.6}{\varepsilon^2} \right]$$

The bayonet tube of the DHR system is simulated and it is composed of one pipe for the LBE channel and two pipes to model the descending and ascending air side.

The region number 2 is the 3D component which simulates the volume between the main vessel and the internals. The nodalization scheme is obtained to compare the LBE temperature in the exact position of the thermocouples into the pool, in order to investigate the capability of the code to reproduce thermal stratification and mixing convection phenomena. The model consists of 51 axial levels, 4 radial meshes and 8 azimuthal intervals. The mono-dimensional model and the 3D component is hydraulically coupled with 12 junctions and the heat dispersions through the internals and the main vessel were evaluated with several heat structures.


The dimensions of the whole model are summarized in Tab. 2.3.

#### 2.2.4 Simulation results

The simulation has been carried out using the most accurate LBE thermo-physical properties correlations; recommended by NEA (Ref. [2.9]). The boundary conditions applied for the simulations are summarized in Tab. 2.2. The test starts in no-power steady state conditions, where the argon injection, the FW and the air mass flow rate and the FPS are disabled. At 25000 s the transition from enhanced to natural circulation occurs: the FPS thermal power decreases to the decay heat value, the Ar injection system and the FW mass flow rate are disabled and the DHR is fed by air flow rate. The simulated value of the thermal power supplied by the FPS has been reduced of 5% of the electrical signal to take into account the dissipations which occur in the cables and connectors of the outer circuits, which does not contribute to the thermal power supplied.

Fig. 2.12 depicts the comparison between the LBE mass flow rate measured by the Venturi flow meter (in red) and calculated by R5-3D (in black). Unless the experimental fluctuations, R5-3D well reproduces the LBE mass flow rate through the main flow path, in both GHC and NC conditions; after the transition, the code slightly overestimates the mass flow (about 0.5 kg/s). Fig. 2.13 shows the LBE temperature trend at the inlet and the outlet of the FPS active zone. At the inlet section, the code underestimates the LBE temperature, due to the lower temperature calculated inside the pool. The analysis of the pool temperature will be carried out in the following. At the outlet of the HS, the LBE temperature changes considering different sub-channels, due to the heat dissipation through the hexagonal shell. In order to valuate this effect, Fig. 2.13 shows the temperature measured by the TCs T-FPS-36 (in a central sub-channel) and T-FPS-34 (in a external sub-channel), comparing with the LBE temperature evaluated by the code in the same positions. The Fig. 2.13 shows that in the simulations a more predominant effect of the heat dissipation during the full power operation occurs. Then, after the transition, the calculations are in good agreement with the experimental data, highlighting that the code well reproduces the heat dissipation through the FPS external shell.



 <b>RICERCA SISTEMA ELETTRICO</b>	<u>Title:</u> Development of BE numerical tools for LFR design and safety analysis (2018)	<u>Distribution</u> <b>PUBLIC</b>	<u>Issue Date</u> 29.01.2019	<u>Pag.</u>
	<u>Project:</u> ADP ENEA-MSE PAR 2017	Ref. ADPFISS-LP2-167	Rev. 0	32 di 163

The temperature drop across the HX is compared in Fig. 2.14; the primary inlet and outlet temperature follows a similar trend of the FPS. The HX inlet temperature is lower than the FPS outlet temperature (about 30 K), due to the heat dissipations through the walls of the fitting volume, the riser and the separator, highlighting a good prediction of the heat dissipations by the code. After the simulated station blackout, the temperature drop across the HX is due to the heat dissipation through the cylindrical shell, which are well predicted by R5-3D. Fig. 2.15 depicts the comparison of the DHR temperature drop of the LBE. During the first 25000 s, the temperature distribution along the DHR primary side is strongly affected by the thermal stratification of the LBE inside the pool, due to the low air mass flow rate on the secondary side. After the transition, the air starts to flow along the DHR and the LBE temperature is well predicted by the code. In the last part of the test, the inlet temperature is a slightly overestimated, due to the buoyancy effects inside the pool.

One of the main tasks of the activity is the investigation of the capability of RELAP5-3D to reproduce three-dimensional phenomena occurring in large volumes, such as the pool of HLM reactor. CIRCE facility offers useful data for this evaluation. The analysis, presented from Fig. 2.16 to Fig. 2.18, is carried out at final conditions of the full power operation (25000 s) and at two instants of the NC conditions (at 80000 s, 200000 s), showing the evolution of the LBE temperature during the whole test. From Fig. 2.16 to Fig. 2.18 the calculation results are compared with the experimental data, measured by the 119 TCs installed inside the pool (see Fig. 2.8). In the picture (a), the temperature obtained averaging the data acquired by the thermocouples A, B, C, D and E is compared with the temperature calculated in the same position (between the HX and the DHR) by R5-3D; in the same way, the average temperature of the TCs F and G and the temperature measured by TCs I and H are compared with the simulation results in pictures (b), (c) and (d).


The experimental campaign highlighted that phenomena of mixing convection do not occur inside the pool; the LBE temperature assumes the same value at each level. This result is also obtained by R5-3D; for this reason, the analysis is focused on the vertical thermal stratification. The test starts at uniform conditions inside the pool (about 600 K). After the activation of the gas injection system, of FPS and of FW system, the LBE temperature in the upper part of the pool starts to increase, due to the heat dissipations from the primary flow path, and the temperature in the lower part starts to decrease, due to the cold LBE exiting the HX. The qualitative trend of the LBE temperature is the same of the DHR inlet and outlet in the first 25000 seconds. The axial distribution of the temperature is shown in Fig. 2.16, which highlights that the code is able to reproduce the qualitative trend of the temperature inside the pool. The underestimation of the temperature is probably due to the overestimation of the heat losses toward the environment.

After the simulated station blackout, the temperature in the upper part of the pool rapidly decreases, due to the reduction of the LBE temperature through the main flow path. Fig. 2.17 shows the comparison at 80000 s; during the experiment, the gradient between 5 m and 7 m, rapidly reduces, obtaining a slightly uniform temperature of about 575 K, and the second gradient moves downward at the DHR outlet level, where the cold LBE exits. The code well reproduces this transition. After that, the temperature inside the pool increases, following the same trend of the primary flow path. The code is able to reproduce this evolution, evaluating very well the level where the thermal stratification occurs.

### 2.3 Conclusive remarks

The aims of the experimental campaign performed on CIRCE-ICE have been to investigate the main thermal-hydraulic phenomena which characterize the HLM systems and to provide data for the validation of the computational code. The experiment has reproduced a protected loss of heat sink (PLOHS) plus a loss of flow (LOF) simulating the total loss of primary flow, the loss of the secondary circuit, the consequent scram of the reactor and the activation of the DHR system. The goal of the activity has been to investigate the capability of RELAP5-3D to reproduce the transition between gas enhanced circulation to natural circulation and the three-dimensional phenomena inside the large pool.



 <b>RICERCA SISTEMA ELETTRICO</b>	<b>Title:</b> Development of BE numerical tools for LFR design and safety analysis (2018)	<u>Distribution</u> <b>PUBLIC</b>	<u>Issue Date</u> 29.01.2019	<u>Pag.</u>
	<b>Project:</b> ADP ENEA-MSE PAR 2017	Ref. ADPFISS-LP2-167	Rev. 0	33 di 163

The thermal-hydraulic model has been developed in order to compare the main parameters in the exact position of the instrumentations. At this purpose, a mono-dimensional nodalization scheme has been developed to reproduce the primary and the secondary main flow path and a detailed three-dimensional component to model the pool.

The comparison between the experimental data and the calculations results has highlighted the capability of R5-3D to reproduce the thermal-hydraulic behavior of the main primary flow path. The code is able to reproduce the LBE circulation in both gas-enhanced and natural conditions; moreover, the LBE thermal-hydraulic properties correlations, implemented in RELAP5-3D as described in Ref. [2.8], well simulate the coolant behavior and the HLM default correlations for the heat exchange, assuming little corrections following the actual state of art, provide good estimation of the thermal power exchanged through the main mono-dimensional components.

One of the main tasks of the activity has been to investigate the capability of RELAP5-3D to reproduce 3D thermal-hydraulic phenomena inside large volumes, such as HLM pools. At this purpose, CIRCE facility, equipped with 119 TCs to obtain the LBE temperature inside the pool, offers useful data. The comparison between experimental data and simulation results highlights that the movement and the mixing convection of the fluid inside the pool is well reproduced. The main phenomenon which occurs inside the pool is the axial thermal stratification, due to the heat losses through the wall of the primary flow path. The code is able to reproduce the heat dissipations and the LBE temperature trend inside the pool. Slight discrepancy has been noticed in the central part of the pool, probably due to the prediction of the heat dissipations in this level. In fact, the operative range of the heat exchange correlation implemented in RELAP5-3D are not respected in a large volume such as a pool. The fitting volume provides a large heat exchange area in this axial level and an underestimation of the heat transfer coefficient on the pool side provides a slight underestimation of the heat dissipated through its wall. The future activities should be focused on the development and the implementation of correlations for the estimation of the HTC in large HLM volumes.

Parameters	Value
Outside diameter (mm)	1200
Wall thickness (mm)	15
Material	AISI 316L
Max LBE inventory (ton)	90
Temperature range (K)	473 to 773

**Tab. 2.1 – CIRCE S100 main parameters**

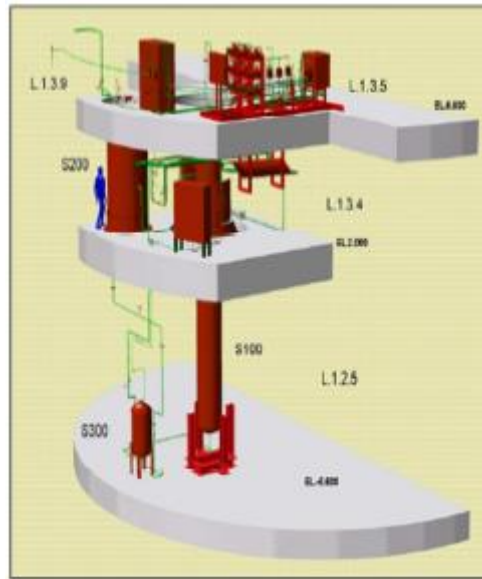
Parameters	GHC	NC
Duration (h)	8	97
Electical power supplied (kW)	600	23
Ar injection (NI/s)	5.2	0
Feed-water mass flow rate (kg/s)	0.5	0
DHR air injection (kg/s)	~0	0.289

**Tab. 2.2 – TEST IV boundary conditions**

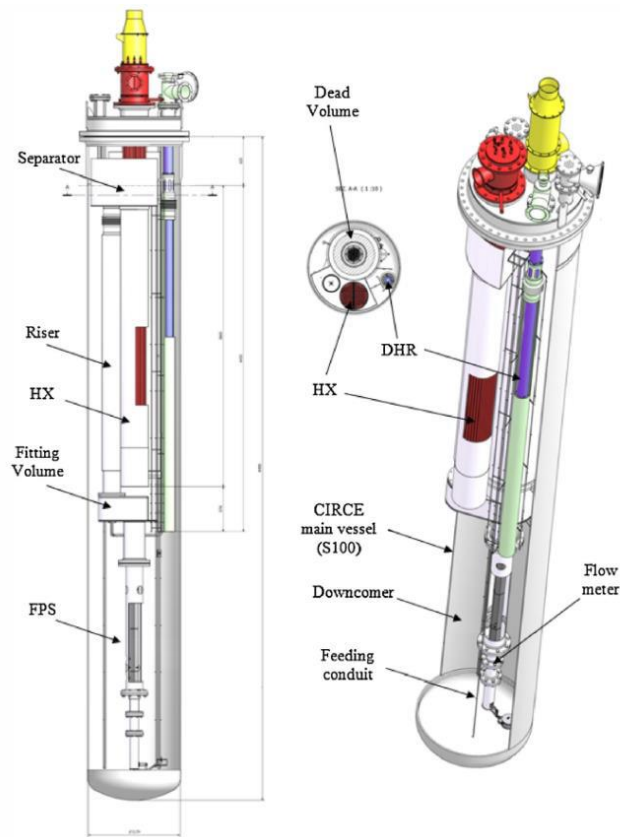
Parameters	Value
Number of hydrodynamic volumes	1929
Number of hydrodynamic junctions	4856
Number of heat structure mesh points	15353

**Tab. 2.3 – CIRCE-ICE nodalization scheme: main parameters**

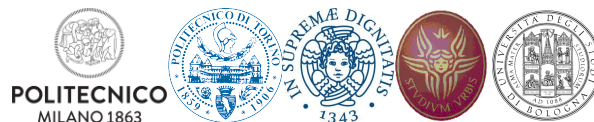


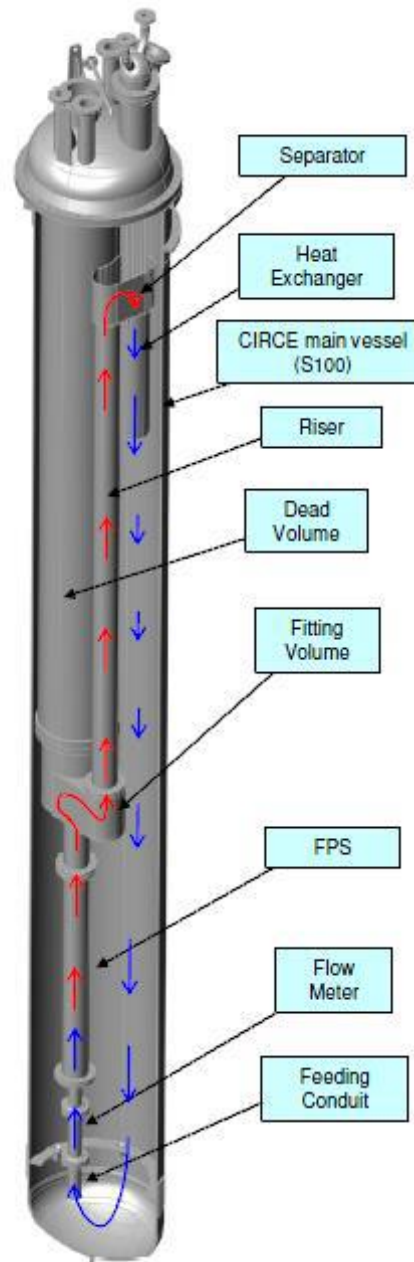


*Fig. 2.1 – CIRCE isometric view*

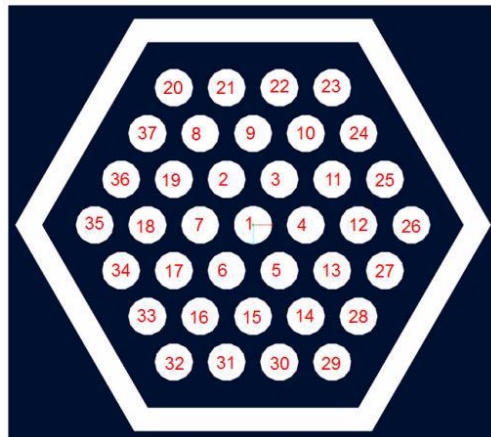


*Fig. 2.2 – ICE test section*

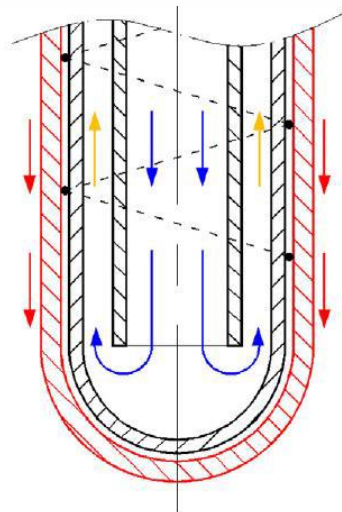




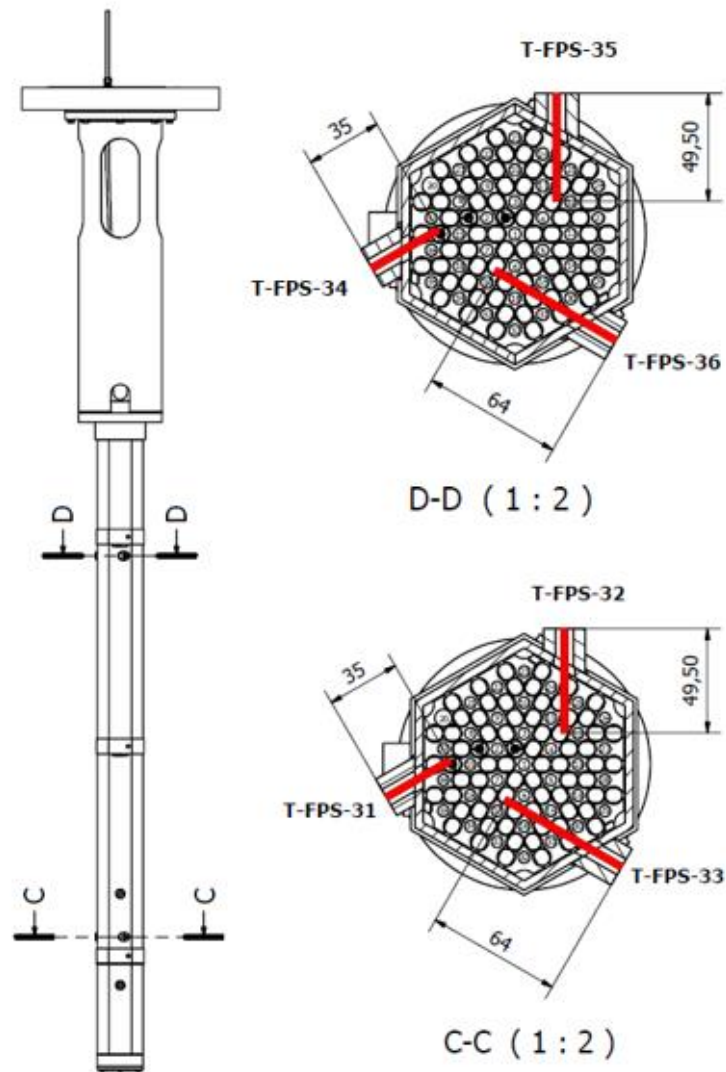
*Fig. 2.3 – ICE test section: primary flow path*



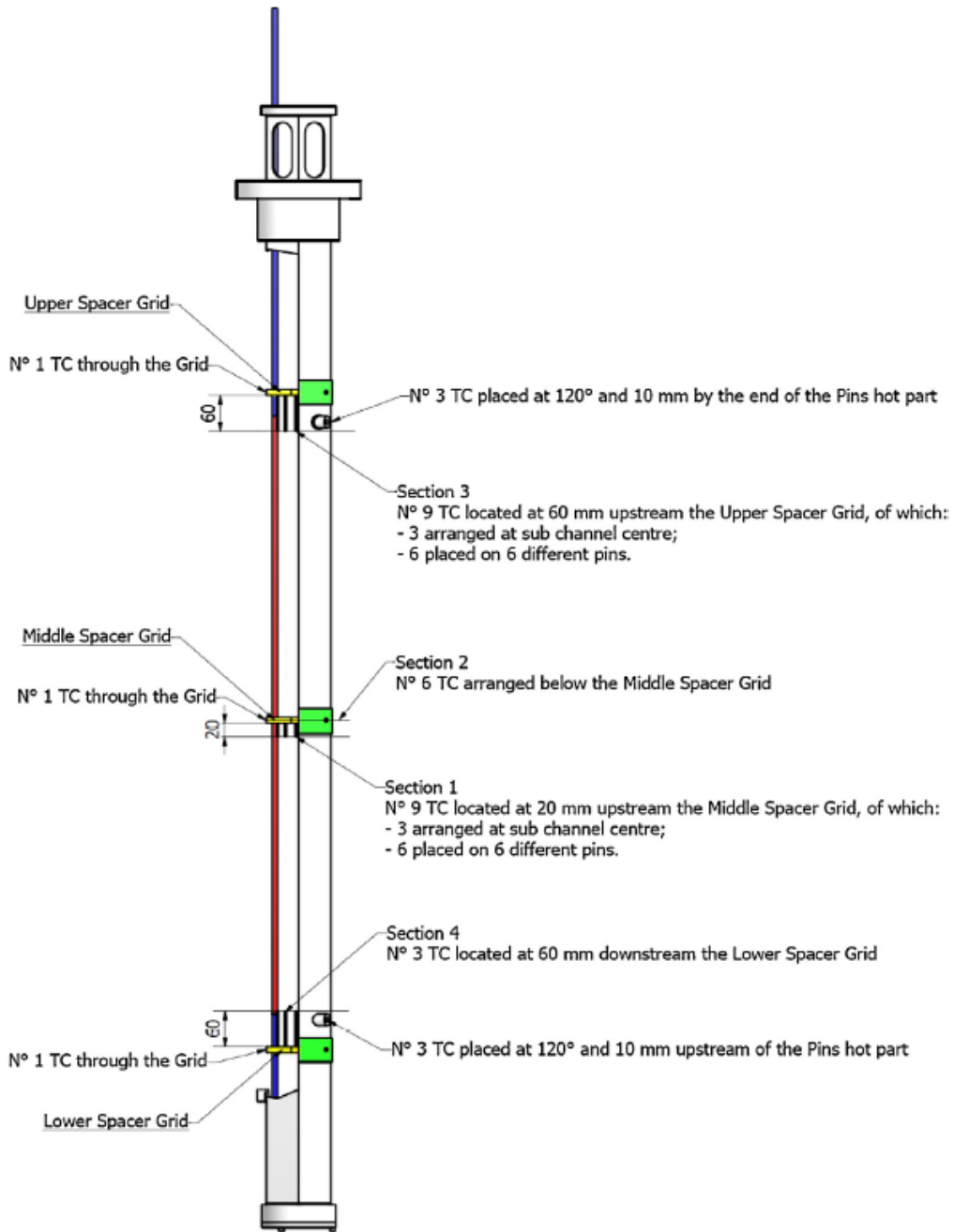
*Fig. 2.4 – FPS cross section*



*Fig. 2.5 – HX bayonet tube*

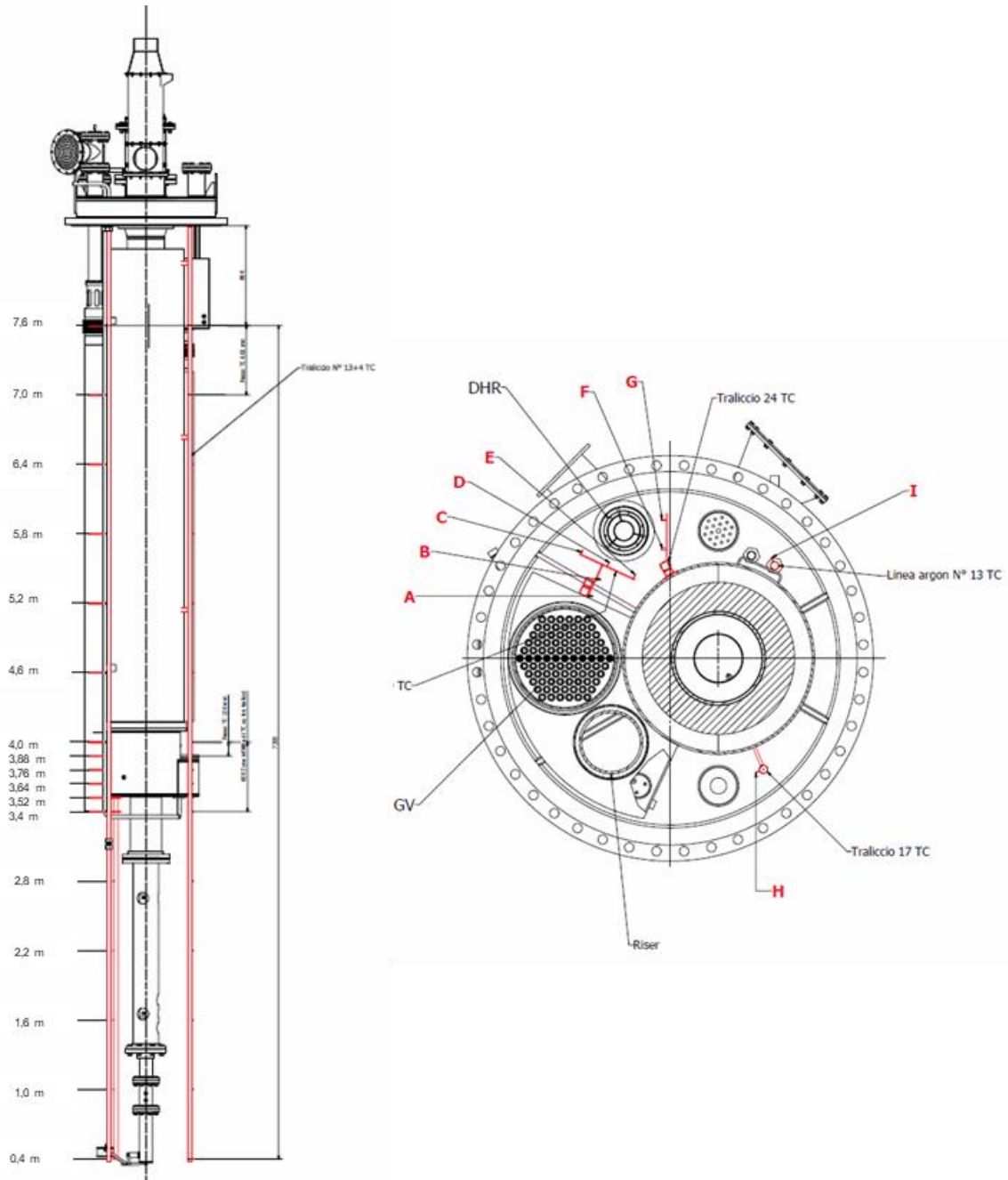


*Fig. 2.6 – CIRCE instrumentation: FPS (1)*

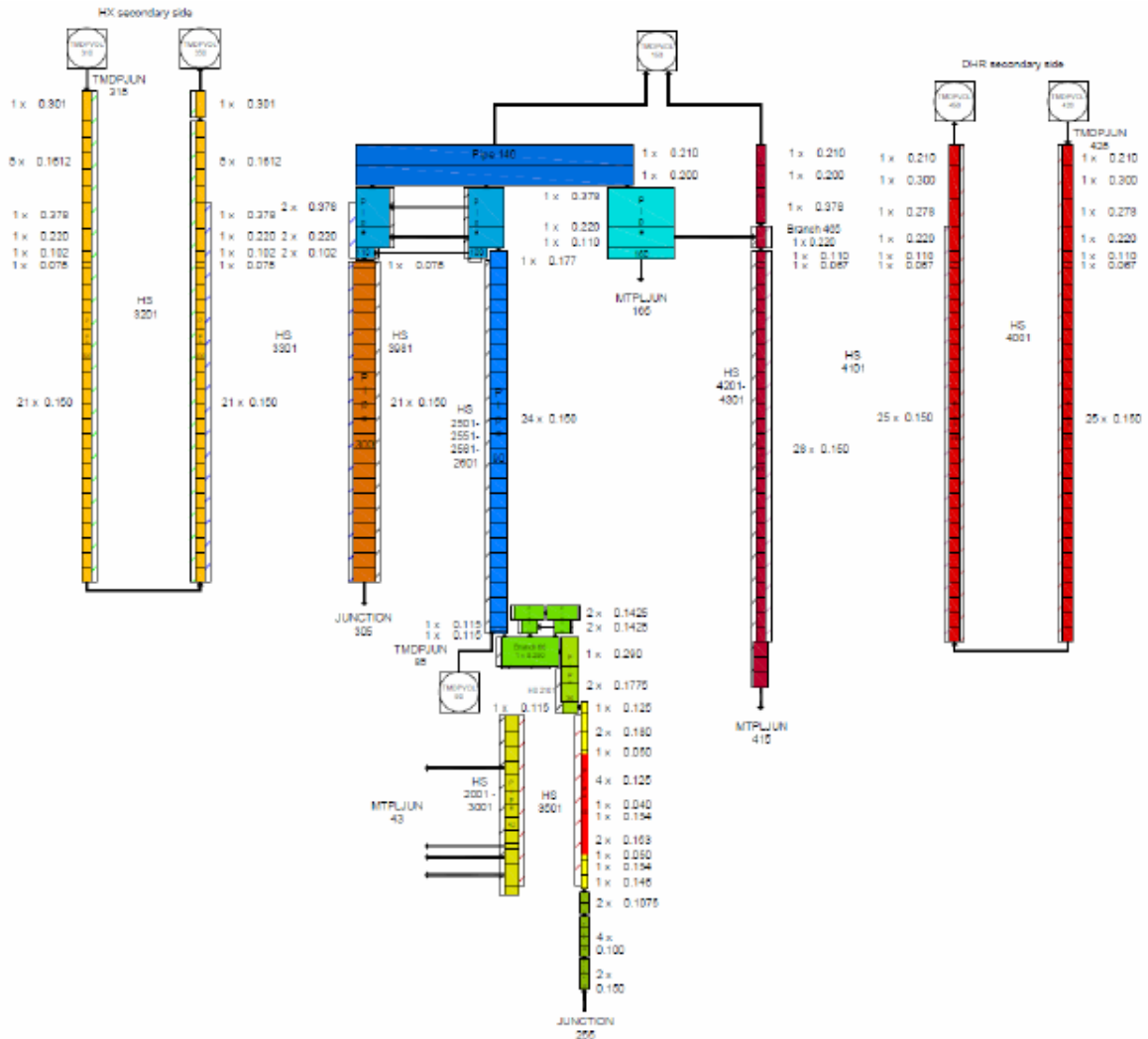


*Fig. 2.7 – CIRCE instrumentation: FPS (2)*



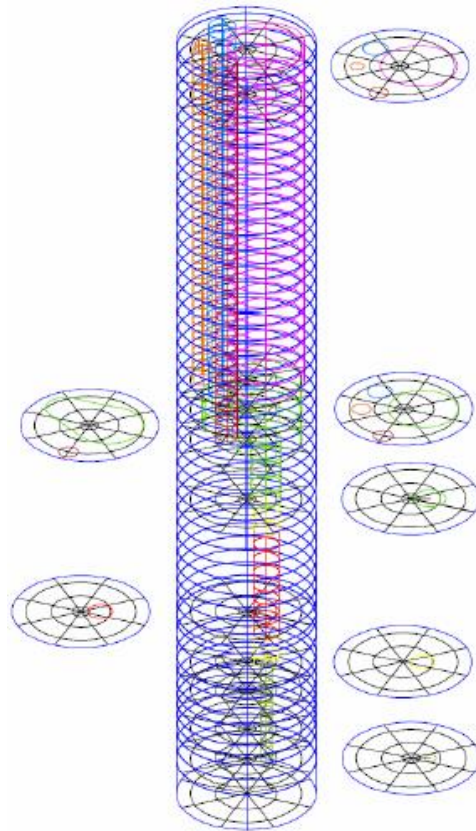


*Fig. 2.8 – CIRCE instrumentation: pool*

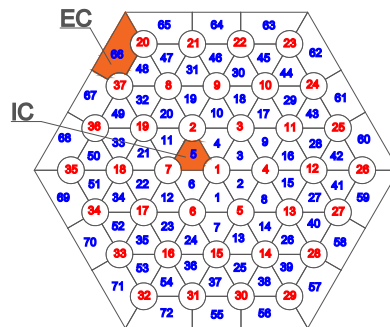


*Fig. 2.9 – Nodalization scheme: mono-dimensional model*





*Fig. 2.10 – Nodalization scheme: multi-dimensional model*



*Fig. 2.11 – Nodalization scheme: FPS*

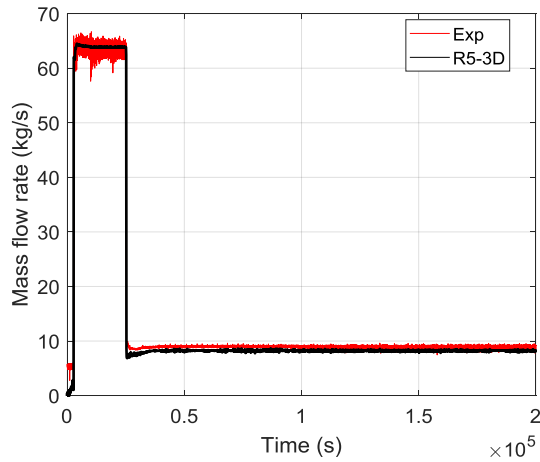


Fig. 2.12 – LBE mass flow rate

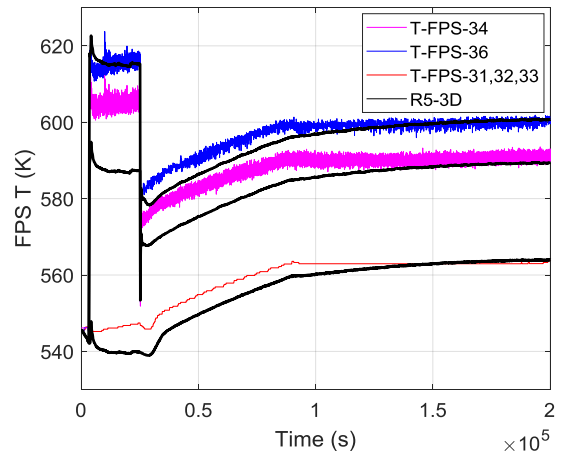


Fig. 2.13 – FPS inlet/outlet temperature

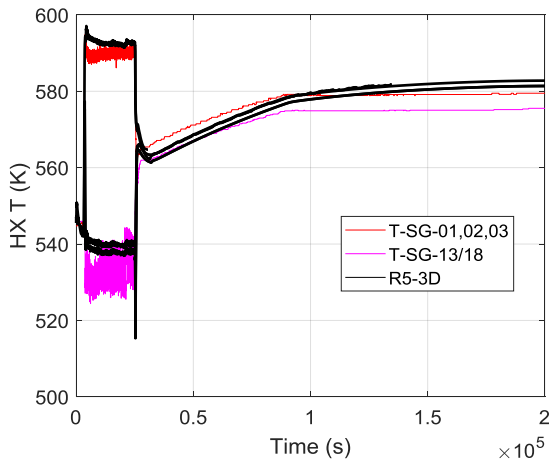


Fig. 2.14 – HX inlet/outlet temperature

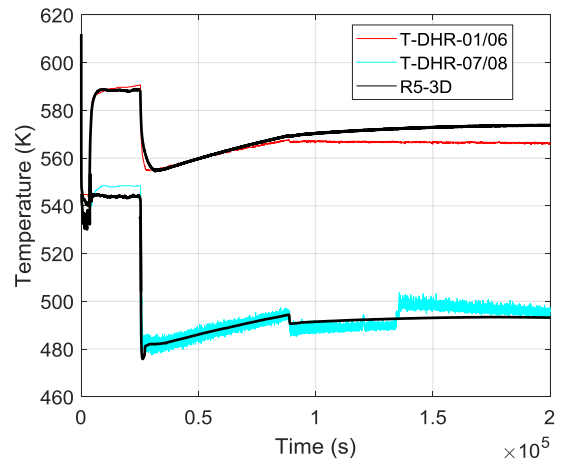
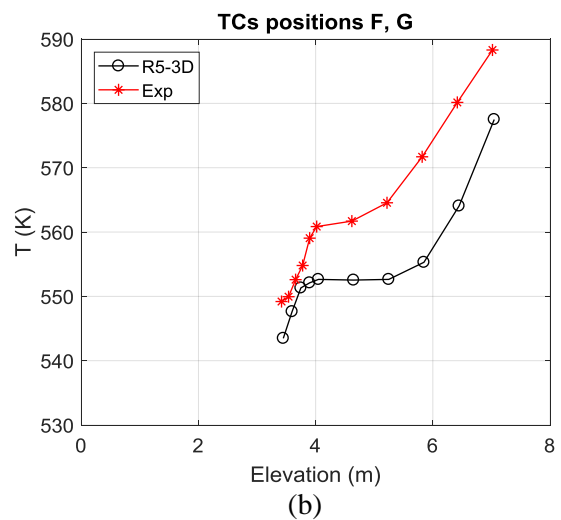
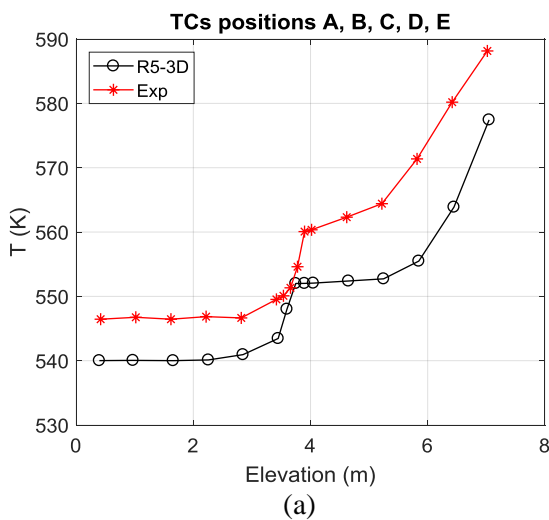


Fig. 2.15 – DHR inlet/outlet temperature



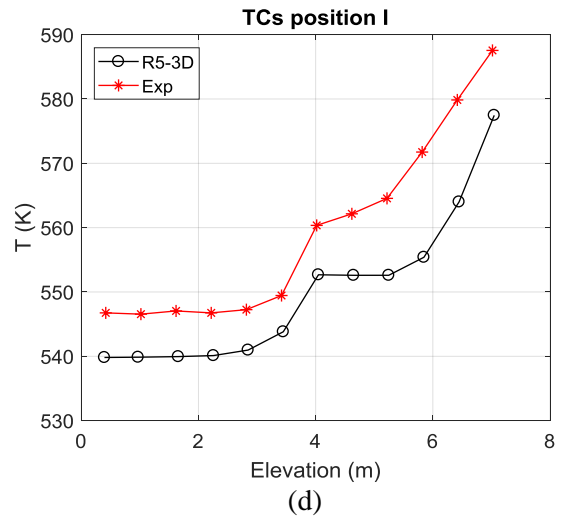
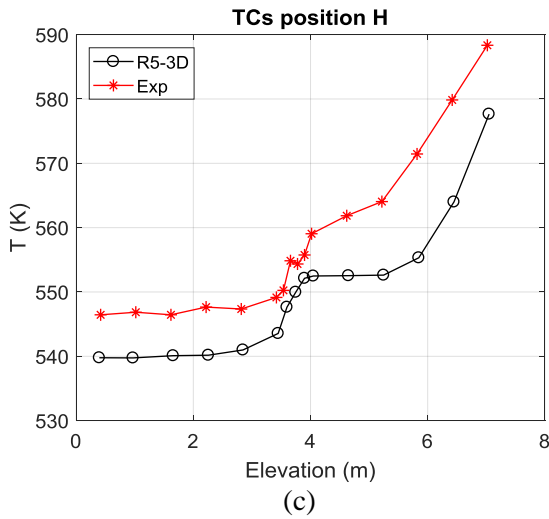


Fig. 2.16 – TS and MC: 25000 s

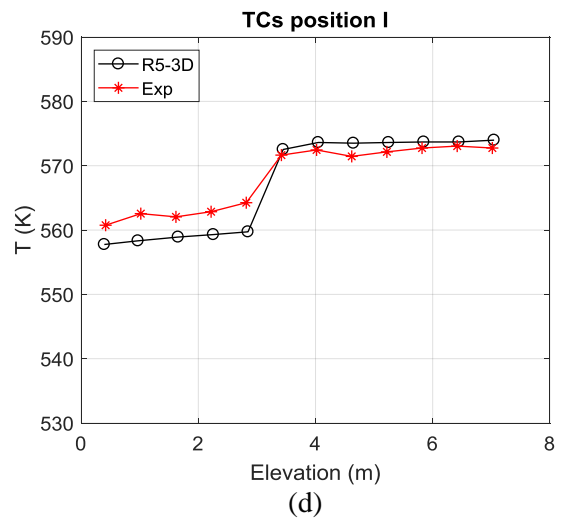
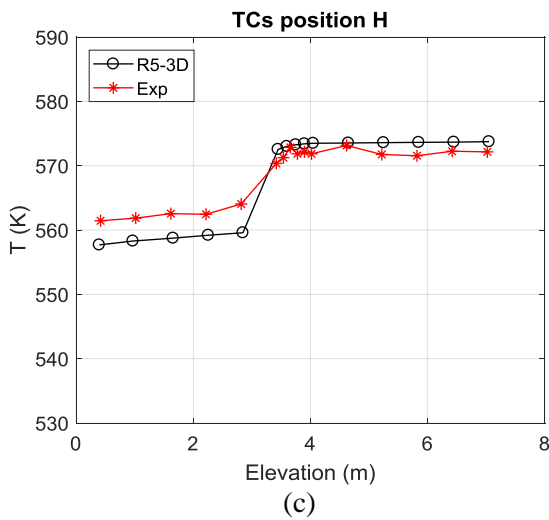
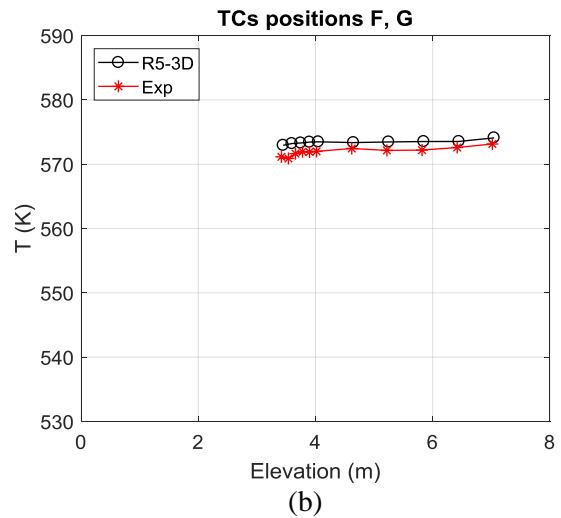
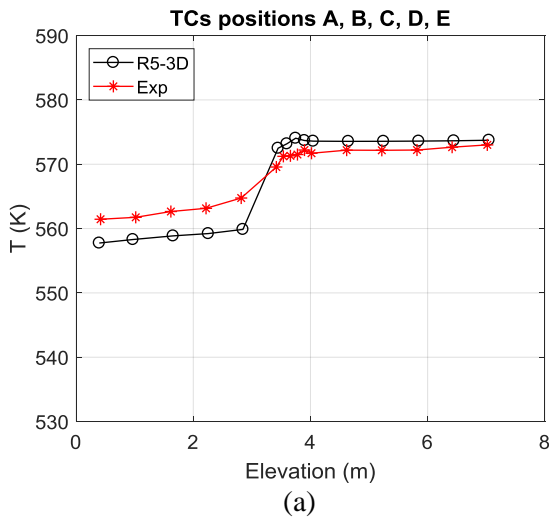


Fig. 2.17 – TS and MC: 80000 s



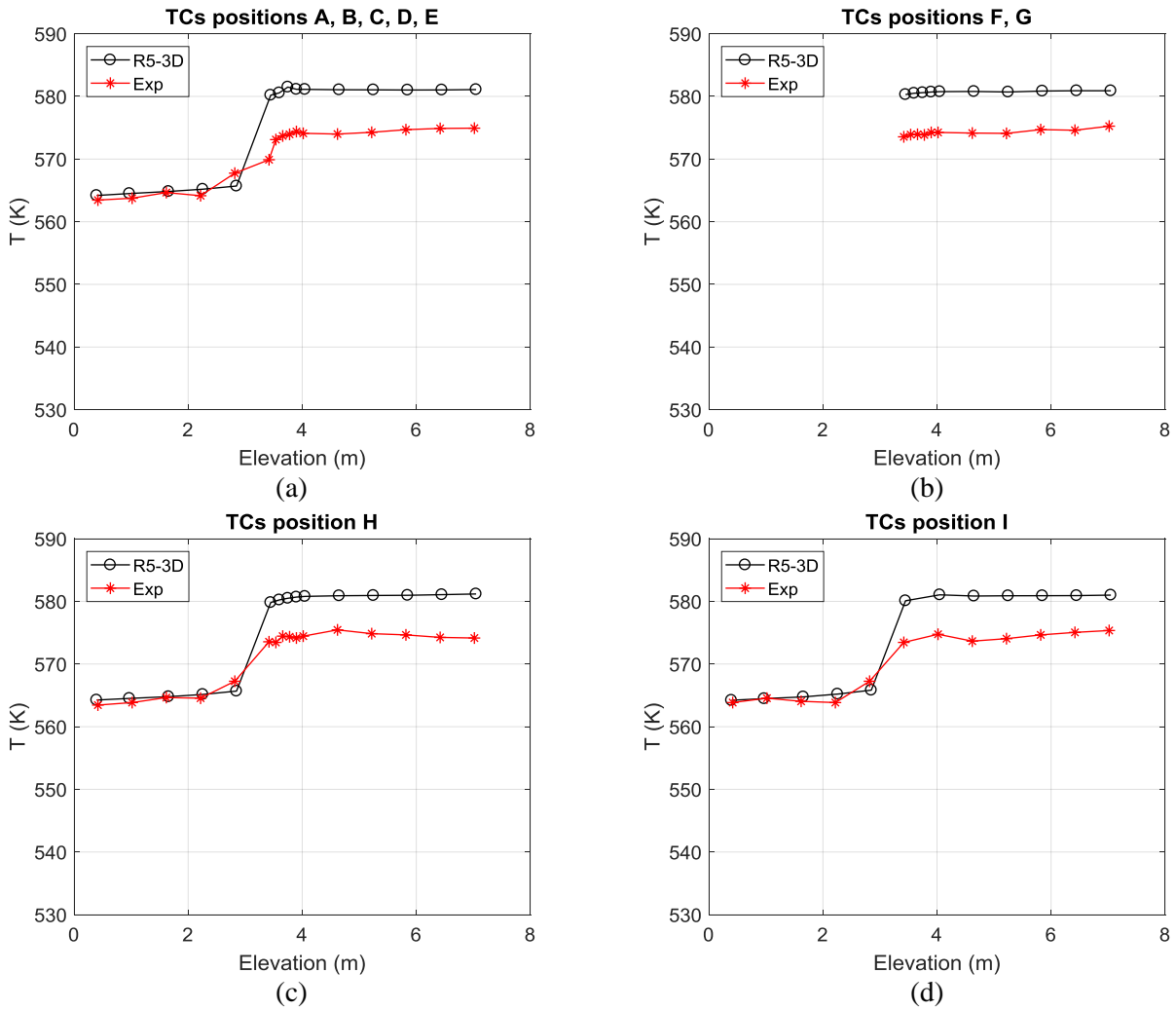



Fig. 2.18 – TS and MC: 200000 s




 <b>RICERCA SISTEMA ELETTRICO</b>	<b>Title:</b> Development of BE numerical tools for LFR design and safety analysis (2018)	<u>Distribution</u> <b>PUBLIC</b>	<u>Issue Date</u> 29.01.2019	<u>Pag.</u>
	<b>Project:</b> ADP ENEA-MSE PAR 2017	Ref. ADPFISS-LP2-167	Rev. 0	45 di 163

## 2.4 List of References

- [2.1] L. Gramiccia, D. Vitale Di Maio, F. Giannetti, M. Tarantino, D. Rozzia, A. Toti, *Definizione ed implementazione preliminare di un laboratorio per l'investigazione della termofluidodinamica dei metalli liquidi (Double-wall bayonet tube steam generator for LFR application. Preliminary characterization)*. Report RdS/2011/50, 2011.
- [2.2] A. Gandini, L. Cretara, F. Giannetti, M. Frullini, V. Peluso, *Attività di analisi di sensitività con metodologie GPT applicate a noccioli critici e sottocritici raffreddati a piombo*. Report RdS/2012/37, 2012.
- [2.3] L. Ferroni, F. Giannetti, J. Manzano, M. Ciotti, *Studi di sostenibilità sui sistemi nucleari refrigerati a piombo*. CERSE-UNIRM RL 1190/2013, 2013.
- [2.4] C. Parisi, F. Giannetti, A. Naviglio, G. Caruso, *Determinazione dei parametri di sicurezza del core e dell'andamento del burnup di un reattore veloce refrigerato a metallo liquido*. ADPFISS-LP2-000, 2013.
- [2.5] A. Cammi, S. Lorenzi, R. Ponciroli, L. Ferroni, F. Giannetti, D. Vitale Di Maio, V. Covicchio, *Studi di sostenibilità volti a massimizzare l'utilizzo del combustibile e a minimizzare le scorie nucleari con i sistemi veloci refrigerati a piombo*. ADPFISS-LP2-045, 2014.
- [2.6] F. Giannetti, D. Vitale Di Maio, A. Naviglio, G. Caruso, *Thermal-hydraulic analysis of an innovative decay heat removal system for lead-cooled fast reactors*. Nucl. Eng. Des. 305, 168-178, <http://dx.doi.org/10.1016/j.nucengdes.2016.05.005>, 2016.
- [2.7] N. E. Todreas, M. S. Kazimi, *Nuclear System – Thermal Hydraulic Fundamentals*. Taylor & Francis, ISBN 0-89116-935-0, 1993.
- [2.8] P. Balestra, F. Giannetti, G. Caruso, A. Alfonsi, *New RELAP5-3D lead and LBE thermophysical properties implementation for safety analysis of Gen IV reactors*. Sci. Technol. Nucl. Install., <http://dx.doi.org/10.1155/2016/1687946>, 2016.
- [2.9] OECD/NEA Nuclear Science Committee, *Handbook on Lead-bismuth Eutectic Alloy AND Lead Properties, Materials Compatibility, Thermal-hydraulics and Technologies*. 2015.
- [2.10] D. Rozzia, A. Del Nevo, M. Tarantino, V. Narcisi, D. Vitale di Maio, F. Giannetti, G. Caruso, *ALFRED-SGBT. Preliminary characterization by the HERO test section*. ADPFISS-LP2-100, 2015.
- [2.11] M. Tarantino, D. Rozzia, A. Del Nevo, F. Giannetti, *CIRCE-HERO test setup*. Tech. Rep. D4.3, H2020 SESAME project, 2016.
- [2.12] V. Narcisi, F. Giannetti, A. Del Nevo, M. Tarantino, G. Caruso, *Pre-test analysis of the protected loss of primary pump transient in CIRCE-HERO facility*. J. Phys. Conf. Ser. 923 (012005). <http://dx.doi.org/10.1088/1742-6596/923/1/012005>
- [2.13] V. Narcisi, F. Giannetti, A. Del Nevo, M. Tarantino, G. Caruso, *Pre-test analysis of accidental transients for ALFRED SGBT mock-up characterization*. Nucl. Eng. Des. 333, 181-195, <https://doi.org/10.1016/j.nucengdes.2018.04.015>, 2018.
- [2.14] V. Narcisi, F. Giannetti, G. Caruso, D. Rozzia, A. Del Nevo, M. Tarantino, *Installazione della sezione di prova HERO nella facility CIRCE: sviluppo nodalizzazione e progettazione della campagna sperimentale*. ADPFISS-LP2-133, 2016.
- [2.15] V. Narcisi, P. Lorusso, F. Giannetti, A. Del Nevo, M. Tarantino, *Analisi di pre-test della campagna sperimentale CIRCE/HERO con codici di sistema*. ADPFISS-LP2-151, 2017.




 <b>RICERCA SISTEMA ELETTRICO</b>	<u>Title:</u> Development of BE numerical tools for LFR design and safety analysis (2018)	<u>Distribution</u> <b>PUBLIC</b>	<u>Issue Date</u> 29.01.2019	<u>Pag.</u>
	<u>Project:</u> ADP ENEA-MSE PAR 2017	Ref. ADPFISS-LP2-167	Rev. 0	46 di 163

- [2.16] V. Narcisi, F. Giannetti, P. Lorusso, M. Tarantino, A. Del Nevo, G. Caruso, ***Thermal stratification analysis in CIRCE-ICE pool facility with RELAP5-3D model***. Proc. Of Global Symposium on Lead and Lead Alloy Based Nuclear Energy Science – GLANST2017, Seoul, Republic of Korea, September 2016.
- [2.17] V. Narcisi, F. Giannetti, M. Tarantino, D. Martelli, G. Caruso, ***Pool temperature stratification analysis in CIRCE-ICE facility with RELAP5-3D© model and comparison with experimental tests***. J. Phys. Conf. Ser. 923 (01 2006), <http://dx.doi.org/10.1088/1742-6596/923/1/012006>, 2017.
- [2.18] A. Del Nevo, A. Subioli, V. Narcisi, F. Giannetti, ***Application of RELAP5-3D on Phenix Experimental Test***. ADPFISS – LP2 – 144, 2017
- [2.19] M. Tarantino, D. Martelli, G. Barone, I. Di Piazza, N. Forgione, ***Mixed convection and stratification phenomena in a heavy liquid metal pool***. Nucl. Eng. Des. 286, 261-277, <http://dx.doi.org/10.1016/j.nucengdes.2015.02.012>, 2015.
- [2.20] INL, ***The RELAP5-3D© Code Development Team, RELAP5-3D© Code Manual Volume IV: Models and Correlations***. INL/MIS-15-36723, Revision 4.3, October 2015
- [2.21] M. Schikorr, E. Bubelis, L. Mansani, K. Litfin, ***Proposal for pressure drop prediction for a fuel bundle with grid spacers using Rehme pressure drop correlations***. Nuclear Engineering and Design, 240 1830-42, <https://doi.org/10.1016/j.nucengdes.2010.03.039>, 2010.

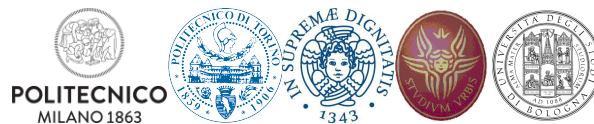





 <b>RICERCA SISTEMA ELETTRICO</b>	<u>Title:</u> Development of BE numerical tools for LFR design and safety analysis (2018)	<u>Distribution</u> <b>PUBLIC</b>	<u>Issue Date</u> 29.01.2019	<u>Pag.</u>
	<u>Project:</u> ADP ENEA-MSE PAR 2017	Ref. ADPFISS-LP2-167	Rev. 0	47 di 163

### 3 APPLICATION OF RELAP5-3D ON PHENIX EXPERIMENTAL TESTS


*F. Giannetti, V. Narcisi, A. Subioli, A. Del Nevo*



 <b>RICERCA SISTEMA ELETTRICO</b>	<u>Title:</u> Development of BE numerical tools for LFR design and safety analysis (2018)	<u>Distribution</u> <b>PUBLIC</b>	<u>Issue Date</u> 29.01.2019	<u>Pag.</u>
	<u>Project:</u> ADP ENEA-MSE PAR 2017	Ref. ADPFISS-LP2-167	Rev. 0	48 di 163

*(Page intentionally left blank)*



 <b>RICERCA SISTEMA ELETTRICO</b>	<u>Title:</u> Development of BE numerical tools for LFR design and safety analysis (2018)	<u>Distribution</u> <b>PUBLIC</b>	<u>Issue Date</u> 29.01.2019	<u>Pag.</u>
	<u>Project:</u> ADP ENEA-MSE PAR 2017	Ref. ADPFISS-LP2-167	Rev. 0	49 di 163

### 3.1 Background and references

The assessment of nuclear power plant (NPP) performances during accidental scenario is the main issue of the safety analysis. Until recent years, most of the safety analyses were successfully performed using thermal-hydraulics system code (SYS-TH), reproducing transient conditions typical of postulated accidents. However, the SYS-TH codes present some limitations when complex feedback exists between core neutronics and thermal-hydraulics, when innovative coolants are used for the core heat removal (for example liquid metals or molten salt) or when multidimensional phenomena are involved in particular configurations of a NPP (Ref. [3.1]).

In a scenario where the energy demand is constantly growing and the sustainability is a fundamental aspect of the energy production, especially in terms of CO<sub>2</sub> emissions, the nuclear energy is expected to play a crucial role. In this framework, the Generation IV International Forum (GIF) proposes six innovative nuclear system concepts which meet the requirements introduces for the Generation IV (GEN-IV) reactors: sustainability, economics proliferation resistance, safety and reliability. In these concepts, the Sodium-cooled Fast Reactor (SFR) is considered one of the most promising technologies and the nearest-term deployable system for the actinide management; the much of the basic SFR technology has been established in former fast reactor programs, as the Phénix End-of-Life tests (Ref. [3.2]). Phénix is a SFR operated in France and this experimental campaign has been conducted before the definitive shutdown of the reactor (Ref. [3.3]).

A dissymmetrical configuration test, from the End-of-Life series, has been selected as a benchmark transient into H2020 SESAME project (<http://sesame-h2020.eu/>), in order to demonstrate the capability of the system thermal-hydraulics codes (standalone or in coupling configuration with CFD codes) to predict the three-dimensional pool phenomena. This activity, carried out in synergy with SESAME project, aims to validate the RELAP5-3D<sup>®</sup> code in simulating pool-type liquid metal cooled fast reactor in accidental scenario, identifying code limitations and source of uncertainties. The activity also tries to improve the understanding of thermal-hydraulic processes and phenomena observed in dissymmetrical test and to develop a reliable approach for the application of thermal-hydraulic system codes in safety analysis of new generation fast reactor systems. Indeed, transients and thermal-hydraulic phenomena relevant for the analysis of liquid metal fast reactors are expected to occur in PHENIX, similarly as larger scale fast reactor systems. This implies that models and correlations that affect the code's calculation of the phenomena of interest can be assessed in a range of thermal-hydraulic parameters representative of candidate designs (Ref. [3.4]).

In the past years, the blind calculations analysis was presented. After the blind phase, CEA provided the experimental data to the benchmark participants. In this report, the post-test analysis, carried out with RELAP5-3D, has been discussed.


### 3.2 Body of the report concerning the ongoing activities

#### 3.2.1 Phénix reactor

Phénix is a sodium cooled pool-type fast reactor of 563 MWth, with an electric output of approximately 250 MWe, located at the Marcoule nuclear site, near Orange, France. The NPP construction began in November 1968 and the first connection to the French national electricity grid was in December 1973. During the summer of 1976, due to small sodium losses in two intermediate heat exchangers, the plant was temporarily stopped to repair the failures found. The problems of the two IHXs have never been solved but they were closed and, from 1993 to the end of the electricity production in 2009, the reactor has been operated at a reduced power of 350 MWth (140 MWe) (Ref. [3.5], [3.6] and [3.7]).

Fig. 3.1 shows the reactor block, which is a suspended type. The reactor is composed of four vessels, all supported by the upper cover slab. The cover head is attached to a concrete slab by 21 suspension hangers and it is closed off with a flat roof equipped with penetrations necessary for the passage of components and



 <b>RICERCA SISTEMA ELETTRICO</b>	<u>Title:</u> Development of BE numerical tools for LFR design and safety analysis (2018)	<u>Distribution</u> <b>PUBLIC</b>	<u>Issue Date</u> 29.01.2019	<u>Pag.</u>
	<u>Project:</u> ADP ENEA-MSE PAR 2017	Ref. ADPFISS-LP2-167	Rev. 0	50 di 163

instrumentation. The main vessel ensures the biological protection; it is 10 metres high and 11.8 m in diameter and it contains about 800 tons of primary sodium. Any possible sodium leaks are contained by the double-enveloped vessel, which is welded to the upper part of the main vessel. The roof and the double envelope vessel are both thermally insulated. The external one is the primary containment vessel, an ordinary steel tank which envelopes the internal vessels. The primary containment vessel is welded under the concrete slab and is maintained in a nitrogen atmosphere; its role is to contain radioactive products in the event of a severe accident. The final emergency cooling system is welded onto the outside wall of the third vessel and it aims to maintain the reactor pit concrete at ambient temperature and to ensure the decay heat removal, in the event of a loss of normal cooling systems. Inside the main vessel, the primary vessel separates the sodium coolant in two pools (hot and cold). The primary vessel is composed from a shell which is followed from a conical area that contains twelve channels equipped with sleeves for primary pumps, intermediate heat exchangers and other components. This is followed by a new shell that envelopes the core and is welded to the lateral shielding support (Ref. [3.5], [3.6] and [3.7]).

The primary system is equipped with six intermediate heat exchangers (straight-tube type, see Fig. 3.2 and Fig. 3.3), connected in pairs to the three secondary loops, which are equipped with the mechanical pump, located inside the expansion tank, a buffer tank and the auxiliary systems, which ensure the sodium storage, filling, and purification. Each of them feeds a steam generator that supply the thermal power to the tertiary circuit, based on a Rankine cycle where the operating fluid is the water. The hot primary coolant, contained inside the hot pool, moves through the shell side of the intermediate heat exchangers (IHX) decreasing the temperature and then is collected inside the cold pool. Three primary pumps (Fig. 3.4) drive the sodium from the cold pool to the diagrid, that guarantees the correct distribution of the coolant mass flow rate to each sub-assembly (SA). Another function of the diagrid is to redirect about 10% of the operating flow to the vessel cooling system (VCS), and, together with the strongback and the conical shell, of supporting the above structures. The VCS operation is presented in Fig. 3.5; the cold sodium moves upward inside the zone between the conical shell and the main vessel, refrigerating the latter. Then the sodium is poured in cold pool.


The reactor core consists of an array of hexagonal assemblies, represented in Fig. 3.6. Each assembly is characterized by an overall length of 4.3 m; the fuel is mixed uranium-plutonium oxide (Ref. [3.5] and [3.8]). A central fissile zone, composed by two regions of different enrichment values, is surrounded by annular fertile zones and further out by steel reflectors and lateral neutron shielding rods especially designed to limit the activation of the secondary cooling sodium in the intermediate heat exchangers. The fuel, which is mixed uranium-plutonium oxide, has a Pu enrichment of 18% in the central region (inner core) and an enrichment of 23% in the periphery region (outer core). This difference is designed to “level out” the neutron flux and homogenize heating. The fuel sub-assemblies (SA) contain MOX in the form of 217 pins, which are composed of a stack of pellets, and depleted uranium oxide, which acts as axial blanket, formed by 217 pins in the lower part, and by 37 pins in the upper part; they are all enclosed in a stainless-steel cladding. The spacer wires fix the pins correct positions and they guarantee the flow of sodium and optimize heat exchange. The fuel bundle is located inside a hexagonal stainless-steel wrapper equipped, in the lower part, with a foot that guarantees the positioning of the SA in the diagrid and the inlet for the sodium mass flow rate (see Fig. 3.7).

### 3.2.2 Dissymmetric test

Before the final shutdown of the PHENIX reactor, an experimental program was set up in order to collect data for code assessment and to address the design of new SFR with respect to fuel, materials, neutronics and thermal hydraulics. The experimental campaign, belonging to the End-of-Life tests, includes:

- The natural convection test, dedicated to the establishment of natural circulation in the primary, secondary and steam generator casing systems;



 <b>RICERCA SISTEMA ELETTRICO</b>	<u>Title:</u> Development of BE numerical tools for LFR design and safety analysis (2018)	<u>Distribution</u> <b>PUBLIC</b>	<u>Issue Date</u> 29.01.2019	<u>Pag.</u>
	<u>Project:</u> ADP ENEA-MSE PAR 2017	Ref. ADPFISS-LP2-167	Rev. 0	51 di 163

- The dissymmetrical test characterized by the manual trip of a secondary pump leading to the injection of hot sodium in 1/3 of the cold pool.

During the 2009, two asymmetrical tests were performed, one on each secondary loop (LOOP 1 and LOOP 3). The results of the tests are similar and it proves the repeatability of the test; because of this similarity, only the test on the LOOP 1 are presented in this activity.

The dissymmetrical test supports liquid metal reactor plant design and it demonstrates the effectiveness of the natural circulation cooling characteristics. The test started with nominal steady state conditions, thus at full power and flow. The initiating event was the trip of the secondary coolant pump (on the LOOP 1) in which the speed is reduced from 700 to 100 rpm in about 13 s, producing azimuthal and axial dissymmetry in the cold pool: the lack of the cooling created a hot shock in the cold pool at the outlet of the IHX 1 IHX 3. After 5 seconds from the beginning of the test, the automatic shutdown occurred (the control rods are inserted at velocity of 1.4 mm/s in 45) and the speed of secondary pump on the loop 3 was reduced from 700 to 110 rpm in about 60 s, after the turbine trip signal. At 48 seconds the scram command has been operated and the test stopped after 1800 seconds (Ref. [3.3]). The sequence of the events is summarized in Tab. 3.1.

### 3.2.3 Phénix model

RELAP5-3D<sup>®</sup> is the latest in the series of RELAP5 codes, developed at the Idaho National Laboratory (INL). It is a highly generic code that, in addition to calculating the behavior of a reactor coolant system during a transient, can be used for the simulation of a wide variety of hydraulic and thermal transients in both nuclear and non-nuclear systems involving mixtures of vapor, liquid, non-condensable gases, and nonvolatile solute. RELAP5-3D<sup>®</sup> (R5-3D) has fully integrated, multi-dimensional thermal hydraulic and kinetic modeling capability. This allows the applicability of the code to the full range of postulated reactor accidents. It has implemented all features and models previously available in the ATHENA code (INL): several working fluids (e.g. helium, hydrogen, lead-bismuth, lithium, lithium-lead, molten salts, sodium, sodium-potassium, etc.) and a magneto-hydrodynamic model (Ref. [3.9] and [3.10]).


The nodalization of Phénix NPP is composed of 6940 hydraulic volumes, 11840 hydraulic junctions, 6888 heat structures, and 40170 mesh points in the heat structures. The model consists of:

- A multi-dimensional (MULTID) component, modeling the pools, the diagrid and the core bypass;
- A mono-dimensional model, reproducing the zones where a predominant 1D flow is expected (i.e. hexagonal fuel assemblies; heat exchangers; pump suction and feeding conduit, VCS, and gas plenum).

The MULTID component models the diagrid, the core bypass, the hot pool and the cold pool. It is composed by 35 axial lengths, 6 radial rings and 12 azimuthal sectors. The first three rays are chosen to divide the core in three zones (fuel zone, blanket-reflector zone, and natural circulation zone), and the rays four, five and six are chosen to uniformly divide the cold pool (ray four measures up to the axle of the IHXs and the PPs, ray five is chosen to have the azimuthal sectors with the same area of ray four, and ray six corresponds to the greater dimension of the primary vessel). The number of azimuthal meshes is chosen on the basis of the geometrical positions of the PPs and IHXs (see Fig. 3.8) and the axial mesh lengths of the cold and hot pool regions and of the other components (reactor zone, skirt and PPs pipes, IHX, and VCS) are consistent with the vertical sliced approach (see Fig. 3.9). Each 1D component is placed according with the 3-D geometrical specifications and the relevant elevations are preserved. In order to represent the real quantity of fluid contained in each volume of MULTID component, the porosity factor and the junction factor are used.

The dead zone and the top part of the pool, that includes the layer of argon, have been modelled with two BRANCH components. The level of cold pool (the zone between the primary vessel and the vessel cooling



 <b>RICERCA SISTEMA ELETTRICO</b>	<u>Title:</u> Development of BE numerical tools for LFR design and safety analysis (2018)	<u>Distribution</u> <b>PUBLIC</b>	<u>Issue Date</u> 29.01.2019	<u>Pag.</u>
	<u>Project:</u> ADP ENEA-MSE PAR 2017	Ref. ADPFISS-LP2-167	Rev. 0	52 di 163

system) and the correspondent layer of argon above it have been modelled with PIPE and BRANCH component. The different SAs (inner fuel, outer fuel, radial blanket, ARA, control rod, ASA, B4C shielding and storage) are modeled with PIPE components composed of 20 meshes, according with the geometrical specification, which have the axial lengths equal or sub-multiple with respect of the meshes of the 3D component. Their connections, below with the diagrid and above with the hot pool, are modelled with several MTPLJUN connected to the correspondent zones of MULTID component. The reactor core is divided into three main parts:


- the assemblies of the inner core and the outer core regions, the first 7 rows, modeled one by one, according to the geometrical specifications;
- the blanket/reflector/storage zone, rows greater than 7, modeled with 36 equivalent PIPE components, with the radial blanket, the ARA and the storage assemblies grouped separately, according to the azimuthal configuration. Each equivalent PIPE represents for the blanket 80/12 of SA, for the ARA 208/12 of SA and for the storage 41/12 of SA;
- the shielding zone where the SAs (i.e. ASA and B4C shielding) are modeled with 24 equivalent PIPE components distributed along the twelve azimuthal meshes. Each equivalent PIPE represents for the ASA 297/12 of SA and for the B4C shielding 765/12 of SA.

Not having been delivered any geometrical details of the subassemblies orifices or form loss coefficients as function of Re to the benchmark participants, fuel assembly orifices (represented with the passage areas and K-loss implemented in the MTPLJUN component) have been set up based on mass flow rate data and overall dynamic pressure drops in the nominal steady state (see Fig. 3.10 and Fig. 3.11). The power generated by each SA is imposed, during the nominal and transient state, with a GENERAL TABLE, where the trend of the power, as function of the time, is indicated. The heat exchange between the inner/outer core fuel assemblies and sodium is modeled with 6 heat structures: three to represent the zones in which the power is generated and three to represent the passive zones. The three active zones consist of the lower axial blanket, the upper axial blanket and the fuel. Their heat structures are modeled with 12 nodes and the first two are made of helium, UO<sub>2</sub>, steel 316 and the last of helium, MOX and steel 316, according to the geometrical specifications. The three passive zones consist of SA foot, hexagonal wrapper tube and axial shielding. Their heat structures are modeled with 4 nodes, are made of steel 316 and connect the PIPE representing the SA with the corresponding MULTID zone. While the passive heat structures of the other type of SAs are modeled in the same way, as described above, the active ones differ in shape and materials.

The pumps are simulated with an ascending pipe, which reproduces the annular inlet of the component, connected with the correspondent region of the cold pool, with the PUMP component and with the descending pipe which leads the primary coolant to the diagrid. The nodalization scheme is depicted in Fig. 3.12. The homologous curves of the PUMP components are set-up using PHENIX reference data. The IHXs primary side are modeled separately with PIPE components connected upstream and downstream with the correspondent region of hot pool and cold pool. The IHXs secondary sides are modeled separately with pipe components from an inlet and outlet collectors (dummy) and fed with imposed boundary conditions. Fig. 3.12 shows the representative nodalization scheme of the heat exchangers. Primary and secondary sides of DOTE components are modeled and disabled closing the connections between the IHXs 2 and the hot pool, to prevent the primary mass flow rate passing through. The diagrid is modelled with branch component connected below with the strongback and above with the SAs and the bypass region. The nodalization scheme of the vessel cooling system and the strongback are shown in Fig. 5.12; it consists of the pipe 945, connected upstream with the diagrid, on the top with the gas plenum (972), and downstream with the corresponding regions of cold pool.

The pressure drop in the rod bundle is evaluated using Cheng and Todreas correlation for laminar, turbulence and transition flows, as in Ref. [3.11]. For the evaluation of the heat transfer coefficient (HTC) for liquid



	<u>Title:</u> Development of BE numerical tools for LFR design and safety analysis (2018)	<u>Distribution</u> <b>PUBLIC</b>	<u>Issue Date</u> 29.01.2019	<u>Pag.</u>
	<u>Project:</u> ADP ENEA-MSE PAR 2017	Ref. ADPFISS-LP2-167	Rev. 0	53 di 163

metals, RELAP5-3D<sup>®</sup> uses two different correlations depending on the geometry (non-bundle or bundle) (Ref. [3.9]), for all convective wall heat transfer (turbulent forced, laminar forced, and natural). For non-bundles the Seban-Shimazaki correlation is used:

$$Nu = 5.0 + 0.025Pe^{0.8}$$

where Pe is the Peclet number. When Pe goes to zero, the Nusselt number tends to 5 in order to reproduce the HTC in natural circulation conditions. For the HTC evaluation in bundle geometry, the Westinghouse correlation is integrated in RELAP5-3D<sup>®</sup> (Ref. [3.10]) and it is used to calculate the heat transfer coefficient inside the SAs:

$$Nu = 4.0 + 0.33 \left(\frac{p}{D}\right)^{3.8} \left(\frac{Pe}{100}\right)^{0.86} + 0.16 \left(\frac{p}{D}\right)^5$$

where p is the rod pitch and D the rod diameter. The correlation is developed for a range of pitch to diameter ratio from 1.1 to 1.4 and Pe from 10 to 5000. The IHXs are characterized by a p/D equal to 1.43; for this reason, the H. Graber & M. Rieger correlation in Ref. [3.12], not implemented in the current version of R5-3D, is selected to evaluate the HTC in the IHXs primary side:

$$Nu = 0.25 + 6.2 \frac{p}{D} + \left(-0.007 + 0.032 \frac{p}{D}\right) Pe^{(0.8-0.024\frac{p}{D})}$$

developed in  $1.2 < p/D < 2.0$ . In the operational range of temperature, the two correlations have a similar gradient of Nu versus Pe; therefore, a constant HTC multiplication factor equal to 1.4, calculated as the ratio of H. Graber & M. Rieger and Westinghouse correlations, has been applied in the IHX primary side model.


### 3.2.4 Results

In order to obtain the initial conditions for the transient test, the operational conditions are analyzed. The Tab. 3.2 summarizes the nominal boundary conditions and the main results obtained after 3000 s of problem time. The screenshot of the coolant temperature profiles in the most representative section is reported in Fig. 3.14. This provide the temperature distributions at the end of steady state calculation. It should be noted that the screenshot includes the temperature of selected SA channels (according with the nodalization approach) belonging to the corresponding section (i.e. azimuthal sector). They are: one selected SA per each rank from 1 to 7, one SA per type (three) for the ranks >7, and one SA per type for the ranks in natural circulation. This last group experiences higher coolant temperatures because they are blind channels, thus not fed by the PP.

Starting from the steady state conditions, the dissymmetric test is reproduced following the sequence of events shown in Tab. 3.1 (Ref. [3.4]). At the beginning of the test the exchanged power through IHXs is 344.11 MWth (170.132MWth by loop 1 and 173.981 MWth by loop 3). Immediately the secondary mass flow rate of the loop 1 (L1) decreases, provoking the quick reduction of the thermal power removed by the IHX-K and the IHX-M. Fig. 3.15 compares the thermal power removed by L1 and the L3. The delay of the power reduction of the loop 3, due to the delay time of the secondary pump 3 trip, is also highlighted in Fig. 3.16. During the first 30 s of the test, the thermal power removed by the L3 increases up to the 83% of the total power; at this time the power removed by the L1 reaches and maintains the value of about 20 MW, while the power removed by the L3 continues to decrease, reaching the same value of L1 at about 70 s. These considerations shown how the exchanged power through IHXs is dissymmetrical at the beginning of the transient. After 200 s from the beginning of the transient, the symmetric conditions are recovered.

Fig. 3.17 compares the outlet temperature of the IHX-M And IHX-G, respectively connected with L1 and L3. At the bottom edge of the IHX-M, the temperature of the primary coolant quickly increases to the peak



 <b>RICERCA SISTEMA ELETTRICO</b>	<u>Title:</u> Development of BE numerical tools for LFR design and safety analysis (2018)	<u>Distribution</u> <b>PUBLIC</b>	<u>Issue Date</u> 29.01.2019	<u>Pag.</u>
	<u>Project:</u> ADP ENEA-MSE PAR 2017	Ref. ADPFISS-LP2-167	Rev. 0	54 di 163

of 500°C and, after a delay time of about 30 s, also the outlet temperature of the IHX-G reaches the maximum value of 490°C. Hence, being the two hot shocks different for time and value, a dissymmetric distribution of the temperature inside the cold pool is produced, as shown in Fig. 3.18.

In the first seconds of the transient, the decrease of the thermal power removed by the L1 causes an increase of temperature at the IHX-K and IHX-M outlets. After 20 s from the beginning of the test, due to the temperature increase (which results in a density decrease), the hot sodium flows up in the cold pool and then cold sodium is sucked by the primary pump 1 (PP1), as shown by the small peak in Fig. 3.19 (black line). With a delay of about 45 s, the same effect, but more accentuated, occurs at the outlet sections of IHX-J and IHX-G. After 70 s, the hotter fluid reaches the inlet section of the PP3 because the upper part of the cold pool is heated during the previous phase. This causes a peak temperature of about 402°C at the pump 3 inlet (see Fig. 3.19, green line). After that, the sodium temperature at the bottom of the two zones becomes uniform and the inlet temperature of the pump 3 reaches the same temperature of the pump 1, following the same trend. In the first phase of the transient the inlet temperature of the pump 2 remains always greater than the others, but the difference decreases with the progress of time. The dissymmetric temperature trend causes a different density at the pumps inlet and, consequently, a small mass flow rate variation, as shown in Fig. 3.20.

Fig. 3.21 highlights the temperature increase through the core, showing the average inlet and outlet temperatures. As expected, the inlet temperature follows the same trend of the PP inlet temperatures. After the automatic shutdown, the PPs are maintained in operation, and the primary mass flow rate remains quite constant, as shown in Fig. 3.20. This lead to a quick reduction of the core outlet temperature, during the first 50 s. Then, while the temperature difference between the inlet and the outlet decreases, due to the scram command, the outlet temperature increases, following the inlet temperature, and it reaches the maximum value of 440°C.

The inlet temperature of the IHXs follows the same trend of the core outlet, as shown in Fig. 3.22. The cold shock in the hot pool is seen with a delay by the IHX inlets and it is less severe due to the thermal mixing with the mass of hot sodium over the core.

### 3.3 Conclusive remarks

In the framework of the H2020 SESAME project, the dissymmetric test, belonging to the End of Life Test series of Phénix reactor, has been selected as the transient test for a validation. This test offered useful data for the validation of the thermal-hydraulic system codes, focusing on the capability of the codes to reproduce relevant 3D asymmetry during accident scenario.

“Sapienza” University of Rome developed a detailed thermal-hydraulic nodalization scheme, aiming to reproduce three-dimensional effects inside the pools and suitable to develop point kinetic model for 3D NK coupling calculation. The first two phases of the activity were concluded with the realization of the reactor model and the calculation of the blind simulations. After the distribution of the experimental data, the comparison the experiment and with the simulations of the other participants, provided useful information to improve the model. This report has been focused on the third phase of the activity: the post test simulations.

The comparison between the full power calculations and the experimental data has highlighted the capability of RELAP5-3D to reproduce the normal operation of a pool-type sodium-cooled fast reactor. Starting from the steady state results, the transient calculation has been carried out, assuming the dissymmetric test boundary conditions. The comparison with the experimental data has highlighted a good capability of the code to reproduce three-dimensional asymmetric effect inside the cold pool, which influenced the behavior of the reactor in the short term. Also in the long term, after the recovery of the symmetrical conditions, the code has highlighted a good prediction of the main thermal-hydraulic quantities.



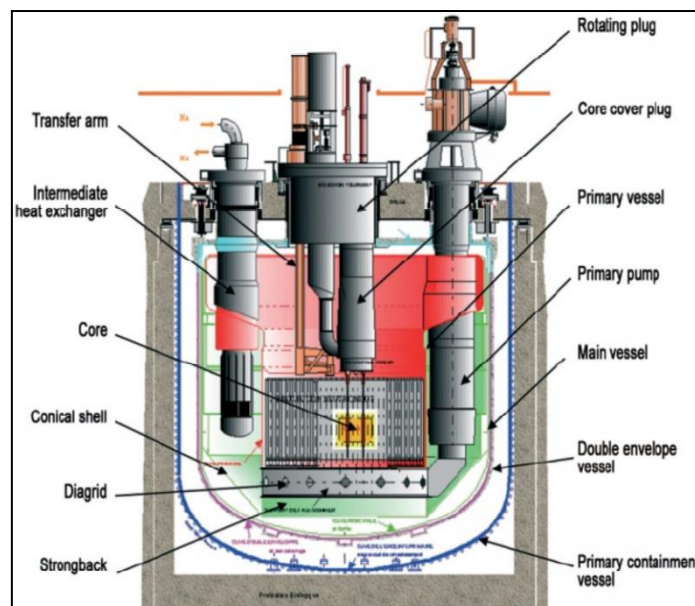


Action	Time (s)
Secondary pump trip (on loop1): speed reduced from 700 to 100 rpm in about 13 s	0
Automatic shutdown: insertion of the control rods (1.4 mm/s) in 45 s. Turbine trip. Secondary pump speed reduced (on the other loop) from 700 to 110 rpm in about 60 s	5
Scram	48
End of test	1800

*Tab. 3.1 – Dissymmetrical test: sequence of events*

Quantity	Unit	R5-3D
Primary circuit balance	MW	340.87
T secondary system IHX inlet	K	593.65
T secondary system IHX outlet	K	786.66
MF IHX-1A secondary system	kg/s	347.13
T Core inlet	K	659.97
T Core outlet	K	792.91
T primary system IHX inlet	K	792.16
T primary system IHX outlet	K	659.73
MF Total PP	kg/s	2211.45
MF Total core	kg/s	1992.45
MF VCS	kg/s	219.00

*Tab. 3.2 – Steady state conditions*



*Fig. 3.1 – Reactor block*

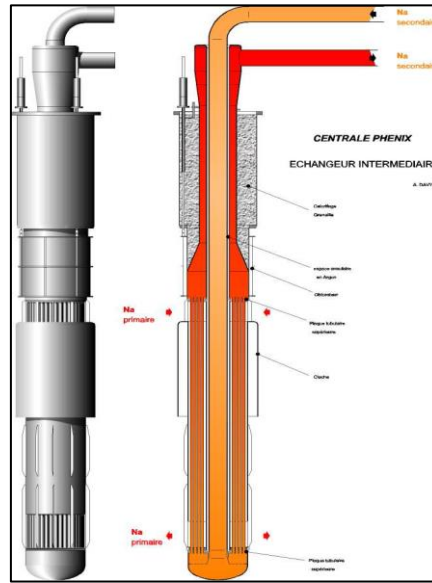


Fig. 3.2 – Intermediate heat exchanger

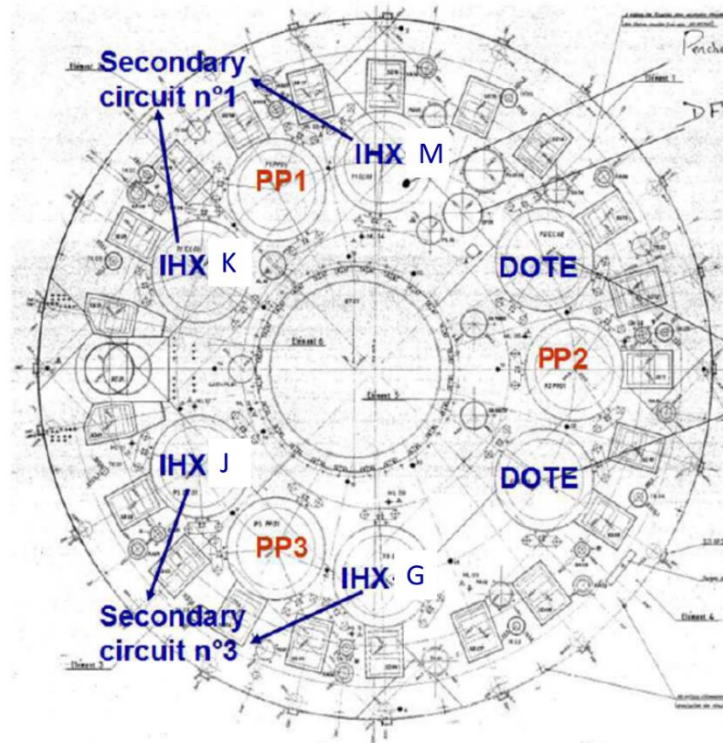
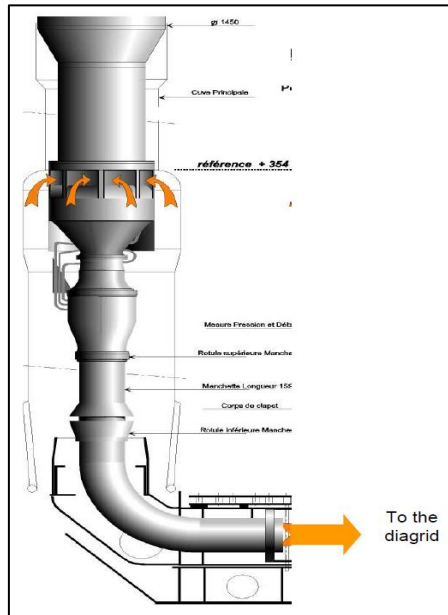
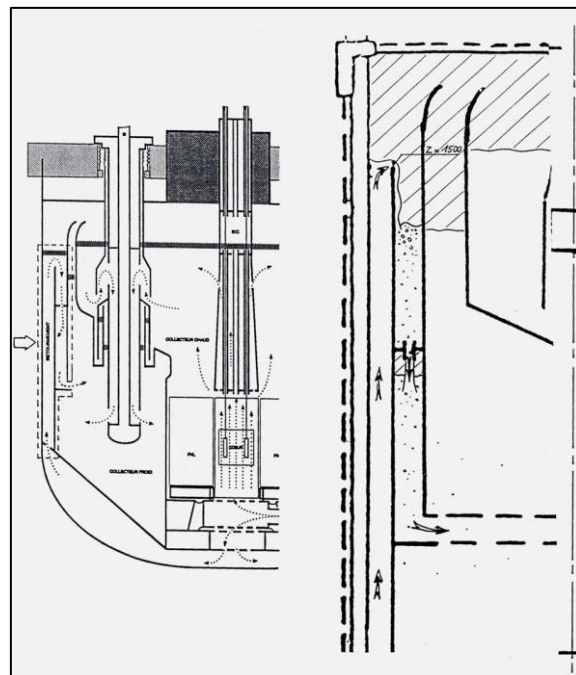


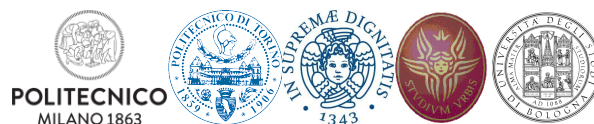
Fig. 3.3 – Reactor top view

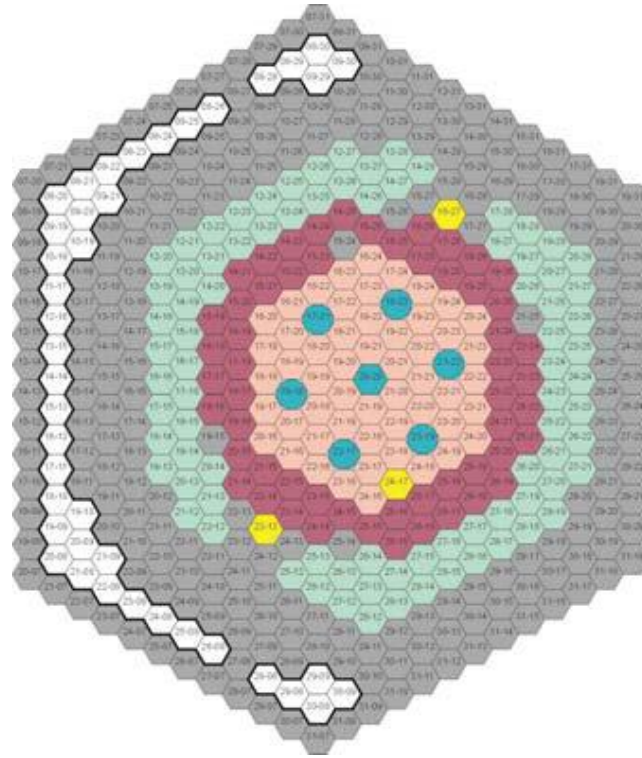


*Fig. 3.4 – Primary pump*

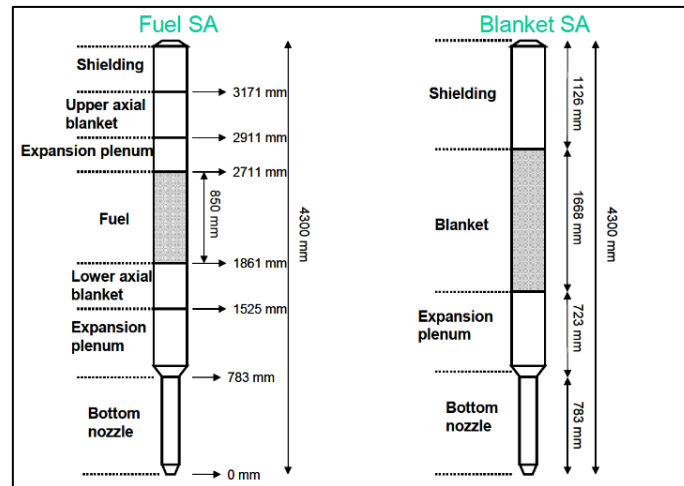


*Fig. 3.5 – Vessel cooling system flow path*

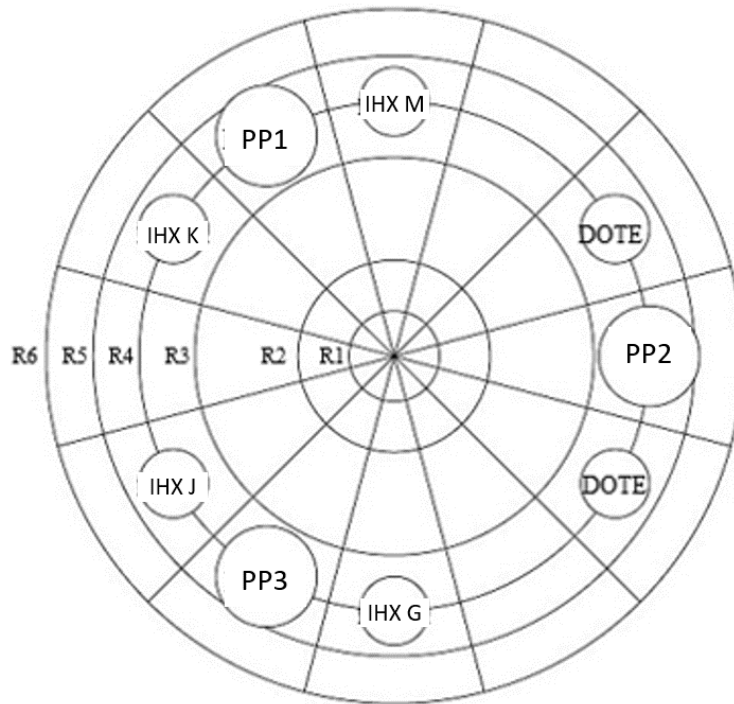




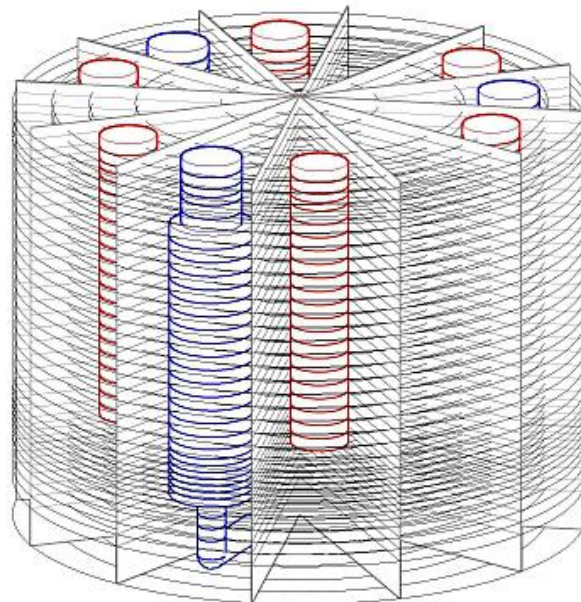
*Fig. 3.6 – Reactor core top view*



*Fig. 3.7 – Fuel and fertile SA axial composition*



*Fig. 3.8 – Overview of radial and azimuthal meshes of MULTID component*



*Fig. 3.9 – Scheme of MULTID component for porosity factor*

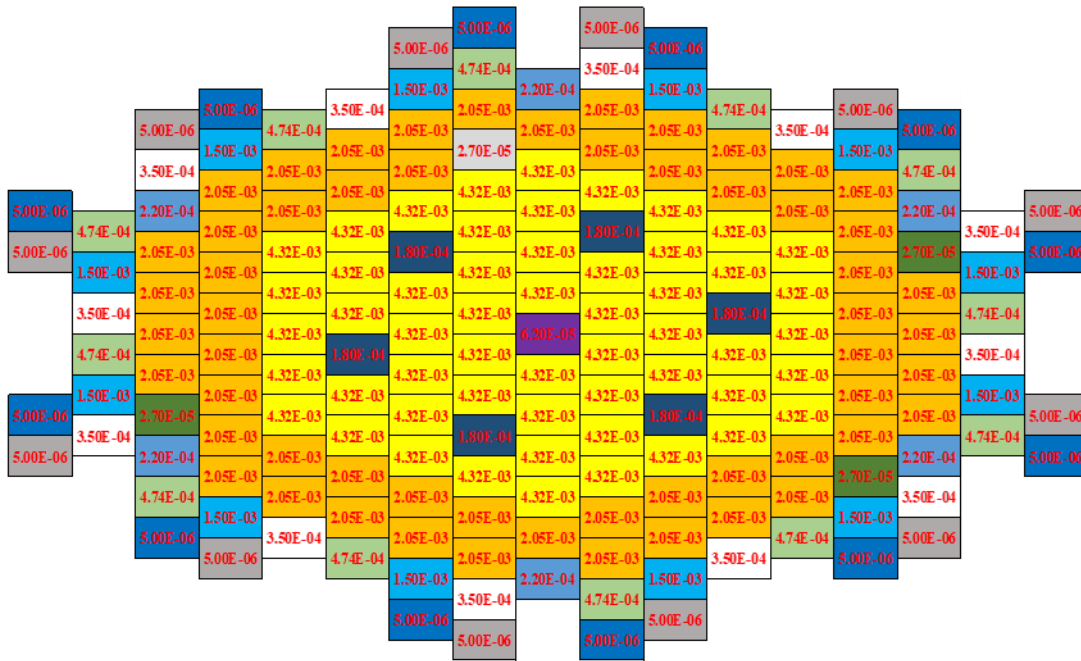


Fig. 3.10 – SAs inlet area (m<sup>2</sup>)

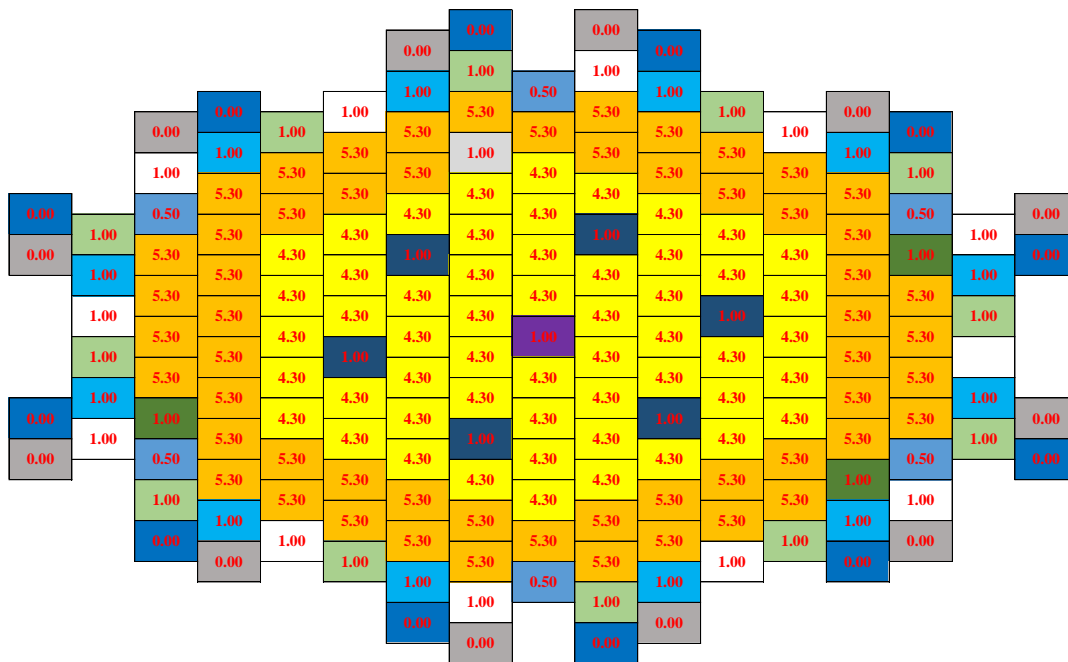


Fig. 3.11 – SAs inlet K loss



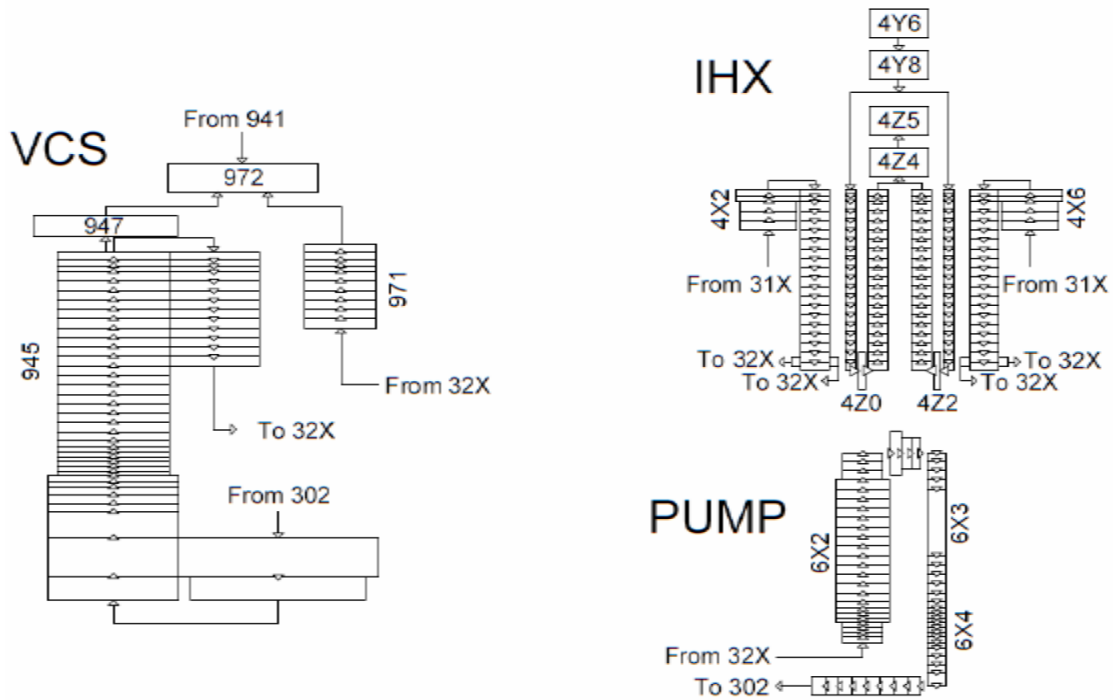


Fig. 3.12 – Pumps, IHXs and VCS nodalization scheme

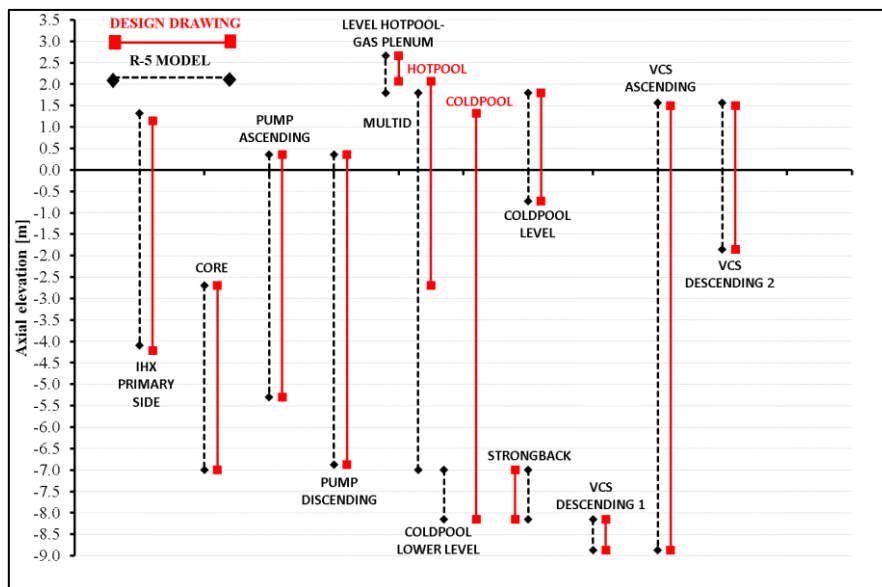
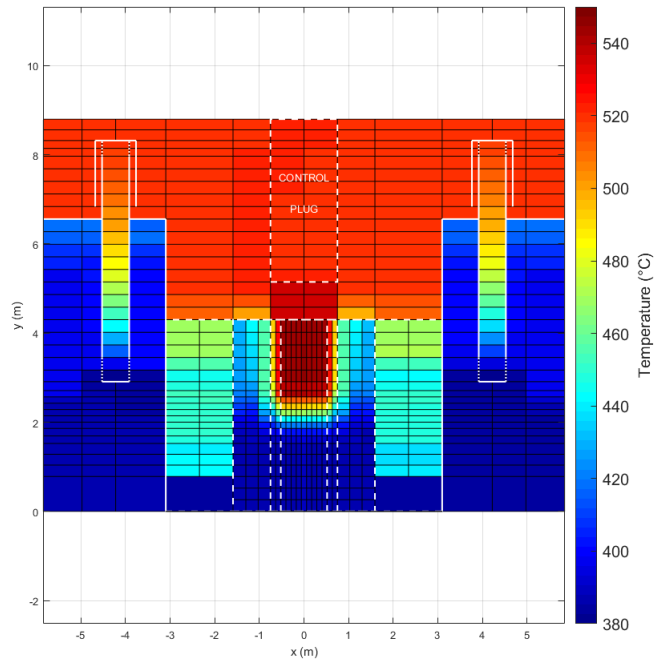
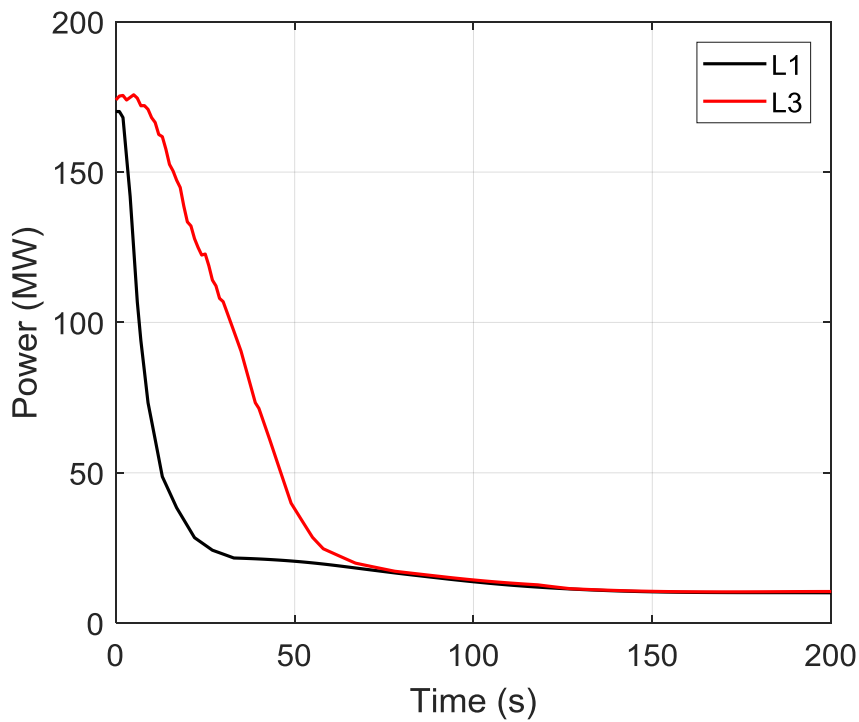


Fig. 3.13 – Comparison of the model and design relevant height

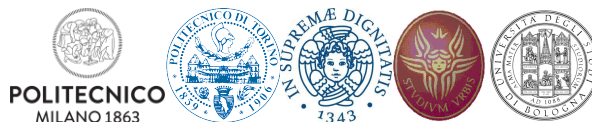




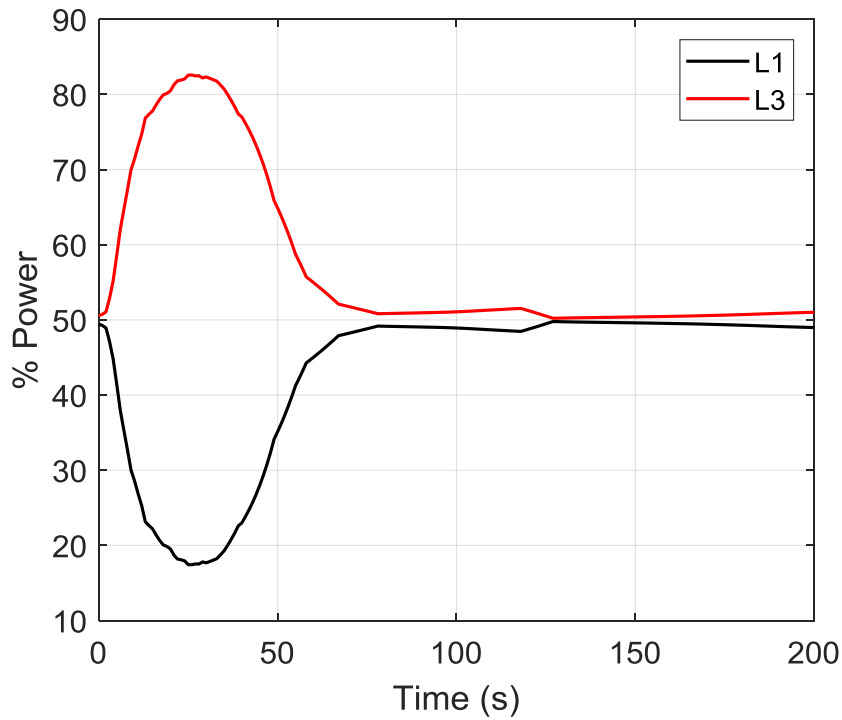
*Fig. 3.14 – Steady state conditions*



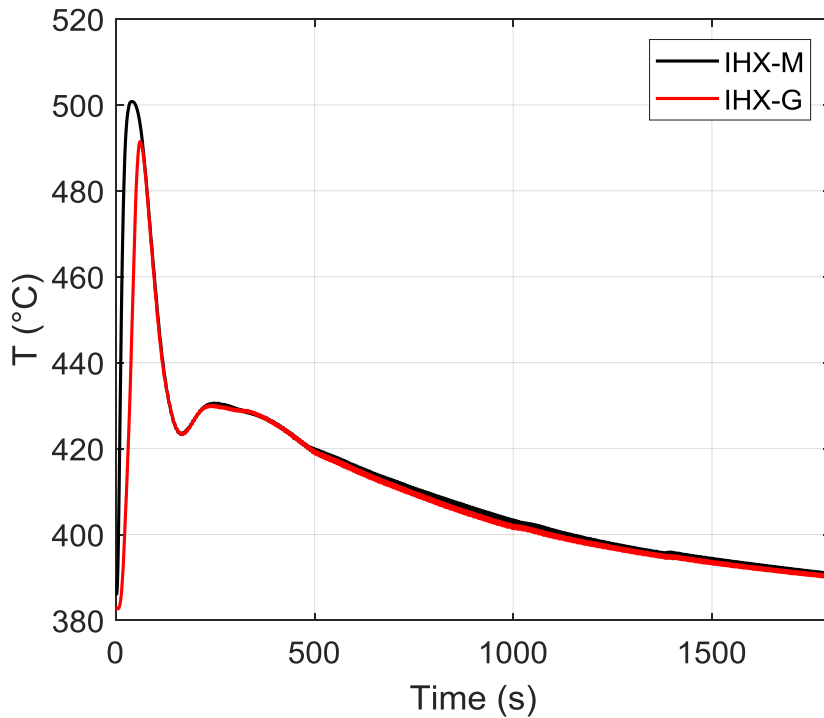
*Fig. 3.15 – Power removed by IHXs*





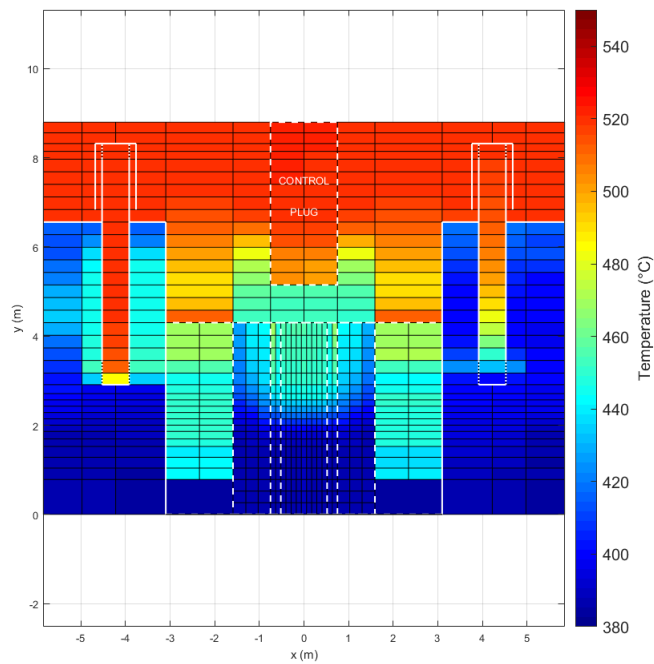


*Fig. 3.16 – Power % removed by IHXs*

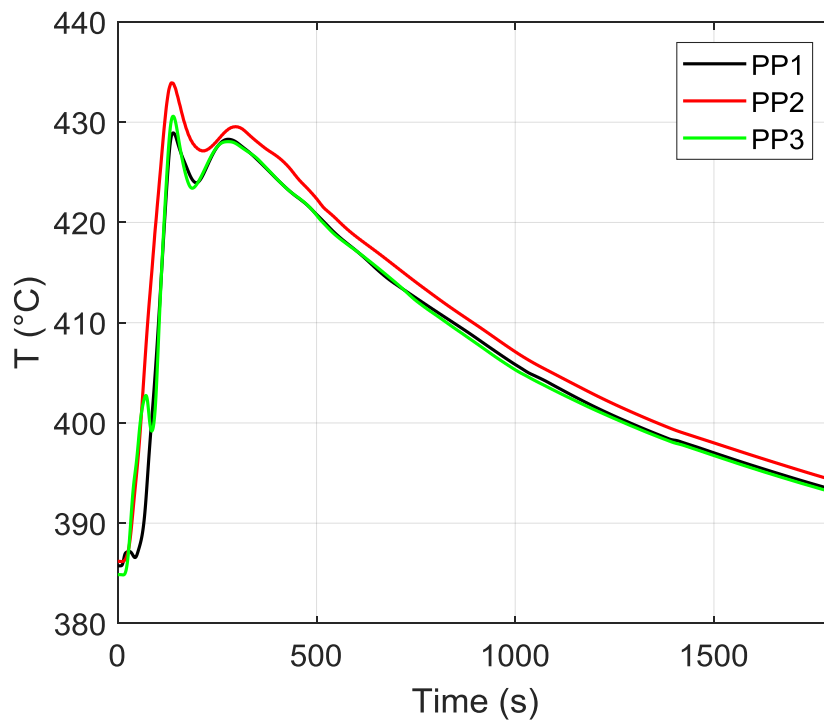


*Fig. 3.17 – IHXs outlet coolant temperature*



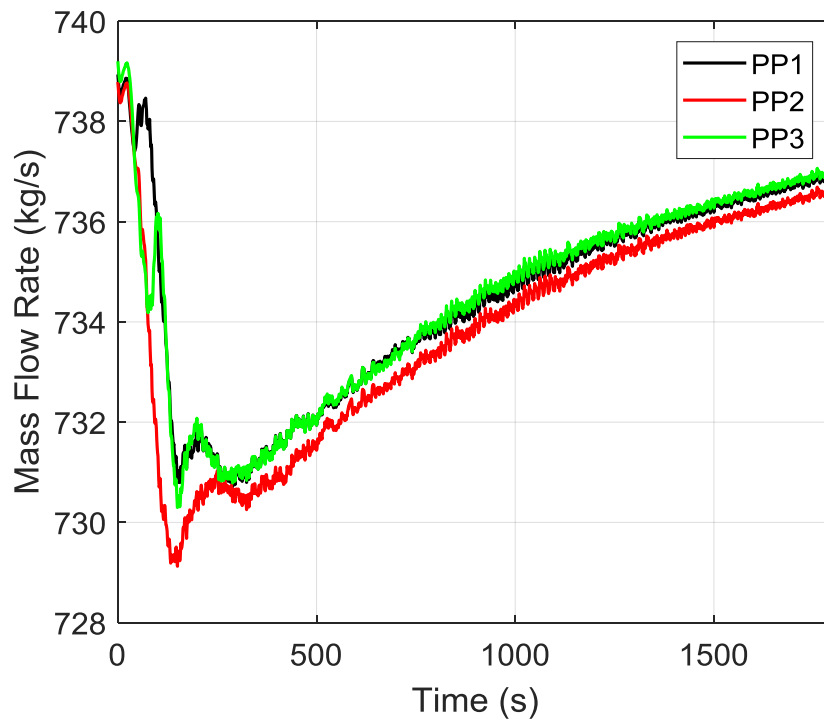


*Fig. 3.18 – Transient conditions*

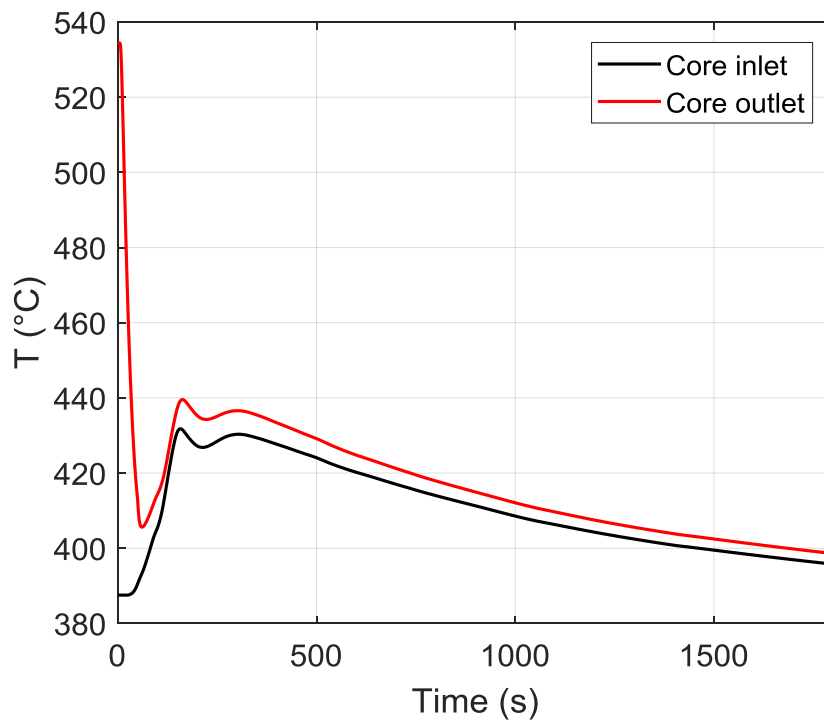


*Fig. 3.19 – Primary pumps inlet temperatures*



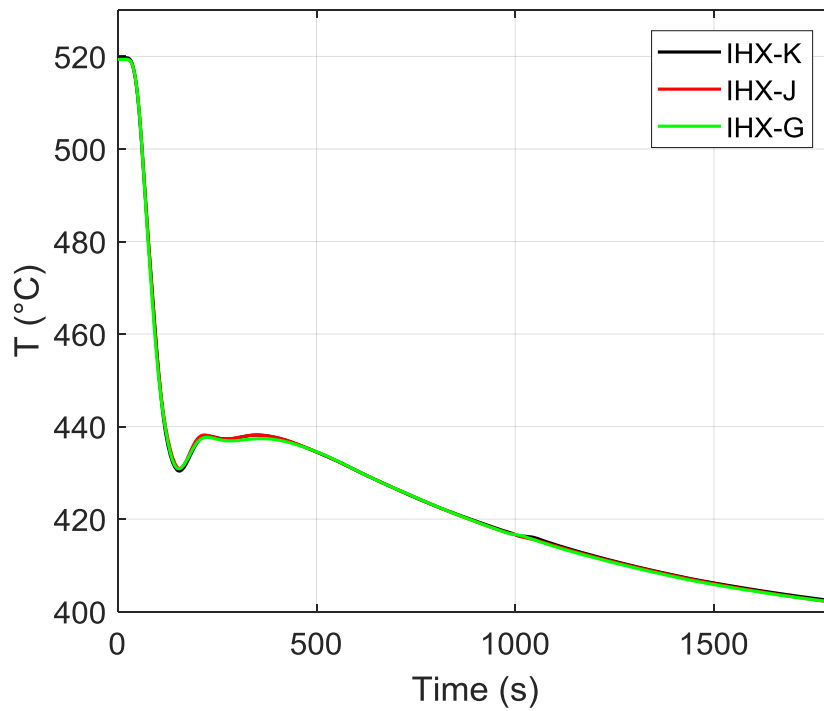


*Fig. 3.20 – Primary pumps mass flow rate*




*Fig. 3.21 – Core temperature*





*Fig. 3.22 – IHXS inlet temperatures*




 <b>RICERCA SISTEMA ELETTRICO</b>	<b>Title:</b> Development of BE numerical tools for LFR design and safety analysis (2018)	<u>Distribution</u> <b>PUBLIC</b>	<u>Issue Date</u> 29.01.2019	<u>Pag.</u>
	<b>Project:</b> ADP ENEA-MSE PAR 2017	Ref. ADPFISS-LP2-167	Rev. 0	67 di 163

### 3.4 List of References


- [3.1] A. Del Nevo, A. Subioli, V. Narcisi, F. Giannetti, *Application of RELAP5-3D on Phenix Experimental Test*. Tech. Rep., ADPFISS – LP2 – 144, 2017.
- [3.2] OECD NUCLEAR ENERGY AGENCY – GIF, *GIF Annual Report 2017*. Tech. Rep., 2017.
- [3.3] B. Grosjean, S. Li, *PHENIX dissymmetric test description*. Tech Rep., 2016.
- [3.4] F. Giannetti, V. Narcisi, A. Subioli, A. Del Nevo, *Phénix transient analysis for the assessment of RELAP5-3D based on dissymmetric test benchmark*. Proc. Of the 26<sup>th</sup> Int. Conf. on Nucl. Eng. – ICONE26, London, England, July 22-26, 2018. DOI: 10.1115/ICONE26-82419.
- [3.5] J. F. Sauvage, *Phénix 35 years of history: the heart of a reactor*. CEA-EDF, 2004.
- [3.6] IAEA, *Benchmark Analyses on the Control Rod Withdrawal Tests Performed during the PHÉNIX End-of-Life Experiments*. Tech. Rep – TECDOC-1742, 2014.
- [3.7] IAEA, *Benchmark Analyses on the Natural Circulation Test Performed During the Phenix End-of-Life Experiments*. Tech. Rep – TECDOC-1703, 2013.
- [3.8] A. Vasile et al., *The Phénix final tests*. Proc. of Int. Congress on Advances in Nuclear Power Plants – ICAPP 2011, Nice, France, May 2-5, 2011, pp. 11298.
- [3.9] INL, *The RELAP5-3D© Code Development Team, RELAP5-3D© Code Manual Volume II: User's Guide and Input Requirements*. INL/MIS-15-36723, Revision 4.3, October 2015.
- [3.10] INL, *The RELAP5-3D© Code Development Team, RELAP5-3D© Code Manual Volume IV: Models and Correlations*. INL/MIS-15-36723, Revision 4.3, October 2015
- [3.11] A. Del Nevo, E. Martelli, *Validation of a Three-Dimensional Model of EBR-II and Assessment of RELAP5-3D Based on SHRT-17 Test*. Nuc. Tech. Vol. 193, pp 1–14, Jan. 2016. <https://doi.org/10.13182/NT14-152>
- [3.12] W. Pfrang, D.Struwe, *Assessment of Correlations for Heat Transfer to the Coolant for Heavy Liquid Metal Cooled Core Design*. FZKA 7352, October 2007



 <b>RICERCA SISTEMA ELETTRICO</b>	<u>Title:</u> Development of BE numerical tools for LFR design and safety analysis (2018)	<u>Distribution</u> <b>PUBLIC</b>	<u>Issue Date</u> 29.01.2019	<u>Pag.</u>
	<u>Project:</u> ADP ENEA-MSE PAR 2017	Ref. ADPFISS-LP2-167	Rev. 0	68 di 163

*(Page intentionally left blank)*




 <b>RICERCA SISTEMA ELETTRICO</b>	<u>Title:</u> Development of BE numerical tools for LFR design and safety analysis (2018)	<u>Distribution</u> <b>PUBLIC</b>	<u>Issue Date</u> 29.01.2019	<u>Pag.</u>
	<u>Project:</u> ADP ENEA-MSE PAR 2017	Ref. ADPFISS-LP2-167	Rev. 0	69 di 163

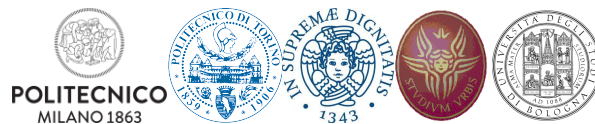
**4 DEVELOPMENT AND VALIDATION OF CODES FOR THE COUPLING OF THE OPENFOAM-SALOME-FEMLCORE-CATHARE SOFTWARE FOR THE STUDY OF 4<sup>TH</sup> GENERATION LEAD-COOLED FAST REACTORS. VALIDATION OF THE COUPLING WITH DATA EXPERIMENTS FROM THE TALL-3D FACILITY.**

*A. Chierici, L. Chirco, R. Da Vià, F. Franceschini, V. Giovacchini,  
A. Cervone, S. Manservigi*




 <b>RICERCA SISTEMA ELETTRICO</b>	<u>Title:</u> Development of BE numerical tools for LFR design and safety analysis (2018)	<u>Distribution</u> <b>PUBLIC</b>	<u>Issue Date</u> 29.01.2019	<u>Pag.</u>
	<u>Project:</u> ADP ENEA-MSE PAR 2017	Ref. ADPFISS-LP2-167	Rev. 0	70 di 163

*(Page intentionally left blank)*





 <b>RICERCA SISTEMA ELETTRICO</b>	<u>Title:</u> Development of BE numerical tools for LFR design and safety analysis (2018)	<u>Distribution</u> <b>PUBLIC</b>	<u>Issue Date</u> 29.01.2019	<u>Pag.</u>
	<u>Project:</u> ADP ENEA-MSE PAR 2017	Ref. ADPFISS-LP2-167	Rev. 0	71 di 163

## 4.1 Background and reference

Generation IV reactors employ designs with many passive safety systems that couple piping in forced motion and pools in natural circulation. One dimensional System Thermal Hydraulics (STH) codes are not accurate for resolving complex transients with mixing and stratification while Computational Fluid Dynamics (CFD) codes are computationally too expensive for resolving large domains. For this reason during this year a multi-scale and multiphysics platform has been developed as a joint effort between ENEA and UNIBO [4.1]-[4.8]. This platform is capable of 1D-3D multi-scale coupling between open, research and commercial codes. In this report we use such a platform to improve the simulation of a thermohydraulic test with natural circulation flow performed in the experimental TALL-3D facility [4.9], Fig. 4.1. Thermal hydraulics of the primary-secondary loop and the 3D-test section is the main subject of the numerical test for the 3D-1D coupling and validation of the code interfaces.

The series of tests, considered here, is the TG03\_S301 [4.10],[4.11]. These tests are forced to natural transient with both main heater and 3D test section heater at constant powers. Loss of flow transients are generally of interest since they can lead to flow oscillations between two parallel flow paths. Complex feedback between 3D phenomena and loop behavior can be expected including limit cycle oscillations (LCO). These experiments define a good framework for testing and evaluating STH and CFD coupling simulations.

In particular we consider again, as shown in Fig. 4.2, the semi-blind test TG03S301(03). The test TG03S301(03) is an unprotected loss of flow with the system initially in fully working conditions.


We use a one-dimensional model of the main circuit described by Cathare and the three-dimensional test section simulated with OpenFOAM code. In order to improve the simulation, we first consider the three-dimensional test section alone with experimental input. Then, in the coupling simulation, we introduce a simple improved model of the TALL-3D main section which takes into account a partial thermal insulation of the main component.

The final and more general purpose is to simulate and validate the computational OpenFOAM-Salome-FemLcore-Cathare platform developed during these years. The layout of the experimental TALL-3D facility is reported in Fig. 4.1 with its geometrical dimensions on the left. It consists of a liquid Lead Bismuth Eutectic (LBE) primary loop with an oil-cooled secondary loop. The primary loop operates above LBE melting point 125°C with  $Re$  in the range of [0, 140000],  $Pr$  in [0.020, 0.045] and  $Pe$  in [0, 350]. The total height of the facility is about 6.5m. The secondary loop is used to control heat balance in the primary loop and is equipped with automatic temperature control system. For details the reader should see [4.9]-[4.13].

The one-dimensional system code computation model is simulated with CATHARE 2.5 code [4.14]-[4.17]. The 1D model is shown in Fig. 4.3, Fig. 4.4. As shown in Fig. 4.3, the left leg consists of the main heater and it is connected on the top to the main tank and on the bottom to the sump tank. The Main Heater is a rod-like electric heating element. The 1D model of the central vertical leg is shown in Fig. 4.3 in the center.

TALL-3D test section is an axial-symmetric cylindrical stainless steel vessel with an inlet at the bottom and an outlet at the top. The dimensions of the test section simulated with OpenFOAM and thermal insulation are provided in Fig. 4.5. The OpenFOAM code is an open-source software that offers a great variety of models[4.18],[4.19]. This code is now part of the computational platform integrated in the SALOME software. The axial-symmetric mesh can be generated both as a two-dimensional mesh or in three-dimensional form by using the GEOM and SMESH modules from SALOME platform.



 <b>RICERCA SISTEMA ELETTRICO</b>	<u>Title:</u> Development of BE numerical tools for LFR design and safety analysis (2018)	<u>Distribution</u> <b>PUBLIC</b>	<u>Issue Date</u> 29.01.2019	<u>Pag.</u>
	<u>Project:</u> ADP ENEA-MSE PAR 2017	Ref. ADPFISS-LP2-167	Rev. 0	72 di 163

## 4.2 Developed boundary conditions in OpenFOAM

Additional boundary conditions have been implemented in OpenFOAM to take into account the heat exchange between TALL-3D main section and the surrounding environment. Moreover these new b.c. should consider the heat exchange between the fluid and the steel disk that is present inside the test section geometry. The influence of these boundary conditions has been evaluated by using experimental data as inlet boundary conditions, for the CFD simulation, instead of the coupling with Cathare code. This procedure allows us to evaluate the effect of the new modeled phenomena on the CFD solution without the influence of the system code. The boundary conditions have been implemented as new code classes within OpenFOAM. The use of each class is explained below.

### 4.2.1 Heat exchange with surrounding environment

The presence of a significant heat exchange between the TALL-3D main section and the surrounding environment can be investigated starting from a simple energy balance. Before the pressure drop, in steady condition, the following two experimental data are considered: mass flow rate  $m \approx 1.9$  kg/s and outlet-inlet temperature difference  $\Delta T \approx 35^\circ\text{C}$ . In this preliminary test we consider constant physical properties calculated at reference temperature  $T_{\text{ref}} = 272.5^\circ\text{C}$ , leading to a specific heat capacity value  $C_p = 147$  J/kgK. These values give a heat flux  $q$ , applied on the heated area, equal to  $88505$  W/m<sup>2</sup>, while the imposed one is  $99900$  W/m<sup>2</sup>. A thermal power  $Q_d \approx 1100$ W is then exchanged with surrounding environment. The boundary condition is modeled as non-constant and non-uniform heat flux applied  $q_d$  on selected wall boundaries. Heat flux  $q_d$  is modeled as

$$q_d = Q_d/A_d = h_{\text{exp}}(T_w - T_{\text{env}}) \quad (4.1)$$

where  $A_d$  is the area of the wall,  $h_{\text{exp}}$  the heat exchange coefficient,  $T_w$  the wall temperature and  $T_{\text{env}}$  the environment temperature. A uniform value of  $h_{\text{exp}}$  can be estimated from steady CFD calculations with the following settings:

- heat flux  $q = 88505$  W /m<sup>2</sup> applied on the heated area
- no heat exchange with the environment
- temperature  $T_w$  calculated as mean integral temperature value of the wall boundaries where heat exchange with the environment will be considered
- constant environment temperature  $T_{\text{env}} = 25^\circ\text{C}$ .

In order to use this boundary condition, the condition needs to be set in the relative OpenFOAM temperature field file.

### 4.2.2 Heat exchange with immersed steel disk.


A simplified model for the heat exchange with the immersed steel disk has been considered. In particular the disk temperature is considered to be uniform, providing a great simplification in modeling the new boundary condition. The following energy balance, for the solid disk, holds

$$dm C_p \Delta T = qdA \Delta t \quad (4.2)$$

Eq. (4.2) refers to the temperature variation  $\Delta T$  of solid mass  $dm$  due to the presence of heat flux  $q$  applied on surface  $dA$  for a time interval  $\Delta t$ . Since the disk temperature is considered to be uniform, equation (4.2) can be integrated over the entire disk volume, leading to the following discrete form

$$m C_p \Delta T = \sum_i q_i A_i \Delta t, \quad (4.3)$$



 <b>RICERCA SISTEMA ELETTRICO</b>	<u>Title:</u> Development of BE numerical tools for LFR design and safety analysis (2018)	<u>Distribution</u> <b>PUBLIC</b>	<u>Issue Date</u> 29.01.2019	<u>Pag.</u>
	<u>Project:</u> ADP ENEA-MSE PAR 2017	Ref. ADPFISS-LP2-167	Rev. 0	73 di 163

where  $q_i$  refers to the heat flux applied over the surface  $A_i$  of  $i$ -th boundary element. At each time step the solid temperature is calculated as

$$T_{new} = T_{old} + \sum_i q_i A_i \frac{\Delta t}{m c_p} \quad (4.4)$$

The boundary condition is then implemented as a non-uniform heat flux  $q$  that is imposed on the boundary surface that represents the fluid-disk interface. With the new evaluated disk temperature, for each cell having a face on fluid-disk interface the heat flux is calculated as

$$q = -k \frac{T_i - T_{new}}{h} \quad (4.5)$$

where  $T_i$  is the cell temperature value,  $k$  is the thermal conductivity and  $h_i$  is the cell center to boundary face distance. With this new boundary condition a simplified conjugate heat transfer problem can be modeled without the need to solve a system of equations for the temperature distribution inside the solid body. Although the approach is a simplified one, it allows considering additional thermal inertia within the TALL-3D main section.

#### 4.2.3 Results obtained with new boundary conditions

In the present section results are discussed to evaluate the effect of heat exchange between the TALL-3D test section and surrounding environment including the steel disk. This preliminary study can help to understand how the CFD simulation results can be improved. Moreover, improved CFD predictions will lead to improved results of the coupled Cathare-OpenFOAM simulation, as it will be further investigated in future studies. Since heat exchange with surrounding environment is here considered, a different geometry is investigated. In particular the inlet and outlet sections are placed at the same locations where thermocouples TC2.1211 and TC2.2111 are installed on the experimental facility. A sketch of the simulated geometry is shown in Fig. 4.6 (a). Labels for the boundaries on inlet-outlet sections ( $\Gamma_i$  and  $\Gamma_o$ ) and inlet-outlet channels ( $\Gamma_{w,ch,i}$  and  $\Gamma_{w,ch,o}$ ) are shown in Fig. 4.6 (a). On Fig. 4.6 (b) boundary labels are shown on a close up view of the test section and refer to heated surface  $\Gamma_h$ , fluid-disk interface  $\Gamma_d$ , bottom, side and top test section walls ( $\Gamma_{w,b}$ ,  $\Gamma_{w,s}$  and  $\Gamma_{w,t}$ ). For a better understanding of the new modeling hypothesis effects, the following cases are considered:


- case A: base case, adiabatic boundary conditions along solid boundaries and fluid-disk interface
- case B: modeled heat exchange with surrounding environment on boundary  $\Gamma_{w,ch,i}$
- case C: same as case B with additional heat exchange on  $\Gamma_d$
- case D: heat dispersion  $\Gamma_{w,ch,o}$  and heat exchange on  $\Gamma_d$

A comparison between experimental values and results obtained for case A are shown in Fig. 4.7. In particular mean temperature difference between outlet and inlet sections are shown in Fig. 4.7 (a). Outlet temperature values are reported in Fig. 4.7 (b).

It can be seen that outlet temperature values increase with time for  $t > 1020$ . After a rapid increase of temperature values, oscillations are observed from experimental data, with peak values occurring almost every 200 seconds from time  $t=1200$ . Results obtained for case A show a sudden temperature increment followed by a decrement on long time scale.

From time  $t \approx 1500s$  temperature values slowly increase again. Temperature oscillations are slightly observed from Figure 2.7 (b), while they are somehow depicted in Fig. 4.7 (a). With case B heat exchange with surrounding environment is taken into account. On the heated surface  $\Gamma_h$  the constant heat flux



 <b>RICERCA SISTEMA ELETTRICO</b>	<b>Title:</b> Development of BE numerical tools for LFR design and safety analysis (2018)	<u>Distribution</u> <b>PUBLIC</b>	<u>Issue Date</u> 29.01.2019	<u>Pag.</u>
	<b>Project:</b> ADP ENEA-MSE PAR 2017	Ref. ADPFISS-LP2-167	Rev. 0	74 di 163

$q=99900 \text{ W/m}^2$  is imposed. Heat dispersion effect is considered distributed along inlet channel external wall. Heat exchange coefficient  $h$  is evaluated following the procedure explained in Sect. 4.2.1. Comparisons between obtained results for cases A and B, with experimental data, for outlet-inlet temperature difference and for outlet temperature values are shown in Fig. 4.8 (a) and (b) respectively. It can be seen that the steady outlet temperature values overlap the experimental ones, showing that the heat transfer coefficient  $h$ , used to model the heat flux applied on boundary  $\Gamma_{w, \text{ch}, \text{in}}$ , has been correctly estimated. As a consequence of the greater heat flux value applied on the heated surface, higher temperature values are obtained during the transitory.

For times  $t > 1300\text{s}$  obtained temperature values are slightly closer to experimental values but temperature fluctuations are not yet simulated. Improved results have been obtained from the simulation of case C, as can be seen from the comparison of outlet-inlet temperature difference and outlet temperature values shown in Fig. 4.9 (a) and (b) respectively. Heat exchange between the fluid and the steel disk introduces thermal inertia and reduces the outlet temperature peak value at  $t=1100\text{s}$ . Differently from cases A and B, a second temperature peak value is observed at  $t=1300\text{s}$ . It can be seen that the heat exchange with the disk has an influence in time interval  $t \in [1020\text{s}; 1900\text{s}]$  since for  $t > 1900\text{s}$  results obtained for case C overlap those obtained for case B. It is interesting to notice the time evolution of temperature difference between values on outlet section and steel disk values. The difference is always positive (mean outlet temperature greater than disk temperature value), with the exception of a small time interval at the beginning of the transitory, where the disk is hotter than fluid mean temperature at outlet section. This phenomenon causes the additional temperature peak value that was not observed with cases A and B, since the disk exchanges heat back to the fluid. A comparison of results for cases A, B, C, D and experimental data are reported in Fig. 4.11 (a) and (b). It can be seen that if heat dispersion effects are distributed along boundary  $\Gamma_{w, \text{ch}, \text{o}}$  then a sensible outlet temperature values decrease is obtained at the beginning of the transitory, with a phenomenon that is not observed from experimental values. Temperature oscillations are observed as in results of case C, but obtained values are in worst agreement with experimental data. Having seen the importance of the heat exchange with the steel disk, even with a simplified model, we consider a heat exchange with the steel body of the test section, namely on boundaries  $\Gamma_{w, \text{b}}$ ,  $\Gamma_{w, \text{s}}$  and  $\Gamma_{w, \text{t}}$  as a final case E. Three boundaries are considered as three different bodies, so each one has a different uniform temperature value.

Time evolution of outlet temperature for cases A, C and E, together with experimental data, is shown in Fig. 4.12. The presence of these additional heat exchanges show relative little influence at the beginning of the transitory while a more sensible effect is observed for  $t > 1300\text{s}$ , when higher outlet temperature values are obtained, in particular with a better agreement with experimental data.


From the results obtained with these newly implemented boundary conditions in OpenFOAM code we can conclude that both heat exchange between TALL-3D main section and surrounding environment and conjugate heat transfer between the fluid and solid bodies (steel disk and test section steel body) must be considered to improve the CFD prediction during the transitory. As a further step, it will be possible to consider also the thermal inertia of the test section steel disk body where the heat flux is applied. Moreover the improved CFD model of TALL-3D test section will lead to improved results of the Cathare-OpenFOAM coupled simulation, as will be considered in future studies.

## 4.3 Model of the TALL-3D test section with simple heat dispersion effects

### 4.3.1 Geometry and physical properties of the basic new model

In order to improve the simulation presented in the previous report [4.9] we introduce a more detailed model of the three-dimensional test section of the TALL-3D facility. This new model includes external heat dispersion effects and further physical details. We consider the LBE properties temperature dependent as in Tab. 4.1. As seen in [4.9] the introduction of heat dispersion is needed for the matching of experimental



 <b>RICERCA SISTEMA ELETTRICO</b>	<u>Title:</u> Development of BE numerical tools for LFR design and safety analysis (2018)	<u>Distribution</u> <b>PUBLIC</b>	<u>Issue Date</u> 29.01.2019	<u>Pag.</u>
	<u>Project:</u> ADP ENEA-MSE PAR 2017	Ref. ADPFISS-LP2-167	Rev. 0	75 di 163

results. We have seen that the experimental heat balance, inlet temperature and outlet temperature, do not hold when full istion of the three dimensional component is considered.

The theoretical balance and the numerical evaluation of the inlet temperature and outlet temperature can be compared with the experimental ones only when the system is not considered fully isolated. The dispersion coefficients has been evaluated by matching the initial stationary energy balance when the pump is still full operational. However for accurate coefficients new experimental data should be provided in future.

In order to do this we considered a more detailed geometry as shown in Fig. 4.13. In particular we define the inlet and outlet as the segments AB (IN) and HG (OUT), respectively. The inlet channel is defined by the surface segment CB (CB) and the axis AH (AX). The outlet channel is defined by the surface segment GF (GF) and the axis AH. We label CB with downleftwall (DWNL) and GF with upleftwall (UWNL). The disk is located into the rectangular region NMLI (DKS). The right wall, which is a surface of the cylinder, is split into two parts: the part on the top EO, uprightwall (URW), and the part in the bottom DO, downrightwall (DRW). The simulation is axial symmetric and therefore is computed over a cylindrical region cut by a 5 degree arc. The symmetrical walls are called left (SYMLW) and right wall (SYMRW) surface. The surface limited by FE and CD are labeled topwall (TOP) and botwall (BOT), respectively.


#### 4.3.2 Boundary conditions

In order to improve the model, different boundary conditions will be imposed on each part of the boundary. For the Navier-Stokes equation we have two properties ( $\rho, \mu$ ) and three state variables ( $p, \varphi, U$ ) where  $\varphi$  is a scalar flux defined in OpenFOAM as linearInterpolate(U) & mesh.Sf(). The main velocity boundary conditions are defined as in Tab. 4.2. The zero fixedValue condition over the boundary defines the extrapolated velocity values. The boundary condition on  $v_t$ , described with turbulent variables, defines properly the turbulent boundary conditions. The properties and the state variables of the Navier-Stokes equation are computed as volumetric fields which take values on the boundary defined in Tab. 4.3. It is easy to note that in OpenFOAM every boundary field, including the properties, can be provided with boundary values. This is a common procedure since finite volume method provides state values at the center of the cell and does not provide direct values on the boundary itself. For the energy equation we have three properties ( $\rho, \alpha_{eff}, C_p$ ) and one state variable (T). The temperature boundary conditions are defined as in Tab. 4.4. As one can see new boundary conditions are imposed on the wall of the three-dimensional test section. These boundary conditions impose a heat flux at the boundary due to the heat dispersion effects of the walls. This allows us to decrease the outlet temperature and improve the matching with experimental data. The properties and the other state variables of energy equation are computed as volumetric fields which take values on the boundary defined in agreement with conditions written in Tab. 4.5. The density  $\rho$  and the effective thermal conductivity  $\alpha_{eff} = \alpha + v_t/Pr_t$  are variable with temperature and flow motion and therefore boundary values are important to compute heat fluxes.

This is very important for the definition of the external flux since in finite volume only the temperature gradient is usually imposed, not the heat flux. The turbulence model used in this simulation is the  $\kappa-\omega$  two-equation model. In Tab. 4.6 and Tab. 4.7 the boundary conditions of the  $\kappa$  and  $\omega$  turbulent state variables are reported together with the turbulent conditions for the velocity field which are applied on the turbulent viscosity  $v_t$ .

The  $kqRWallFunction$  boundary condition provides a suitable condition for turbulence  $k$  field for the case of medium-high Reynolds number flow using wall functions. It is an implementation of a simple modification of the zero-gradient condition. The  $\omega WallFunction$  provides a wall function constraint on turbulence specific dissipation  $\omega$ . The values are computed using  $\omega = \sqrt{\omega_{vis}^2 + \omega_{log}^2}$  where  $\omega_{vis}$  is omega in viscous region and  $\omega_{log}$  is  $\omega$  in logarithmic region.



 <b>RICERCA SISTEMA ELETTRICO</b>	<u>Title:</u> Development of BE numerical tools for LFR design and safety analysis (2018)	<u>Distribution</u> <b>PUBLIC</b>	<u>Issue Date</u> 29.01.2019	<u>Pag.</u>
	<u>Project:</u> ADP ENEA-MSE PAR 2017	Ref. ADPFISS-LP2-167	Rev. 0	76 di 163

The nutWallFunction boundary condition provides a wall function on the wall stress based on velocity field. This boundary condition required the values of  $C_{mu}$ , Von Karman constant  $\kappa$ , the model coefficients  $E$  and  $\beta_1$ .

#### 4.3.3 Initial conditions of the coupled simulation


In order to solve the coupled problem we need to combine the simulation of the main circuit with Cathare code and the 3D test section with OpenFOAM code. In the rest of the work the one-dimensional problem is labeled problem C while the CFD with problem OF. In order to set the initial conditions we need to compute an initial state which satisfies the one-dimensional equation. For this reason a solution of this high nonlinear system is computed for the one-dimensional model in its steady state. We start with inlet temperature for the PIPE3D set to 270°C. The flow rate is set to 4.75Kg/s with density  $\rho = 10448\text{Kg/m}^3$ . The one-dimensional code has a variable time step. We start with  $dt = 0.01$  and allow maximal time step value of 1s. After 2000s the temperature reaches the steady value reported in Tab. 4.9. The initial condition for OpenFOAM boundary field before the stabilization are reported in Tab. 4.8.

The coupling between the system code and the three-dimensional problem is achieved by a defective algorithm, i.e. a mutual exchange of boundary conditions between the problems. In order to obtain a stable coupling between the two problems both the systems must reach the same thermal-dynamical working conditions. For this reason we couple the system code and the three-dimensional problem after the system code stabilization and perform stabilization iterations of the coupled 1D-3D problem for 500s. The coupling must satisfy boundary conditions at the 1D-3D interfaces. For the energy balance equation we impose the temperature evaluated by the system code on the surface inlet (IN), an homogeneous Neumann condition on the outlet (OUT). Constraints on the axial component of the momentum balance equation must be set. We impose the flow rate evaluated by the system code on the inlet surface and a vanishing Neumann condition on the axis. The initial condition for the stabilization process is a constant temperature field with  $T = 272^\circ\text{C}$  and a vanishing velocity in the entire domain. We consider initial steady state for turbulent flow model case ( $\kappa-\omega$ ) in OpenFOAM code and turbulent viscosity  $\nu_t$  with turbulent thermal diffusivity  $\alpha_t$  as reported in Tab. 4.8. We remark that the stabilization process is used as the initial condition for the coupling of the one and three-dimensional problems.

#### 4.3.4 CATHARE stand alone and previous model simulations

In Ref. [4.9], we simulated the evolution of an Unprotected Loss of Flow going from forced to natural circulation flow for the test TG03S301(03) with Cathare standalone. We consider the system at  $t = 0^-$  in fully working conditions. The main initial conditions in forced circulation are obtained as a steady state and they are shown in Tab. 4.9. At  $t = 0^+$  the pump stops working while the power supplied through the rod in MH leg and 3D vessel heater are not switched off. Due to the lack of secondary side mass flow rate measurement, the oil flow rate has been calculated starting from the loss of enthalpy in the primary side, then with a thermal balance in the secondary side. The flow rate evolution in the three legs is presented in Fig. 4.15. We report the experimental data in the time interval  $[0, 1000\text{s}]$  since we do not have other experimental data on this semi-blind test. In Fig. 4.15, mass flow rates  $\dot{m}$  and temperature  $T$  at the points S3-S4 of the central leg are reported as a function of time  $t$ . In this Figure one can see the comparison between the Cathare stand-alone simulations and experimental results. The Cathare results are labeled with C and the experimental results with E. The mass flow results are matched fairly while the temperature results show large discrepancies. In Fig. 4.16, mass flow and temperature at reference points for STH Cathare stand alone and CFD OpenFOAM are shown. In particular these behaviors at reference points S4 and S3 of the central leg can be seen on the top and bottom of Fig. 4.16, respectively. The Cathare stand-alone results are labeled with C and the Open Foam  $k-\omega$  with  $k\omega$ . The application of the three-dimensional correction is clear. With these results is easy to think that the STH code does not give a very accurate results. However OpenFOAM results, as in all the other models, show an increase of the inlet temperature for large times which leads to high values inside the 3D-test section. Again it seems that the experimental results of the test section have heat losses that are not taken into account.



 <b>RICERCA SISTEMA ELETTRICO</b>	<u>Title:</u> Development of BE numerical tools for LFR design and safety analysis (2018)	<u>Distribution</u> <b>PUBLIC</b>	<u>Issue Date</u> 29.01.2019	<u>Pag.</u>
	<u>Project:</u> ADP ENEA-MSE PAR 2017	Ref. ADPFISS-LP2-167	Rev. 0	77 di 163

#### 4.3.5 Cathare-OpenFOAM coupling with heat dispersion in the TALL-3D test section.

The coupling between Cathare and OpenFOAM with two-equation turbulent  $k-\omega$  model uses the defective coupling algorithm with overlapping meshes. The one-dimensional mesh is defined over all the domain and a three-dimensional mesh is defined only over the three-dimensional test region. We solve at each time step the three-dimensional code (OpenFOAM) and the one-dimensional system code (Cathare) over the overlapping domain. For this simulation, we consider two of the six reference points shown on the right of Fig. 4.4: S3 (BELOW3D28) and S4 (ABOVE3D1) in the central vertical leg. The point S3 (BELOW3D28) is the 1D/3D matching interface for state and turbulent variables at the inlet section of the three-dimensional domain. The point S4 (ABOVE3D1) is the 3D/1D matching interface for the outlet section of the three-dimensional domain. The meshes are generated with GUTHARE for the one-dimensional case and with SALOME modules for the three-dimensional one. The coupling algorithm for OpenFOAM-Cathare coupling can be schematized as follows [4.9]:

- a) Stabilization of the STH Problem (Cathare); stabilization of state and turbulent variables of the CFD problem to Cathare setup (OpenFOAM);
- b) For each time step:
  - b1) Defective correction from 3D near the outlet of the TALL-3D component and one step solution for the one-dimensional code for velocity, temperature and pressure fields;
  - b2) Boundary conditions from 1D at the inlet section of 3D geometry one step solution for the three-dimensional code for state and turbulent variables.

For details one can see the defective algorithm described in [4.9]. The energy correction is obtained by computing the entalpy source ENT LEXT inside the energy equation. We define

$$\text{ENT LEXT} = h_{S4} - \alpha \text{Cp}(T_{1D} - T_{3D}), \quad (2.6)$$

where  $\alpha$  is a constant and  $h_{S4}$ ,  $T_{S4}$  are the entalpy and the temperature at point S4. The  $T_{3D}$  is the average temperature at the outlet of the 3D test section which has been computed at each OpenFOAM time step. This temperature is imposed on Cathare and the resulting matching is almost perfect at each time step. The momentum correction is obtained by computing DP LEXT as


$$\text{DP LEXT} = \text{DP LEXT}_0 - \beta(\Delta p_{3D} - \Delta p_{1D}), \quad (2.7)$$

where  $\Delta p_{3D}$  and  $\Delta p_{1D}$  are the pressure losses when the gravity contribution is subtracted. The value  $\text{DP LEXT}_0$  is the old value of  $\text{DP LEXT}$  which is directly read from the one-dimensional code. The constant  $\beta$  is set constant. In Fig. 4.17, mass flow and temperature at reference points for experimental data and Cathare-OpenFOAM coupling are shown. In particular these behaviors at reference points S4 and S3 of the central leg can be seen on the top and bottom of Fig. 4.17, respectively. The experimental results are labeled with E and the Cathare-OpenFOAM coupling with S. The application of heat dispersion effects on the wall decreases the inlet and outlet temperature. This is needed when one desired matching experimental data. However the oscillations period and their amplitude are not reproduced in a very accurate way. In details in Fig. 4.18 velocity modulus and streamline profiles over the 3D test component at time  $t = 0, 4, 20, 80, 180, 580, 1780$  and  $2780$ s are shown. In Fig. 4.19, temperature  $T$  over the same interval of time is reported. Finally in Fig. 4.20 the turbulent viscosity  $\nu_t$  is reported.

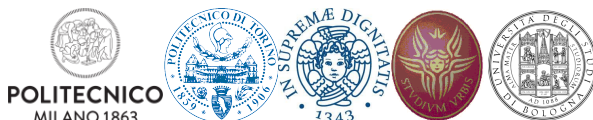
#### 4.4 Role of the activity, general goals and future development.

In previous reports we have studied the TALL-3D plant where the mono-dimensional component is modeled with Cathare code while the three-dimensional regions with OpenFOAM code. The model for TALL-3D has been developed in the previous report and coupling simulations with laminar and turbulent flow have been studied for different configurations. In this report we have studied and improved the modeling of the




 <b>RICERCA SISTEMA ELETTRICO</b>	<u>Title:</u> Development of BE numerical tools for LFR design and safety analysis (2018)	<u>Distribution</u> <b>PUBLIC</b>	<u>Issue Date</u> 29.01.2019	<u>Pag.</u>
	<u>Project:</u> ADP ENEA-MSE PAR 2017	Ref. ADPFISS-LP2-167	Rev. 0	78 di 163

simulation of a thermohydraulics test with natural circulation flow performed in the experimental TALL-3D facility with the goal of developing a multiscale and multiphysics computational platform for studying issues of LFR technology based on open-source and commercial software in a strict collaboration between the University of Bologna and ENEA (see Refs. [4.1]-[4.8]). In this work additional boundary conditions have been implemented in OpenFOAM to take into account the heat exchange between the TALL-3D main section and the surrounding environment. This new model takes into account the exchange in the region between the fluid and the steel disk that is present inside the test section geometry. The influence of these boundary conditions has been evaluated by using experimental data as inlet boundary conditions, for the CFD simulation, instead of the coupling with Cathare code. This procedure has allowed us to evaluate the effect of the new modeled phenomena on the CFD solution without the influence of the system code. The boundary conditions have been implemented as new code classes within OpenFOAM. A simple model with boundary conditions that reproduce dispersion effects has been studied. The one-dimensional system code standalone produces high temperature and the corrections of three-dimensional CDF code improve in the right direction. However the results show the difficulties to model coupling that is accurate in all different regimes and physical configurations. For these reasons a lot of work should be done both in the STH code and CFD modeling on the LFR platform. The experimental test series from the TALL-3D facility is a unique set of data which does not gives only average values but real profiles of temperature inside liquid metal flow needed for real CFD evaluations.





 <b>RICERCA SISTEMA ELETTRICO</b>	<u>Title:</u> Development of BE numerical tools for LFR design and safety analysis (2018)	<u>Distribution</u> <b>PUBLIC</b>	<u>Issue Date</u> 29.01.2019	<u>Pag.</u>
	<u>Project:</u> ADP ENEA-MSE PAR 2017	Ref. ADPFISS-LP2-167	Rev. 0	79 di 163


Property	Unit	Correlation	Temperature	error $\pm$
Molar mass	kg/mol	0.20898		
Melting temperature	K	544.6		
Latent heat	kJ/kg	53.3	-	-
Sat. vapour pressure	Pa	$2.67 \times 10^{10} \exp(-22858/T)$	545-1831	40
Surface tension	N/m	$(420.8 - 0.081T) \times 10^{-3}$	545-1400	
Density	g/m <sup>3</sup>	$10725 - 1.22T$	545-1300	2
Sound velocity	m/s	$1616 + 0.187T - 2.2 \times 10^{-4}T^2$	545-1800	5
Bulk modulus	Pa	$(30.22 - 2.8 \times 10^{-3}T - 3.720 \times 10^{-6}T^2) \times 10^9$	545-1800	3
Isobaric specific	J/kg.K	$118.2 + 5.934 \times 10^{-3}T + 7.183 \times 10^{-6}T^2$	545-1300	7
Dynamic viscosity	Pa.s	$4.456 \times 10^{-4} \exp(780/T)$	545-1300	5
Electric resistivity	$\Omega$ m	$(98.96 + 0.0554 \times T) \times 10^{-8}$	545-1420	0.8
Thermal conductivity	W/mK	$7.34 + 9.5 \times 10^{-3}T$	545-1000	10

*Tab. 4.1 – Physical properties used in the modeling of the TALL-3D facility.*

region	type for U	type for $\phi$	type for p
SYMLW	wedge	wedge	wedge
IN	fixedValue uniform (0 0.793699 0)	calculated	zeroGradient
OUT	zeroGradient	calculated	fixedValue
URW	zero fixedValue	calculated	zeroGradient
SYMRW	wedge	wedge	wedge
DSK	fixedValue	calculated	zeroGradient
TOP	zero fixedValue	calculated	zeroGradient
TOP	zero fixedValue	calculated	zeroGradient
DRW	zero fixedValue uniform (0 0 0)	calculated	zeroGradient
CB + GF	zero fixedValue	calculated	zeroGradient

*Tab. 4.2 - OpenFOAM boundary field U,  $\phi$  and p for the Navier-Stokes equation.*



 <b>RICERCA SISTEMA ELETTRICO</b>	<u>Title:</u> Development of BE numerical tools for LFR design and safety analysis (2018)	<u>Distribution</u> <b>PUBLIC</b>	<u>Issue Date</u> 29.01.2019	<u>Pag.</u>
	<u>Project:</u> ADP ENEA-MSE PAR 2017	Ref. ADPFISS-LP2-167	Rev. 0	80 di 163

region	type for $\rho$	type for $\mu$
SYMLW	wedge	const prop.
IN	zeroGradient	const prop.
OUT	zeroGradient	const prop.
URW	zeroGradient	const prop.
SYMRW	wedge	const prop.
DSK	zeroGradient	const prop.
TOP	zeroGradient	const prop..
TOP	zeroGradient	const prop.
DRW	zeroGradient	const prop.
CB + GF	zeroGradient	const prop.


*Tab. 4.3 - OpenFOAM boundary properties values for the Navier-Stokes equation.*

bc region	$T$	$q$	$T_{ref}$
SYMLW	wedge		
IN	fixedValue;		uniform 272.6
OUT	zeroGradient		
URW	externalHeatFluxTemperature	uniform 9900.	uniform 21
SYMRW	wedge		
DSK	zeroGradient		
TOP	externalHeatFluxTemperature	uniform 0.	uniform 21.
BOT	externalHeatFluxTemperature	uniform 0.	uniform 21.
DRW	externalHeatFluxTemperature	uniform 0.	uniform 21.
CB + GF	zeroGradient		

*Tab. 4.4 - OpenFOAM boundary field for temperature  $T$  of the heat equation.*

bc region	type for $\rho$	type for $\alpha_{eff}$	type for $C_p$
SYMLW	wedge	wedge	wedge
IN	zeroGradient	zeroGradient	zeroGradient
OUT	zeroGradient	zeroGradient	zeroGradient
URW	zeroGradient	zeroGradient	zeroGradient
SYMRW	wedge	wedge	wedge
DSK	zeroGradient	zeroGradient	zeroGradient
TOP	zeroGradient	zeroGradient	zeroGradient
BOT	zeroGradient	zeroGradient	zeroGradient
DRW	zeroGradient	zeroGradient	zeroGradient
CB + GF	zeroGradient	zeroGradient	zeroGradient



 <b>RICERCA SISTEMA ELETTRICO</b>	<b>Title:</b> Development of BE numerical tools for LFR design and safety analysis (2018)	<u>Distribution</u> <b>PUBLIC</b>	<u>Issue Date</u> 29.01.2019	<u>Pag.</u>
	<b>Project:</b> ADP ENEA-MSE PAR 2017	Ref. ADPFISS-LP2-167	Rev. 0	81 di 163

**Tab. 4.5 - OpenFOAM boundary field for properties of the heat equation.**


bc region	kappa (bc)	omega (bc)	nut (bc)
SYMLW	type wedge	type wedge	type wedge
IN	type turbulentIntensityKineticEnergyInlet intensity 0.05 U; $\phi$ value uniform 0.0035	type turbulentMixingLengthFrequencyInlet mixingLength 0.0012 phi; k value uniform 73.9486	type calculated value uniform 3.19e-05
OUT	type turbulentIntensityKineticEnergyInlet intensity 0.05 U; $\phi$ value uniform 0.0035	type zeroGradient	type calculated value uniform 1.e-6
URW	type kqRWallFunction value uniform 0.0035;	type omegaWallFunction	type nutWallFunction Cmu 0.09 kappa 0.41; E 9.8 value uniform 1.e-6
SYMRW	type wedge	type wedge;	type wedge

**Tab. 4.6 - OpenFOAM boundary field for temperature turbulent variables ( $k, \omega$ ) and turbulent property  $\nu_t$  of the  $k-\omega$  two equation model (I).**

bc region	kappa (bc)	omega (bc)	nut (bc)
DSK	type kqRWallFunction value uniform 0.0035;	fixedValue uniform 800.;	type nutWallFunction Cmu 0.09 kappa 0.41; E 9.8 value uniform 1.e-6
TOP	type kqRWallFunction value uniform 0.0035;	fixedValue uniform 800.;	type nutWallFunction Cmu 0.09; kappa 0.41; E 9.8 value uniform 1.e-6
BOT	type kqRWallFunction value uniform 0.0035;	fixedValue uniform 800.;	type nutWallFunction Cmu 0.09; kappa 0.41; E 9.8 value uniform 1.e-6
DRW	type kqRWallFunction value uniform 0.0035;	fixedValue uniform 800.;	type nutWallFunction Cmu 0.09; kappa 0.41; E 9.8 value uniform 1.e-6
CB + GF	type kqRWallFunction value uniform 0.0035;	fixedValue uniform 800.;	type nutWallFunction Cmu 0.09 kappa 0.41; E 9.8 value uniform 1.e-6

**Tab. 4.7 - OpenFOAM boundary field for temperature turbulent variables ( $k, \omega$ ) and turbulent property  $\nu_t$  of the  $k-\omega$  two equation model (II).**



 <b>RICERCA SISTEMA ELETTRICO</b>	<u>Title:</u> Development of BE numerical tools for LFR design and safety analysis (2018)	<u>Distribution</u> <b>PUBLIC</b>	<u>Issue Date</u> 29.01.2019	<u>Pag.</u>
	<u>Project:</u> ADP ENEA-MSE PAR 2017	Ref. ADPFISS-LP2-167	Rev. 0	82 di 163

	variable type	spatial distribution	value
$\alpha$	constant		7.882e-6
$\nu$	constant		1.899e-7
$\beta$	constant		1.248e-4;
$T_{ref}$	constant		272.5;
Pr	constant		0.02626;
$Pr_t$	constant		1.7
$C_p$	internalField	uniform	146
$\rho$	internalField	uniform	10360
$\alpha_{eff}$	internalField	uniform	7.882e-6
$\nu_t$	internalField	uniform	1.e-6
$T$	internalField	uniform	307
$\mathbf{U}$	internalField	uniform	(0 0 0)
$p$	internalField	uniform	0
$\kappa$	internalField	uniform	0.0035
$\omega$	internalField	uniform	10

**Tab. 4.8 - Initial condition for OpenFOAM volume field before coupling.**

	Initial Condition	Unit
T BELOW3D	272.6	$^{\circ}C$
T ABOVE3D	308.2	$^{\circ}C$
MH power	10300	W
LBE mass flow rate	4.75222	kg/s
Oil outlet temperature	126	$^{\circ}C$
Oil mass flow rate	1.	[kg/s]

**Tab. 4.9 - Initial state condition for the one-dimensional Problem C (Cathare). The STH code initial condition satisfies the steady state equation.**



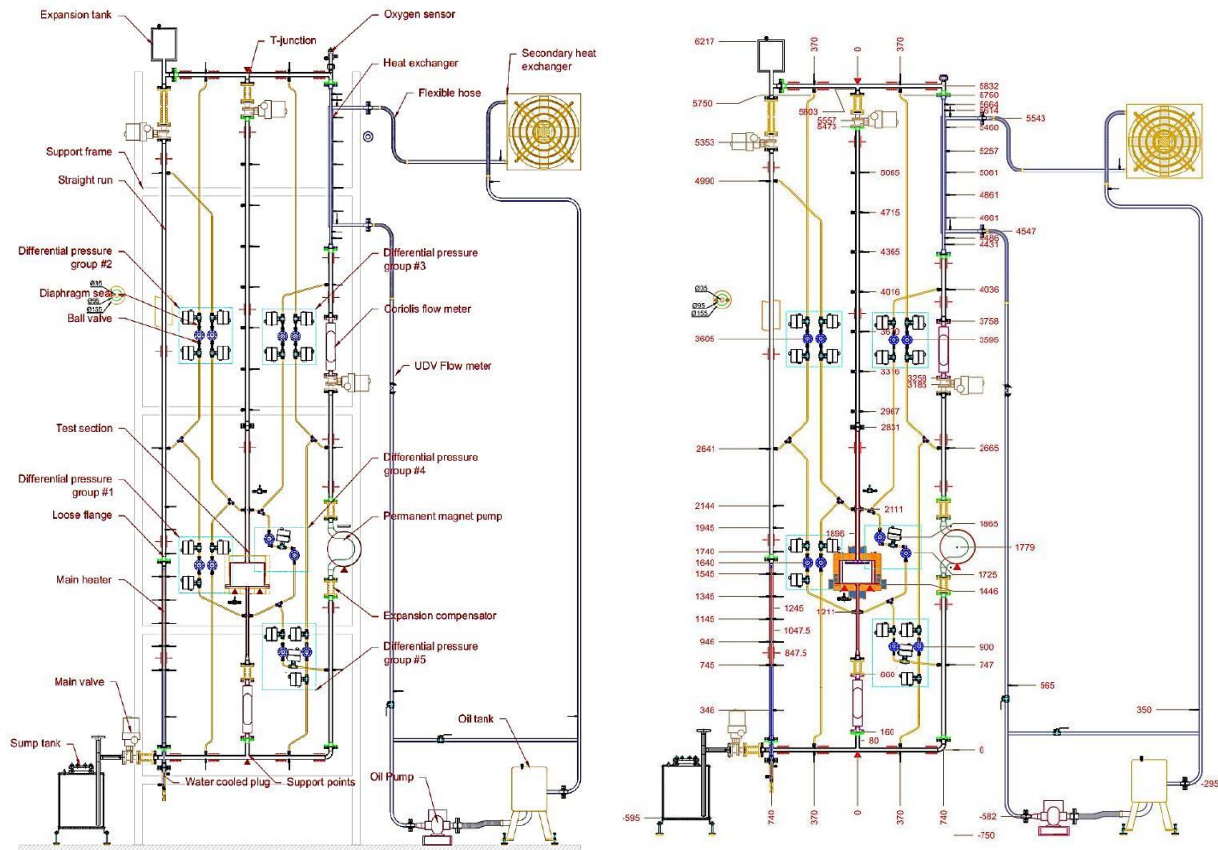


Fig. 4.1 - TALL-3D facility (left) with geometric dimensions (right).

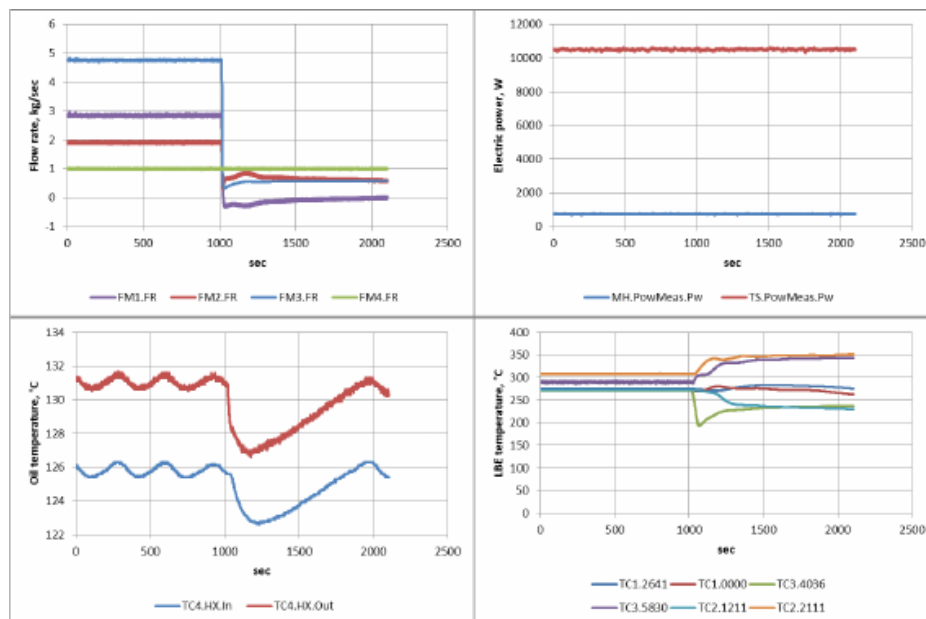


Fig. 4.2 - Experimental data for test series TG03S301(03) [4.9].



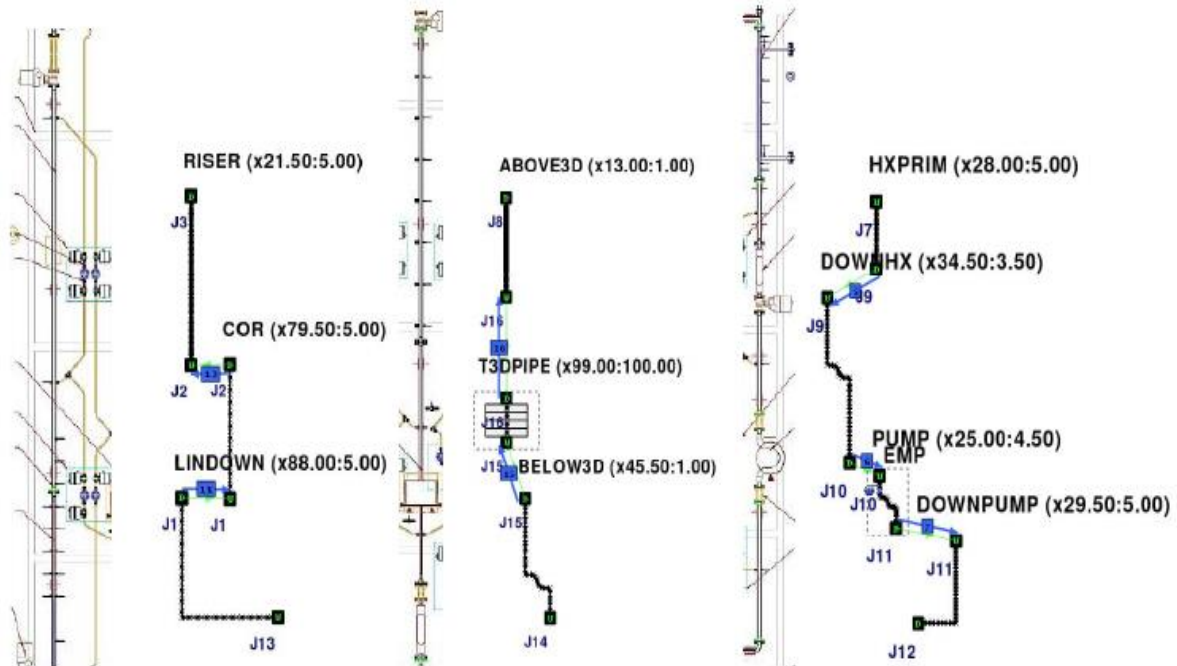


Fig. 4.3 - STH modeling for TALL-3D. Left, central and right vertical leg (from left to right) in 1D system model with 3D test section [4.9].

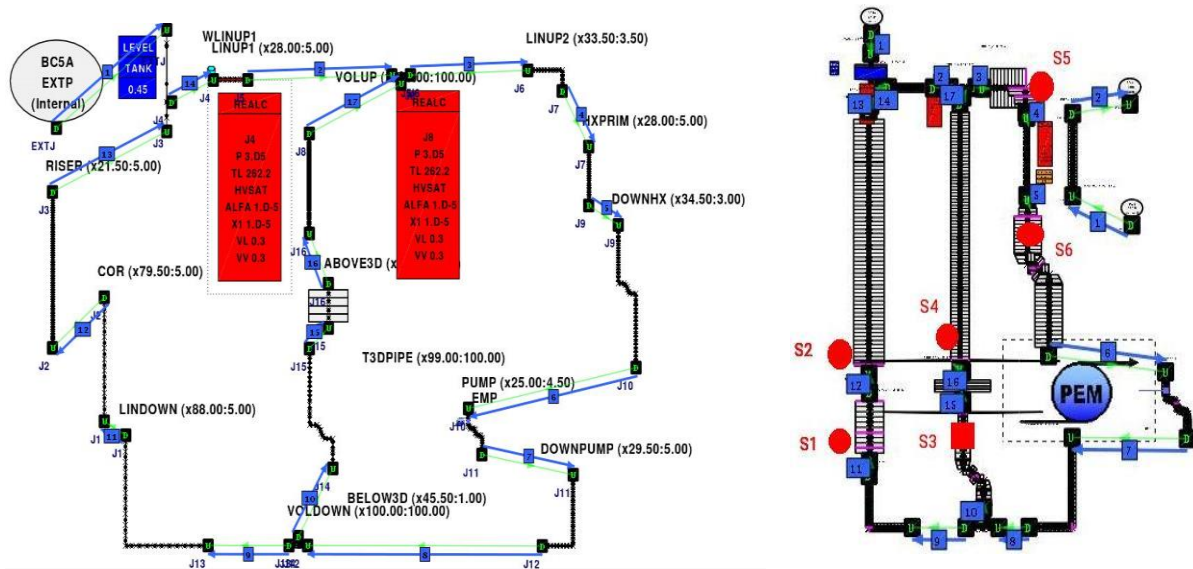


Fig. 4.4 - STH modeling for TALL-3D. One-dimensional CATHARE model (left) and point of interests S1-S2 of the left leg (right), S3-S4 of the central leg and S5-S6 of the right vertical leg. For details see [4.9].

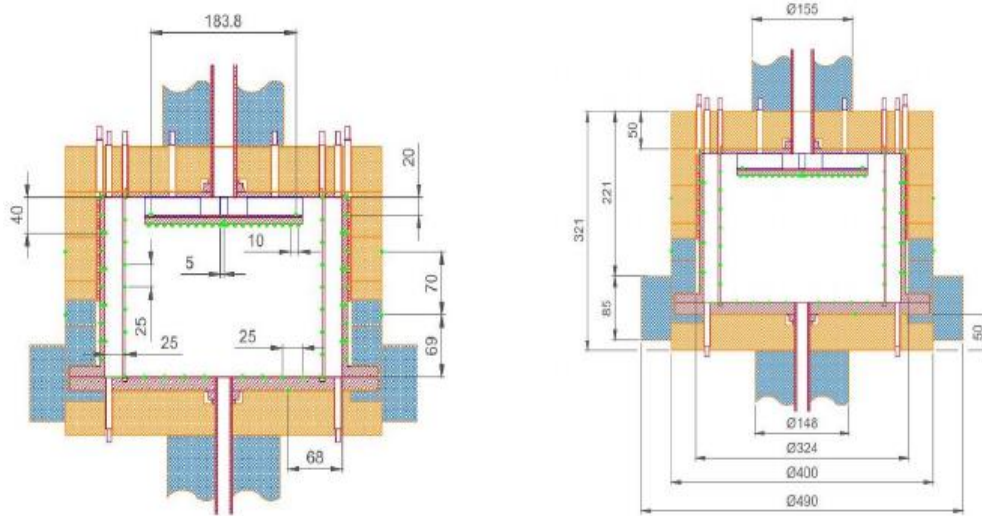
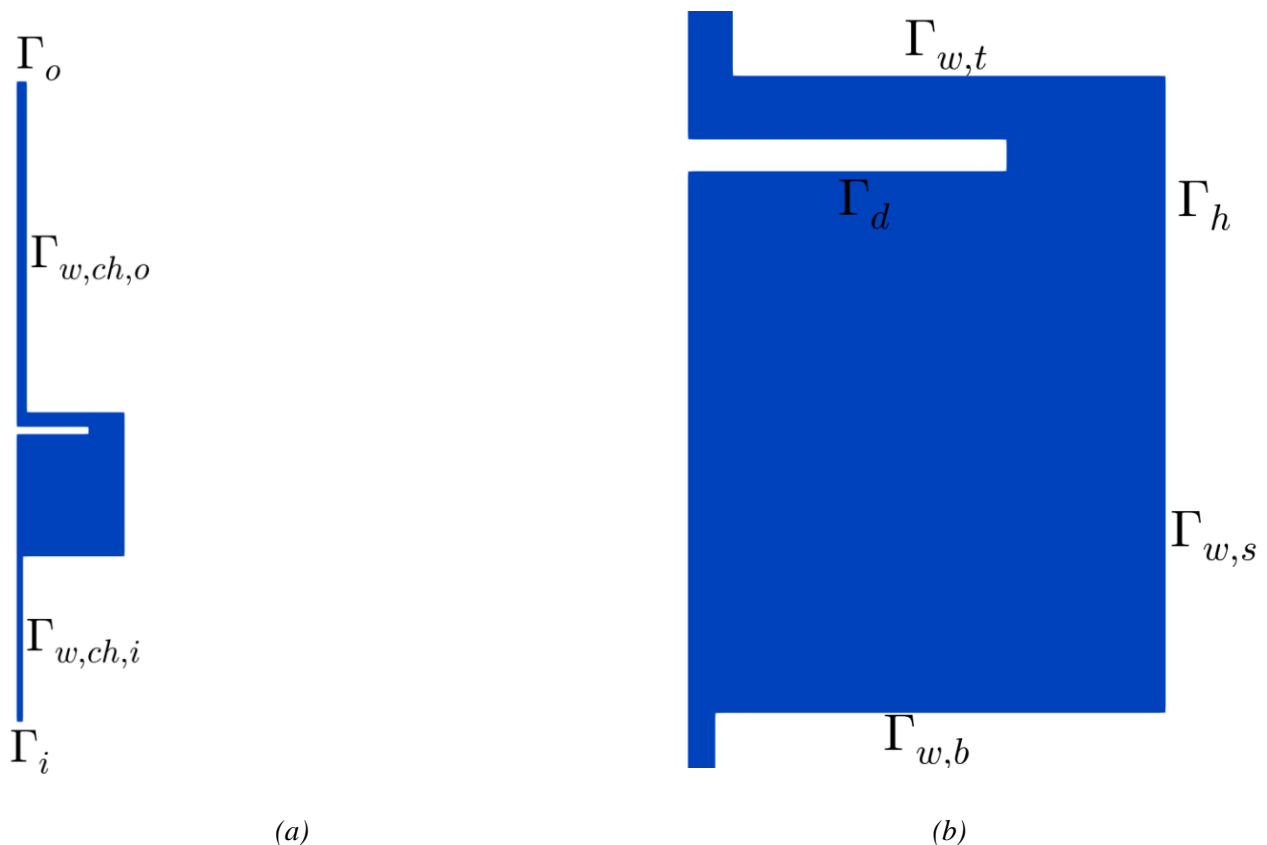


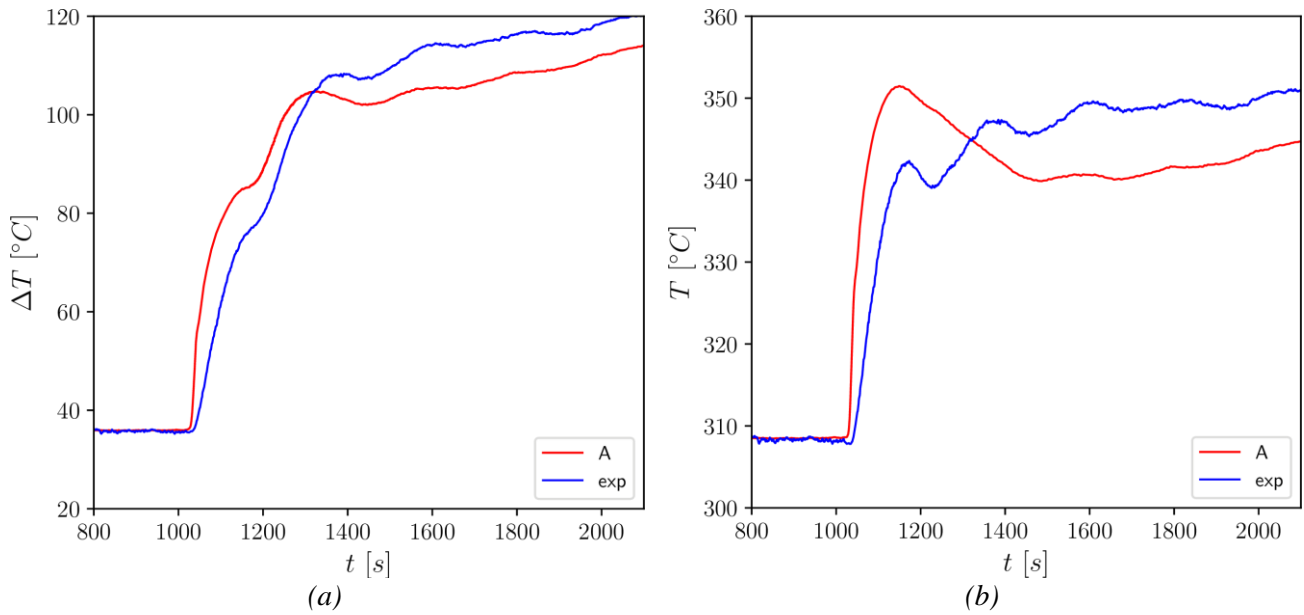
Fig. 4.5 - Modelling for TALL-3D. Geometry and dimensions.



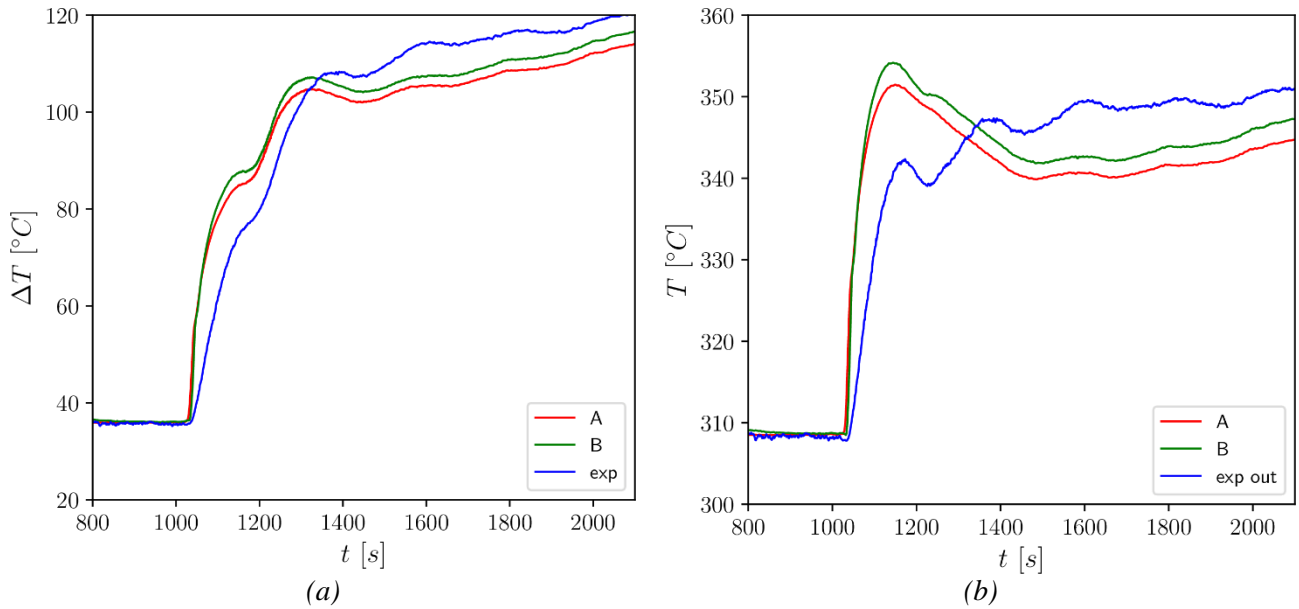
(a)

(b)

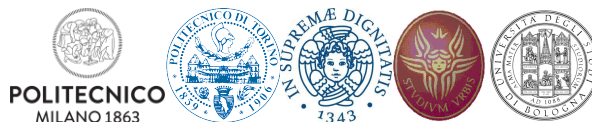
Fig. 4.6 - Simulated geometry for the study with heat exchange between the TALL-3D main section and the surrounding environment between fluid and steel disk (a) together with a close up view of the test section (b).



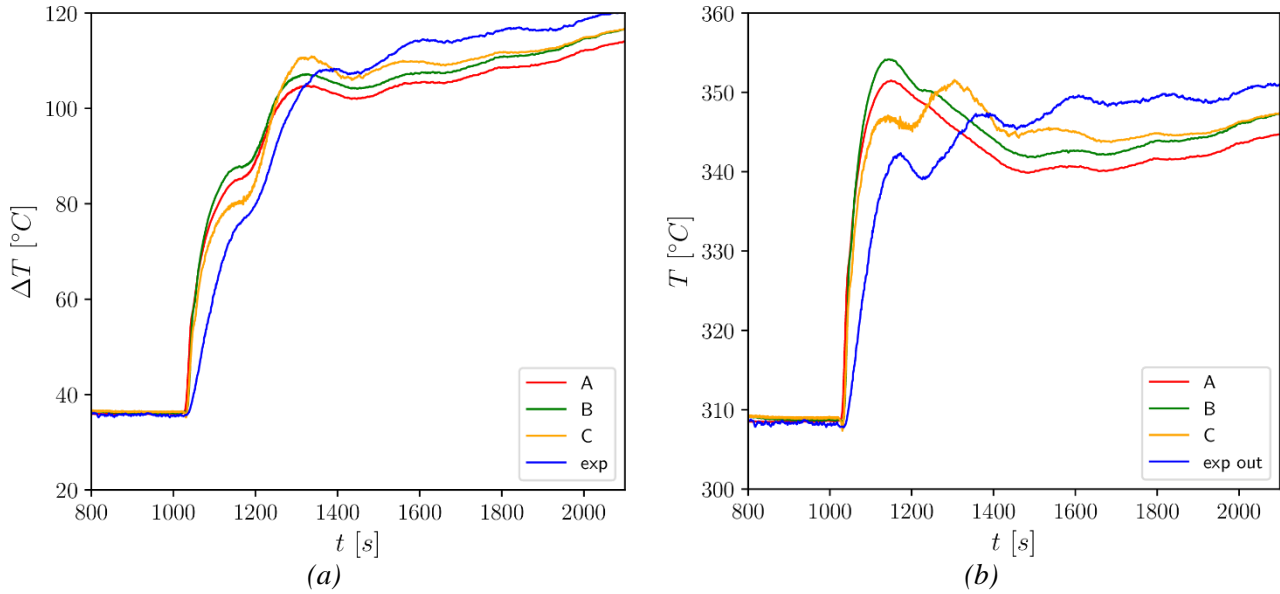
**Fig. 4.7 - Comparison between case A and experimental values of temperature difference between outlet and inlet section (a) and outlet temperature values (b).**



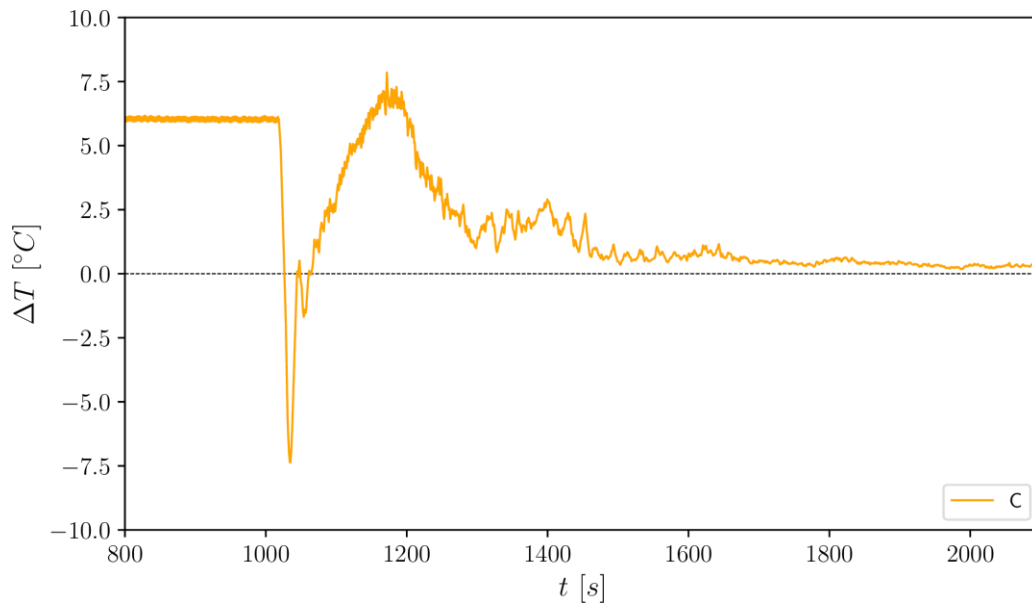
**Fig. 4.8 - Comparison between case A, case B and experimental values of temperature difference between outlet and inlet section (a) and outlet temperature values (b).**



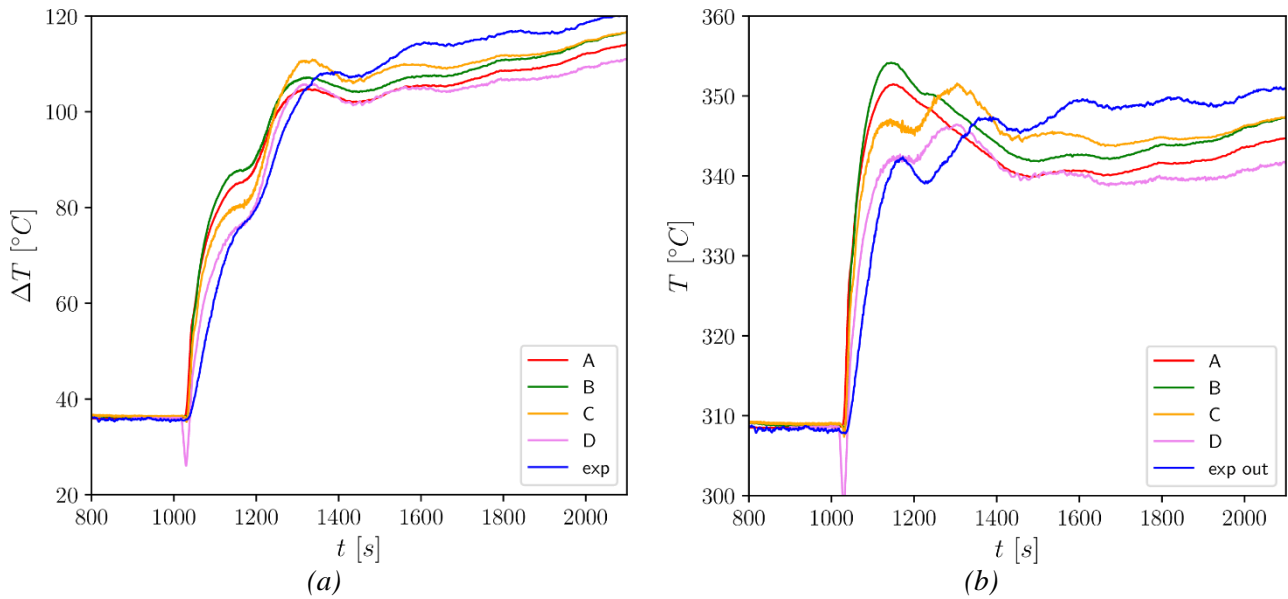




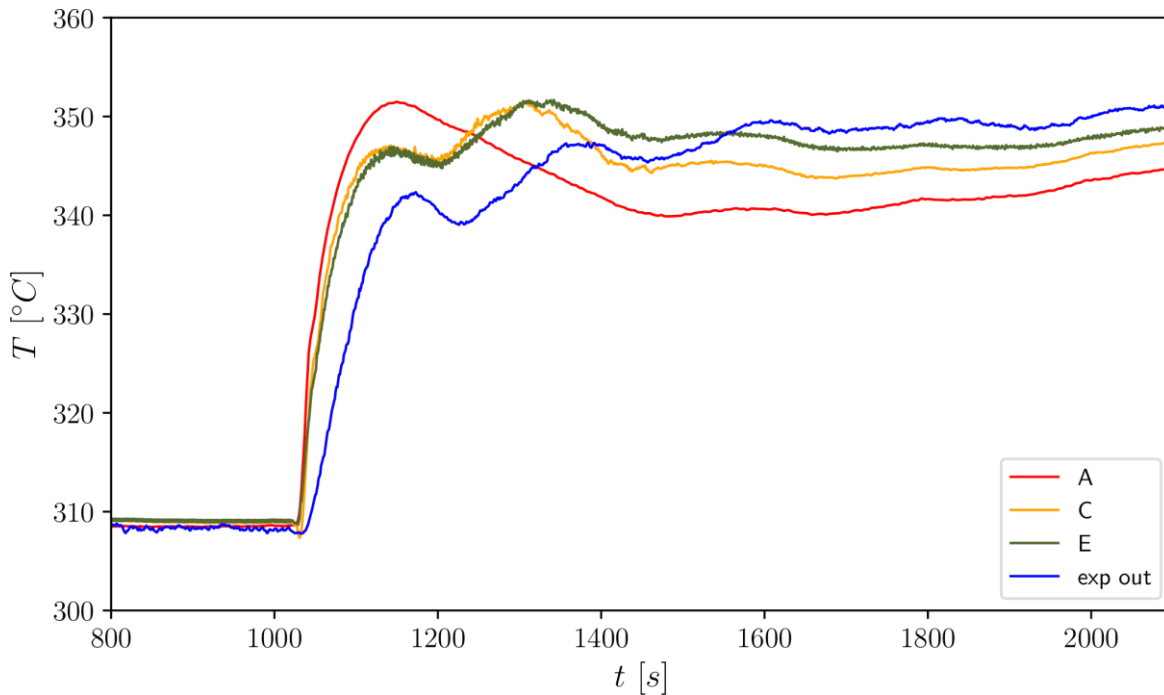
**Fig. 4.9 - Comparison between case A, B, C and experimental values of temperature difference between outlet and inlet section (a) and outlet temperature values (b).**



**Fig. 4.10 - Different profile between outlet and steel disk temperature values for case C.**

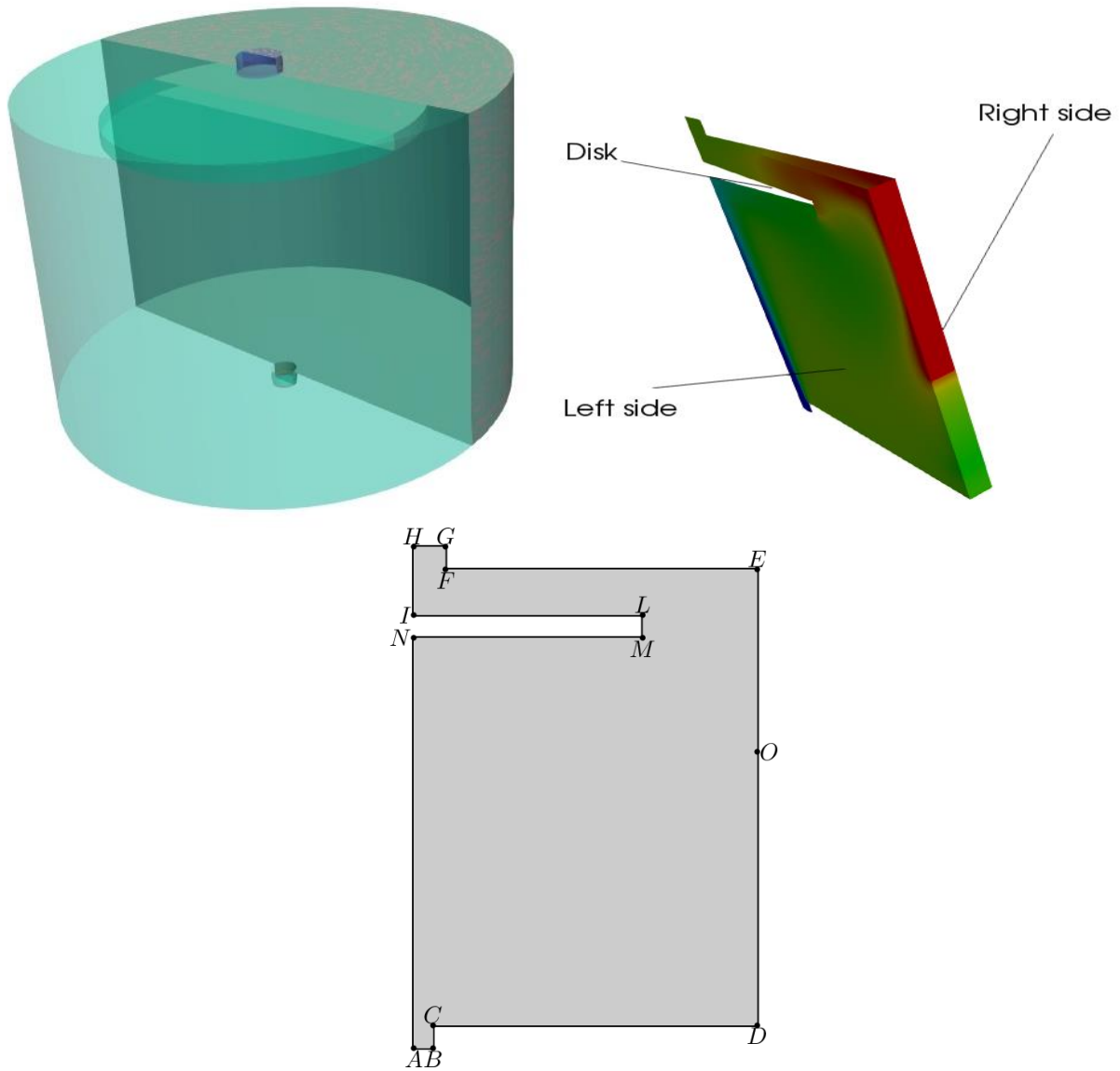


**Fig. 4.11 - Comparison between case A, B, C, D and experimental values of temperature profiles between outlet and inlet section (a) and outlet temperature values (b).**

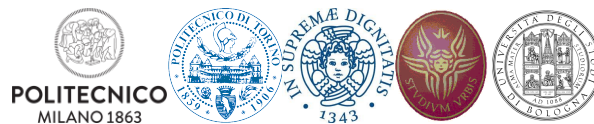
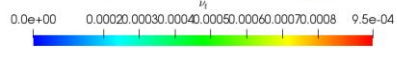
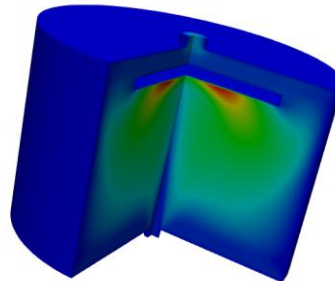
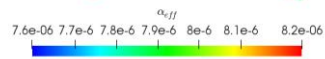
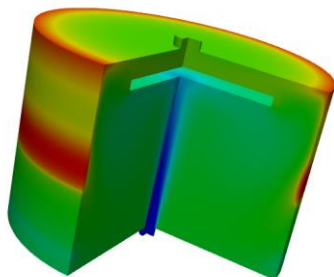
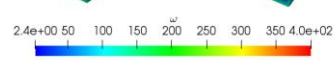
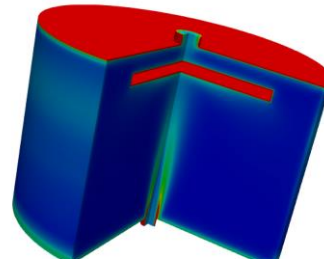
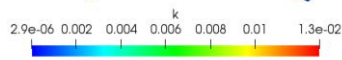
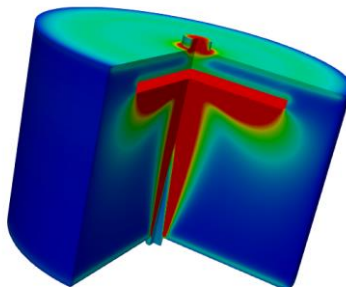
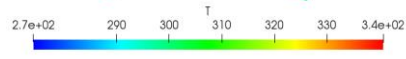
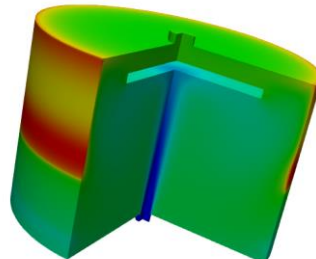
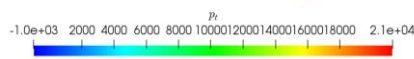
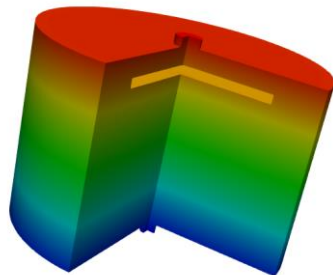
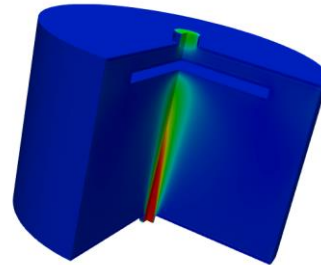
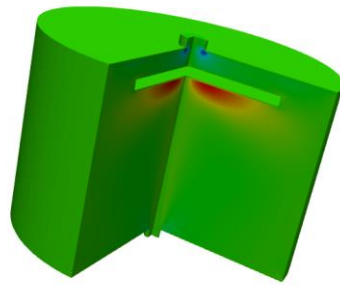


**Fig. 4.12 - Comparison of outlet temperature values between cases A, C, E and experimental data.**

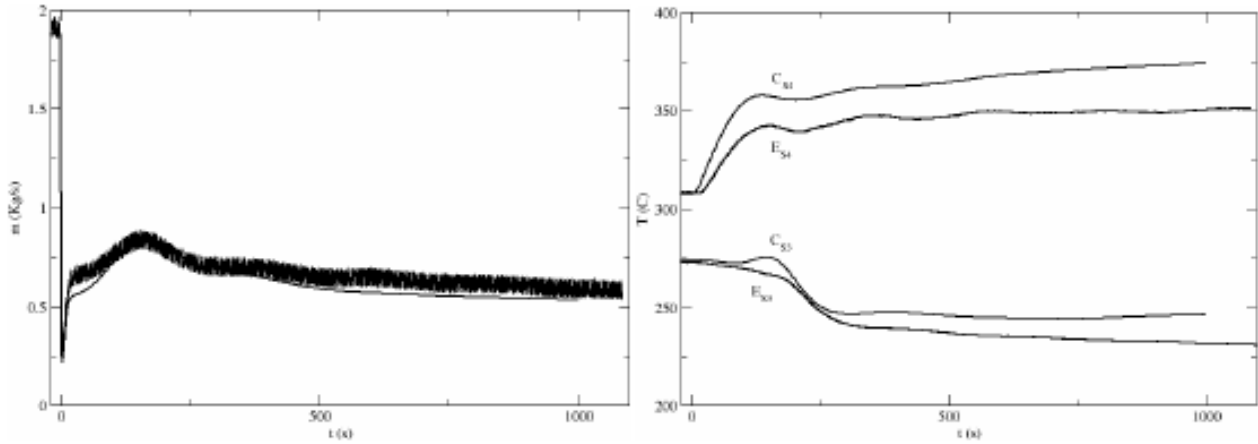




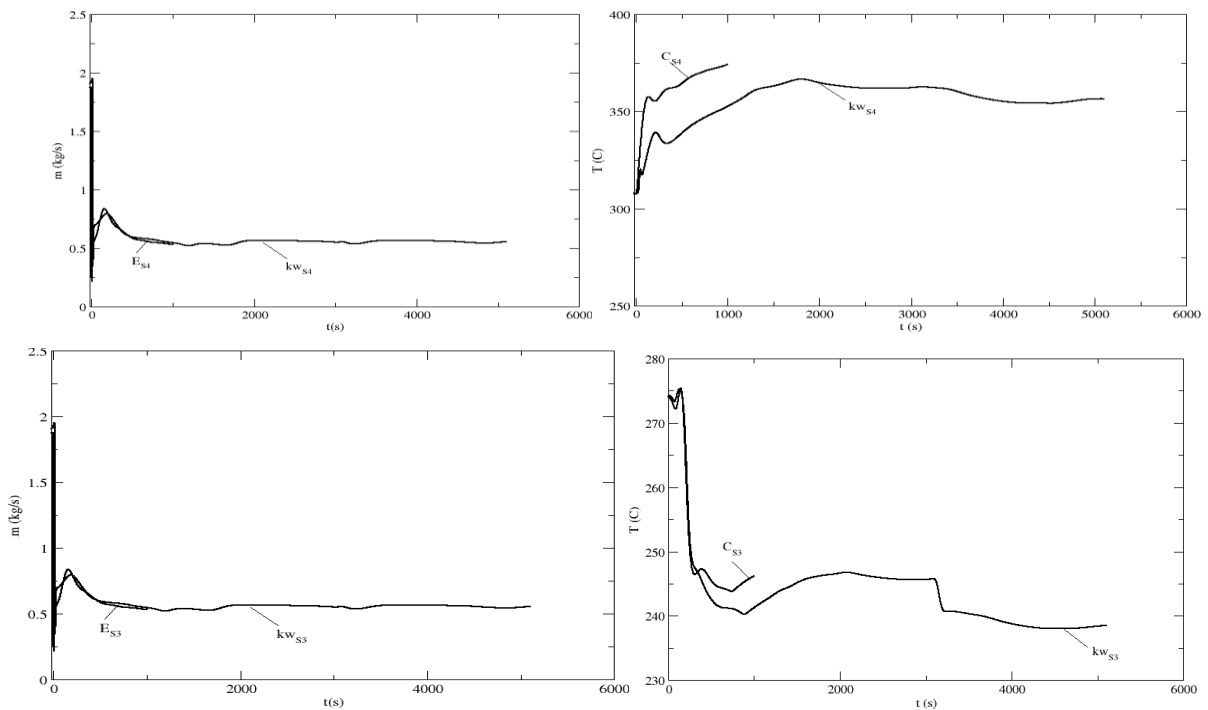
**Fig. 4.13 - Geometry: HA=axis (AX), NMLI=disk (DSK), EO=uprightwall (URW), DO=downrightwall (DRW), FE=top (TOP), CD=bottom (BOT), AB=inlet (IN), HG=outlet (OUT), CB=downleftwall (CB), GF=upleftwall (GF).**



**Fig. 4.14 - Initial steady state and turbulent variables for CFD OpenFOAM code with the turbulent flow model  $\kappa\text{-}\omega$ .**

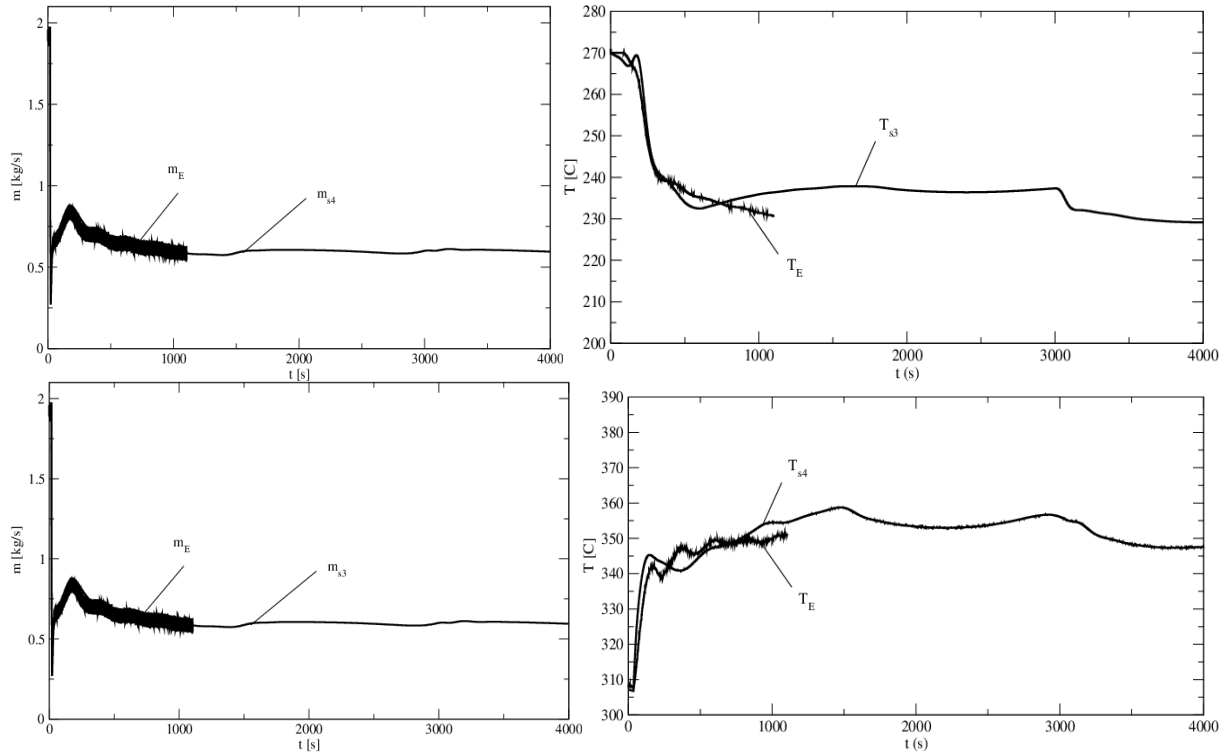


**Fig. 4.15 - Cathare standalone simulation. Computed mass flow rate  $m$  (left) and temperature (right) at the points S3-S4 of the central leg as a function of time  $t$ , from [4.9].**



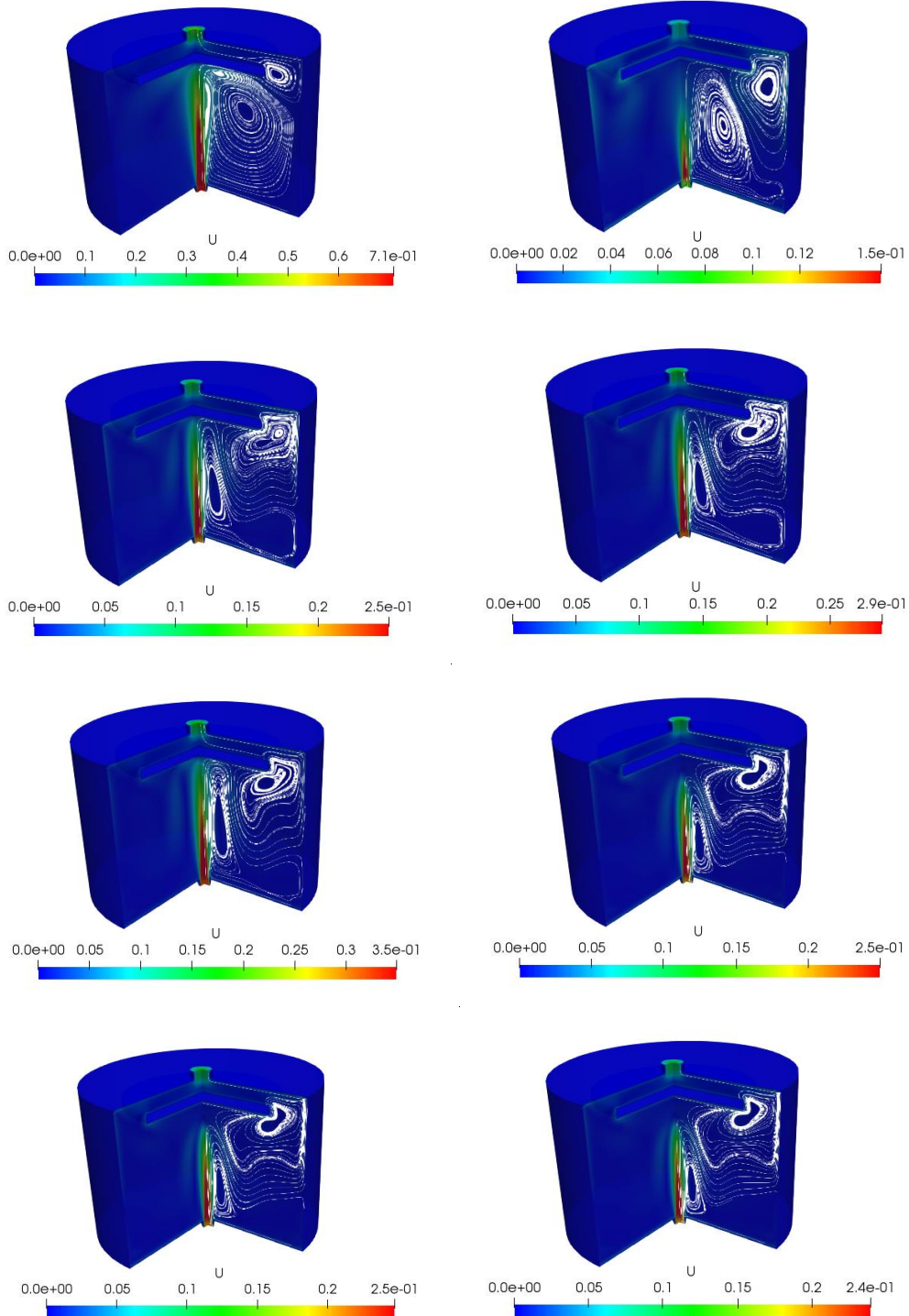
**Fig. 4.16 - Mass flow rate (right) and temperature (left) at reference point S4 (top) and S3 (below) of the central leg for Cathare standalone (C) and coupling Cathare-OpenFoam with  $k\text{-}\omega$  turbulence model.**





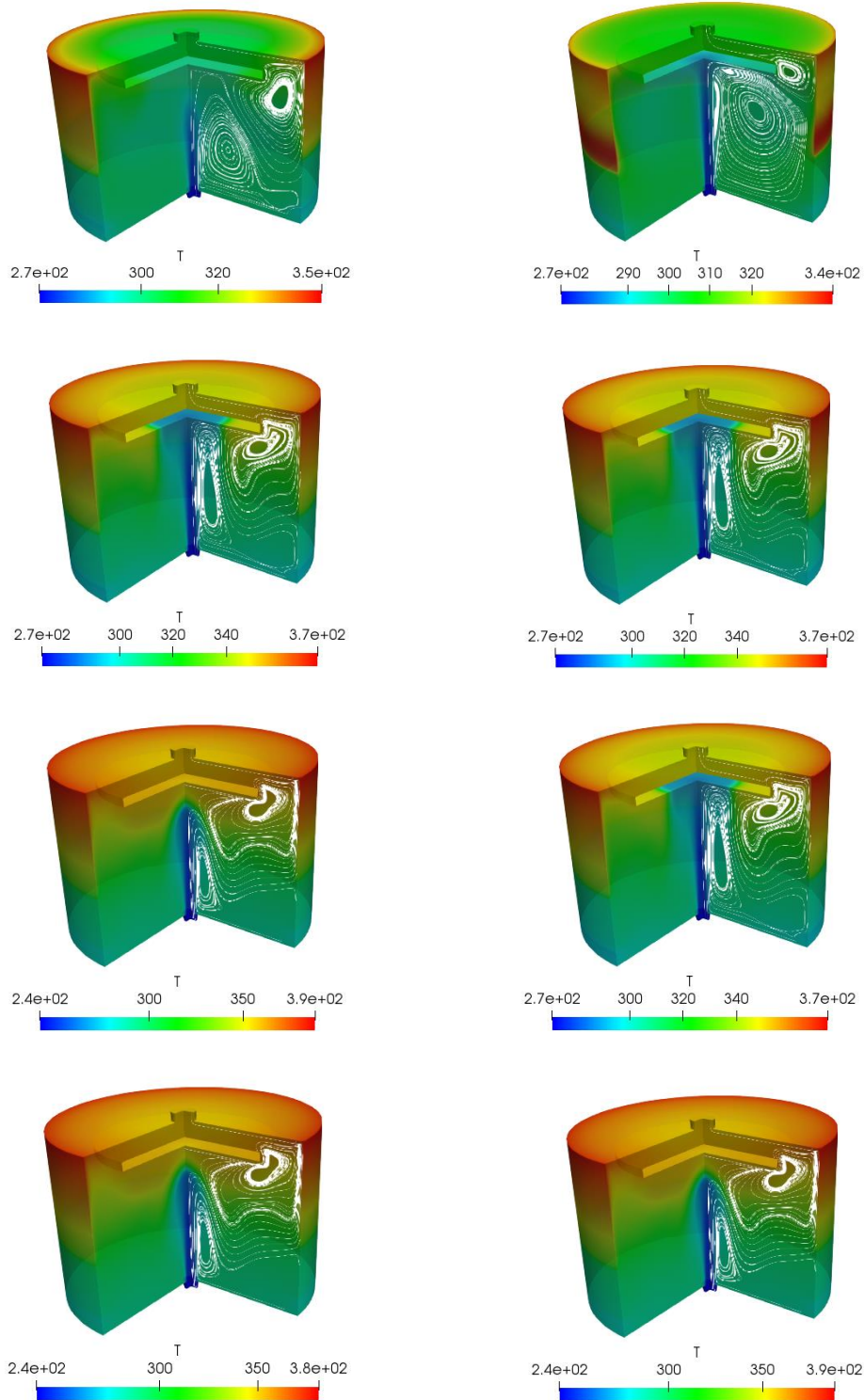
**Fig. 4.17 - Mass flow rate (right) and temperature (left) at reference point S4 (top) and S3 (below) of the central leg for experimental data (E) and coupling Cathare-OpenFOAM with heat dispersion on the TALL-3D test section.**





**Fig. 4.18 - Velocity module  $U$  and streamline profiles over the 3D test component at time  $t = 0, 4, 20, 80, 180, 580, 1780$  and  $2780$ s by using two-equation  $\kappa\text{-}\omega$  turbulence model in OpenFOAM.**

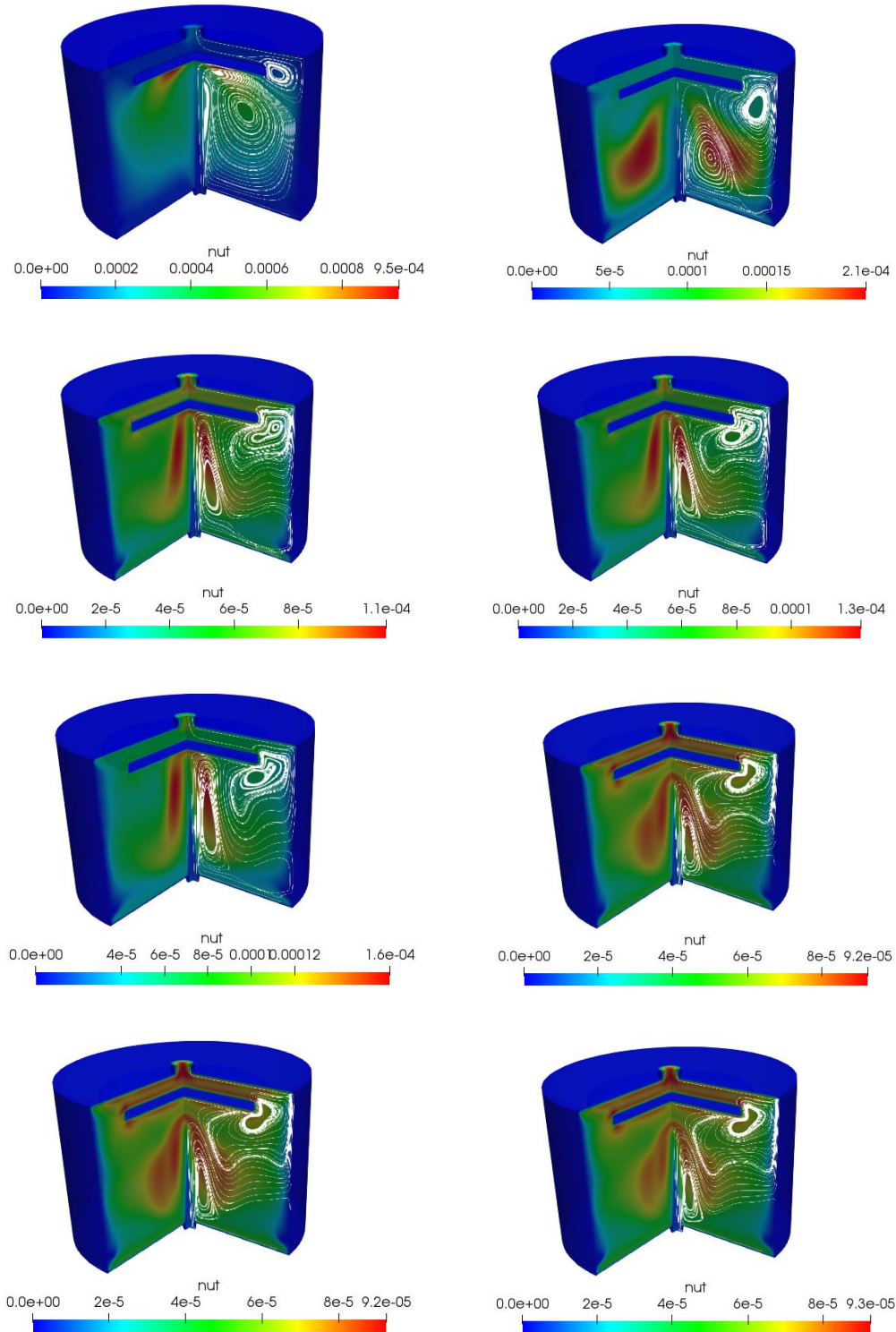




**Fig. 4.19 - Temperature  $T$  and streamline profiles over the 3D test component at time  $t = 0, 4, 20, 80, 180, 580, 1780$  and  $2780$ s by using two-equation  $\kappa\text{-}\omega$  turbulence model in OpenFOAM.**








**Fig. 4.20 - Turbulent viscosity  $\nu_t$  and streamline profiles over the 3D test component at time  $t = 0, 4, 20, 80, 180, 580, 1780$  and  $2780$ s by using two-equation  $\kappa\text{-}\omega$  turbulence model in OpenFOAM.**




 <b>RICERCA SISTEMA ELETTRICO</b>	<u>Title:</u> Development of BE numerical tools for LFR design and safety analysis (2018)	<u>Distribution</u> <b>PUBLIC</b>	<u>Issue Date</u> 29.01.2019	<u>Pag.</u>
	<u>Project:</u> ADP ENEA-MSE PAR 2017	Ref. ADPFISS-LP2-167	Rev. 0	96 di 163

#### 4.5 List of References

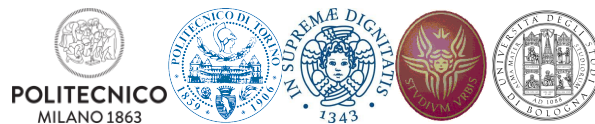
- [4.1] A. Cervone and S. Manservisi, "A three-dimensional cfd program for the simulation of the thermohydraulic behavior of an open core liquid metal reactor," Tech. Rep. lin-thrg 108, 2008.
- [4.2] S. Bnà, S. Manservisi, and O. L. Bot, "Simulation of the thermal-hydraulic behavior of liquid metal reactors using a three-dimensional finite element model," tech. rep., 2010.
- [4.3] G. Bornia, M. Finelli, S. Manservisi, V. Mikhin, M. Polidori, and K. Voukelatou, "Development and validation of femlcore code for the thermal hydraulics of open cores," tech. rep., 2011.
- [4.4] G. Bornia, D. Cerroni, S. Manservisi, M. Polidori, and F. Donato, "Femlcore code: parallelization, turbulence models and code integration," tech. rep., 2012.
- [4.5] D. Cerroni, S. Manservisi, and E. Vincenzi, "Developing multiscale transient simulations with femlcore code," tech. rep., 2013.
- [4.6] D. Cerroni, R. D. Vià, S. Manservisi, F. Menghini, and G. Pozzetti, "Integration of the femlcore code in the salome platform," tech. rep., 2014.
- [4.7] A. Attavino, D. Cerroni, A. Cervone, L. Fancellu, and S. Manservisi, "Femlcore-cathare coupling on salome platform," Tech. Rep. RL 1361/CERSE-UNIBO, 2015.
- [4.8] R. Da Vià, D. Cerroni, A. Cervone, and S. Manservisi, "Validation of the femlcore-cathare coupling model of the tall-3d facility," Tech. Rep. RL 1362/CERSE-UNIBO, 2016.
- [4.9] A. Cervone, A. Chierici, L. Chirco, R. D. Vià, V. Giovacchini, F. Franceschini, and S. Manservisi, "Development and validation of codes for the coupling of the openfoamsalome-femlcore-cathare software for the study of 4th generation lead-cooled fast reactors. validation of the coupling with data experiments from the tall-3d facility. reactor," Tech. Rep. Unibo-Cirten 3100, 2017.
- [4.10] D. Grishchenko, M. Jeltsov, K. Koop, A. Karbojian, W. Villanueva, and P. Kudinov, "The tall-3d facility design and commissioning tests for validation of coupled sth and cfd codes," Nuclear Engineering and Design, vol. 290, pp. 144–153, 2015.
- [4.11] P. KUDINOV, D. Grishchenko, I. Mickus, K. K. Koop, and M. Jeltsov, "Tall-3d setup for first series," Tech. Rep. WP4,D4.5,KTH, 2016.
- [4.12] M. Jeltsov, K. Koop, D. Grishchenko, A. Karbojian, W. Villanueva, and P. Kudinov, "Development of tall-3d facility design for validation of coupled sth and cfd codes," vol. Proceedings of The 9th International Topical Meeting on Nuclear Thermal-Hydraulics, Operation and Safety (NUTHOS-9), 2012.
- [4.13] D. Grishchenko, M. Jeltsov, K. Koop, A. Karbojian, W. Villanueva, and P. Kudinov, "Design and commissioning tests of the tall-3d experimental facility for validation of coupled sth and cfd codes," vol. THINS 2014 International Workshop, 2014. 25
- [4.14] D. Bestion, "The physical closure laws in the cathare code," Nuclear Engineering and Design, vol. 124, pp. 229–245, 1990.
- [4.15] F. Barre and M. Bernard, "The cathare code strategy and assessment," Nuclear Engineering and Design, vol. 124, pp. 257–284, 1990.
- [4.16] M. Robert, M. Farvacque, M. Parent, and B. Faydide, "Cathare 2 v2.5: a fully validated cathare version for various applications," tech. rep., 2003.
- [4.17] G. Geffraye, O. Antoni, M. Farvacque, D. Kadri, G. Lavialle, B. Rameau, and A. Ruby, "Cathare 2 v2.5\_2: a single version for various applications," Nuclear Engineering and Design, vol. 241, pp. 4456–4463, 2011.




 <b>RICERCA SISTEMA ELETTRICO</b>	<u>Title:</u> Development of BE numerical tools for LFR design and safety analysis (2018)	<u>Distribution</u> <b>PUBLIC</b>	<u>Issue Date</u> 29.01.2019	<u>Pag.</u>
	<u>Project:</u> ADP ENEA-MSE PAR 2017	Ref. ADPFISS-LP2-167	Rev. 0	97 di 163

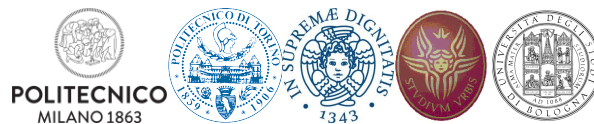
[4.18] T. O. Foundation, “Openfoam, user guide, version 6,” Tech. Rep. 1, 2018.


[4.19] F. Moukalled, L. Mangani, and M. Darwish, The Finite Volume Method in Computational Fluid Dynamics An Advanced Introduction with OpenFOAM and Matlab. Springer, 2016.



 <b>RICERCA SISTEMA ELETTRICO</b>	<u>Title:</u> Development of BE numerical tools for LFR design and safety analysis (2018)	<u>Distribution</u> <b>PUBLIC</b>	<u>Issue Date</u> 29.01.2019	<u>Pag.</u>
	<u>Project:</u> ADP ENEA-MSE PAR 2017	Ref. ADPFISS-LP2-167	Rev. 0	98 di 163

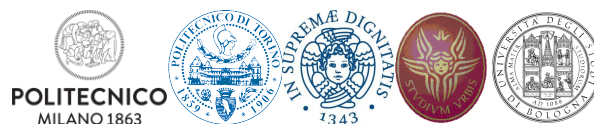
*(Page intentionally left blank)*




 <b>RICERCA SISTEMA ELETTRICO</b>	<u>Title:</u> Development of BE numerical tools for LFR design and safety analysis (2018)	<u>Distribution</u> <b>PUBLIC</b>	<u>Issue Date</u> 29.01.2019	<u>Pag.</u>
	<u>Project:</u> ADP ENEA-MSE PAR 2017	Ref. ADPFISS-LP2-167	Rev. 0	99 di 163

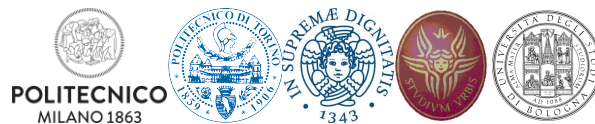
## 5 THREE-DIMENSIONAL NEUTRONIC-THERMAL-HYDRAULIC DYNAMICS MODELLING: SERPENT-OPENFOAM-FRENETIC COMPARISON AND APPLICATION TO ALFRED DESIGN


*N. Abrate, R. Bonifetto, S. Dulla, E. Guadagni, G. F. Nallo, P. Ravetto,  
L. Savoldi, D. Valerio, R. Zanino*



 <b>RICERCA SISTEMA ELETTRICO</b>	<u>Title:</u> Development of BE numerical tools for LFR design and safety analysis (2018)	<u>Distribution</u> <b>PUBLIC</b>	<u>Issue Date</u> 29.01.2019	<u>Pag.</u>
	<u>Project:</u> ADP ENEA-MSE PAR 2017	Ref. ADPFISS-LP2-167	Rev. 0	100 di 163

*(Page intentionally left blank)*



 <b>RICERCA SISTEMA ELETTRICO</b>	<u>Title:</u> Development of BE numerical tools for LFR design and safety analysis (2018)	<u>Distribution</u> <b>PUBLIC</b>	<u>Issue Date</u> 29.01.2019	<u>Pag.</u>
	<u>Project:</u> ADP ENEA-MSE PAR 2017	Ref. ADPFISS-LP2-167	Rev. 0	101 di 163

## 5.1 Introduction

The activities carried out by Politecnico di Torino (Polito) in the field of multiphysics modelling for lead-cooled fast reactors in the program PAR2017 [5.1] have led to two main outcomes related to the ALFRED design modelling:

- The code FRENETIC [5.2] has been benchmarked against a reference constituted by a full-core Serpent calculation coupled to a CFD model of a fuel assembly implemented in OpenFoam [5.3];
- On the basis of the good agreement obtained, an updated version of the ALFRED model has been implemented in FRENETIC, with excellent consistency with the Serpent-OpenFoam reference for what regards the steady-state configuration of the reactor.

The ALFRED design in FRENETIC is characterized by a 6-group energy model for the neutron balance equations (see Fig. 5.1), and the main heterogeneities of the core and surrounding materials have been properly accounted for (see the FRENETIC radial view in Fig. 5.2 as compared to the Serpent model in Fig. 5.3). The resulting multiplication eigenvalue resulted being  $k_{eff}=1.08194$ , in very good agreement (around 70 pcm difference) with the  $1.08122\pm 3\text{pcm}$  evaluated by Serpent.

## 5.2 ALFRED steady-state critical configuration in FRENETIC

On the basis of the excellent results of the activity performed in the frame of PAR 2017, it has been decided to proceed with the utilization of the code FRENETIC to perform some simulations allowing to characterize the multi-physics behavior of the ALFRED core and address some safety-relevant transient cases.

The first aspect to be addressed regards the actual steady-state condition that a multi-physics code adopts as initial condition for a transient calculation and how such steady-state is achieved.


As can be seen from the previous results, the multi-physics simulation of the ALFRED core (with all safety rods withdrawn) has led to a multiplication constant above criticality of around 8000 pcm. Such result is consistent with design requirements regarding excess reactivity, and such excellent reactivity is in the real system compensated by the movement of the control and safety rods to achieve, and maintain, a critical condition during operation.

When such situation is to be simulated with a multi-physics code, the common practice is to “force” the system to be critical at the beginning of the time-dependent simulation by dividing the multiplication terms in the neutron balance equations by this “initial”  $k_{eff}$ . It is however true that, if such value is far from unity, the resulting “critical” state may be characterized by different physical conditions, in terms of spatial and spectral neutron distribution, with influence on the following transient simulation.

For the above reasons, and in order to be more representative of the ALFRED core configuration when in operation, the previous set-up has been modified by changing the position of the control rods, in order to start from a configuration closer to criticality. This operation has led to the core configuration as in Fig. 7.4, to be compared to the previous setup (as in the PAR 2017 report) given in Fig. 5.5.

In this new configuration the control rods are inserted with a  $\Delta_z = 29\text{ cm}$  and the related FRENETIC mesh has been modified, requiring a new spatial homogenization procedure. Following this modification, the steady state calculation with FRENETIC gives  $k_{eff} = 1.01294$ , and the power distribution within the core has been modified as illustrated in Fig. 5.6.



 <b>RICERCA SISTEMA ELETTRICO</b>	<u>Title:</u> Development of BE numerical tools for LFR design and safety analysis (2018)	<u>Distribution</u> <b>PUBLIC</b>	<u>Issue Date</u> 29.01.2019	<u>Pag.</u>
	<u>Project:</u> ADP ENEA-MSE PAR 2017	Ref. ADPFISS-LP2-167	Rev. 0	102 di 163

Starting from this configuration, some time-dependent simulations have been carried out, as detailed in the following sections.

### 5.3 ALFRED time-dependent neutronic simulation: safety rod insertion

The Initiating Event here modelled is the insertion in the core of one of the safety rods, with a total insertion time of 9 seconds, leading to the fast shutdown of the reactor (see Fig. 5.7). This first analysis is carried out neglecting the thermal-hydraulic feedbacks, therefore running the FRENETIC code in NE stand-alone mode; this approach allows to appreciate the pure neutronic reactivity effects associated to the safety rods.

The results presented in Fig. 5.8 show how the insertion of the safety rod leads to a fast decrease of the power generation. The evident change of slope in reactivity around at 5 seconds is due to a faster insertion of the SR in the time interval [5,9] seconds. Since the rod is in a region with a high neutron importance, the effects are significant. Indeed, the power generation reach approximately zero in almost 50 seconds. However, it must be noted that if the thermal-hydraulic feedbacks were present, the negative insertion of reactivity would be damped. In conclusion, this case can be considered as an estimation on the reactivity worth of one safety rod insertion. Another aspect to be highlighted is the fact that this transient implies a significant distortion of the radial neutron flux distribution, and therefore of the radial power map (see Fig. 5.9). This particular kind of transient is not suitable for simulation by means of point kinetics approach.

### 5.4 ALFRED time-dependent coupled NE-TH simulations: LOFA

The following cases have been simulated exploiting the Multiphysics capabilities of FRENETIC; thus running the code in coupled NE-TH mode. In this first transient a LOFA accident is simulated: the mass flow rate of all coolant pumps is reduced following the exponential behavior reported in Fig. 5.10. A similar transient has been simulated with FRENETIC in the frame of a IAEA CRP focused on the EBR-II reactor, proving that this kind of transient can be suitably modeled by adopting a point-kinetic approach [5.4].

The assumed reduction of the flow rate neglects natural circulation effects, the quantification of which would require the presence of an external module for the primary circuit of the reactor. Therefore, the present results constitute a conservative estimate of the system evolution in the logic of safety.

In Fig. 5.11 the behavior of the reactivity and generated power during this transient is shown. As expected, feedback effects associated to the increase of the fuel temperature lead to a significant reduction of the generated power.


Fig. 5.12 shows instead the evolution of the maximum fuel and coolant temperature within the central FA. As expected, the decreased flow rate leads to an increase of the coolant temperature, which is in competition with the reduction of the generated power within the FA.

### 5.5 ALFRED time-dependent coupled NE-TH simulations: reactivity insertion

One of the most challenging transients for a full-core multiphysics code is the reactivity insertion arising from an accidental removal of one or more control rods (CRs). This can be interpreted as a particular kind of Unprotected Transient of Over Power, UTOP. If only a subset of the CRs is removed from the core, the shape of the neutron flux is significantly distorted, therefore this transient cannot be reliably simulated by means of a point kinetics approach, Fig. 5.13. Moreover, feedback effects play a major role in compensating the reactivity insertion, therefore a purely NE simulation would not be sufficient for simulating the actual reactor behavior. shows the first second of simulation (where four CRs are withdrawn in a total time of 2s). This partial result is due to the fact that this simulation currently takes prohibitively long time, as the adaptive timestep selection for the quasistatic method [5.6] cannot unleash its potential within the framework





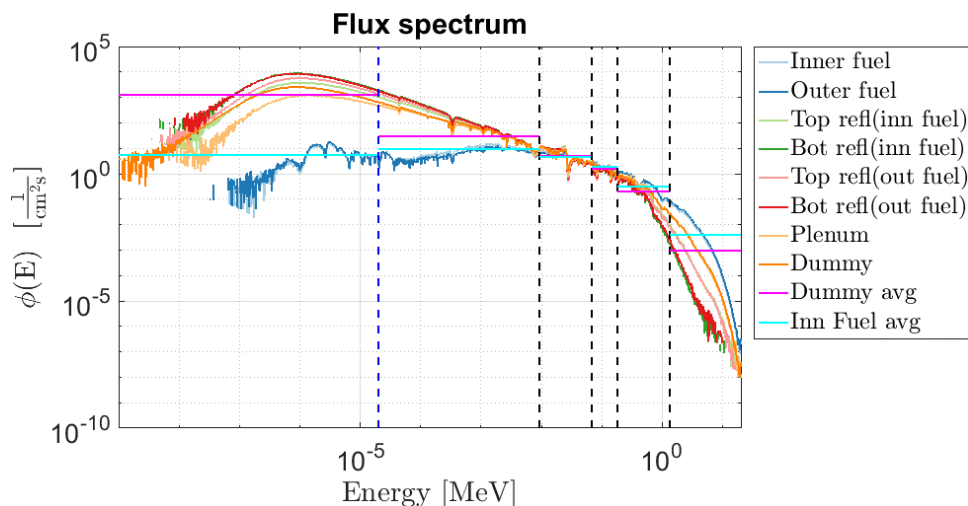
 <b>RICERCA SISTEMA ELETTRICO</b>	<u>Title:</u> Development of BE numerical tools for LFR design and safety analysis (2018)	<u>Distribution</u> <b>PUBLIC</b>	<u>Issue Date</u> 29.01.2019	<u>Pag.</u>
	<u>Project:</u> ADP ENEA-MSE PAR 2017	Ref. ADPFISS-LP2-167	Rev. 0	103 di 163

of the currently implemented coupling strategy. We are working towards a solution for the problem, for the purpose of simulating in a FRENETIC fashion also this kind of transient.

## 5.6 Conclusive remarks


The activities carried out at PoliTO in the framework of PAR 2018 have been focused on the application of the FRENETIC code to the time-dependent simulation of the ALFRED core, starting from the successful results of the benchmark activity carried out in PAR2017.

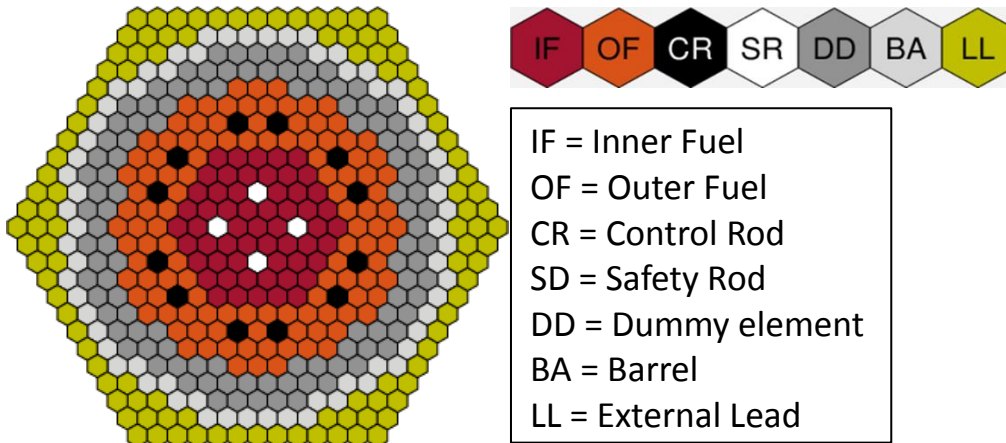
The core model has been furtherly improved to correctly represent the critical, equilibrium condition of the system, and different perturbations have been introduced to study the most significant physical phenomena of this design. The simulations performed also allowed to identify some limitation in the applicability of FRENETIC for what regards the computational efficiency, related to some optimization aspects of the NE module currently not exploited totally in the coupled simulation mode. This observation is now leading the current research work, to improve the computational performances of FRENETIC.



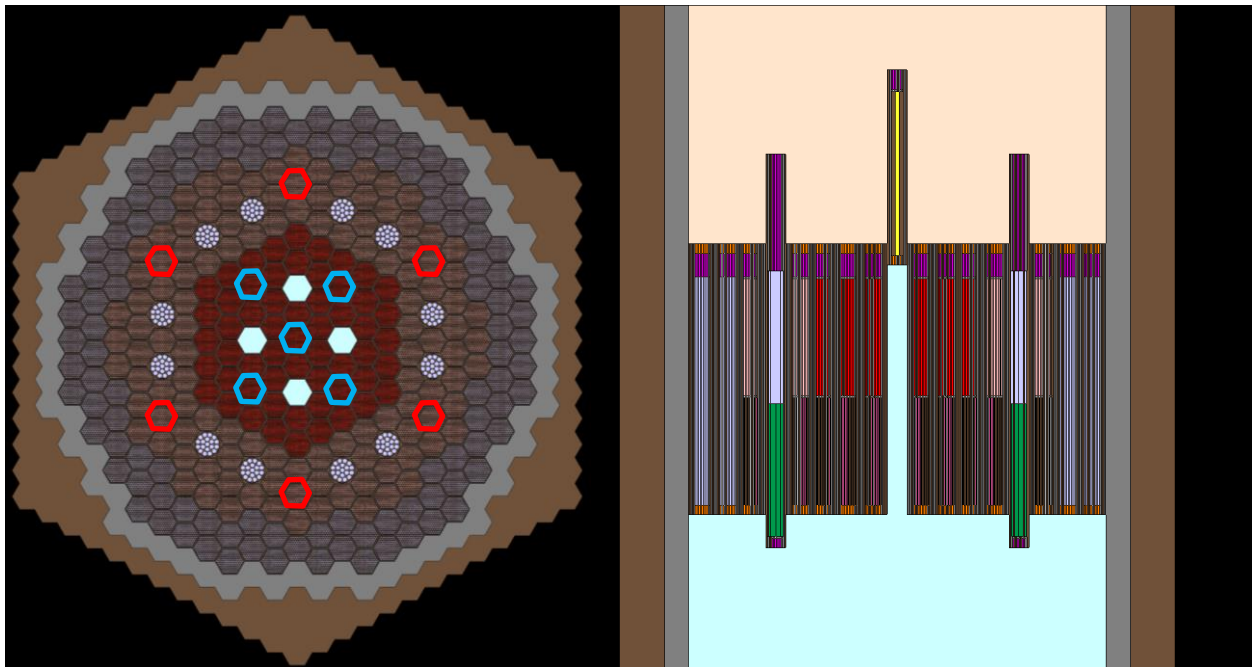
**Fig. 5.1 – Neutron flux spectra computed by Serpent for selected regions of the core. Black dashed lines identify the 5-group energy subdivision originally adopted, while the blue dashed line identifies the additional group added to better account for the reflector spectrum.**



 <b>RICERCA SISTEMA ELETTRICO</b>	<u>Title:</u> Development of BE numerical tools for LFR design and safety analysis (2018)	<u>Distribution</u> <b>PUBLIC</b>	<u>Issue Date</u> 29.01.2019	<u>Pag.</u> 
	<u>Project:</u> ADP ENEA-MSE PAR 2017	Ref. ADPFISS-LP2-167	Rev. 0	104 di 163



*Fig. 5.2 – Radial scheme of the FRENETIC model of the ALFRED core.*



*Fig. 5.3 Radial (left) and axial (right) view of the ALFRED configuration simulated in Serpent.*



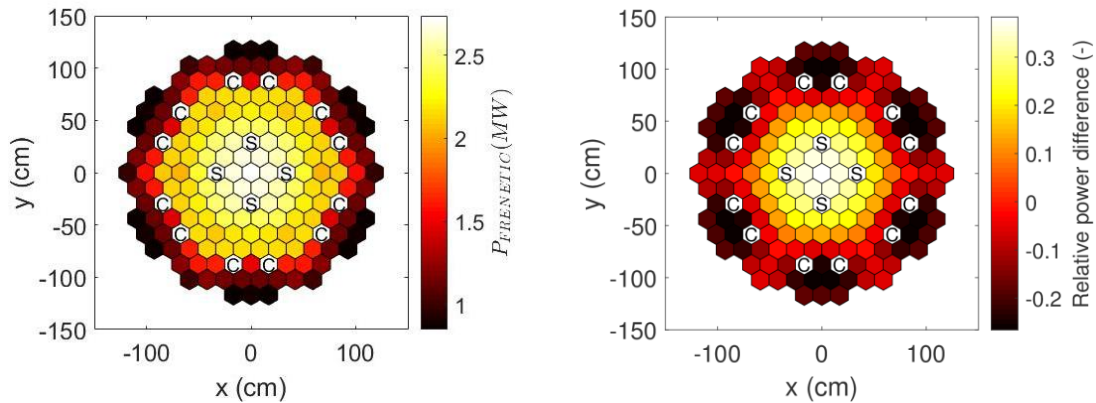


Fig. 5.4: core configuration with rod position adjusted to reach a condition closer to criticality.

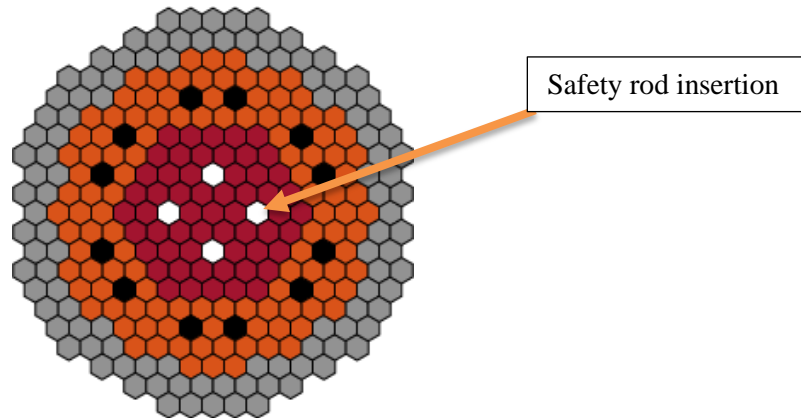


Fig. 5.5: ALFRED core configuration as in the benchmark calculations against Serpent/OpenFoam [5.1].

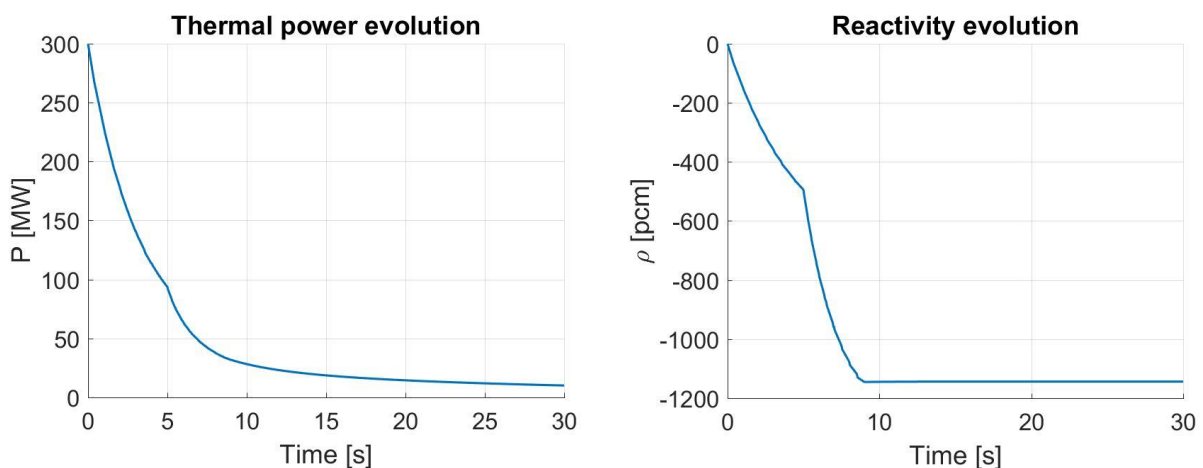




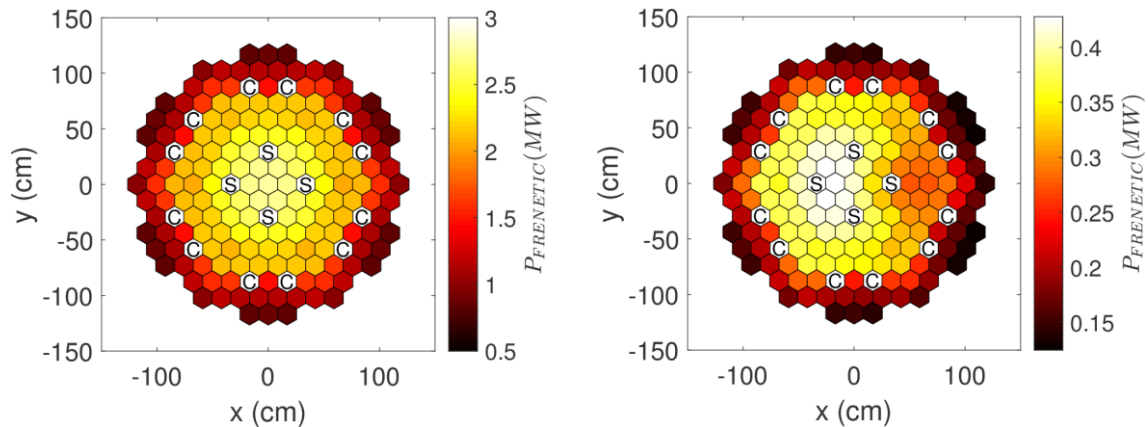
**Fig. 5.6:** Core power distribution with rods insertion adjusted to reach a condition closer to criticality (left) and relative difference with respect to the previous case.



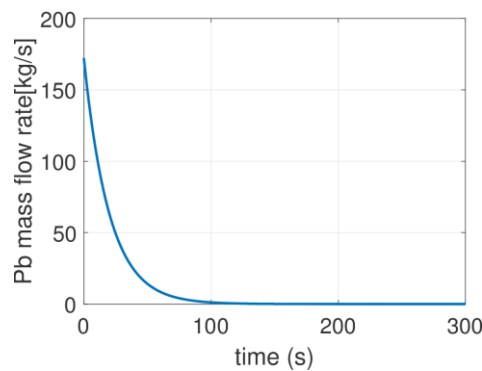
**Fig. 5.7:** Identification of the position of the safety rod inserted in the pure NE transient.



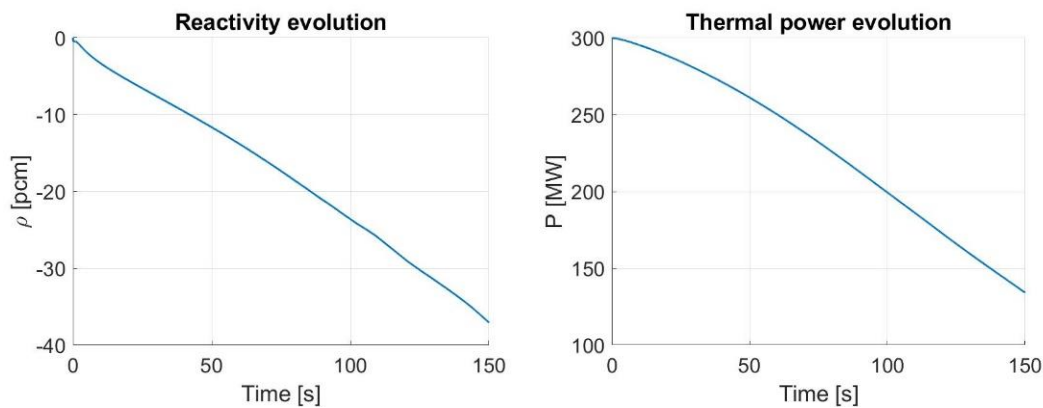
**Fig. 5.8:** Thermal power and reactivity evolution in the safety rod insertion NE transient.




**Fig. 5.9: Safety rod insertion transient: radial power map (in MW per FA) at  $t=0s$  (left) and  $t=7s$  (right). Different scales are adopted to highlight the differences and the spatial distortion around the safety rod location.**

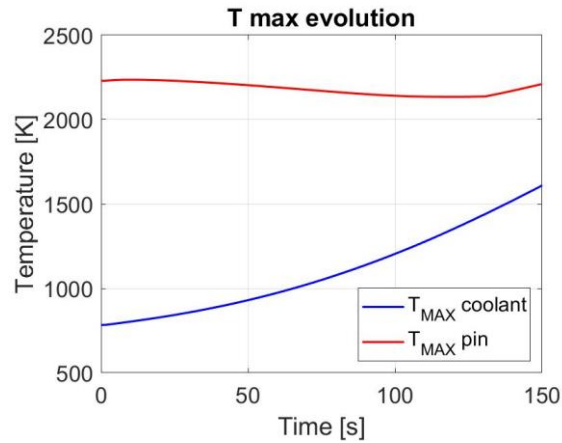


**Fig. 5.10: Mass flow rate reduction adopted in the LOFA simulation.**

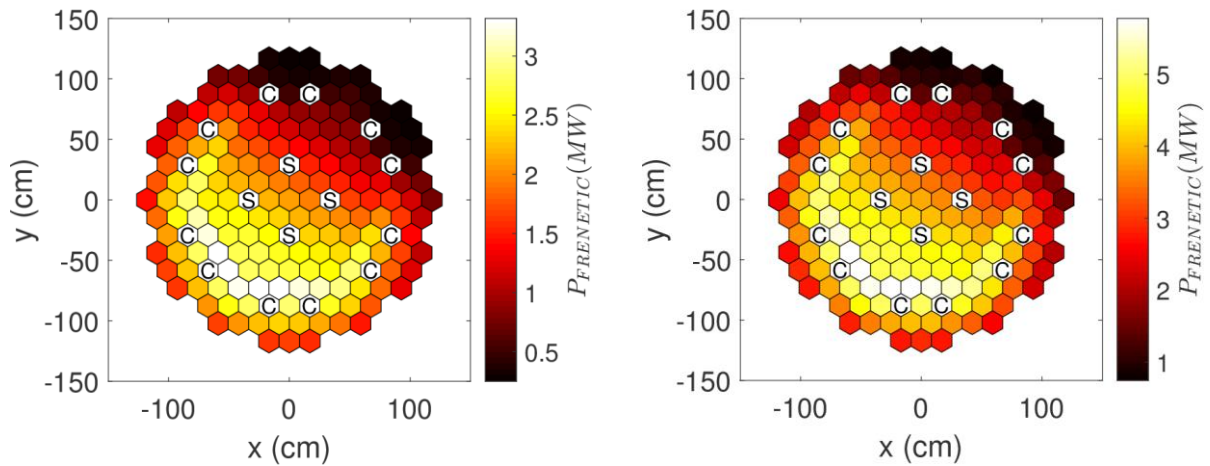


**Fig. 5.11: Reactivity and thermal power evolution during the LOFA.**

 <b>RICERCA SISTEMA ELETTRICO</b>	<u>Title:</u> Development of BE numerical tools for LFR design and safety analysis (2018)	<u>Distribution</u> <b>PUBLIC</b>	<u>Issue Date</u> 29.01.2019	<u>Pag.</u>
	<u>Project:</u> ADP ENEA-MSE PAR 2017	Ref. ADPFISS-LP2-167	Rev. 0	108 di 163




*Fig. 5.12: Evolution of the maximum temperature for both the coolant and the fuel in the central fuel assembly during the LOFA.*



*Fig. 5.13: Radial power map (in MW per FA) at  $t=0s$  (left) and  $t=1s$  (right) during the control rod extraction transient.*




 <b>RICERCA SISTEMA ELETTRICO</b>	<u>Title:</u> Development of BE numerical tools for LFR design and safety analysis (2018)	<u>Distribution</u> <b>PUBLIC</b>	<u>Issue Date</u> 29.01.2019	<u>Pag.</u>
	<u>Project:</u> ADP ENEA-MSE PAR 2017	Ref. ADPFISS-LP2-167	Rev. 0	109 di 163

## List of References

- [5.1] *Development of best estimate numerical tools for LFR design and safety analysis*, PAR 2017 Report, November 2018.
- [5.2] R. Bonifetto, S. Dulla, P. Ravetto, L. Savoldi, R. Zanino, *A full-core coupled neutronic/thermal-hydraulic code for the modeling of lead-cooled nuclear fast reactors*, Nuclear Engineering and Design, 261, 85-94, 2013. DOI: 10.1016/j.nucengdes.2013.03.030.
- [5.3] E. Guadagni, R. Bonifetto, A. Cammi, S. Dulla, S. Lorenzi, G. F. Nallo, L. Savoldi, P. Ravetto, R. Zanino, *Numerical benchmark of the FRENETIC multiphysics code*, presented at ICONE conference, London, UK, Jul. 22-26, 2018.
- [5.4] D. Caron, R. Bonifetto, S. Dulla, V. Mascolino, P. Ravetto, L. Savoldi, D. Valerio, R. Zanino, *Full-core coupled neutronic/thermal-hydraulic modelling of the EBR-II SHRT-45R transient*, International Journal of Energy Research, 42(1), 2018. DOI: 10.1002/er.3571.
- [5.5] R. Zanino, R. Bonifetto, L. Savoldi Richard, A. Del Nevo, *Benchmark and preliminary validation of the thermal-hydraulic module of the FRENETC code against EBR-II data*, proceedings of ATH 2014, Reno, Nevada, June 15-19, 2014.
- [5.6] D. Caron, S. Dulla, P. Ravetto, *Adaptive time step selection in the quasi-static methods of nuclear reactor dynamics*, Annals of Nuclear Energy, 105, 266-281, 2017.




 <b>RICERCA SISTEMA ELETTRICO</b>	<u>Title:</u> Development of BE numerical tools for LFR design and safety analysis (2018)	<u>Distribution</u> <b>PUBLIC</b>	<u>Issue Date</u> 29.01.2019	<u>Pag.</u>
	<u>Project:</u> ADP ENEA-MSE PAR 2017	Ref. ADPFISS-LP2-167	Rev. 0	110 di 163

*(Page intentionally left blank)*





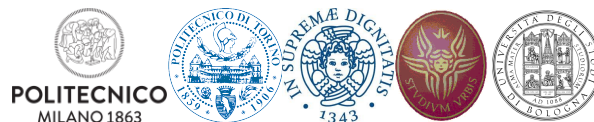
 <b>RICERCA SISTEMA ELETTRICO</b>	<u>Title:</u> Development of BE numerical tools for LFR design and safety analysis (2018)	<u>Distribution</u> <b>PUBLIC</b>	<u>Issue Date</u> 29.01.2019	<u>Pag.</u>
	<u>Project:</u> ADP ENEA-MSE PAR 2017	Ref. ADPFISS-LP2-167	Rev. 0	111 di 163


## 6 MONTE CARLO – CFD COUPLING FOR LFR MULTIPHYSICS MODELLING

*A. Cammi, S. Lorenzi, C. Castagna*

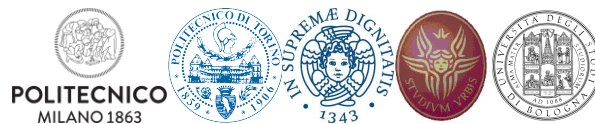



**POLITECNICO**  
MILANO 1863



 <b>RICERCA SISTEMA ELETTRICO</b>	<u>Title:</u> Development of BE numerical tools for LFR design and safety analysis (2018)	<u>Distribution</u> <b>PUBLIC</b>	<u>Issue Date</u> 29.01.2019	<u>Pag.</u>
	<u>Project:</u> ADP ENEA-MSE PAR 2017	Ref. ADPFISS-LP2-167	Rev. 0	112 di 163

*(Page intentionally left blank)*



 <b>RICERCA SISTEMA ELETTRICO</b>	<u>Title:</u> Development of BE numerical tools for LFR design and safety analysis (2018)	<u>Distribution</u> <b>PUBLIC</b>	<u>Issue Date</u> 29.01.2019	<u>Pag.</u>
	<u>Project:</u> ADP ENEA-MSE PAR 2017	Ref. ADPFISS-LP2-167	Rev. 0	113 di 163

## 6.1 Background and references

The activity is related to the improvement of a multi-physics modelling of Lead-cooled Fast Reactor (LFR). The multi-physics approach allows evaluating a wide set of core parameters (e.g., temperature field, velocity field, and neutron fluxes) [6.1]-[6.3]. This advantage may be valuable for core designing, when verifying the satisfaction of the operational constraints.

In particular, we present a Monte Carlo - CFD coupling aimed at improving the present LFR multiphysics modelling. This way, the neutronics code (SERPENT) is provided with more realistic temperature profiles leading to an improvement in reactivity and power outcomes. On the other hand, the thermal-hydraulics code (OpenFOAM) is provided with more realistic volumetric fission power distribution which leads to an improvement in temperature profile estimation.

Along with the design support, this activity is also aimed at providing assistance to the code verification of the FRENETIC code, in collaboration with Politecnico di Torino.


### 6.1.1 Monte Carlo - CFD coupling

The LFR technology's severe design limits, along with a relatively low operational experience on heavy liquid metal cooled reactors, require dedicated tools of analysis to study the steady state and the transient behaviour of these GIF-IV systems. The multiphysics interaction between neutronics and thermal hydraulics can be studied with several approaches that are tailored on specific needs from the view point of accuracy and computational time. Diffusion method, deterministic and Monte Carlo approaches are the main options for the neutronics modelling. Subchannel analysis codes and Computational Fluid Dynamics (CFD) codes are the possible options as for the thermal-hydraulics modelling.

Even if coupling with simplified neutronics and thermal-hydraulics approach have been already investigated, only recently, thanks to the increased availability of computational power, the scientific community started to study the multiphysics interaction between neutronics and thermal-hydraulics with high-fidelity modelling options [6.4]-[6.6]. This is the case of the Monte Carlo – CFD coupling which is investigated in this activity. Monte Carlo approach allows accurate results and a flexible implementation, especially with respect to legacy codes in the study of Generation-IV reactors. On the other hand, besides the strong computational burden, coupling neutronics/thermal-hydraulics techniques can present instability behavior [6.8], especially when stochastic neutron transport approaches are employed due to the impossibility to adopt the common techniques used for the solution of non-linear problems (see Fig. 6.1).

The tools used for the coupling are OpenFOAM and Serpent. OpenFOAM is an open source library for numerical simulation in continuum mechanics using Finite Volume Method. The toolkit is very flexible thanks to the object-oriented programming, allowing users to customize, extend and implement complex physical model [6.9],[6.10]. OpenFOAM grants the parallelization of the developed solvers thanks to dedicated routines based on geometrical domain decomposition. Serpent is a three dimensional continuous energy Monte Carlo (MC) neutron transport code, developed by the VTT Technical Research Centre in Finland [6.11]. Its application is focused on lattice physics application ranging from the generation of homogenized few-group constants for reactor simulation code to fuel cycle analysis. The choice of these two codes is motivated by the strong compatibility of OpenFOAM with Serpent. The output of the finite volume being the "average" values of the fields in the cells of the domain, it is very suitable for passing temperatures and density fields to a Monte Carlo code for neutron transport. Moreover, Serpent was developed with a direct interface with OpenFOAM, that can be employed during transport and burnup calculations. This strong compatibility was the ultimate reason to choose this software and methods combination.



 <b>RICERCA SISTEMA ELETTRICO</b>	<u>Title:</u> Development of BE numerical tools for LFR design and safety analysis (2018)	<u>Distribution</u> <b>PUBLIC</b>	<u>Issue Date</u> 29.01.2019	<u>Pag.</u>
	<u>Project:</u> ADP ENEA-MSE PAR 2017	Ref. ADPFISS-LP2-167	Rev. 0	114 di 163

## 6.2 Body of the report concerning the ongoing activities

The activity focuses on the development of a Monte Carlo – CFD coupling for the ALFRED reactor. In the first section of this paragraph, the two techniques considered for the coupling are presented. In the second and third section, we briefly present the model adopted for the neutronics (full core SERPENT of ALFRED) and for the thermal-hydraulics (FA model of ALFRED with OpenFOAM). In the fourth section, the results of the coupling for a one-sixth FA are presented.

### 6.2.1 Monte Carlo – CFD coupling techniques

Neutron transport is strongly influenced by temperature and density distributions in all materials. This influence lies in the macroscopic cross sections:

$$\Sigma_{reactivity} = N(T) \cdot \sigma_{reactivity}(T) \quad (6.1)$$

This dependency of the neutronics on thermal hydraulic variables can be written in symbolic form as:

$$\phi = \mathcal{N}(\Theta) \quad (6.2)$$

$$q = \mathcal{N}(\Theta) \quad (6.3)$$

This dependency of temperature on the volumetric power distribution can be written in symbolic form as:

$$\Theta = \mathcal{T}(q) \quad (6.4)$$

where the operator  $\mathcal{T}$  associates the solution of the thermal hydraulic problem to the input volumetric power distribution  $q$ .

Having explored all the main feedbacks, a symbolic representation of the coupled system can be built. Starting from the neutron transport problem in equation 2.3 and substituting equation 2.4, follows:

$$q = \mathcal{N}(\mathcal{T}(q)) \quad (6.5)$$


This means that the neutron flux distribution that solves the coupled problem is the fixed point of the coupled system. Most coupled calculations, currently, use a fixed-point iteration algorithm. The stability of such algorithm is case dependent and is left to the user to determine an appropriate under-relaxation factor for each individual case—the exception is an adaptive method based on stochastic approximation [6.12] which is stable for every coupled case and is optimized in terms of calculation time if the thermal hydraulics is solved in a simple and computationally inexpensive way. Pounders [6.13] suggests to use a simple estimate of the spectral radius of a fixed-point iteration in order to estimate a near-optimal under-relaxation factor for coupled neutronic and thermal-hydraulic calculations.

### The fixed-point coupling method

Since the neutron flux distribution that solves the coupled problem is the fixed point of the coupled problem, the fixed-point method can be used to solve it. The fixed-point method is a computational method used to solve the generic problem

$$\mathbf{x} = \mathbf{G}(\mathbf{x}) \quad (6.6)$$



 <b>RICERCA SISTEMA ELETTRICO</b>	<u>Title:</u> Development of BE numerical tools for LFR design and safety analysis (2018)	<u>Distribution</u> <b>PUBLIC</b>	<u>Issue Date</u> 29.01.2019	<u>Pag.</u>
	<u>Project:</u> ADP ENEA-MSE PAR 2017	Ref. ADPFISS-LP2-167	Rev. 0	115 di 163

and consists in iterating the following:

$$\mathbf{x}_{n+1} = \mathbf{G}(\mathbf{x}_n) \quad (6.7)$$

starting from a chosen starting condition  $\mathbf{x}_0$ . The fixed-point method is a general numerical method and can be applied to any problem in which the solution is the fixed point of a certain function. The stability of this algorithm entirely depends on the Jacobian matrix associated to the fixed-point problem

$$J_{i,j} = \frac{\partial G_i}{\partial x_j} \quad (6.8)$$

and it can be shown that this algorithm is stable if [6.13]

$$\varrho(J) < 1 \quad (6.9)$$

where  $\varrho(J)$  is the spectral radius of the jacobian matrix associated to the fixed-point problem, i.e.,

$$\varrho(J) = \max\{|\lambda_1|, \dots, |\lambda_N|\} \quad (6.10)$$

and  $\lambda_k$  are the eigenvalues of the Jacobian matrix. The fixed-point method is therefore conditionally stable, and in cases in which the method is unstable the problem can be solved by introducing an under-relaxation step, i.e. by substituting the already defined iteration with the following:

$$\mathbf{x}_{n+1} = \alpha \mathbf{G}(\mathbf{x}_n) + (1 - \alpha) \mathbf{x}_n \quad 0 \leq \alpha \leq 1 \quad (6.11)$$

The  $\alpha$  parameter is called under-relaxation factor and the effect of the underrelaxation is dampening the variation of the unknown  $x$  in the iteration. The new iteration can be written as:

$$\mathbf{x}_{n+1} = \mathbf{G}_\alpha(\mathbf{x}_n), \quad \mathbf{G}_\alpha(\mathbf{x}) = \alpha \mathbf{G}(\mathbf{x}) + (1 - \alpha) \mathbf{I} \mathbf{x} \quad 0 \leq \alpha \leq 1 \quad (6.12)$$

The stability of the under-relaxed fixed-point method depends on the eigenvalues of the new Jacobian matrix


$$J_{i,j} = \alpha \frac{\partial G_i}{\partial x_j} + (1 - \alpha) \delta_{i,j} \quad (6.13)$$

which depend in turn on the under-relaxation factor. It can be proved that not all under-relaxation factors are suitable for the stabilization of the method for a considered case but each case has its maximum under-relaxation factor that stabilizes the problem. An under-relaxation factor equal to 1 obviously corresponds to a standard non-relaxed fixed-point method. The under-relaxation factor can be a constant set by the user or it can change from one iteration to the next, like in the *stochastic approximation* algorithm, described in the next section.

In the specific case of the coupling between neutronics and thermal hydraulics, the fixed-point method was implemented in the following loop:

1. Start from chosen temperature and density fields  $T_0, \rho_0$
2. Solve the neutron transport problem  $\tilde{q}_{n+1} = \mathcal{N}(T_n, \rho_n)$



 <b>RICERCA SISTEMA ELETTRICO</b>	<u>Title:</u> Development of BE numerical tools for LFR design and safety analysis (2018)	<u>Distribution</u> <b>PUBLIC</b>	<u>Issue Date</u> 29.01.2019	<u>Pag.</u>
	<u>Project:</u> ADP ENEA-MSE PAR 2017	Ref. ADPFISS-LP2-167	Rev. 0	116 di 163

3. If this is not the first coupled iteration, perform an under-relaxation step  $q_{n+1} = \alpha \tilde{q}_{n+1} + (1 - \alpha)q_n$ ; if this is the first iteration instead take  $q_1 = \tilde{q}_1$
4. Solve the heat transfer problem  $\{T_{n+1}, \rho_{n+1}\} = \mathcal{T}(q_{n+1})$
5. Check the convergence, calculating the relative variation  $\Delta_{n+1}$  of the power distribution

$$\Delta_{n+1} = \frac{\int |q_{n+1} - q_n| dV}{\int |q_n| dV} \quad (6.14)$$

If convergence is reached end loop. Otherwise, loop back to point (2).

This can be more easily visualized with the flow chart in Fig. 6.2.

#### The stochastic approximation algorithm

Numerical stability is a critical aspect of coupled neutronics and thermal hydraulics calculations handled with the fixed-point method, being it conditionally stable. Therefore under-relaxation is necessary in order to ensure the convergence of the volumetric power distribution in unstable cases it but up to this point no a priori information is available on a suitable under-relaxation factor. This means that the user has full responsibility on the stabilization of a coupled case if no other analysis has been previously conducted. A solution to this problem can be found in the stochastic approximation algorithm [6.12].

The stochastic approximation algorithm is a fixed-point coupling method in which the under-relaxation factor and the number of neutron histories are changed at each iteration following an optimization criterion and in particular the underrelaxation factor follows a rule such that any case is effectively stabilized and the simulation time is minimized. This method was conceived in a framework in which the thermal hydraulics are solved with one-dimensional codes for subchannel analysis, which are computationally cheap, and the neutron transport with Monte Carlo codes, which instead have a high computational cost for high precision calculations. Therefore, in order to minimize the calculation time, the number of neutron histories must be minimized.

The optimization is carried on by having the under-relaxation factor equal to the relative computational cost of the iteration

$$\alpha_n = \frac{s_n}{\sum_{i=1}^n s_i} \quad (6.15)$$

where  $s_n$  is the number of neutron histories at iteration n, and proportional to the statistical error involved in Monte Carlo calculations


$$\epsilon \sim \frac{1}{\sqrt{s}} \quad (6.16)$$

This second requirement gives

$$\alpha_n \propto \frac{1}{\sqrt{\sum_{i=1}^n s_i}} \quad (6.17)$$

and both requirements combined generate two rules that determine at each coupled iteration the number of neutron histories and the under-relaxation factor that have to be used:



 <b>RICERCA SISTEMA ELETTRICO</b>	<u>Title:</u> Development of BE numerical tools for LFR design and safety analysis (2018)	<u>Distribution</u> <b>PUBLIC</b>	<u>Issue Date</u> 29.01.2019	<u>Pag.</u>
	<u>Project:</u> ADP ENEA-MSE PAR 2017	Ref. ADPFISS-LP2-167	Rev. 0	117 di 163

$$\left\{ \begin{array}{l} \alpha_n = \frac{s_n}{\sum_{i=1}^n s_i} \\ s_n = \frac{s_1 + \sqrt{s_1^2 + 4s_1 \sum_{i=1}^n s_i}}{2} \end{array} \right. \quad (6.18)$$

From this rules, it follows that the first iteration has always  $\alpha = 1$  and

$$\lim_{n \rightarrow \infty} \alpha_n = 0 \quad (6.19)$$

The stochastic approximation method was implemented as well in this work and in particular the number of neutron histories was modified at each iteration by changing the number of active cycles in the neutron transport simulation. This implementation can be easily visualized in Fig. 6.3.

In detail, the structure of the algorithm is as follows:

1. Start from chosen temperature and density fields  $T_0, \rho_0$
2. If this is the first coupled iteration, input the number of active cycles for the first iteration  $s_1$  and have  $\alpha_1 = 0$ . Otherwise, calculate the new values of  $s_{n+1}, \alpha_{n+1}$
3. Solve the neutron transport problem  $\tilde{q}_{n+1} = \mathcal{N}(T_n, \rho_n)$
4. If this is not the first coupled iteration, perform an under-relaxation step  $q_{n+1} = \alpha_{n+1} \tilde{q}_{n+1} + (1 - \alpha_{n+1}) q_n$ ; if this is the first iteration instead take  $q_1 = \tilde{q}_1$
5. Solve the heat transfer problem  $\{T_{n+1}, \rho_{n+1}\} = \mathcal{T}(q_{n+1})$
6. Check the convergence, calculating the relative variation  $\Delta_{n+1}$  of the power distribution

$$\Delta_{n+1} = \frac{\int |q_{n+1} - q_n| dV}{\int |q_n| dV} \quad (6.20)$$

If convergence is reached end loop. Otherwise, loop back to point (2).

### 6.2.2 Full core SERPENT model of the ALFRED reactor


A detailed model of ALFRED is set up with a heterogeneous description of the reactor. The SERPENT model represents the 171 FAs, 110 dummy elements, 12 CRs and 4 SRs, the inner vessel and the surrounding lead (Fig. 6.4a). The zones above and below the active zone are also modelled (Fig. 6.4b) in order to take into account the CRs and SRs position as well as the contribution of these zones to the reactivity effect (i.e., in particular for the lead density). For the isotopic composition of the input materials concerning ALFRED (fuel, cladding, coolant, control rods), the reader may refer to [6.14]. Fig. 6.5 illustrates the power peaking factor (ppf) distribution inside one-fourth of reactor core for the first Beginning of Cycle (BOC). The maximum ppf is 1.28, which is related to the most powerful fuel assembly with the power of 2.25MW.

A first verification of this model has been performed comparing some relevant core parameters (see Tab. 6.1) with the results obtained with the deterministic transport code ERANOS and the Monte Carlo code MCNPX during the LEADER project [6.14]. An additional comparison has been also carried out considering the main reactivity feedback (see Tab. 6.2). The results can be considered satisfactory as first verification of the model.

### 6.2.3 CFD model for the FA of ALFRED

The conjugate heat transfer multi region model available in the OpenFOAM has been used for the modelling of the thermal-hydraulics allowing the study of both the fuel and the coolant. The solver



 <b>RICERCA SISTEMA ELETTRICO</b>	<u>Title:</u> Development of BE numerical tools for LFR design and safety analysis (2018)	<u>Distribution</u> <b>PUBLIC</b>	<u>Issue Date</u> 29.01.2019	<u>Pag.</u>
	<u>Project:</u> ADP ENEA-MSE PAR 2017	Ref. ADPFISS-LP2-167	Rev. 0	118 di 163

*chtMultiRegionFoam* implements the mass, momentum and energy equations for the fluid and of the heat diffusion equation for the solid. In this analysis, the solver uses the SIMPLE (Semi-Implicit Method of Pressure-Linked Equations) algorithm for finding the steady-state configuration.

The model of fluid flow is based on Reynolds-Averaged Navier-Stokes (RANS) equations for mass and momentum conservations plus the energy equation.

$$\begin{cases} \rho(\mathbf{u} \cdot \nabla)\mathbf{u} - \nabla \cdot \left[ -p\mathbf{I} + (\mu + \mu_t)(\nabla\mathbf{u} + (\nabla\mathbf{u})^T) - \frac{2}{3}\rho k\mathbf{I} \right] = 0 \\ \nabla \cdot \rho\mathbf{u} = 0 \\ \rho C_p \mathbf{u} \cdot \nabla T - \nabla \cdot \left[ C_p \left( \frac{\mu}{Pr} + \frac{\mu_t}{Pr_t} \right) \nabla T \right] = 0 \end{cases} \quad (6.21)$$

Due to the high Reynolds number characterizing the flow in the ALFRED reactor, a turbulence model is applied in the RANS framework. In particular, k- $\varepsilon$  model is used as a turbulence model [6.15] where k is the turbulence kinetic energy and  $\varepsilon$  is the turbulence dissipation rate calculated based on the following equations.

$$\begin{cases} \nabla \cdot (\rho\mathbf{u}k) - \nabla \cdot (\rho D_k \nabla k) = G_k - \frac{2}{3}\rho(\nabla \cdot \mathbf{u})k - \rho\varepsilon + S_k \\ \nabla \cdot (\rho\mathbf{u}\varepsilon) - \nabla \cdot (\rho D_\varepsilon \nabla \varepsilon) = \frac{C_1 G_\varepsilon \varepsilon}{k} - \left( \frac{2}{3}C_1 - C_{3,RDT} \right) \rho(\nabla \cdot \mathbf{u})\varepsilon - C_2 \rho \frac{\varepsilon^2}{k} + S_\varepsilon \\ \mu_t = \rho C_\mu \frac{k^2}{\varepsilon} \end{cases} \quad (6.22)$$

These two equations implemented in OpenFOAM are different from the original k- $\varepsilon$  model. The second term on the right hand side incorporates the Rapid Distortion Theory (RDT) contribution, buoyancy contribution are not included, and the coefficient  $C_3$  is not the same as  $C_{3,RDT}$  [6.10]. Tab. 6.3 shows the default model coefficients applied in OpenFOAM model.

The model for the solid region, i.e., the fuel, implements the heat equation

$$\nabla \cdot \left[ \frac{k_f}{\rho_f C_{p,f}} \nabla T \right] = q \quad (6.23)$$


The cladding and gap region are not modelled to not compromise the quality of the mesh. In order to take into account their effect in terms of temperature distribution, two thermal resistances are considered in the interface between the fuel and the coolant. In particular, a thermal resistance for the cladding (length of 0.6 mm) and the helium gap (length of 0.15 mm) are added, with thermal conductivity of  $15 \text{ W m}^{-1} \text{ K}^{-1}$  and  $1.125 \text{ W m}^{-1} \text{ K}^{-1}$  respectively.

As for the boundary conditions, the coolant inlet temperature and velocity are kept constant ( $400 \text{ }^\circ\text{C}$  and  $1.4 \text{ m/s}$ , respectively), as well as outlet pressure. Since the single CFD model is not capable of evaluating the heat flux, the latter is taken from a constant value that will be provided by the SERPENT code in the coupling mode.

The correlations adopted for density and thermal conductivity of the coolant and the fuel are reported in Tab. 6.4.





 <b>RICERCA SISTEMA ELETTRICO</b>	<u>Title:</u> Development of BE numerical tools for LFR design and safety analysis (2018)	<u>Distribution</u> <b>PUBLIC</b>	<u>Issue Date</u> 29.01.2019	<u>Pag.</u>
	<u>Project:</u> ADP ENEA-MSE PAR 2017	Ref. ADPFISS-LP2-167	Rev. 0	119 di 163

The geometry of one-sixth of the FA used in the coupling with SERPENT is shown in Fig. 6.6a. The mesh is composed by 860310 cells for the coolant and by 615679 cells for the fuel (Fig. 6.6b). A sensitivity analysis has been carried out to ensure that the temperature distribution does not change with further refinement of the mesh.

#### 6.2.4 SERPENT – OpenFOAM coupling for one-sixth of FA

Both the fixed-point and the stochastic approximation algorithms have been implemented for the Monte Carlo – CFD coupling. Some modifications have been taken in the OpenFOAM solver, in particular:

1. the volumetric power distribution is included in the energy equation for solid materials, reading it from a separate OpenFOAM input file;
2. the relative integral variation of the volumetric power distributions from the previous iteration to the current one is calculated, in order to perform a convergence check with the wrapper code at each coupled iteration;
3. the relative density in fluid materials with respect to a reference density is calculated. This feature was used in order to feed the density field to Serpent 2.

The coupling is carried out by a bash script in the Linux environment. The wrapper code manages the process and is capable to restart the calculation from a determined iteration. A configuration file, read by the bash script at each iteration, reports the settings of the simulation.


The Serpent – OpenFOAM coupling for the ALFRED reactor is tested on a one-sixth of FA [6.18]. Thanks to the relative low reactivity feedbacks of this fast system, both the fixed-point coupling method (with a moderate high under-relaxation factor equal to 0.8) and the stochastic approximation allows a fast convergence of the calculation, reaching a steady state after few iterations (Fig. 6.7). The value of  $\Delta_n$  does not decrease increasing the number of iteration since it is affected by the statistical fluctuation of the Monte Carlo method. An increase the number of neutron histories simulated can lead to a reduction of the relative power variation at convergence.

From CFD calculations, we obtain the distribution of the temperature field. The mean temperature is 1284 °C for the fuel and 440 °C for the lead, calculated over the volumes. Fig. 6.8 shows the temperature contours, along the radial direction, obtained at the middle of the active region. The temperature of the coolant is higher near the border of the fuel pins, reaching differences until 70 °C with the regions near the wall. For external FA, this difference could be higher. The fuel temperature, as expected, is maximum at the center of the pins, with differences more than 1300 °C with the border, according to the study of the fuel pin design reported in [6.19]. The velocity profile along the axial direction are shown in Fig. 6.9.

### 6.3 Role of the activity, general goals and future development

The activity is the step forward of the development of a multi-physics code for lead-cooled fast reactor aimed at supporting both the design choice and the verification of other numerical tools. This tool is meant to represent an additional tool to be used in combination with the classic system codes in order to give a deeper insight about the complex physical phenomena occurring in the reactor (and their mutual interactions). In particular, the Monte Carlo – CFD coupling developed in this activity is aimed at obtaining a better accuracy in the neutronics/thermal-hydraulics modelling of the ALFRED reactor. Along with the design support, this activity is aimed at providing assistance to the code verification of the FRENETIC code, in collaboration with Politecnico di Torino. Two coupling approaches has been tested on a one-sixth of LFR, providing both good results and making possible the coupling between a Monte Carlo and a CFD code.



 <b>RICERCA SISTEMA ELETTRICO</b>	<u>Title:</u> Development of BE numerical tools for LFR design and safety analysis (2018)	<u>Distribution</u> <b>PUBLIC</b>	<u>Issue Date</u> 29.01.2019	<u>Pag.</u>
	<u>Project:</u> ADP ENEA-MSE PAR 2017	Ref. ADPFISS-LP2-167	Rev. 0	120 di 163

Near-term efforts will focus on efficient use of the available computational resources (i.e., parallelization, optimization) and easy modification of the modelling description with OpenFOAM to develop a multi-physics platform. In addition, extension to the entire fuel assembly and to the entire core can be considered prior development of a porous media approach in order to reduce the computational burden of the coupled calculation.

#### 6.4 Activity PAR 2018 – Porous media approach for the LFR design and safety analysis

As stated in the previous chapter, the development of this activity is focusing on the development of a porous media approach to enlarge the application field of the developed coupling scheme.

In particular for fuel assemblies and full core geometry of LFR, the computational burden can become impracticable for coupled simulations between CFD and Monte Carlo codes. On one hand, the limit of CFD is the high computational cost for mesh cells up to millions or more, that affects computational time and memory requirements. On the other hand, Monte Carlo codes, that are characterized by high flexibility and accuracy, require more computational effort than the legacy of deterministic code.

To overcome this issue, a porous media approach can be employed, in order to adopt a coarse mesh for the complex geometry characterizing the structural elements of the core. This approach relies on the assumption that the interested region can be treated with a so-called “porous” region with the addition to models that reproduce the effect of the real structure, and in particular the interaction of the fluid with the sub-scale structure in terms of momentum and energy balance.

The governing equations for fluid flow in porous media can be derived from RANS equations. The equations of mass, momentum and energy conservation are

$$\frac{\partial \gamma \rho}{\partial t} + \nabla \cdot (\gamma \rho \mathbf{u}) = 0 \quad (6.24)$$

$$\frac{\partial \gamma \rho \mathbf{u}}{\partial t} + \nabla \cdot (\gamma \rho \mathbf{u} \mathbf{u}) = \nabla \cdot [(\mu + \mu_T) \nabla \mathbf{u}] - \nabla \gamma p + \gamma \mathbf{F}_s \quad (6.25)$$


$$\frac{\partial \gamma \rho e}{\partial t} + \nabla \cdot (\gamma \rho \mathbf{u} e) = \nabla \cdot [\gamma (k + k_T) \nabla T] + \gamma \mathbf{F}_s \mathbf{u} + \gamma Q_s \quad (6.26)$$

in which the following terms are considered:

- the porosity term  $\gamma$  which it takes into account that only a part of the volume is occupied by the fluid.
- the  $F_s$  term which represents the drag force applied by the sub-scale structures on the fluid. This term is linearly or quadratically proportional to the velocity. On the other hand, this dependence can be calculated with the typical correlation employed for the pressure drop. In this sense, the information calculated with a full CFD calculation are substituted with the engineering correlation calculated on the sub-scale components.
- the heat source  $Q_s$  term which refers to the volumetric heat exchanged between the fluid and sub-scale structure. This can be expressed as a heat transfer between the fluid and the structure which – once again – can be calculated with the typical correlation for the heat transfer coefficient.

The effort in the PAR2018 is aimed at investigating the porous media approach and its future implementation in the present coupling strategy.



 <b>RICERCA SISTEMA ELETTRICO</b>	<u>Title:</u> Development of BE numerical tools for LFR design and safety analysis (2018)	<u>Distribution</u> <b>PUBLIC</b>	<u>Issue Date</u> 29.01.2019	<u>Pag.</u> 
	<u>Project:</u> ADP ENEA-MSE PAR 2017	Ref. ADPFISS-LP2-167	Rev. 0	121 di 163

	SERPENT	ERANOS [14]	MCNPX [14]
Max power in FA (MW)	2.25	2.42	2.21
Total worth of 12 CRs (pcm)	-8511	-9100	-8500
Total worth of 4 SRs (pcm)	-2957	-3700	-3300
Effective delayed neutron fraction (pcm)	336	336	-

*Tab. 6.1 – Comparison of some core parameters.*

	SERPENT	ERANOS [14]
Doppler constant (pcm)	-580 ± 18	-555
Lead expansion coefficient (pcm/K)	-0.282 ± 0.113	-0.271
Axial fuel expansion (pcm/K)	-0.153 ± 0.019	-0.148
Axial cladding expansion (pcm/K)	+0.044 ± 0.006	+0.037
Axial wrapper expansion (pcm/K)	+0.036 ± 0.006	+0.022
Radial grid expansion (pcm/K)	-0.766 ± 0.007	-0.762

*Tab. 6.2 – Comparison of the reactivity coefficients, BoC.*

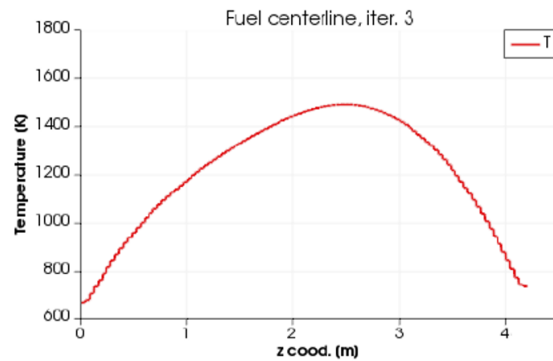
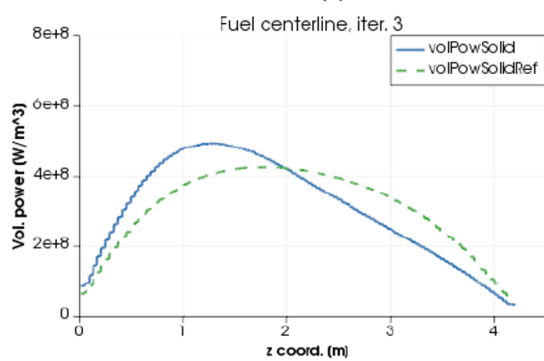
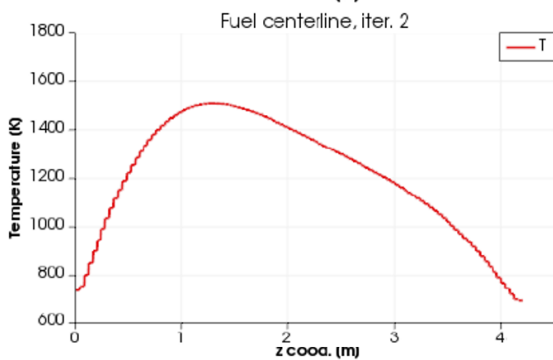
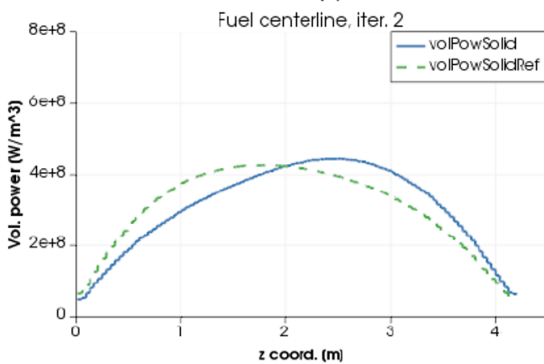
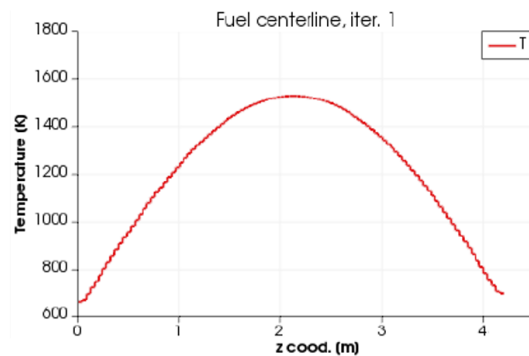
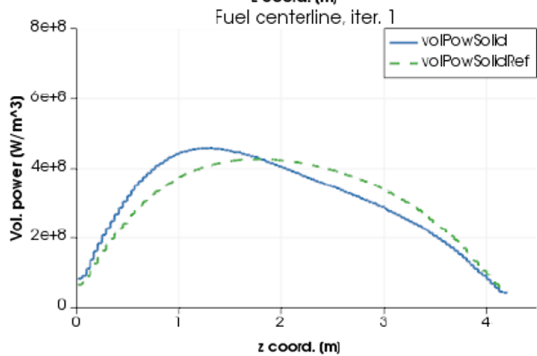
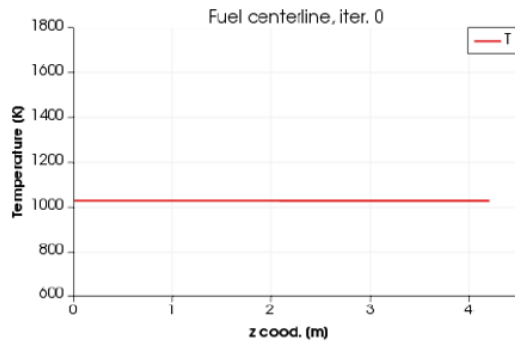
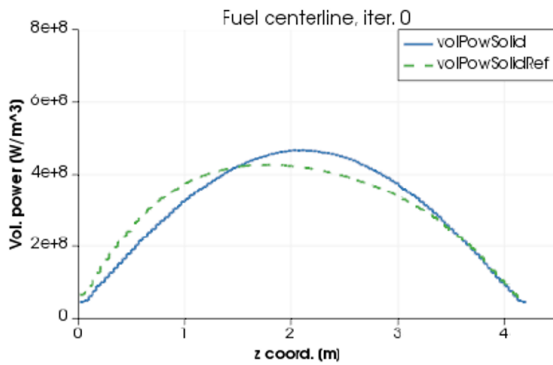
$C_\mu$	$C_1$	$C_2$	$C_{3,RDT}$
0.09	1.44	1.92	0

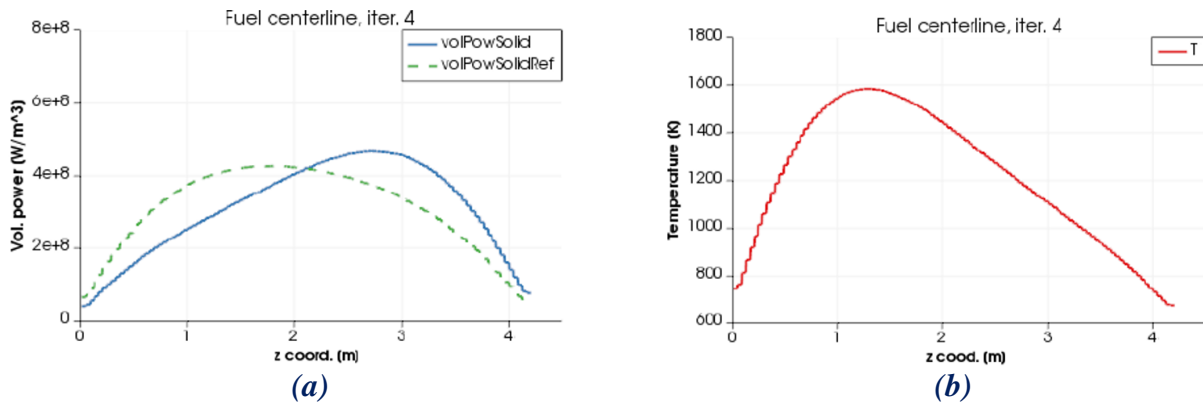
*Tab. 6.3 – Default parameters applied in the OpenFOAM solver for k-ε turbulence model.*

Parameter	Correlation	Reference
Lead density	$\rho \text{ (kg m}^{-3}\text{)} = 11367 - 1.1944 \cdot T \text{ (K)}$	[6.16]
Lead thermal conductivity	$\lambda \text{ (W m}^{-1}\text{ K}^{-1}\text{)} = 9.2 - 0.011 \cdot T \text{ (K)}$	[6.16]
Fuel density	$\rho \text{ (kg m}^{-3}\text{)} = 10443$	[6.14]
Fuel thermal conductivity	$\lambda \text{ (W m}^{-1}\text{ K}^{-1}\text{)} = \left( \frac{1}{0.197 + 2.885 \cdot 10^{-4} \cdot T \text{ (K)}} + 7.64 \cdot 10^{-11} T \text{ (K)}^3 \right) \cdot 1.157$	[6.17]

*Tab. 6.4 – Correlations for density and thermal conductivity of coolant and fuel.*







**Fig. 6.1 – Unstable behavior of Monte Carlo – CFD coupling (EPR case). Evolution of a) volumetric power, b) fuel temperature in the first 4 iterations.**

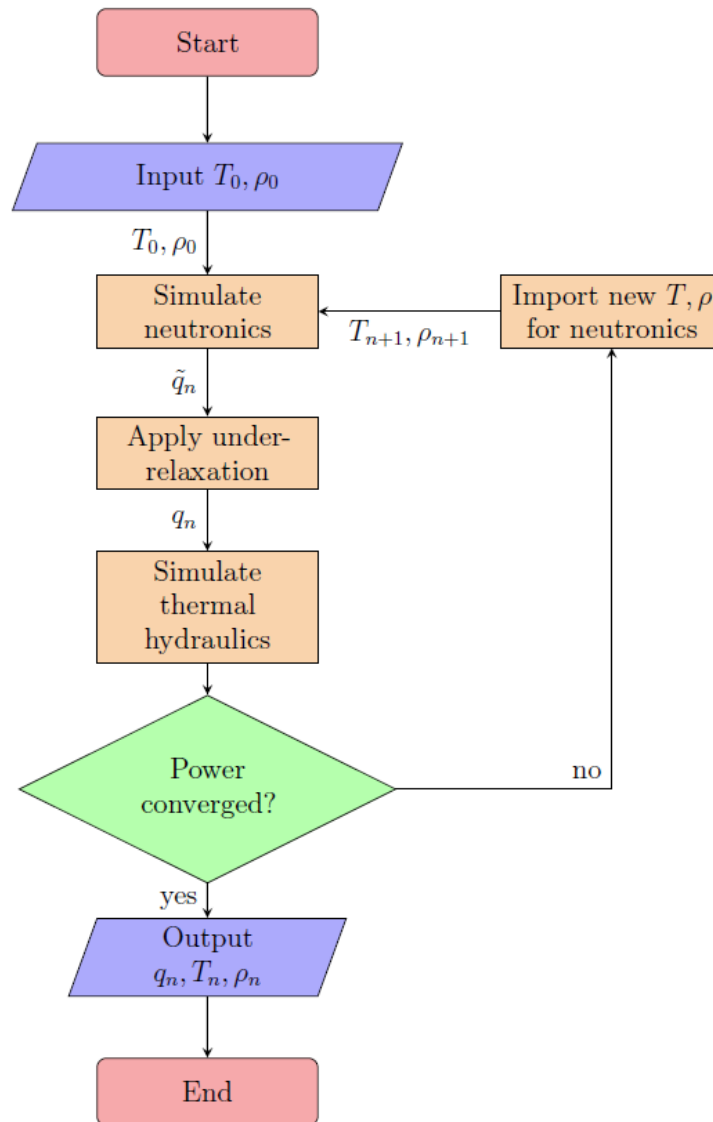


Fig. 6.2 – The fixed-point coupling algorithm.

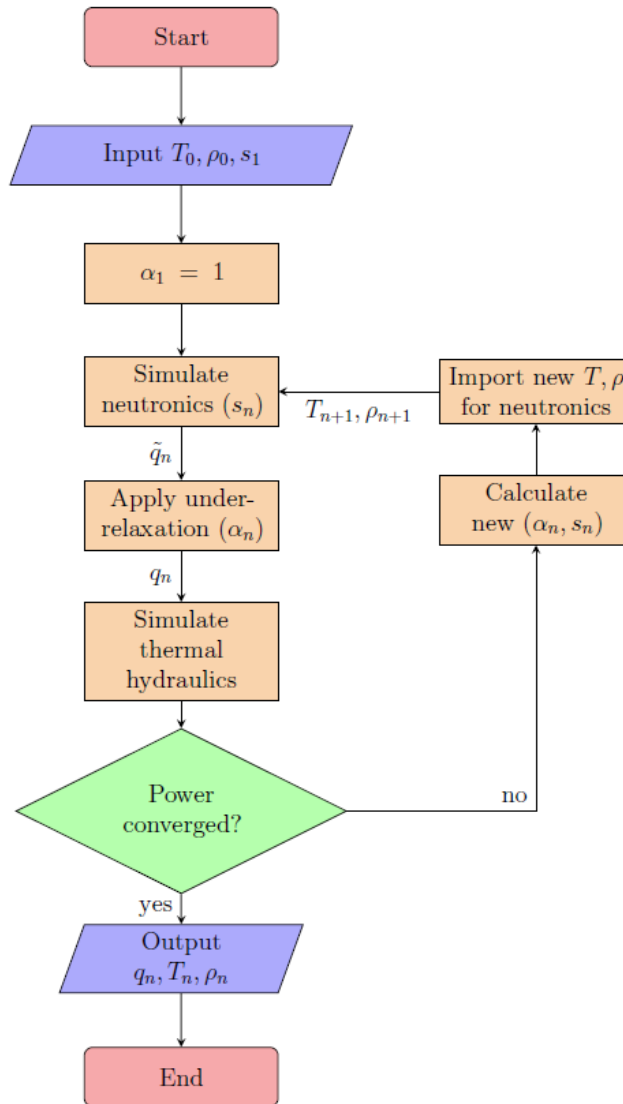


Fig. 6.3 – The stochastic approximation coupling algorithm

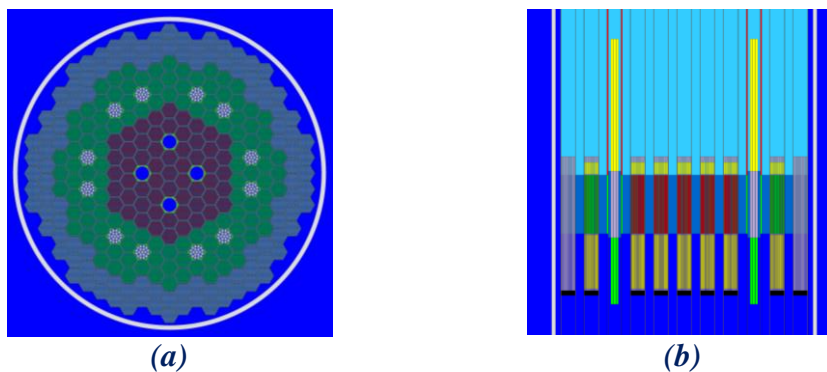

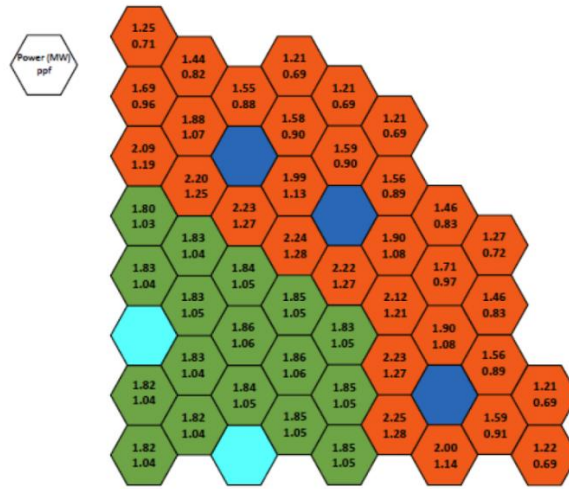
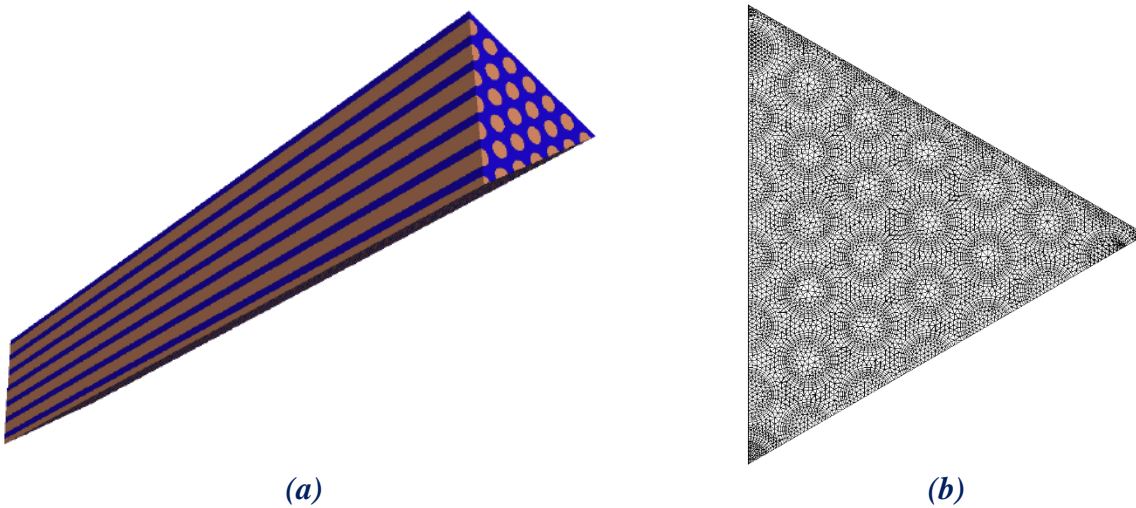


Fig. 6.4 – Radial view (a) and longitudinal view (b) of the SERPENT model of the ALFRED reactor.

 <b>RICERCA SISTEMA ELETTRICO</b>	<u>Title:</u> Development of BE numerical tools for LFR design and safety analysis (2018)	<u>Distribution</u> <b>PUBLIC</b>	<u>Issue Date</u> 29.01.2019	<u>Pag.</u>
	<u>Project:</u> ADP ENEA-MSE PAR 2017	Ref. ADPFISS-LP2-167	Rev. 0	126 di 163




*Fig. 6.5 – Power peaking factor of one-fourth of ALFRED reactor core for BOC.*

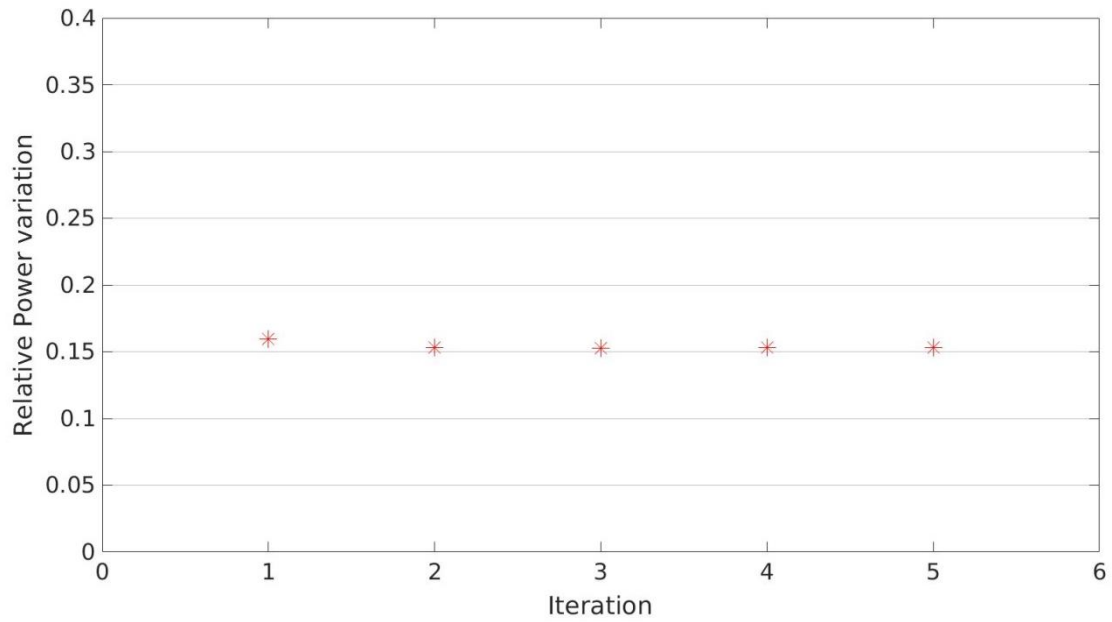


*Fig. 6.6 – a) Geometry and b) mesh of ALFRED one-sixth of FA.*

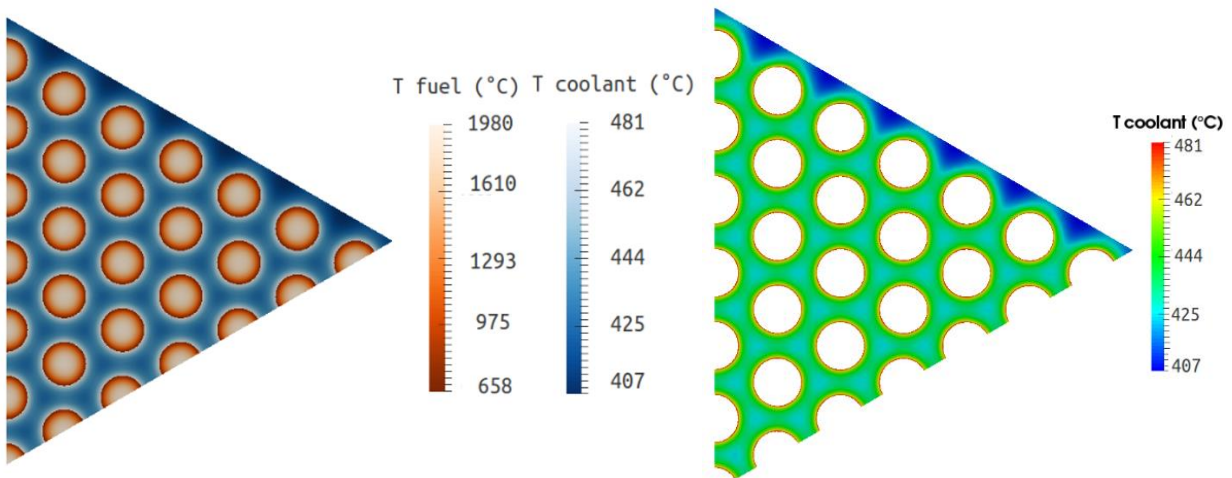




 <b>RICERCA SISTEMA ELETTRICO</b>	<u>Title:</u> Development of BE numerical tools for LFR design and safety analysis (2018)	<u>Distribution</u> <b>PUBLIC</b>	<u>Issue Date</u> 29.01.2019	<u>Pag.</u> 
	<u>Project:</u> ADP ENEA-MSE PAR 2017	Ref. ADPFISS-LP2-167	Rev. 0	127 di 163




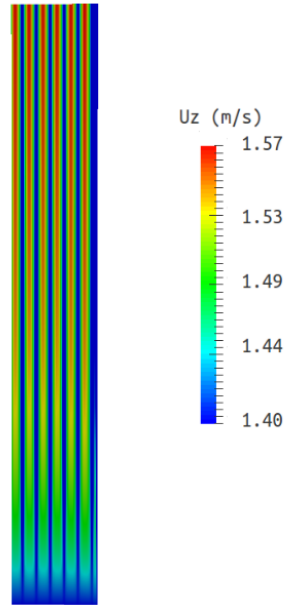
*Fig. 6.7 – Relative power variation at each iteration for the fixed-point scheme.*



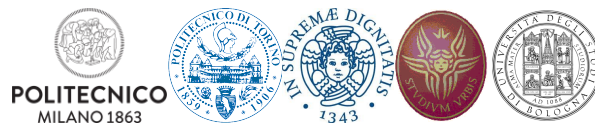
*Fig. 6.8 – Temperature profile calculated with the Monte Carlo – CFD coupling scheme.*




 <b>RICERCA SISTEMA ELETTRICO</b>	<u>Title:</u> Development of BE numerical tools for LFR design and safety analysis (2018)	<u>Distribution</u> <b>PUBLIC</b>	<u>Issue Date</u> 29.01.2019	<u>Pag.</u>
	<u>Project:</u> ADP ENEA-MSE PAR 2017	Ref. ADPFISS-LP2-167	Rev. 0	128 di 163



*Fig. 6.9 – Velocity profile calculated with the Monte Carlo – CFD coupling scheme.*




 <b>RICERCA SISTEMA ELETTRICO</b>	<u>Title:</u> Development of BE numerical tools for LFR design and safety analysis (2018)	<u>Distribution</u> <b>PUBLIC</b>	<u>Issue Date</u> 29.01.2019	<u>Pag.</u>
	<u>Project:</u> ADP ENEA-MSE PAR 2017	Ref. ADPFISS-LP2-167	Rev. 0	129 di 163

## 6.5 List of References


- [6.1] A. Cammi, V. Di Marcello, L. Luzzi, V. Memoli, M.E. Ricotti, A multi-physics modelling approach to the dynamics of Molten Salt Reactors, *Ann. Nucl. Energy.* 38 (2011) 1356–1372. doi:10.1016/j.anucene.2011.01.037.
- [6.2] M. Aufiero, A. Cammi, O. Geoffroy, M. Losa, L. Luzzi, M.E. Ricotti, H. Rouch, Development of an OpenFOAM model for the Molten Salt Fast Reactor transient analysis, *Chem. Eng. Sci.* 111 (2014) 390–401. doi:10.1016/j.ces.2014.03.003.
- [6.3] A. Cammi, V. Di Marcello, L. Luzzi, V. Memoli, The multi-physics modelling approach oriented to safety analysis of innovative nuclear reactors, *Adv. Energy Res.* 5 (2011) 171–214.
- [6.4] D. Kotlyar, Y. Shaposhnik, E. Fridman, E. Shwageraus, Coupled neutronic thermo-hydraulic analysis of full PWR core with Monte-Carlo based BGCore system, *Nucl. Eng. Des.* 241 (2011) 3777–3786. doi:10.1016/j.nucengdes.2011.07.028.
- [6.5] M. Vazquez, H. Tsige-Tamirat, L. Ammirabile, F. Martin-Fuertes, Coupled neutronics thermal-hydraulics analysis using Monte Carlo and sub-channel codes, *Nucl. Eng. Des.* 250 (2012) 403–411. doi:10.1016/j.nucengdes.2012.06.007.
- [6.6] N. Capellan, J. Wilson, S. David, O. Méplan, J. Brizi, A. Bidaud, A. Nuttin, P. Guillemin, 3D coupling of Monte Carlo neutronics and thermal-hydraulics calculations as a simulation tool for innovative reactor concepts, *Proc. Glob. 2009.* (2009) 1358–1367.
- [6.7] M. Aufiero, M. Fratoni, A new approach to the stabilization and convergence acceleration in coupled Monte Carlo–CFD calculations: The Newton method via Monte Carlo perturbation theory, *Nucl. Eng. Technol.* 49 (2017) 1181–1188. doi:10.1016/j.net.2017.08.005.
- [6.8] P. Bianchini, Computational features of neutronics and thermal hydraulics coupled simulations, Politecnico di Milano, 2017.
- [6.9] H.G. Weller, G. Tabor, H. Jasak, C. Fureby, A tensorial approach to computational continuum mechanics using object-oriented techniques, *Comput. Phys.* 12 (1998) 620–631.
- [6.10] OpenFOAM, OpenFOAM, (2016). <http://www.openfoam.org/>.
- [6.11] J. Leppänen, M. Pusa, T. Viitanen, V. Valtavirta, T. Kaltiaisenaho, The Serpent Monte Carlo code: Status, development and applications in 2013, (2015). doi:10.1016/j.anucene.2014.08.024.
- [6.12] J. Dufek, W. Gudowski, Stochastic Approximation for Monte Carlo Calculation of Steady-State Conditions in Thermal Reactors, *Nucl. Sci. Eng.* 152 (2006) 274–283. doi:10.13182/NSE06-2.
- [6.13] J.M. Pounders, Stability and near-optimal underrelaxation of coupled reactor physics calculations, in: *Phys. React. 2016, PHYSOR 2016 Unifying Theory Exp. 21st Century*, 2016.
- [6.14] G. Grasso, C. Petrovich, D. Mattioli, C. Artioli, P. Sciora, D. Gugiu, G. Bandini, E. Bubelis, K. Mikityuk, The core design of ALFRED, a demonstrator for the European lead-cooled reactors, *Nucl. Eng. Des.* 278 (2014) 287–301. doi:10.1016/j.nucengdes.2014.07.032.
- [6.15] B.E. Launder, D.B. Spalding, The numerical computation of turbulent flows, *Comput. Methods Appl. Mech. Eng.* (1974). doi:10.1016/0045-7825(74)90029-2.
- [6.16] OECD, N.E. Agency, Handbook on Lead-bismuth Eutectic Alloy and Lead Properties, Materials Compatibility, Thermal-hydraulics and Technologies, 2015. doi:ISBN 978-92-64-99002-9.
- [6.17] Y. Philipponneau, Thermal conductivity of (U, Pu)O<sub>2</sub>-x mixed oxide fuel, *J. Nucl. Mater.* 188 (1992) 194–197. doi:10.1016/0022-3115(92)90470-6.



 <b>RICERCA SISTEMA ELETTRICO</b>	<u>Title:</u> Development of BE numerical tools for LFR design and safety analysis (2018)	<u>Distribution</u> <b>PUBLIC</b>	<u>Issue Date</u> 29.01.2019	<u>Pag.</u>
	<u>Project:</u> ADP ENEA-MSE PAR 2017	Ref. ADPFISS-LP2-167	Rev. 0	130 di 163

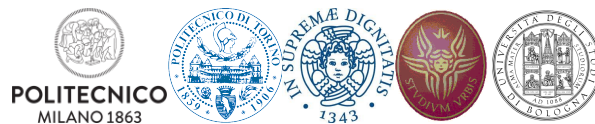
- [6.18] C. Castagna, S. Lorenzi, A. Cammi, A Multi-physics Modelling Approach for the analysis of Lead Fast Reactors, in: Proc. 27th Int. Conf. Nucl. Energy New Eur. Portoroz, Slov. Sept. 10 - 13, 2018.
- [6.19] L. Luzzi, A. Cammi, V. Di Marcello, S. Lorenzi, D. Pizzocri, P. Van Uffelen, Application of the TRANSURANUS code for the fuel pin design process of the ALFRED reactor, Nucl. Eng. Des. 277 (2014) 173–187. doi:10.1016/j.nucengdes.2014.06.032.




 <b>RICERCA SISTEMA ELETTRICO</b>	<u>Title:</u> Development of BE numerical tools for LFR design and safety analysis (2018)	<u>Distribution</u> <b>PUBLIC</b>	<u>Issue Date</u> 29.01.2019	<u>Pag.</u>
	<u>Project:</u> ADP ENEA-MSE PAR 2017	Ref. ADPFISS-LP2-167	Rev. 0	131 di 163

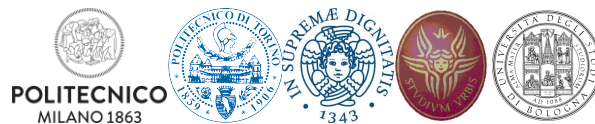
## 7 SIMMER III-RELAP5 COUPLING CODES DEVELOPMENT


*N. Forgone, S. Khani, G. Barone, F. Galleni*



 <b>RICERCA SISTEMA ELETTRICO</b>	<u>Title:</u> Development of BE numerical tools for LFR design and safety analysis (2018)	<u>Distribution</u> <b>PUBLIC</b>	<u>Issue Date</u> 29.01.2019	<u>Pag.</u>
	<u>Project:</u> ADP ENEA-MSE PAR 2017	Ref. ADPFISS-LP2-167	Rev. 0	132 di 163

*(Page intentionally left blank)*



 <b>RICERCA SISTEMA ELETTRICO</b>	<u>Title:</u> Development of BE numerical tools for LFR design and safety analysis (2018)	<u>Distribution</u> <b>PUBLIC</b>	<u>Issue Date</u> 29.01.2019	<u>Pag.</u>
	<u>Project:</u> ADP ENEA-MSE PAR 2017	Ref. ADPFISS-LP2-167	Rev. 0	133 di 163

## 7.1 Background

As part of the development of a coupling interface between the codes SIMMERIII and RELAP5[7.1], an analysis of the results from the simulation of two different test cases is presented in this section as research development respect to the activity performed inside PAR 2017. The conditions for these simulations were taken from the experimental setup proposed for the campaign which is planned to be conducted at the LIFUS5/Mod3 experimental facility; a concise summary of this setup is presented below. However, for further details about the facility, the coupling tool and the settings of the simulation the reader may refer to the first part of this report.

The simulation involves the injection of water at different temperatures into a tank filled with a liquid lead-lithium alloy. The current computational setup is summarized in Tab. 7.1, whilst the initial conditions in the so called SB1 Tank are shown in Fig. 7.1. The whole injection line is simulated with RELAP5 (except a short section at the end) and the SB1 Tank is simulated by SIMMERIII. These conditions differ from the proposed experimental setup; however, even with this modification, the proposed setup can be considered valid for the preliminary assessment of the complete simulation. Furthermore, as mentioned above, the exact experimental setting is yet to be decided.

It is important to notice that the quantitative analysis described below is a continuation of the work partially introduced in the first part of the report, in which only qualitative results were shown and that are briefly presented in the next section.

## 7.2 Qualitative results


The system stays at rest for 1 second (Fig. 7.1) and then, when the valve controlled by RELAP5 is opened, the water starts to enter in the SIMMER domain through the injection line. After 1.04 seconds the virtual wall which separates the injection region and the vessel vanishes and the water is injected into the tank; the temperature increase in the region where the water and the lead-lithium get in contact is due to the chemical reaction of the water with the PbLi.

## 7.3 Qualitative results

From Fig. 7.2 to Fig. 7.5 the evolution in time of the main properties is presented. The figures show the results of the two different cases, namely at different temperatures. Fig. 7.2 shows the behavior of the liquid fraction inside the first cell of the SIMMERIII domain; as it can be seen, in the case at higher temperature the liquid volume fraction does not stay constant throughout the entire “resting” period (0 to 1 seconds) but it decreases slightly: this is due to the evaporation of a small fraction of water which is close to the boiling temperature at 1 bar. . Since it is not possible to impose the liquid fraction injected in the computational domain of SIMMER, this evaporation might have a significant impact on the mass of liquid water actually injected in the vessel. Indeed the total mass injected in the case at low temperature is somewhat smaller than the mass in the other case (120 grams at 300K and 129 grams at 360K), although it has not been possible, at this stage, to fully understand the cause of this difference. This is an issue that will certainly need to be addressed, in order to investigate cases at higher temperatures.

The pressure directly after the injection line shows a first peak and then a slower increase to a steady state at a higher value (Fig. 7.3); this behaviour is seen in both the cases. The pressure reached during the first peak is essentially the same at the two different temperatures (~ 15 bar), whilst the case at lower temperature reaches a steady state which is at a lower pressure (~ 40 bar) than the case at higher temperature (~ 45 bar). The occurrence of this relatively large offset between the steady state pressures of the two cases (5 bars) might have different explanations (e.g., the formation of water vapour inside the injection line) and it surely



 <b>RICERCA SISTEMA ELETTRICO</b>	<u>Title:</u> Development of BE numerical tools for LFR design and safety analysis (2018)	<u>Distribution</u> <b>PUBLIC</b>	<u>Issue Date</u> 29.01.2019	<u>Pag.</u>
	<u>Project:</u> ADP ENEA-MSE PAR 2017	Ref. ADPFISS-LP2-167	Rev. 0	134 di 163

needs further investigation. However, it is already important that the simulation was able to properly capture the first pressure peak, since it is a critical phenomenon for the assessment of the vessel.

Fig. 7.4 presents the global temperature (mass averaged) inside the vessel. The two cases show a similar trend, with the vessel temperature slightly decreasing during the injection and then increasing again and reaching a plateau once the vessel is isolated. As expected the temperature of the water has a negligible effect on the cooling down of the vessel, since the mass injected is significantly lower than the mass of lead-lithium inside the tank. The temperature increase is then due to the combination of two effects: the pressurization of the vessel and the heat generated by the chemical reactions.

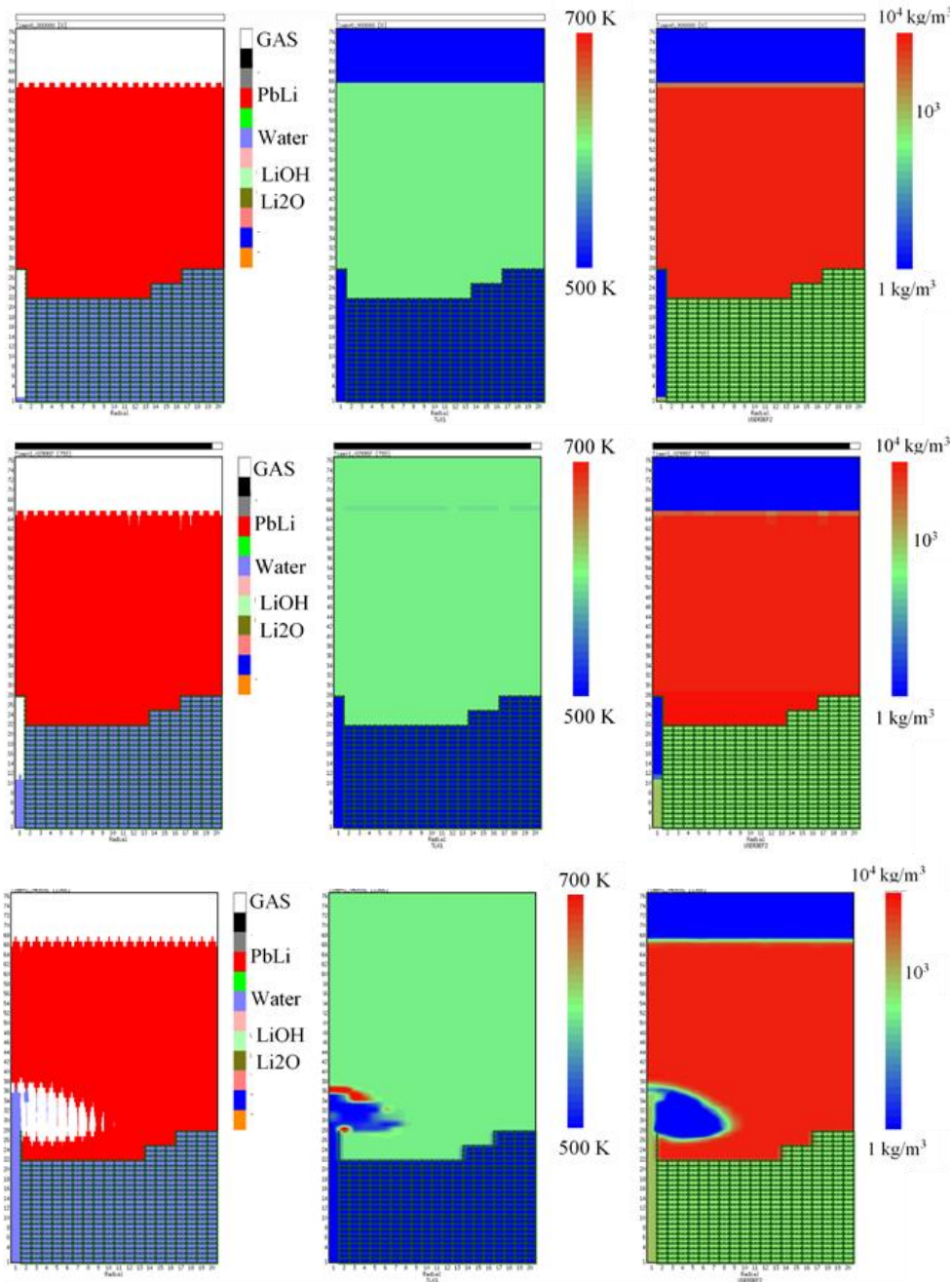
The hydrogen generated during the transient is presented in Fig. 7.5, which shows the mass of H<sub>2</sub> inside the vessel. The trend is well captured, with the production of H<sub>2</sub> starting sharply at the beginning of the injection in the vessel, slowing down when the lid is closed and continuing until an equilibrium is reached. The mass produced seems to vary with the temperature of the coolant, with a higher final mass for the case at higher temperature. This might be due to the slightly larger amount of water injected in this case, but this explanation has not yet been verified.

Parameter	Design Value
<b>Abs. pressure in S1-B tank (bar)</b>	1
<b>PbLi temperature in S1-B tank (°C)</b>	330
<b>Injected water temperature (°C)</b>	30 / 90
<b>Injected water mass (g)</b>	~120
<b>Abs. pressure in injection line (bar)</b>	1
<b>Gas cylinder pressure (bar)</b>	155
<b>Free gas volume fraction (m<sup>3</sup>)</b>	0.25

*Tab. 7.1 – Initial and boundary conditions for the SIMMER/RELAP5 simulation of LIFUS5.*







*Fig. 7.1 – Injection transient, qualitative results. Time = 0 to 1 secs (TOP), time = 1.03 (MIDDLE), time = 1.05 (BOTTOM)*

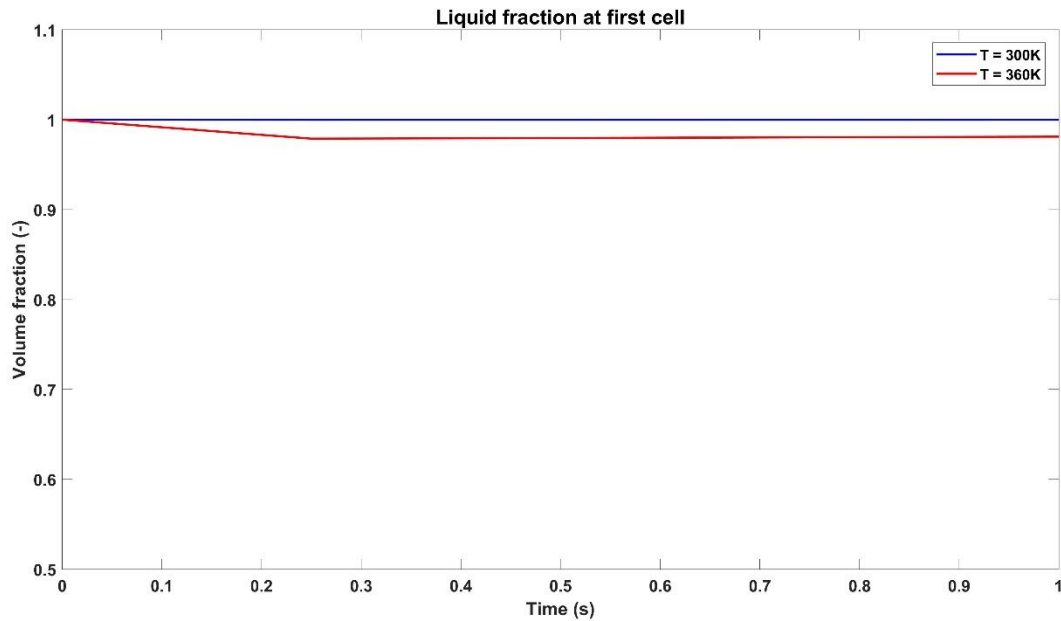


Fig. 7.2 – Time evolution of liquid fraction at first cell

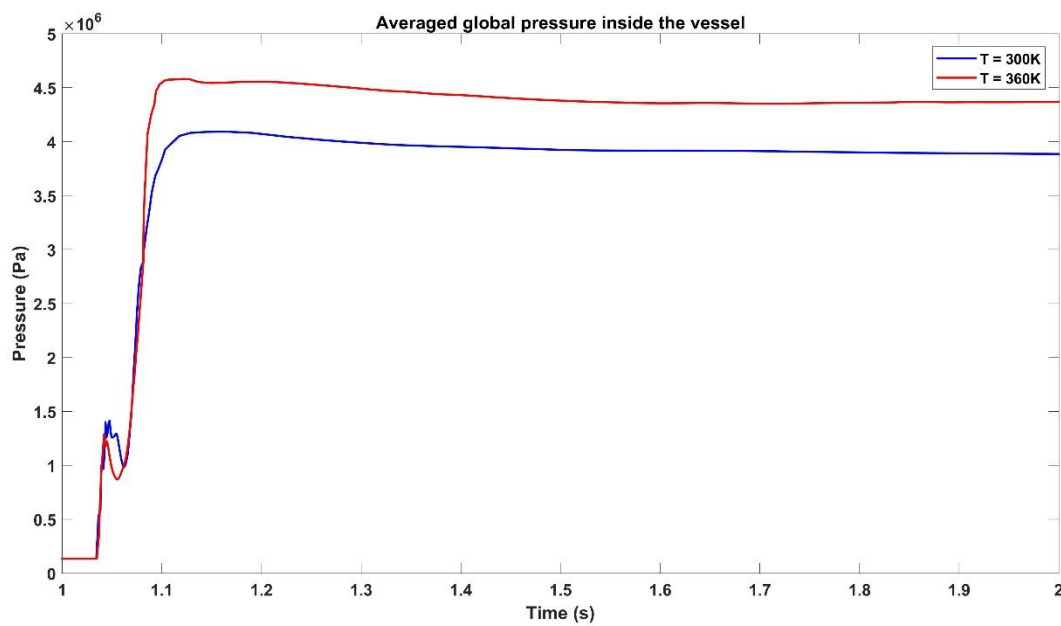
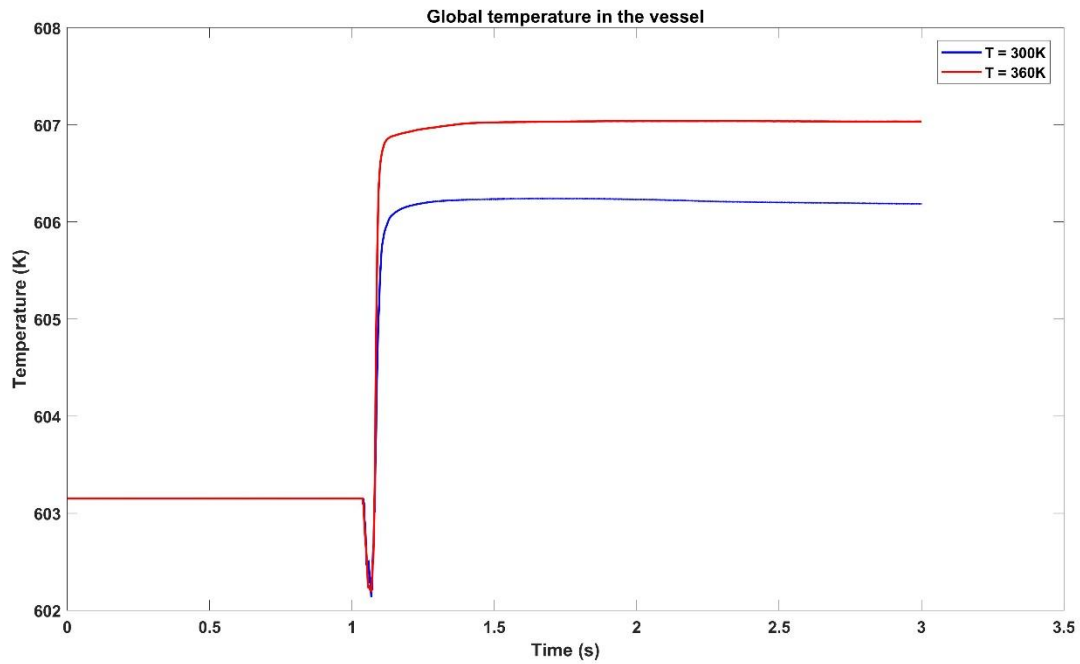
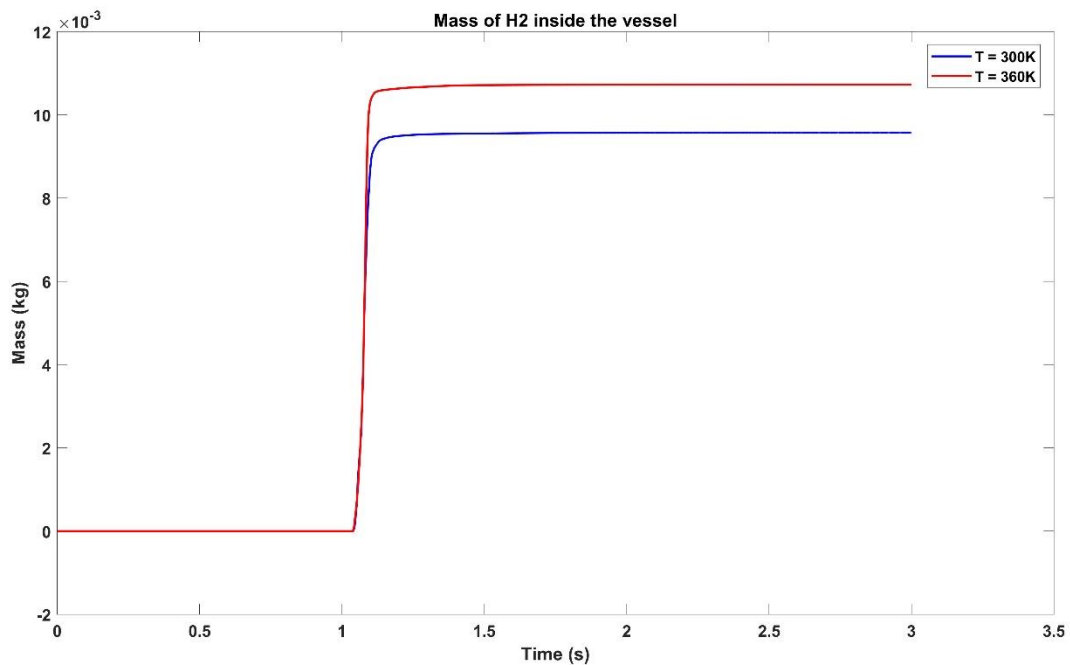


Fig. 7.3 – Time evolution of global pressure in the vessel






*Fig. 7.4 – Time evolution of global temperature (mass averaged) inside the vessel*

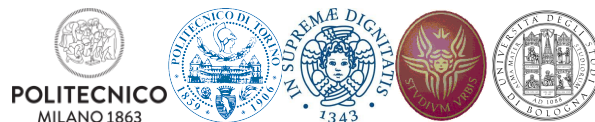



*Fig. 7.5 – Time evolution of hydrogen mass inside the vessel*

 <b>RICERCA SISTEMA ELETTRICO</b>	<u>Title:</u> Development of BE numerical tools for LFR design and safety analysis (2018)	<u>Distribution</u> <b>PUBLIC</b>	<u>Issue Date</u> 29.01.2019	<u>Pag.</u>
	<u>Project:</u> ADP ENEA-MSE PAR 2017	Ref. ADPFISS-LP2-167	Rev. 0	138 di 163

## 7.4 List of References

- [7.1] *Development of best estimate numerical tools for LFR design and safety analysis*, PAR 2017 Report, November 2018.



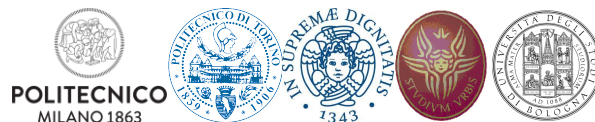
 <b>RICERCA SISTEMA ELETTRICO</b>	<u>Title:</u> Development of BE numerical tools for LFR design and safety analysis (2018)	<u>Distribution</u> <b>PUBLIC</b>	<u>Issue Date</u> 29.01.2019	<u>Pag.</u>
	<u>Project:</u> ADP ENEA-MSE PAR 2017	Ref. ADPFISS-LP2-167	Rev. 0	139 di 163


## 8 FUEL-COOLANT CHEMICAL INTERACTION

*E. Macerata, M. Mariani, M. Giola, M. Negrin, E. Mossini*

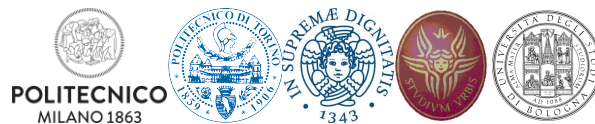



**POLITECNICO**  
MILANO 1863



 <b>RICERCA SISTEMA ELETTRICO</b>	<u>Title:</u> Development of BE numerical tools for LFR design and safety analysis (2018)	<u>Distribution</u> <b>PUBLIC</b>	<u>Issue Date</u> 29.01.2019	<u>Pag.</u>
	<u>Project:</u> ADP ENEA-MSE PAR 2017	Ref. ADPFISS-LP2-167	Rev. 0	140 di 163

*(Page intentionally left blank)*



 <b>RICERCA SISTEMA ELETTRICO</b>	<u>Title:</u> Development of BE numerical tools for LFR design and safety analysis (2018)	<u>Distribution</u> <b>PUBLIC</b>	<u>Issue Date</u> 29.01.2019	<u>Pag.</u>
	<u>Project:</u> ADP ENEA-MSE PAR 2017	Ref. ADPFISS-LP2-167	Rev. 0	141 di 163


## 8.1 Progress of the computational and experimental activities

During the extension period of PAR2018, the activities developed within PAR2017 have been continued. In particular, attempts have been made and are still in progress in order to perform a thermodynamic analysis of the ternary U-O-Pb and La-O-Pb systems with the OpenCalphad software by exploiting the thermodynamic data estimated by the DFT-GGA approach. Difficulties have arisen from the compilation of a database compatible with OpenCalphad. The achievement of this objective is fundamental to make a breakthrough in developing a flexible and easy tool to have first indications about the chemical compatibility of the complex systems such as those involved in LFRs.

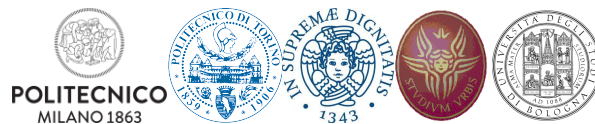
The experimental activities started in the previous period have still to be completed by performing the ICP-MS analyses of the lead used in the reactivity experiments in order to check a possible metal release from the pellet under the experimental conditions considered. Such analyses have not yet been carried out due to a breakdown of the instrumentation. Following the lesson learnt from the previous experimental activities, efforts have been dedicated to re-design the experimental set-up, in particular the sample holder and a suitable gas purifier to reduce oxygen content during the thermal treatment. The indications drawn from the experimental activities performed up to now are only preliminary in nature. It will be paramount to perform further experiments in order to test numerous experimental conditions and check the role of several parameters.

Experimental and computational results will have to be then combined together in a complementary way to try to achieve an understanding of the chemical phenomena. These will enable to develop computational tools able to foresee the chemical behavior of the fuel-coolant system useful to the technological development of LFRs.




 <b>RICERCA SISTEMA ELETTRICO</b>	<u>Title:</u> Development of BE numerical tools for LFR design and safety analysis (2018)	<u>Distribution</u> <b>PUBLIC</b>	<u>Issue Date</u> 29.01.2019	<u>Pag.</u>
	<u>Project:</u> ADP ENEA-MSE PAR 2017	Ref. ADPFISS-LP2-167	Rev. 0	142 di 163

*(Page intentionally left blank)*






 <b>RICERCA SISTEMA ELETTRICO</b>	<u>Title:</u> Development of BE numerical tools for LFR design and safety analysis (2018)	<u>Distribution</u> <b>PUBLIC</b>	<u>Issue Date</u> 29.01.2019	<u>Pag.</u>
	<u>Project:</u> ADP ENEA-MSE PAR 2017	Ref. ADPFISS-LP2-167	Rev. 0	143 di 163

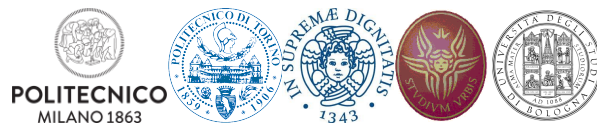
## 9 CFD ANALYSIS OF FLOW BLOCKAGE IN THE ALFRED FA


*R. Marinari, D. Martelli, I. Di Piazza*



 <b>RICERCA SISTEMA ELETTRICO</b>	<u>Title:</u> Development of BE numerical tools for LFR design and safety analysis (2018)	<u>Distribution</u> <b>PUBLIC</b>	<u>Issue Date</u> 29.01.2019	<u>Pag.</u>
	<u>Project:</u> ADP ENEA-MSE PAR 2017	Ref. ADPFISS-LP2-167	Rev. 0	144 di 163

*(Page intentionally left blank)*



 <b>RICERCA SISTEMA ELETTRICO</b>	<u>Title:</u> Development of BE numerical tools for LFR design and safety analysis (2018)	<u>Distribution</u> <b>PUBLIC</b>	<u>Issue Date</u> 29.01.2019	<u>Pag.</u>
	<u>Project:</u> ADP ENEA-MSE PAR 2017	Ref. ADPFISS-LP2-167	Rev. 0	145 di 163

## 9.1 Abstract

In the context of GEN-IV heavy liquid metal-cooled reactors safety studies, the flow blockage in a fuel sub-assembly is considered one of the main issues to be addressed and one of the most important and realistic accident for Lead Fast Reactors (LFR) fuel assembly. The blockage in a fast reactor Fuel Assembly (FA) may have serious effects on the safety of the plant leading to the FA damaging or melting.

The external or internal blockage of the FA may impair the correct cooling of the fuel pins, be the root cause of anomalous heating of the cladding and of the wrapper and potentially impact also fuel pins not directly located above or around the blocked area. In order to model the temperature and velocity field inside a wrapped FA under unblocked and blocked conditions, detailed CFD thermal hydraulic analyses of the FA are required.

ALFRED is a 300 MW<sub>th</sub> Lead-cooled fast reactor GEN.IV concept. The advanced conceptual design of the reactor was carried out within the LEADER EU project in the last years. In the SESAME EU project specific thermal-hydraulic experiments and simulations were addressed to explore the basic phenomenology of some accidental events like internal flow blockage.

A CFD computational model of the ALFRED FA is built for thermal hydraulic analysis of relevant internal blockage scenarios. The whole model of the ALFRED Fuel Assembly is first presented and calculation of flow and temperature field in nominal condition is carried out. RANS simulations of idealized blockage scenarios like one sector and two-sectors blockage are performed adopting three different spacer grid location (under the active length, at half active length, above the active length). Results showed that the most likely blockage in the lower grid positioned before the active region do not perturb the temperature distribution in the fuel assembly, while the central grid ones have strong consequences and leads to a clad temperature peak behind the blockage with possible clad failure.

On the other hand, the most severe case on the upper grid (2 sectors blockage) showed a manageable temperature maximum (700°C) at the end of the active region due to the lower mass flow rate in the FA.


As a conclusion lower and upper grid blockages perturb only marginally the temperature field and do not lead to serious clad failure involving only creep long-term effects, while a blockage in the active region leads to serious clad damage and possible clad deformation and fusion.

## 9.2 Introduction

Among the reactor technologies being considered by the Generation IV International Forum (GIF), the heavy liquid metal (HLM)-cooled system seems to be a promising choice for the fulfilment of the Generation IV goals [9.1]. Indeed, several European and international projects are heading their research efforts on the development of HLM-cooled reactors. The most significant reactor concepts developed in Europe are: ALFRED, MYRRHA and SEALER. ALFRED (Advanced Lead Fast Reactor European Demonstrator) represents the European demonstrator of a Lead Fast Reactor (LFR), with the intention to show the viability of the lead technology for usage in a future commercial power plant [9.2].

The thermal-hydraulic of HLMs is an important aspect for the development of the GEN-IV LFR, being tightly linked to the safety aspects of the liquid metal reactors. Indeed, liquid metals (LMs) are characterized by a Prandtl (Pr) number lower than unity; therefore, the heat transfer mechanisms are strongly affected by the molecular thermal conduction, even at large Reynolds (Re) numbers. In this context, the evaluation of the heat transfer coefficient inside the sub-channels of a fuel rod bundle is indispensable for the assessment of the core coolability during normal and accidental conditions.



 <b>RICERCA SISTEMA ELETTRICO</b>	<u>Title:</u> Development of BE numerical tools for LFR design and safety analysis (2018)	<u>Distribution</u> <b>PUBLIC</b>	<u>Issue Date</u> 29.01.2019	<u>Pag.</u>
	<u>Project:</u> ADP ENEA-MSE PAR 2017	Ref. ADPFISS-LP2-167	Rev. 0	146 di 163

One the most severe accidental condition is the flow blockage of a Fuel assembly. The flow blockage accident in a Fuel Assembly (FA) of a nuclear reactor consists of a partial or total occlusion of the flow passage area. This leads in general to a degradation of the heat transfer between the FA and the coolant potentially causing a temperature peak in the clad which can eventually lead to the fusion of the clad itself. A partial blockage at the fuel assembly foot may be dangerous for the integrity of the FA (e.g. Fermi 1 fuel meltdown accident), see NRC [9.3] and Bertini[9.4]; in this latter case the phenomena can be investigated and assessed by an integral system code in order to devise proper mitigation actions. On the other hand, an internal blockage can be even more dangerous and it is not easy to detect; this kind of blockage can be more effectively modelled and studied by a proper use of a CFD code.

Regarding the sodium fast reactors, they generally adopt wire-spaced bundles, and the accumulation of debris from failed fuel pins or broken wires, generally occurs *along* the wire. Therefore, in this case, the preferential shape of the blockage is elongated and it follows the helicoid wire [9.5].

For grid-spaced fuel assemblies, experimental results on blockage growth available in literature show that particles with sizes spread around the subchannel dimensions are collected at the spacer grid. A horizontal *plate like* particle bed with strong radial growth tendency was found [9.5]. In this paper the attention is focused on the grid-spaced bundles. From these remarks, the most likely internal blockage in a grid-spaced bundle is at the spacer grids, and, if the spacer grid is positioned in the active region, a remarkable effect can be evidenced and a possible damage can occur.

A first conceptual study of the flow blockage in the ALFRED FA can be found in [9.6]. In the paper the authors work on an idealized geometry to investigate the basic physical phenomena involved. Two different effects can be distinguished:


- A *local* effect due to the stagnation-recirculation/wake region downstream of the blockage, with a local minimum of the heat transfer and a clad temperature peak;
- A *global* effect due to the lower mass flow rate in the blocked subchannels; this effect leads to an increase of the bulk fluid temperature with respect to the ‘unblocked’ regions and a consequent peak in the clad temperature at the end of the active region.

According to [9.6], the local effect is dominant for large blockages while the global effect for small blockages. From the literature is not very clear if the recirculation region downstream the blockage is dominated by turbulence. Han and Fontana [9.7] assessed that, adopting the proper scales, the dimensionless temperature peak in the recirculation region is independent by Reynolds and Prandtl number, i.e. by turbulence level and the nature of fluid. Probably a systematic comparison between different coolants is missing in the literature, and any conclusion can be misleading. In any case, in References, the specific literature for flow blockage *in liquid metal cooled bundles* was reported, i.e. sodium and lead, being the flow blockage phenomena in light water reactors a quite different matter because of the unity order of the Prandtl number ([9.7]-[9.10]). For the GEN-IV heavy liquid metal technology, the flow blockage must be considered the most severe accident for the core integrity. In fact, most of the known accident that have occurred in the LBE cooled fast reactors of the Alpha-class Russian nuclear submarines, are apparently caused by a flow blockage accident, see [9.11].

An interesting review of flow blockage phenomena is given by Han and Fontana [9.7], that was mainly focused on the sodium cooled fuel assembly.

With the typical approach of the ‘70s, Kirsch [9.10] developed a simplified theory to describe the thermo-fluid dynamic phenomena downstream the blockage. The basic assumption is that turbulent diffusion



 <b>RICERCA SISTEMA ELETTRICO</b>	<u>Title:</u> Development of BE numerical tools for LFR design and safety analysis (2018)	<u>Distribution</u> <b>PUBLIC</b>	<u>Issue Date</u> 29.01.2019	<u>Pag.</u>
	<u>Project:</u> ADP ENEA-MSE PAR 2017	Ref. ADPFISS-LP2-167	Rev. 0	147 di 163

dominates both for momentum and for energy, and thus the molecular heat transfer is negligible. With this hypothesis, the author shows that for sufficiently high Reynolds and Peclet numbers, the dimensionless temperature distribution in the wake is independent of the Reynolds and the Prandtl number, i.e. by the flow and the nature of the fluid. Comparison between experimental results in sodium and water seems to partially confirm these conclusions with a difference between the two dimensionless temperature distributions of 25%. This difference is probably due to the residual influence of the coolant. Therefore, according to the author, it could be possible to have a ‘universal’ *dimensionless* temperature profile function of the fraction  $\beta$  of the blocked flow area. From this point of view, the main difference between sodium and lead as coolant is the possible onset of boiling in sodium due to the lower boiling temperature (890 °C) with positive reactivity feedback and power excursion. In lead, with a boiling temperature of 1740 °C, this scenario is unlikely in the case of flow blockage but pin failure may still occur.

In the last years, due to the growing interest in the developing of GEN-IV prototypes and demonstrators, the interest in sodium-cooled and lead-cooled bundles is high again. Nevertheless, only a small number of CFD studies appeared in the literature and sometimes these studies adopted simplified models for the bundle (porous media) and the focus was on the whole reactor [9.12]. Generally, system codes like RELAP are commonly adopted by the safety analysts to compute flow blockage in reactor Fuel Assemblies [9.13], although the local nature of the involved phenomena does not fully justify this common practice. An intermediate practice is to apply subchannels codes to evaluate these phenomena, see e.g. [9.8] for SFR.

In this paper, CFD is systematically adopted to model and simulate the internal flow blockage in a grid-spaced HLM cooled fuel assembly of the GEN-IV reactor ALFRED.

### 9.3 Models and Methods

From the arguments in the previous section, it is evident that the internal flow blockage is basically a local phenomenon, and the main issue to investigate is the thermal-hydraulic behaviour of the region downstream of the obstacle because it determines the clad temperature peak. For this reason, a local fully detailed CFD analysis was carried out in order to assess the impacts of a flow blockage. The viscous sub-layer was resolved with several points in all the simulations presented here. A value of  $y^+ \sim 1$  is guaranteed in the whole domain. The grid spacers were included in the model. A model of the whole FA is made to compute the nominal case without blockage and all the blockage cases.


From a physical point of view, the reactivity feedback due to the temperature variation in the domain has not been considered at this stage. A conservative constant power distribution was considered as well, neglecting the axial power profile typical of the nuclear reactors. Constant thermo-physical properties were assumed for Lead at 450°C, according to Tab. 9.1 [9.14]. For the clad material (SS 15-15 Ti), constant physical properties were considered at 450 °C according to Tab. 9.2 [9.15].

Investigations carried out within the LEADER FP7 EU project showed that the maximum clad temperature to avoid long term creep in the Ti 15-15 cladding material is 650 °C, this value will be the reference for discussing blockage effects on the FA.

### 9.4 Numerical methods

The general purpose code ANSYS CFX (V.18) was used for all the numerical simulations presented in this paper. The code employs a coupled technique, which simultaneously solves all the transport equations in the whole domain through a false time-step algorithm. The linearized system of equations is preconditioned in order to reduce all the eigenvalues to the same order of magnitude. The multi-grid approach reduces the low frequency error, converting it to a high frequency error at the finest grid level; this results in a great acceleration of convergence. Although, with this method, a single iteration is slower than a single iteration in



 <b>RICERCA SISTEMA ELETTRICO</b>	<u>Title:</u> Development of BE numerical tools for LFR design and safety analysis (2018)	<u>Distribution</u> <b>PUBLIC</b>	<u>Issue Date</u> 29.01.2019	<u>Pag.</u>
	<u>Project:</u> ADP ENEA-MSE PAR 2017	Ref. ADPFISS-LP2-167	Rev. 0	148 di 163

the classical decoupled (segregated) SIMPLE approach, the number of iterations necessary for a full convergence to a steady state is generally of the order of  $10^2$ , against typical values of  $10^3$  for decoupled algorithms.

The SST (Shear Stress Transport)  $k-\omega$  model by Menter [9.16] is extensively used in this paper. It is formulated to solve the viscous sub-layer explicitly, and requires several computational grid points inside this latter. The model applies the  $k-\omega$  model close to the wall, and the  $k-\varepsilon$  model (in a  $k-\omega$  formulation) in the core region, with a blending function in between. It was originally designed to provide accurate predictions of flow separation under adverse pressure gradients, but it was applied to a large variety of turbulent flows and is now the default and most commonly used model in CFX-18 and other CFD codes. This structural feature of the model to predict in a good way flow separation and recirculation gives a good confidence in applying the model to compute flow blockage in fuel subassemblies. The turbulent Prandtl number in the case of lead was fixed to 1.1, according to the suggestion of the literature [9.17].

## 9.5 Alfred Fa CFD Model And Test Matrix

The Fuel Assembly of the ALFRED Lead cooled reactor was considered here as the reference configuration to investigate. The fuel assembly is a wrapped hexagonal lattice bundle with 127 rods, grid-spaced, with rod diameter  $d=10.5\text{ mm}$ , pitch to diameter ratio  $p/d=1.32$  and an active length  $L=0.65\text{ m}$ . The total thermal power of the reactor is  $Q\sim 300\text{ MW}$ .

A sketch of the fuel assembly seen from the top is shown in Fig. 9.1, while in Tab. 9.3 the main geometrical and physical parameters for the ALFRED FA are reported [9.18]. Fig. 9.2 reports a lateral view sketch of the ALFRED Fuel Assembly.


For the unperturbed case without blockage, a total FA mass flow rate of  $\dot{m}_0 = 144.1\text{ kg/s}$  and a constant temperature ( $T_{inlet}=400\text{ }^\circ\text{C}$ ), boundary conditions were imposed at the inlet coherently with the nominal data reported in Tab. 9.3 and corresponding to the average FA conditions, while pressure boundary conditions were imposed at the outlet. At the internal pin wall in the active region, a constant heat flux  $q_{wall}=1\text{ MW/m}^2$  was imposed. This value represents the highest power FA, and thus the analysis is conservative from an engineering point of view. The shape axial peaking factor in the active region has not been considered at this preliminary stage of the design of the FA.

Moreover, a bulk volumetric source term was evaluated from neutronic data and considered in the active part of the domain, to correctly keep into account the gamma power release. The imposed power density in the fluid is  $10\text{ MW/m}^3$ .

For the cases with flow blockage, inlet mass flow rate boundary conditions were imposed coherently to preliminary RELAP5 computations for different area blockage fraction  $\beta$  [9.19]. For an open element, a blockage does not induce any flow variation in the FA, i.e. the average velocity far upstream of the blockage remains unperturbed. On the opposite, for wrapped elements like the one under investigation here, a blockage increases the hydraulic resistance of the element itself, and the mass flow rate through the element is reduced according to the fraction of the area blocked. It has to be noted that the reduction of mass flow rate is not linear with the reduction of pass-through area, therefore the value of mass flow rate used for the simulation was provided by preliminary RELAP5 computations [9.19].

Tab. 9.4 shows the test matrix adopted for the flow blockage computation in the ALFRED FA. Case 0 corresponds to the unblocked nominal case, the BL GRID parameter identifies the grid in which the blockage is located: lower, middle or upper, Btype indicates the Blockage type.



 <b>RICERCA SISTEMA ELETTRICO</b>	<u>Title:</u> Development of BE numerical tools for LFR design and safety analysis (2018)	<u>Distribution</u> <b>PUBLIC</b>	<u>Issue Date</u> 29.01.2019	<u>Pag.</u>
	<u>Project:</u> ADP ENEA-MSE PAR 2017	Ref. ADPFISS-LP2-167	Rev. 0	149 di 163

A 3D sketch of the computational domain is shown in Fig. 9.3; the spike, the shroud and the funnel have been all included in the CFD model as well as the spacer and the structural grids. This model has been used for all the test cases performed. The spacer grids are positioned 200 mm upstream the active region, at the center of the active region, 100 mm downstream the active region, according to designers' suggestions [9.18]. A fluid domain surrounds the spike and the funnel to impose proper boundary conditions. The geometry of the spike has been modified according to the suggestions of the designers [9.18].

The boundary conditions are mass flow rate and temperature, at the inlet section and 0 bar opening pressure at the outlet. The computational mesh has 25 millions of elements and it is hexagonal dominant multi-block quasi-structured. The active region is composed by 15 millions of elements. The meshing strategy leads to a high quality mesh and this feature increases the global quality of results. Fig. 9.4 shows a detail of the computational mesh in the pin bundle region where an inflation layer has been applied in all the domain with  $y^+=1$  at the walls.

All the simulations performed in this paper reached the full convergence both on the RMS of the residuals ( $RMS < 10^{-5}$ ) and on the monitor points placed in the domain.

## 9.6 Results and Discussion

Fig. 9.5 shows the velocity and temperature distributions in a cross section placed 200 mm downstream the beginning of the active region for case 0 (no blockage). The distributions are regular with the velocity maximum and the temperature minimum at the center of the subchannels. As far as the temperature field is conceived, the edge effect can be noticed with a strong local minimum in the side subchannels.

Fig. 9.6 shows the temperature distribution in the clad in the active region. The distribution is linear as expected with a local maximum around 600°C in the corners at the end of the active region.

Fig. 9.7 shows the cross-section averaged pressure distribution along the FA for case0. The pressure drop in the inlet spike is about 22.1 kPa, while the pressure drop in the bare rods between the grids is around 21.0 kPa/m against 23.7 kPa/m of the Cheng and Todreas correlation [9.20].

For case 1, a sector blockage in the lower grid placed 200 mm upstream the beginning of the active region is set in the computation. The resulting vortex downstream the blockage is evidenced in Fig. 9.8, where the velocity contours and vector plot close to the blockage are shown.


As a results, the velocity at the beginning of the active region ( $z=0$ ) is perturbed, see Fig. 9.9, leading to a perturbed temperature field in the clad shown in Fig. 9.10. A maximum at the end of the active region is present due to the lower mass flow rate in the blocked subchannels. Maximum clad temperature is around 610 °C and is of the same order of the corner pin temperature. Therefore, this type of blockage would not cause any damage to the clad and does not lead to its failure.

For case 2, a two sector blockage is fixed at the lower spacer grid. In this case, the vortex is larger and includes a large part of the active region. This is visible in Fig. 9.11, where the streamwise velocity contours at the beginning of the active region is shown.

There is a stagnation region due to the vortex in the double sector : as a results, a local maximum in the active region due to vortex is expected.

Fig. 9.12 shows the temperature distribution in the active region clad for case 2. The figure shows a local maximum due to the recirculation region at the beginning of the active region, and a maximum at the end of



 <b>RICERCA SISTEMA ELETTRICO</b>	<u>Title:</u> Development of BE numerical tools for LFR design and safety analysis (2018)	<u>Distribution</u> <b>PUBLIC</b>	<u>Issue Date</u> 29.01.2019	<u>Pag.</u>
	<u>Project:</u> ADP ENEA-MSE PAR 2017	Ref. ADPFISS-LP2-167	Rev. 0	150 di 163

the active region due to the lower mass flow rate in the blocked subchannels. In this case the maximum temperature is 682 °C and it is not negligible but still acceptable from a safety point of view.

Fig. 9.13 shows the pin temperature distribution for case 3 with a corner ( $\beta=0.15$ ) blockage at the lower spacer grid. A local maximum of about 650 °C is evidenced at the end of the active region as global effect. The temperature is acceptable from a safety point of view and does not lead to clad failure.

Fig. 9.14 shows the maximum pin temperature distribution in the active region for cases 0, 1, 2, 3. It is confirmed that the case 2 (2 sector blockage) is the most severe case with a local maximum at the beginning of the active region and another maximum at the end of the active region; the distribution is all above the other cases. Case 1 and 3 exhibit a linear trend with the maximum at the end of the active region. Case 0 shows the unperturbed solution with a local maximum at the middle spacer grid.

Fig. 9.15 shows the pin temperature distribution for case 4, single sector blockage at the middle spacer grid. The recirculation vortex takes the upper part of the active region and the temperature maxima reflects this fact. In this case the code computes more than 1000 °C as maximum clad temperature, it means that a serious clad failure is expected with local deformation and clad fusion in the active region. Results are even worst for the double sector case 5 where the recirculation region behind the blockage is larger and the high temperature region is more extended. Therefore, any blockage in the active region produces relevant effects on the clad from a safety point of view and leads to serious clad failure.

The effect of blockage in the upper spacer grid is shown in Fig. 9.16 and Fig. 9.17 for the double sector (case 8). In this case the blockage is downstream the active region, therefore the effect of this kind of blockage on the temperature distribution is driven by the distortion of the streamlines upstream the blockage. Fig. 9.16 shows the streamwise velocity contours in the blockage region. Results show that a stagnation region is present upstream the blockage and this region is extended down to the active region in the corner pin. Therefore, an effect on the temperature distribution is expected in the corner pin region. Fig. 9.17 shows the temperature contours in the clad for case 8. The color scale goes from 400°C to 680°C, with a maximum of about 680 °C located in the corner pin as expected. This maximum value is not so far from the unperturbed value of 610°C and it is not dangerous for the pin clad failure.


Fig. 9.18 shows the maximum pin temperature along the streamwise direction in the active region for case 8 and case 0 (unblocked). The higher slope of case 8 depends on the lower mass flow rate imposed in the double sector case from RELAP computations, while the peak at the end of the active region is marginally influenced by the stagnation region upstream the blockage. Results for case 8 (double sector) show that temperature field is similar to the unblocked case 0. The influence of the blockage on clad temperature for case 7(upper sector) and 9(upper corner) is negligible and the solution is similar to what obtained for case 0.

## 9.7 Conclusions

This report described the CFD model and computations of the ALFRED FA in the nominal configuration and different type of internal blockages. In particular, different type of blockages at the spacer grids are studied by CFD RANS simulations. First, a CFD model is created to keep into account the main physical phenomena involved. Then the model is applied to predict different blockages. The accumulation of debris in the three main spacer grids are considered: lower spacer grid (200 mm upstream the active region), middle spacer grid (at the centre of the active region), upper spacer grid (100 mm downstream the end of the active region). Three different type of blockages have been considered: 1 sector ( $\beta=0.15$ ), 2 sectors ( $\beta=0.30$ ) and corner blockage ( $\beta=0.15$ ).





 <b>RICERCA SISTEMA ELETTRICO</b>	<u>Title:</u> Development of BE numerical tools for LFR design and safety analysis (2018)	<u>Distribution</u> <b>PUBLIC</b>	<u>Issue Date</u> 29.01.2019	<u>Pag.</u>
	<u>Project:</u> ADP ENEA-MSE PAR 2017	Ref. ADPFISS-LP2-167	Rev. 0	151 di 163


Results showed that blockages in the middle spacer grid (active region) produce very significant effects and serious damage of the clad is foreseen for any type of blockage.

Results for the lower spacer grid showed the presence of the recirculating vortex extended downstream well inside the active region for the most severe case (2 sectors). This implies, for the 2 sectors blockage, the presence of two temperature maxima, one at the beginning of the active region due to the vortex (local effect) and one at the end of the active region due to the lower mass flow rate in the blocked subchannels (global effect). A peak temperature of 682 °C is foreseen in this latter case and it is a value acceptable from a safety point of view.

For the lower one sector and corner blockages only the global temperature effect is present with a maximum at the end of the active region of 10 °C and 30 °C (respectively) higher than the unblocked case .

Results for the upper spacer grid (downstream the active region) showed that, even in the most severe case of 2 sector blockage, the velocity field in the active region is marginally perturbed and the temperature field is slightly different from the no blockage case 0 with a maximum temperature of 680°C at the end of the active region. Therefore, blockages in the upper spacer grid produce minor effects on the clad temperature and are not relevant from a safety point of view.



 <b>RICERCA SISTEMA ELETTRICO</b>	<u>Title:</u> Development of BE numerical tools for LFR design and safety analysis (2018)	<u>Distribution</u> <b>PUBLIC</b>	<u>Issue Date</u> 29.01.2019	<u>Pag.</u>
	<u>Project:</u> ADP ENEA-MSE PAR 2017	Ref. ADPFISS-LP2-167	Rev. 0	152 di 163

$\rho$ [kg/m <sup>3</sup> ]	Density	10503
$\nu$ [m <sup>2</sup> /s]	Kinematic viscosity	$1.9 \cdot 10^{-7}$
$k$ [W/mK]	Thermal Conductivity	17.15
$c_p$ [J/kgK]	Specific heat at constant pressure	145.9
Pr [-]	Prandtl number	0.01697
$\alpha$ [1/K]	Thermal expansion coefficient	$1.137 \cdot 10^{-4}$

**Tab. 9.1 Physical properties of Lead at 450 °C.**

$\rho$ [kg/m <sup>3</sup> ]	Density	7800
$k$ [W/mK]	Thermal Conductivity	20.2
$c_p$ [J/kgK]	Specific heat at constant pressure	565


**Tab. 9.2 Physical properties of SS 15-15 Ti (Clad material) at 450 °C.**

Rod diameter $d$	10.5 mm
Pitch to diameter ratio $p/d$	1.32
Subchannel Equivalent Diameter $D_{eq}$	9.68 mm
Number of fuel rods in 1 FA	127
Clearance between assemblies	5 mm
Assembly pitch	171 mm
Mean Assembly Power	1.75 MW
Mean Rod Power	13.814 kW
Mean Wall Heat Flux $q_{wall}$	$0.7 \text{ MW/m}^2$
Conservative Wall Heat Flux (for engineering computations)	$1 \text{ MW/m}^2$
Active Height $L$	0.65 m
Lead Inlet Temperature $T_{inlet}$	400 °C
Lead Outlet Temperature $T_{outlet}$	480 °C
Lead Bulk Velocity	1.4 m/s
Lead flow average FA	144.1 kg/s
Bypass flow average FA (3%)	2.76 kg/s
Clad Maximum Temperature (expected under nominal conditions)	550 °C
Total number of FA in the CORE	171
Total Reactor Thermal Power	300 MW

**Tab. 9.3 Basic Geometrical and Thermal-hydraulic parameters of the DEMO ALFRED Core.**

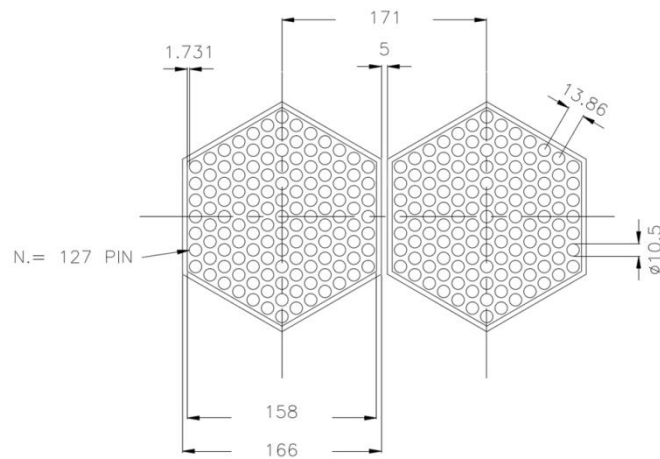
Case N	BL GRID	BIType	$\beta$	$\dot{m}$
0	-	-	0	144.14



 <b>RICERCA SISTEMA ELETTRICO</b>	<u>Title:</u> Development of BE numerical tools for LFR design and safety analysis (2018)	<u>Distribution</u> <b>PUBLIC</b>	<u>Issue Date</u> 29.01.2019	<u>Pag.</u>
	<u>Project:</u> ADP ENEA-MSE PAR 2017	Ref. ADPFISS-LP2-167	Rev. 0	153 di 163

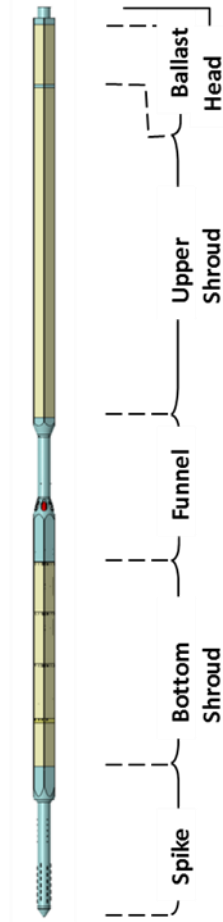
1	Lower	1 Sector	1/6	137.2
2	Lower	2 sectors	1/3	127.1
3	Lower	Corner	0.15	137.0
4	Middle	1 Sector	1/6	137.2
5	Middle	2 sectors	1/3	127.1
6	Middle	Corner	0.15	137.0
7	Upper	1 Sector	1/6	137.2
8	Upper	2 sectors	1/3	127.1
9	Upper	Corner	0.15	137.0

*Tab. 9.4 Test matrix adopted for the flow blockage computations in the ALFRED FA.*

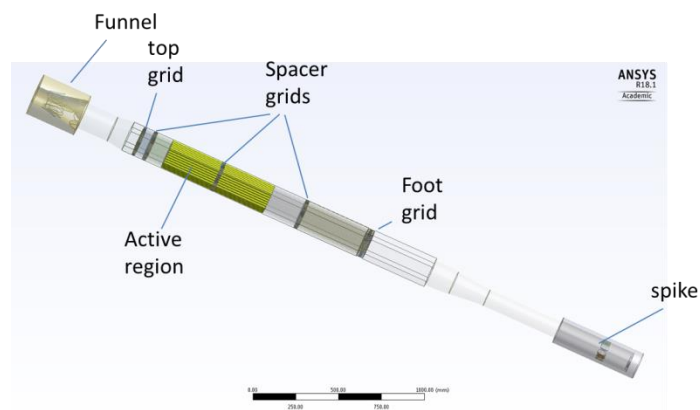


*Fig. 9.1 Sketch of the ALFRED Fuel Assembly: top view.*




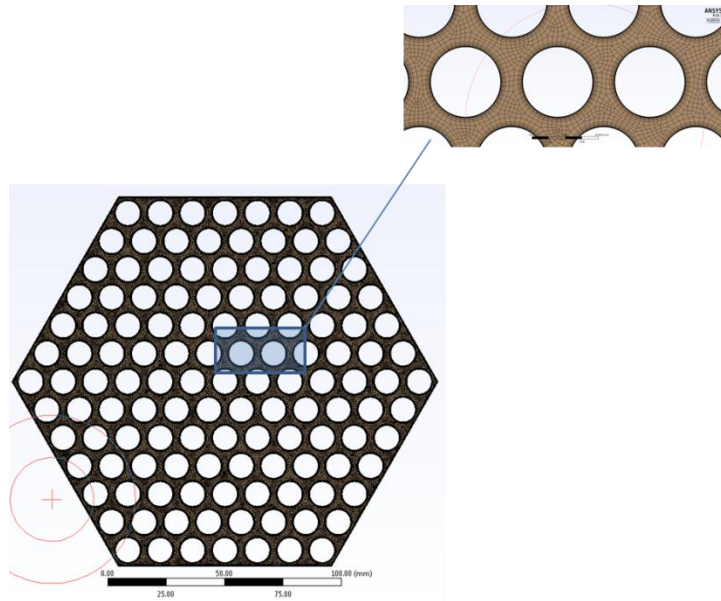


*Fig. 9.2 Sketch of the ALFRED Fuel Assembly: lateral view.*

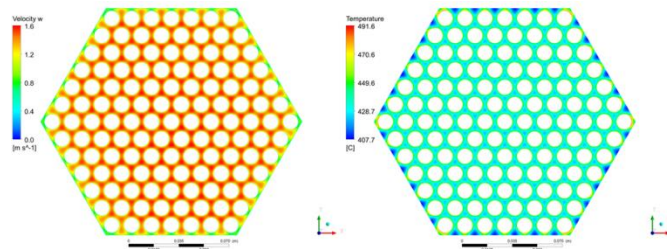


*Fig. 9.3 Sketch of the 3D CFD model adopted.*

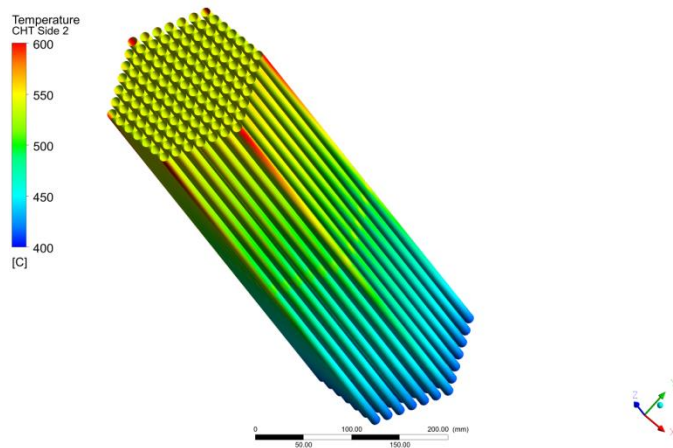
 <b>RICERCA SISTEMA ELETTRICO</b>	<b>Title:</b> Development of BE numerical tools for LFR design and safety analysis (2018)	<b>Distribution</b> <b>PUBLIC</b>	<b>Issue Date</b> 29.01.2019	<b>Pag.</b> 155 di 163
	<b>Project:</b> ADP ENEA-MSE PAR 2017	<b>Ref.</b> ADPFISS-LP2-167	<b>Rev.</b> 0	



*Fig. 9.4 Computational mesh in the fuel pin bundle active region.*



*Fig. 9.5 Velocity and temperature distribution in a cross-section placed 200 mm downstream the beginning of the active region for the unperturbed case 0.*



*Fig. 9.6 Clad temperature distribution for the unperturbed case 0.*



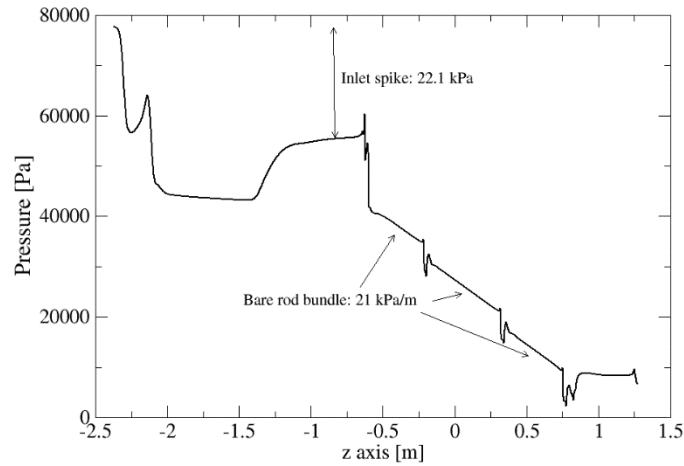


Fig. 9.7 Cross-section averaged pressure distribution along the streamwise direction for case 0.

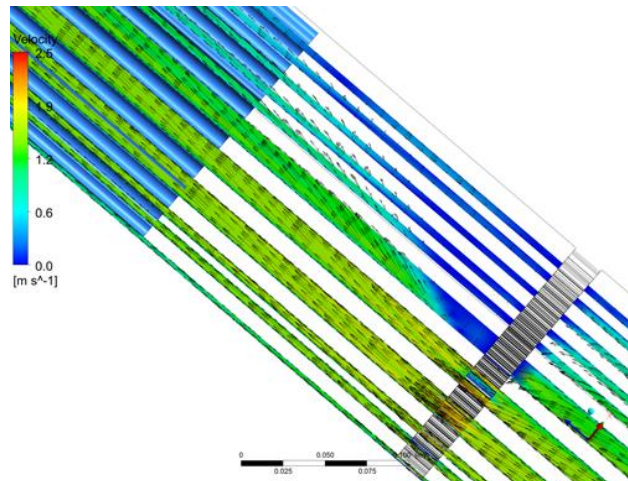


Fig. 9.8 Vortex behind the sector blockage for case 1.

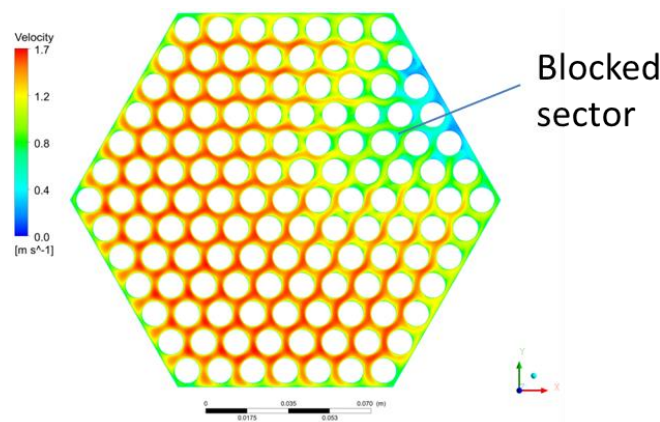


Fig. 9.9 Streamwise velocity contours in a cross section at the beginning of the active region for case 1.

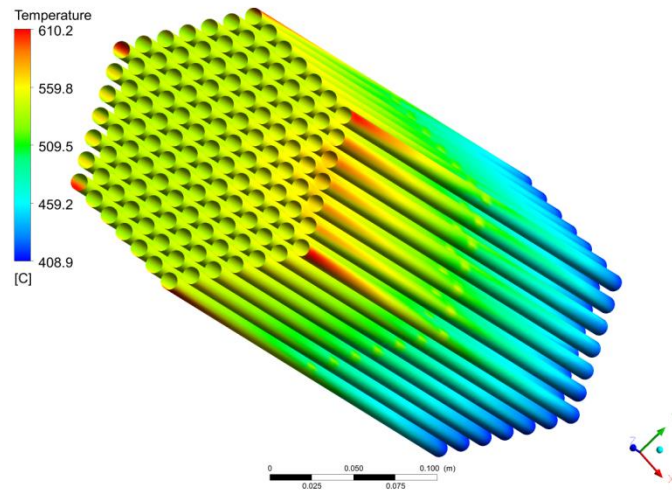


Fig. 9.10 Temperature distribution in the clad for case 1.

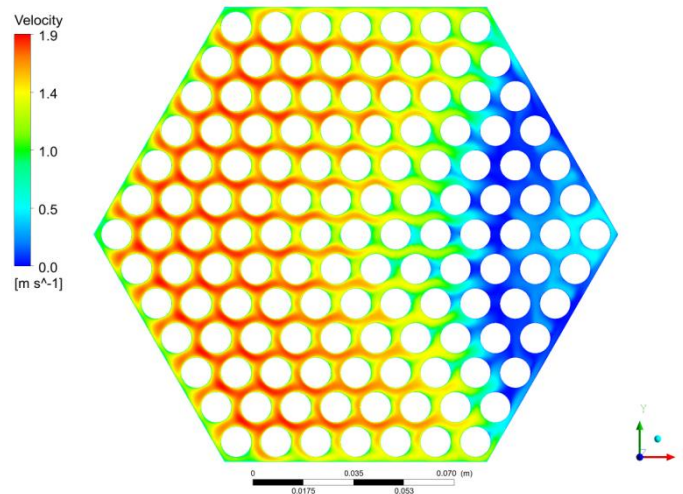


Fig. 9.11 Streamwise velocity contours at the beginning of the active region ( $z=0$ ) for case 2.

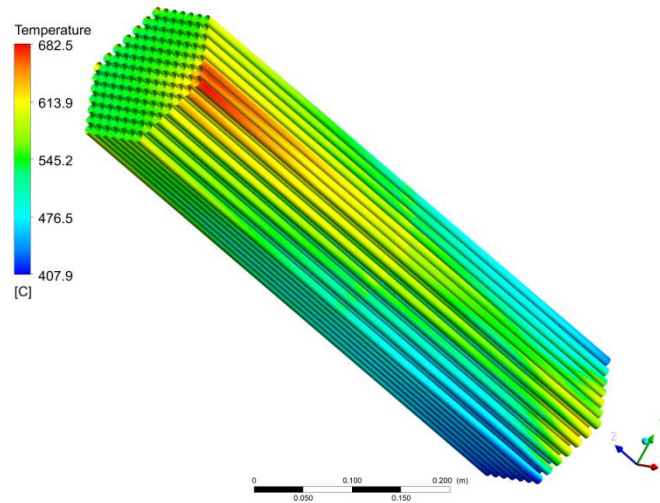


Fig. 9.12 Pin temperature distribution for case 2, double sector blockage at the lower spacer grid.

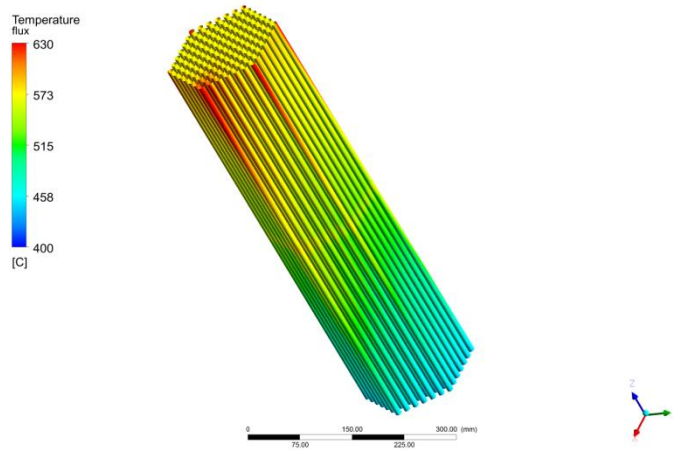


Fig. 9.13 Pin temperature distribution for case 3, corner blockage at the lower spacer grid.

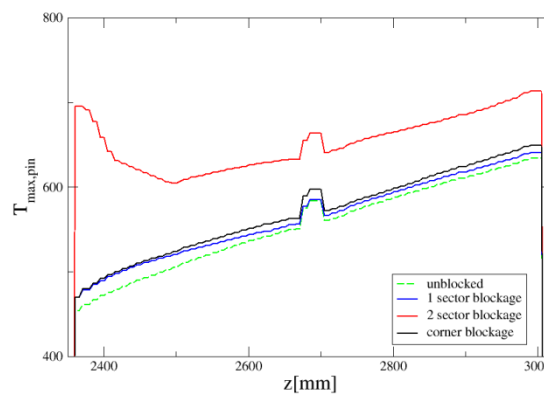


Fig. 9.14 Maximum pin temperature in the active region for the 3 test cases with blockage in the lower grid.



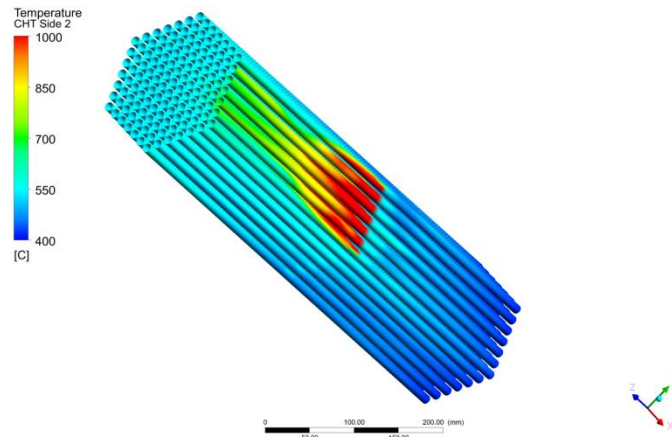


Fig. 9.15 Pin temperature distribution for case 5, single sector blockage at the middle spacer grid.

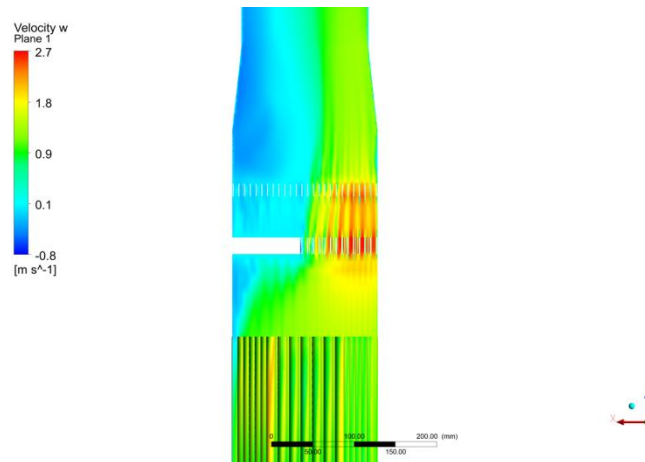


Fig. 9.16 Streamwise velocity contours in the blockage region for case 9 (double sector upper blockage).

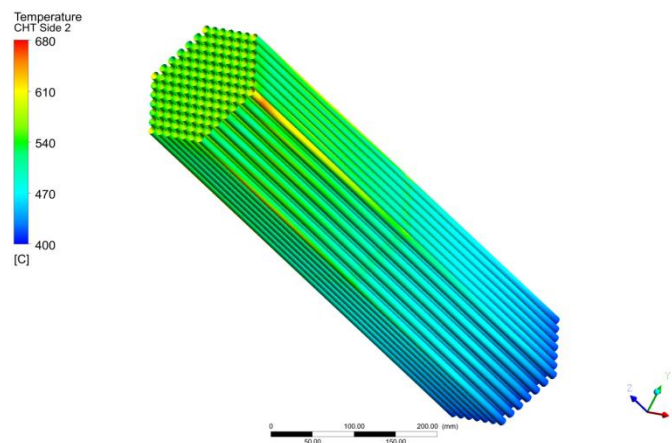

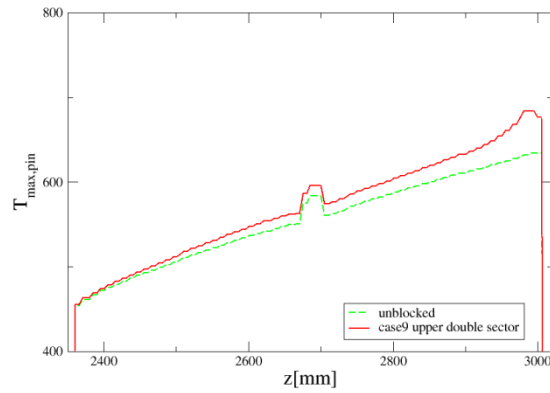



Fig. 9.17 Pin temperature distribution for case 9, double sector blockage at the upper spacer grid.

 <b>RICERCA SISTEMA ELETTRICO</b>	<u>Title:</u> Development of BE numerical tools for LFR design and safety analysis (2018)	<u>Distribution</u> <b>PUBLIC</b>	<u>Issue Date</u> 29.01.2019	<u>Pag.</u> 
	<u>Project:</u> ADP ENEA-MSE PAR 2017	Ref. ADPFISS-LP2-167	Rev. 0	160 di 163



*Fig. 9.18 Maximum pin temperature in the active region for case 8(upper double sector) and case0(unblocked).*




 <b>RICERCA SISTEMA ELETTRICO</b>	<u>Title:</u> Development of BE numerical tools for LFR design and safety analysis (2018)	<u>Distribution</u> <b>PUBLIC</b>	<u>Issue Date</u> 29.01.2019	<u>Pag.</u>
	<u>Project:</u> ADP ENEA-MSE PAR 2017	Ref. ADPFISS-LP2-167	Rev. 0	161 di 163

## 9.8 List of References


- [9.1] OECD Nuclear Energy Agency, "Technology Roadmap Update for Generation IV Nuclear Energy Systems," pp. 1–66, 2014.
- [9.2] M. Frogheri, A. Alemberti, L. Mansani, and A. Nucleare, "The Lead Fast Reactor: Demonstrator (ALFRED) and ELFR Design," *IAEA Conf. FR13*, no. April, 2013.
- [9.3] [NRC "Fermi, Unit 1", NRC Website, 3 February 2011, accessed 17 March 2011.
- [9.4] H.W. Bertini, H.W., "Description of selected accidents that have occurred at nuclear reactor facilities", ORNL/NSIC-176, 1980.
- [9.5] Schultheiss, G.F., (1987) On local blockage formation in sodium cooled reactors. *Nucl. Eng. Des.* 100, 427-433.
- [9.6] I.Di Piazza, F. Magugliani, M. Tarantino, A. Alemberti, (2014) A CFD analysis of flow blockage phenomena in ALFRED LFR demo fuel assembly, *Nucl. Eng. Des.* 276, 202-215.
- [9.7] Han, J.T., Fontana, M.H. (1977) Blockages in LMFBR Fuel Assemblies – A Review. Proc. Winter Annual ASME meeting.
- [9.8] Chang, W.P., Ha, K.S., Suk, S.D., Jeong, H.Y., (2011) A comparative study of the MATRA-LMR-FB calculation with the SABRE result for the flow blockage accident in the sodium cooled fast reactor, *Nucl. Eng. Des.* 241, 5225-5237.
- [9.9] Hooper, J.D., Wood, D.H., (1982) Flow Recovery from a Single Subchannel Blockage in a Square-Pitched Rod Array. *Nucl. Eng. Des.* 74, 91-103.
- [9.10] Kirsch, D., (1975) Investigation on the Flow Temperature Distribution Downstream of Local Coolant Blockages in Rod Bundle Subassemblies, *Nucl. Eng. Des.* 31, 266-279.
- [9.11] Zrodnikov, A.V., Chitaykin, V.I., Gromov, B.F., Grigoryv, O.G., Dedoul, A.V., Toshinski, G.I., Dragunov, Y.G., Stepanov, V.S.. 2000, Use of Russian Technology of ship reactors with lead-bismuth coolant in nuclear power. *Russian Federation Report XA0056274*.
- [9.12] Maity, R.K., Velusamy, K., Selvaraj, P., Chellapandi, P., (2011) Computational fluid dynamic investigations of partial blockage detection by core-temperature monitoring system of a sodium cooled fast reactor. *Nucl. Eng. Des.* 241, 4994-5008.
- [9.13] Lu, Q., Qiu, S., Su, G.H., (2009) Flow Blockage Analysis of a channel in a typical material test reactor core. *Nucl. Eng. Des.* 239, 45-50.
- [9.14] OECD and N. E. Agency, 2015. Handbook on Lead-bismuth Eutectic Alloy and Lead Properties , Materials Compatibility , Thermal- hydraulics and Technologies.
- [9.15] RCC-MRx, 2010. Design and Construction Rules for mechanical components of nuclear installations, ed.AFCEN
- [9.16] Menter, F. R., 1994. Two-equation eddy-viscosity turbulence models for engineering applications. *AIAA J.* 32, 269-289.
- [9.17] Cheng, X., Tak, N.I., (2006) CFD analysis of thermal-hydraulic behaviour of heavy liquid metals in sub-channels, *Nucl. Eng. Des.* 236, 1874-1885.
- [9.18] Alemberti, A., 2018. Private communication.
- [9.19] Bandini, G., Bubelis, E., Schikorr, M., Stempnievicz, M.H., Lazaro, A., Tucek, K., Kudinov, P., Kööp, K., Jeltsov, M., Mansani, L., 2013. Safety Analysis Results of representative DEC accidental transients for the ALFRED reactor, IAEA-CN-199/260.
- [9.20] S. Cheng and N. Todreas, (1986) "Hydrodynamic models and correlations for bare and wire-wrapped hexagonal rod bundles — Bundle friction factors, subchannel friction factors and mixing parameters", *Nucl. Eng. Des.* 92, no. 2, 227-251.



 <b>RICERCA SISTEMA ELETTRICO</b>	<u>Title:</u> Development of BE numerical tools for LFR design and safety analysis (2018)	<u>Distribution</u> <b>PUBLIC</b>	<u>Issue Date</u> 29.01.2019	<u>Pag.</u>
	<u>Project:</u> ADP ENEA-MSE PAR 2017	Ref. ADPFISS-LP2-167	Rev. 0	162 di 163

*(Page intentionally left blank)*



 <b>RICERCA SISTEMA ELETTRICO</b>	<u>Title:</u> Development of BE numerical tools for LFR design and safety analysis (2018)	<u>Distribution</u> <b>PUBLIC</b>	<u>Issue Date</u> 29.01.2019	<u>Pag.</u>
	<u>Project:</u> ADP ENEA-MSE PAR 2017	Ref. ADPFISS-LP2-167	Rev. 0	163 di 163

## DISTRIBUTION LIST

#	NOME	ISTITUZIONE	E-MAIL
1	<i>PAR distribution list</i>		
2			
3			
4			
5			
6			
7			
8			
9			
10			
11			
12			
13			
14			
15			
16			

